

# Numerical Assessment of Propulsive Fuselage Performance in Aircraft Conceptual Design

Anaïs Luisa Habermann

Complete reprint of the dissertation approved by the TUM School of Engineering and Design  
of the Technical University of Munich for the award of the

Doktorin der Ingenieurwissenschaften (Dr.-Ing.)

Chair: Prof. Dr.-Ing. Volker Gümmer

Examiners:

1. Prof. Dr.-Ing. Mirko Hornung
2. Prof. Dr.-Ing. Jens Friedrichs
3. Prof. Dr.-Ing. Sabine Ardey

The dissertation was submitted to the Technical University of Munich on 31.07.2024 and  
accepted by the TUM School of Engineering and Design on 05.03.2025.



# Acknowledgments

The Ph.D. journey is both challenging and rewarding, and though the thesis is an individual achievement my journey has been far from solitary. I am deeply grateful to everybody who accompanied, supported, and inspired me along the way:

To my family, who always support me and never doubt that I can achieve what I set my mind to - *Dankeschön, dass ihr immer für mich da seid.*

To my school and university friends, who ground me by making me translate my niche and nerdy work to what actually counts.

To my (former) colleagues and friends at Bauhaus Luftfahrt e.V., it has been a pleasure working with such a dedicated and friendly team. I have learned so much from all of you over the past years. A special *Dankeschön* to my thesis mentor, Arne Seitz, and to Jochen Kaiser and Fabian Peter — thank you for your time, your thoughtful advice, and your personal support. I am especially grateful to my thesis supervisor, Mirko Hornung, for enabling this work and for his guidance. My sincere thanks also go to Jens Friedrichs and Sabine Ardey for kindly reviewing this thesis, and to Volker Gümmer for chairing the examination committee.

*Danke* Toni, Hagen, and Anna - for making my time in Munich and at Bauhaus Luftfahrt even better, for always finding time for much-needed coffee and chocolate breaks, and for introducing me to fantastic board games, which helped us get through the Covid days. I already miss working with you.

*Ein großes Lob auch an das beste IT-Team am Bauhaus Luftfahrt. Eure kurzfristige und engagierte Unterstützung, selbst in meiner Abwesenheit, hat mir das (Software-)Leben sehr viel einfacher gemacht.*

Throughout this thesis, I had the great opportunity to get to know the aviation research community and meet many bright people who influenced my work. I am particularly thankful to the open-source community for their welcoming spirit. Thank you, Oliver Oxtoby and Johan Heyns, for providing access to the *HiSA* solver and for supporting the addition of the body force model, and Evert Bunschoten for making his body force model validation cases publicly available. Thank you, Jesús Matesanz García, for your insights into the body force model implementation and for hinting me at the *NASA SDT* fan stage validation data, which was kindly provided for use in this thesis by Edmane Envía from *NASA Glenn Research Center*. Additionally, I would like to thank Alejandro Castillo Pardo for making the original *CENTRELINE* fan stage geometry available.

During my time at Bauhaus Luftfahrt I was fortunate to mentor talented students. Thank you, Rebecca Zahn, Anubhav Gokhale, Carlos Mendoza, Marina Freile Ramos, and Nikolaus Romanow for your contributions and fresh perspectives — your work added real value to this thesis.

Above all, *Danke*, Felix – for being there every step of the way. From the very beginning when searching a topic, through the ups and downs of writing this thesis, you were always by my side: encouraging me, challenging me, kicking my ass, and being my "rubber duck" when I needed to talk things through. Thank you for your optimism, patience, and support — especially in the mornings. *Du hast recht, das Leben ist viel schöner zu Zweit.*

Goethe said, „*Man reist nicht, um anzukommen, sondern um zu reisen*“ (“You do not travel to arrive but to travel”). My journey has certainly been one of discovery, learning, and growth. I’m grateful for all it has brought, and I look forward to the new adventures ahead — hopefully finding ways to give back what I have received.



# Abstract

Despite extensive research on the Propulsive Fuselage Concept (PFC), a novel aircraft configuration aimed at reducing aviation's environmental impact, existing numerical models for assessing its aero-propulsive performance in aircraft conceptual design remain inadequate. This research aims to bridge the gap between conventional aircraft design methodology and the challenges attributed to the strong coupling of airframe and propulsion systems inherent to those concepts.

An integral momentum-based bookkeeping approach, joined by key performance indicators, results from a comprehensive review of methods for analyzing the aero-propulsive performance of fuselage-propulsor configurations in aircraft conceptual design. Further, a novel hybrid numerical methodology for assessing a 2D-axisymmetric fuselage-propulsor geometry is proposed. It combines a panel method with a finite volume simulation. A body force model is implemented to accurately predict the bi-directional impact of the fuselage fan on the airflow. The method is developed, validated, and applied to a design parameter study.

The study's findings highlight the intricate, predominantly nonlinear relationship between geometric and operational design parameters and the aero-propulsive and aircraft performance. For the studied configuration, results indicate that the aircraft performance can be improved substantially by minimizing the fuselage-propulsor aggregated force in drag direction through geometric optimization. Direct integration of the numerical method in an aircraft design and sizing framework is not deemed suitable due to the high computational time required by the hybrid numerical approach. However, the method can be employed in a multi-dimensional parameter study to generate inputs for a surrogate model, which can then be seamlessly integrated into an aircraft conceptual design framework.

The developed performance evaluation methodology for PFCs offers insights into optimizing fuselage-propulsor configurations and presents a robust foundation for future advancements in tightly coupled airframe and propulsion concepts toward sustainable aviation.



# Abstract

Trotz umfangreicher Forschungsarbeiten zum Propulsive Fuselage Concept (PFC), einer neuartigen Flugzeugkonfiguration zur Verringerung der Umweltauswirkungen des Luftverkehrs, sind die bestehenden numerischen Modelle zur Bewertung der aeropropulsiven Leistung im Flugzeugvorentwurf unzureichend. Diese Forschungsarbeit zielt darauf ab, die bestehende Lücke zwischen den konventionellen Methoden des Flugzeugvorentwurfs und den Herausforderungen, die durch die starke Kopplung zwischen Flugzeugaerodynamik und Antriebssystem dieser Konzepte entstehen, zu schließen.

Ein Ansatz basierend auf integraler Impulserhaltung, ergänzt durch Leistungsindikatoren, ist das Ergebnis einer umfassenden Studie von Methoden zur Bewertung der aerodynamischen Leistung von Rumpf-Propulsor-Konfigurationen im Flugzeugentwurf. Weiterhin wird ein neuer hybrider numerischer Ansatz für die Analyse einer 2D-achsensymmetrischen Rumpf-Propulsor-Geometrie vorgeschlagen. Er kombiniert eine Panel-Methode mit einer Finite-Volumen Simulation und einem Body-Force-Modell, um die bidirektionalen Auswirkungen von grenzschichteinsaugendem Fan und Rumpfaerodynamik zu modellieren. Die Methode wird implementiert, validiert und in einer beispielhaften Sensitivitätsstudie angewendet.

Die Ergebnisse der Studie verdeutlichen die komplexe, überwiegend nichtlineare Beziehung zwischen geometrischen und operationellen Entwurfsparametern und der Flugzeuleistung. Für die untersuchte Konfiguration zeigen die Ergebnisse, dass die Leistung des Flugzeugs durch eine Minimierung der aggregierten Rumpf-Propulsor-Kraft in Widerstandsrichtung durch geometrische Optimierung erheblich verbessert werden kann. Eine direkte Integration der numerischen Methode in ein Flugzeugvorentwurfsframework ist aufgrund der hohen Rechenzeit, die der hybride Ansatz erfordert, nicht möglich. Die Methode kann jedoch in einer mehrdimensionalen Parameterstudie eingesetzt werden, auf deren Basis ein Ersatzmodell generiert wird, welches in den Flugzeugentwurf integriert werden kann.

Das entwickelte Framework für das Design und die Bewertung von PFCs bietet nicht nur Einblicke in die Optimierung von Rumpf-Propulsor-Konfigurationen, sondern stellt auch eine solide Grundlage für künftige Entwicklungen stark gekoppelter Antriebskonzepte für eine nachhaltige Luftfahrt dar.



# Contents

<b>List of Figures</b>	<b>xiii</b>
<b>List of Tables</b>	<b>xv</b>
<b>List of Symbols</b>	<b>xvii</b>
<b>List of Abbreviations</b>	<b>xxiv</b>
<b>1 Introduction</b>	<b>1</b>
<b>2 Conceptual Aircraft Design of Propulsive Fuselage Concepts</b>	<b>5</b>
2.1 Boundary Layer Ingestion and Propulsive Fuselages . . . . .	5
2.1.1 Boundary Layer Theory . . . . .	5
2.1.2 Boundary Layer Ingestion Benefit . . . . .	7
2.1.3 The Propulsive Fuselage Concept . . . . .	10
2.1.4 Design Challenges of Aircraft Concepts with Boundary Layer Ingestion . . . . .	10
2.2 Propulsive Fuselage Concept Studies in Literature . . . . .	12
2.2.1 Aircraft Concepts . . . . .	12
2.2.2 Conceptual Aircraft Design . . . . .	15
2.2.3 Aero-Propulsive Methods . . . . .	19
2.3 Bookkeeping for Boundary Layer Ingesting Aircraft . . . . .	24
2.3.1 Bookkeeping Schemes . . . . .	25
2.3.1.1 Integral Momentum Methods . . . . .	25
2.3.1.2 Integral Energy Methods . . . . .	26
2.3.2 Figures of Merit . . . . .	27
2.3.2.1 Conventional Performance Indicators . . . . .	27
2.3.2.2 Assessment Criteria . . . . .	28
2.3.2.3 Power Saving Coefficient and Propulsive Efficiency . . . . .	29
2.3.2.4 Thrust Benefit and Net Propulsive Force . . . . .	30
2.3.2.5 Mechanical Flow Power, Power-Based Propulsive Efficiency, and Power Saving Coefficient . . . . .	31
2.3.2.6 Exergy-Recovery Coefficient . . . . .	33
2.4 Synthesis and Research Questions . . . . .	33

<b>3</b>	<b>Review of Numerical Methods for Boundary Layer Ingestion Aero-Propulsive Performance Evaluation</b>	<b>35</b>
3.1	Flow Characteristics of Boundary Layer Ingestion in Transonic Flow Conditions . . . . .	35
3.2	Governing Equations . . . . .	36
3.3	Numerical Methods . . . . .	38
3.4	Most Suitable Method . . . . .	39
<b>4</b>	<b>Unified Performance Bookkeeping Approach for Propulsive Fuselage Concepts</b>	<b>41</b>
4.1	Control Volume and Forces Definition . . . . .	42
4.2	Figures of Merit . . . . .	43
4.2.1	Energy Specific Air Range . . . . .	43
4.2.2	Power Saving Coefficient . . . . .	43
4.2.3	Net Propulsive Force and Boundary Layer Ingestion Efficiency Factor . . . . .	43
4.2.4	Kinetic Energy Defect . . . . .	44
4.2.5	Ingested Defect Ratio . . . . .	45
4.2.6	Radial Distortion . . . . .	45
<b>5</b>	<b>Hybrid Numerical Method for Aero-Propulsive Boundary Layer Ingestion Assessment</b>	<b>47</b>
5.1	Reference Aircraft Configuration . . . . .	48
5.2	Assumptions and Limitations . . . . .	49
5.3	Geometry Parameterization . . . . .	50
5.3.1	Design Parameters . . . . .	50
5.3.2	Intuitive Class/Shape Function Transformation . . . . .	52
5.4	Panel Method . . . . .	55
5.4.1	Potential Flow Solution . . . . .	55
5.4.1.1	Hess-Smith Panel Method . . . . .	55
5.4.1.2	Compressibility Correction . . . . .	57
5.4.2	Integral Boundary Layer Prediction Method . . . . .	58
5.4.2.1	Laminar Boundary Layer . . . . .	60
5.4.2.2	Turbulent Boundary Layer . . . . .	61
5.4.2.3	Transition Prediction . . . . .	63
5.4.2.4	Handling of Separation and Shock Waves . . . . .	64
5.4.2.5	Viscous/Inviscid Coupling . . . . .	64
5.4.3	Validation . . . . .	66
5.5	Interface . . . . .	68
5.5.1	Interface Location . . . . .	68
5.5.2	Potential Flow Interface . . . . .	69

---

5.5.3	Boundary Layer Interface . . . . .	70
5.5.4	Verification . . . . .	75
5.6	Finite Volume Reynolds-Averaged Navier-Stokes Method . . . . .	76
5.6.1	HiSA Solver . . . . .	76
5.6.2	Simulation Setup . . . . .	77
5.6.3	Fan Model . . . . .	79
5.6.3.1	Body Force Model . . . . .	79
5.6.3.2	Implementation . . . . .	81
5.6.3.3	Verification . . . . .	82
5.6.3.4	Validation . . . . .	84
5.6.3.5	Scaling of CENTRELINE Fan Stage . . . . .	91
5.6.4	Grid . . . . .	93
5.6.4.1	Grid Generation . . . . .	93
5.6.4.2	Grid Convergence . . . . .	94
5.6.5	Interface Boundary Condition . . . . .	96
5.7	Verification and (Pseudo-)Validation of Hybrid Method . . . . .	96
<b>6</b>	<b>Parameter Study</b>	<b>101</b>
<b>7</b>	<b>Aircraft Level Considerations</b>	<b>113</b>
7.1	Impact of Fuselage-Propulsor Design on Design Mission Block Fuel . . . . .	113
7.2	Integration of Aero-Propulsive Performance Data in Aircraft Design Framework . . . . .	117
<b>8</b>	<b>Conclusion and Future Directions</b>	<b>121</b>
	<b>Bibliography</b>	<b>137</b>
	<b>Publications</b>	<b>137</b>
	<b>Supervised Student Theses</b>	<b>138</b>
	<b>Appendix</b>	<b>141</b>
A.1	Appendix 1 - Code . . . . .	141
A.2	Appendix 2 - iCST Parameterization . . . . .	141
A.3	Appendix 3 - Overview of Validation Cases . . . . .	146
A.4	Appendix 4 - Interface Location Definition . . . . .	147
A.5	Appendix 5 - Velocity Profile Validation . . . . .	150
A.6	Appendix 6 - Full Finite Volume Grid Convergence Study . . . . .	153
A.7	Appendix 7 - Parameter Study Results . . . . .	155



# List of Figures

1.1	Rendering of the turbo-electric PFC developed in the <i>CENTRELINE</i> project. . . . .	1
2.1	Relationship between BL thickness $\delta$ , displacement thickness $\delta^*$ , and momentum thickness $\theta$ . . . . .	7
2.2	Exemplary comparison of non-BLI and ideal BLI configuration. . . . .	9
2.3	Sketch of a PFC with FF inlet distortion. . . . .	11
2.4	Sketch of first aircraft concepts with BLI propulsion. . . . .	13
2.5	Publications regarding WI, BLI, PFC, and a combination of all keywords since 1993. Publications affiliated with international research institutions since 1993. . . . .	14
2.6	Design studies, which contributed to the integrated aircraft design in the <i>CENTRELINE</i> project. . . . .	17
2.7	Methods employed for the aero-propulsive performance assessment of PFCs in literature. . . . .	21
2.8	Classification of bookkeeping schemes. . . . .	26
2.9	Rating of figures of merit. . . . .	29
2.10	CV for the application of the power balance method. . . . .	31
3.1	BL edge of the powered reference fuselage-propulsor configuration and the bare fuselage derived from RANS CFD results. . . . .	36
3.2	Governing equations and corresponding assumptions to describe the motion of fluids. . . . .	37
4.1	CV scheme employed in current study. . . . .	42
5.1	Overview of hybrid numerical method. . . . .	47
5.2	Sketch of the <i>CENTRELINE</i> aircraft configuration and turbo-electric propulsion system. . . . .	48
5.3	Geometry parameterization. . . . .	51
5.4	Incompressible BL edge velocity distribution for <i>Fuselage</i> geometry. . . . .	57
5.5	Pressure coefficient distribution at edge of BL for <i>Waisted Body</i> and <i>Equivalent Fuselage</i> . . . . .	58
5.6	Curvilinear and axisymmetric coordinate system employed for IBL method. . . . .	59
5.7	BL characteristics for the rear part of the <i>6:1 Spheroid</i> . . . . .	65
5.8	BL characteristics for the <i>Waisted Body</i> at $Ma=0.6$ . . . . .	67
5.9	BL edge and wall pressure coefficient of the reference geometry obtained by FVM, PM, and HPFVM. . . . .	68
5.10	Interface location considerations. . . . .	69
5.11	Velocity and temperature profile difference between PM and FVM results at different fuselage locations for the reference geometry. . . . .	70
5.12	Skin friction and pressure coefficient distribution of the reference geometry for the identification of an adequate PM/FVM interface location. . . . .	71

5.13 Exemplary velocity profile of a turbulent BL. . . . .	72
5.14 Validation of velocity profile prediction for IBL method. . . . .	74
5.15 Velocity and temperature profile difference between FVM and HPFVM results at different fuselage and duct locations for the reference geometry. . . . .	75
5.16 Skin friction coefficient of the reference geometry obtained by FVM, PM, and HPFVM. . . . .	76
5.17 Sketch of the 2D-axisymmetric FVM domain for the reference geometry. . . . .	77
5.18 FV CFD setup validation. . . . .	78
5.19 Exemplary <i>NASA R4</i> rotor cross section. . . . .	80
5.20 Extraction of rotor blade camber and blockage distribution and interpolation of data on the computational grid. . . . .	82
5.21 Mesh 1 and Mesh 2 with corresponding <i>Ma</i> distribution. . . . .	83
5.22 Parallel force verification. . . . .	83
5.23 Blockage term verification. . . . .	84
5.24 Side view of the coarse mesh with full BL resolution for <i>NASA SDT</i> fan stage validation. . . . .	85
5.25 Grid convergence results for <i>NASA SDT</i> fan stage validation. . . . .	87
5.26 Fan stage adiabatic efficiency distribution for BFM design case ( $p_{out} = 897\text{hPa}$ , $\Omega = 87.5\%\Omega_{max}$ ) and $k-\omega$ -SST turbulence model for <i>NASA SDT</i> fan stage grid convergence study. . . . .	88
5.27 Fan stage pressure ratio and <i>Ma</i> distribution at stator exit station for BFM design case ( $p_{out} = 897\text{hPa}$ , $\Omega = 87.5\%\Omega_{max}$ ) for grid 1 with BL resolution and turbulence model variation for <i>NASA SDT</i> fan stage grid convergence study. . . . .	89
5.28 Fan stage pressure ratio and adiabatic efficiency for the <i>NASA SDT</i> validation study. . . . .	90
5.29 Spanwise radial profiles measured at the rotor exit station for the nominal operation point of $87.5\%\Omega_{max}$ ( $Q = 0.02845$ ). . . . .	91
5.30 PFC geometry with scaled <i>CENTRELINE</i> Fan B. . . . .	93
5.31 Grid inside the FF duct for the reference geometry. . . . .	93
5.32 Comparison of pressure and skin friction coefficient distribution along fuselage and nacelle surface for a grid with full BLr resolution compared to wall functions. . . . .	94
5.33 Grid convergence results for hybrid BLI FV domain. . . . .	95
5.34 Normalized velocity distribution of the HPFVM simulation in the vicinity of the nacelle LE for the reference geometry. . . . .	97
5.35 Skin friction and pressure coefficient distribution for the reference geometry for PM (fuselage only), full FVM, and HPFVM. . . . .	98
5.36 Comparison of total pressure distribution for the reference geometry. . . . .	99
6.1 Relationship between FF force, FF shaft power, and <i>FPR</i> . . . . .	102
6.2 Relationship between NPP, FF shaft power, and $f_{\eta,BLI}$ . . . . .	102
6.3 Extended parameter exploration study results. . . . .	104
6.4 Nonlinear aerodynamic behavior for $r_{f,cent}$ parameter variation. . . . .	105

6.5	Pressure and skin friction distribution along nacelle contour for $r_{max}$ variation. . . . .	106
6.6	Static pressure at FF outlet for $\beta_{TE,low}$ variation and $KED_A$ difference between trailing edge and AIP station for $\Theta_{f,cone}$ variation. . . . .	107
6.7	Nacelle and fuselage geometry, static pressure at the nozzle exit, pressure distribution along the fuselage contour, and $Ma$ distribution near the nacelle for $f_{r8,hub}$ variation. . . . .	108
6.8	Nacelle and fuselage geometry for $f_{r,thr,tip}$ variation. . . . .	109
6.9	Nacelle and fuselage geometry, static temperature at the rotor inlet, pressure distribution along the nacelle duct contour, and $T_s$ distribution near the nacelle for $\beta_{rot,in}$ variation. . . . .	110
7.1	Aircraft sensitivity study results for $NPF_{PFC,bare}$ and isolated FF isentropic design shaft power. . . . .	113
7.2	Relationship between $NPF_{PFC,bare}$ , FF shaft power, and BF. . . . .	115
7.3	Design mission fuel burn impact of selected geometric parameters. . . . .	115
7.4	Pressure and skin friction distribution along nacelle contour for $f_{r,2}$ variation. . . . .	116
A.1	Pressure and skin friction coefficient difference between full fuselage-propulsor and isolated fuselage configuration for different geometries. . . . .	147
A.2	Velocity and temperature profiles at different fuselage locations for the reference geometry. . . . .	148
A.3	Distribution of dimensionless velocity in the boundary layer for different velocity profile models based on the results of the IBL method. . . . .	150
A.4	Validation of velocity profile prediction for IBL method. . . . .	151
A.5	Grid convergence for full BLI FV domain. . . . .	153
A.6	Sensitivity study results 1/9. . . . .	156
A.7	Sensitivity study results 2/9. . . . .	157
A.8	Sensitivity study results 3/9. . . . .	158
A.9	Sensitivity study results 4/9. . . . .	159
A.10	Sensitivity study results 5/9. . . . .	160
A.11	Sensitivity study results 6/9. . . . .	161
A.12	Sensitivity study results 7/9. . . . .	162
A.13	Sensitivity study results 8/9. . . . .	163
A.14	Sensitivity study results 9/9. . . . .	164
A.15	Selected parameter study results - surface and FF forces. . . . .	165



# List of Tables

2.1	Assessment criteria for BLI figures of merit. . . . .	28
5.1	Comparison of transition location prediction compared against experimental data. . . . .	63
5.2	Reference values for <i>NASA SDT</i> fan stage validation. . . . .	85
5.3	Results for <i>NASA SDT</i> fan stage grid discretization study. . . . .	87
5.4	Results for grid discretization study for hybrid FV BLI domain with $k-\omega$ -SST turbulence model and fully resolved BL. . . . .	96
5.5	Comparison of integrated surface forces for the reference geometry obtained with FVM, original HPFVM, and with combined pressure and smoothened skin friction distribution. . . . .	97
5.6	Comparison of integrated FF variables for reference geometry with $FPR=1.4$ . . . . .	97
A.1	Geometrical and operational design parameters. . . . .	141
A.2	Design parameters used for iCST parameterization. . . . .	142
A.3	Constraints used for fuselage iCST parameterization. . . . .	143
A.4	Constraints used for nacelle iCST parameterization. . . . .	144
A.5	Overview of employed validation cases. . . . .	146
A.6	Results for grid discretization study for full FV BLI domain with $k-\omega$ -SST turbulence model. . . . .	154



# List of Symbols

## Physical Units

Symbol	Unit	Description
$a$	–	Function Coefficient
$A$	$\text{m}^2$	Area
$\mathbf{A}$		Coefficient Matrix
$A_{i,j}$	–	Normal Influence Coefficient
$AR$	–	Aspect Ratio
$b$	–	Geometric Blockage Factor
$b$	–	Inhomogenous Term
$\mathbf{b}$		Vector of Inhomogenous Terms
$bp$	–	Bernstein Polynomial Coefficient
$BF$	kg	Block Fuel
$BP$		Bernstein Polynomial
$c$	m	Chord Length
$c$	m	Curve Length
$c_p$	$\frac{\text{J}}{\text{kgK}}$	Heat Capacity Ratio at Constant Pressure
$C$	–	Coefficient
$C$	–	Class Function
$C$	–	Weighting Factor
$C^+$	–	Coles Coefficient
$C_E$	–	Entrainment Coefficient
$C_f$	–	Skin Friction Coefficient
$C_p$	–	Pressure Coefficient
$C_{PK}$	–	Net Propulsor Power Coefficient
$\text{CO}_2$		Carbon Dioxide
$d$	m	Diameter
$dp/dx$	$\frac{\text{Pa}}{\text{m}}$	Pressure Gradient
$D$	m	Dimension
$D$	N	Drag
$D_f$	N	Skin Friction Drag
$D_p$	N	Pressure Drag
$\frac{Df}{Dt} = \frac{\partial f}{\partial t} + \mathbf{u} \cdot \nabla f$		Material Derivative
$E$	$\frac{\text{m}^2}{\text{s}^2}$	Specific Total Enthalpy
$E$	W	Energy
$e_a$	–	Approximate Relative Error
$e_{ext}$	–	Extraploated Relative Error
$ERC$	–	Energy Recovery Coefficient
$ESAR$	$\frac{1}{\text{N}}$	Energy Specific Air Range
$f$	–	Factor
$f_{\eta,BLI,bare}$	–	Bare Boundary Layer Ingestion Efficiency Factor

$\mathbf{f}$	N	Vector of Blade Forces
$F$	N	Force
$F_N$	N	Net Thrust
$FPR$	—	Fan Pressure Ratio
$g$	$\frac{m}{s^2}$	Gravity Acceleration
$\mathbf{g}$	$\frac{m}{s^2}$	Gravity Acceleration Vector
$G$	—	Velocity Defect Factor
$h$	$\frac{m^2}{s^2}$	Specific Enthalpy
$h$	—	Representative Cell Size
$h$	m	Height
$h_t$	$\frac{J}{kg}$	Specific Total Enthalpy
$H$	—	Shape Factor
$H^*$	—	Energy Factor
$i$	rad	Incidence Angle
$\dot{I}$	N	Momentum Flow
$I_k$	m	Curvature Integral
$I_p$	m	Pressure Integral
$k$	—	Degree of CST Function
$k$	$\frac{m^2}{s^2}$	Turbulent Kinetic Energy
$k$	$\frac{kg\ mK}{s^2}$	Thermal Conductivity
$K$	—	Pseudoenergy Factor
$KEDA$	W	Area Based Kinetic Energy Defect
$K_{Mach}$	—	Compressibility Coefficient
$l$	m	Length
$L$	m	Total Length
$L$	N	Lift
$L$	—	Likelihood
$m$	m	Mass
$\dot{m}$	$\frac{kg}{s}$	Massflow
$Ma$	—	Mach number
$MAPE$	—	Mean Absolute Percentage Error
$MD_A$	N	Area Based Momentum Defect
$MTOM$	kg	Maximum Take-Off Mass
$n, N$	—	Number
$n$	—	Order of Bernstein Polynomial
$\mathbf{n}$	—	Normal Vector
$N$	—	Exponent
$NO_x$	—	Nitrogen Oxides
$NPF$	N	Net Propulsive Force
$NPP$	W	Net Propulsive Power
$OEM$	kg	Operating Empty Mass
$p$	Pa	Pressure
$p$	—	Apparent Order
$P$	W	Power

$P_K$	W	Net Propulsor Mechanical Flow Power
$P_R$	W	Required Power
$P_S$	W	Net Propulsor Shaft Power
$P_V$	W	Net Pressure Volume Power
$PAV$	Pa	Average Total Pressure
$PSC$	–	Power Saving Coefficient
$PFAV$	Pa	Face Average Total Pressure
$Pr$	–	Prandtl Number
$PR$	–	Pressure Ratio
$q$	Pa	Dynamic Pressure
$Q$	$\frac{m^2}{s}$	Quantity Flow in the BL per Unit Time per Unit Span
$Q$	–	Flow Capacity
$r$	m	Radius
$r$	–	Adiabatic Recovery Factor
$r$	–	Grid Refinement Factor
$r_0$	m	Transverse Radius
$R$	m	Curvature Radius
$R$	–	Recovery Factor
$R$	–	Wake Recovery
$R$	m	Range
$R$	rad	Curvature Radius
$R^2$	–	Coefficient of Determination
$R_{KEDA}$	–	Kinetic Energy Defect Recovery Factor
$Re$	–	Reynolds Number
$Re_\theta$	–	Momentum Thickness Based Reynolds Number
$RMSE$	–	Root Mean Square Error
$s$	m	Local Blade Pitch
$s$	$\frac{J}{kgK}$	Specific Entropy
$S$	$m^2$	Surface Area
$S$	–	Shape Function
$S$		Source Term
$S^+$		External Body Surface
$t$	s	Time
$T$	K	Temperature
$T$	N	Thrust
$TB$	%	Thrust Benefit
$\frac{t}{c}$	–	Thickness-to-Chord Ratio
$u, U$	$\frac{m}{s}$	Velocity
$u$	$\frac{m}{s}$	Tangential Velocity in Boundary Layer
$\bar{u}$	$\frac{m}{s}$	Mean Component of the Velocity
$u'$	$\frac{m}{s}$	Fluctuating Component of the Velocity
$u^+$	–	Dimensionless Velocity
$u_\tau$	$\frac{m}{s}$	Friction Velocity
$v$	$\frac{m}{s}$	Normal Velocity in Boundary Layer

$V$	$\text{m}^3$	Volume
$\mathbf{v}, \mathbf{V}$	$\frac{\text{m}}{\text{s}}$	Velocity Vector
$w$	$\frac{\text{kg}}{\text{s}}$	Mass Flow
$W$	$\frac{\text{l}}{\text{m}}$	Velocity Disturbance
$W$	$\frac{\text{m}}{\text{s}}$	Local Relative Velocity Magnitude
$W(\cdot)$		Law of the Wake
$\mathbf{x}, \mathbf{X}$		Input Vector
$y^+$	—	Dimensionless Wall Distance
$x, y, z$		Cartesian Coordinates
$x, r, \Theta$		Cylindrical Coordinates
$\alpha$	rad	Swirl Angle
$\beta$	—	Ratio of Ingested Boundary Layer
$\beta$	—	Ratio of Ingested Defect
$\beta$	rad	Geometric Angle
$\beta$	—	Pressure Gradient Parameter
$\beta$	—	Ratio of Uningested to Ingested Drag
$\gamma$	rad	Panel Angle
$\gamma$	—	Specific Heat Ratio
$\delta$	m	Boundary Layer Thickness
$\delta$	rad	Local Flow Deviation Angle
$\delta_{ij}$		Kronecker Delta
$\delta^*$	m	Displacement Thickness
$\Delta^*$	$\text{m}^2$	Displacement Area
$\dot{\epsilon}$	W	Mechanical Energy Outflow Rate
$\eta$	Pas	Dynamic Viscosity
$\eta$	—	Efficiency
$\theta$	rad	Geometric Angle
$\theta$	m	Momentum Thickness
$\Theta$	$\text{m}^2$	Momentum Deficit Area
$\Theta^*$	$\text{m}^2$	Kinetic Energy Thickness Area
$\Theta_A$	$\text{m}^2$	Wake Momentum Area
$\kappa$	$\frac{1}{\text{rad}}$	Curvature
$\kappa$	—	Von Karman Constant
$\lambda$	—	Pressure Gradient Parameter
$\mu$	$\frac{\text{Ns}}{\text{m}^2}$	Dynamic Viscosity
$\nu$	$\frac{\text{m}^2 \text{s}}{\text{kg}}$	Kinematic Viscosity
$\xi$	—	Non-Dimensional y-Coordinate
$\Pi$	—	Dimensionless Blade Speed
$\Pi$	—	Modified Pressure Gradient Parameter
$\Pi$	—	Wake Parameter/Strength
$\rho$	$\frac{\text{kg}}{\text{m}^3}$	Density
$\rho$	—	Non-Dimensional Radius
$\sigma$	$\frac{\text{m}^2}{\text{s}}$	Source Strength

$\sigma_{i,j}$	$\frac{\text{N}}{\text{m}^2}$	Components of Viscous Stress Tensor
$\bar{\tau}$	Pa	Viscous Stress Tensor
$\tau_w$	$\frac{\text{kg s}^2}{\text{m}^2}$	Wall Shear Stress
$\varphi$	$\frac{\text{m}^2}{\text{s}}$	Velocity Potential
$\varphi_{\sigma,ij}$	$\frac{\text{m}^2}{\text{s}}$	Disturbance Potential
$\Phi$	N	Force
$\Phi$	W	Dissipation
$\Phi$	rad	Local Body Slope Angle
$\Phi$		Variable
$\Phi_{ext}$		Extrapolated Value
$\psi$	—	Non-Dimensional x-Coordinate
$\omega$	$\frac{\text{m}}{\text{s}^2}$	Specific Dissipation Rate
$\Omega$	—	Rotational Speed
$\nabla$		Nabla Operator

*Sub- and Superscripts*

Symbol	Description
0	Reference
0	Body Surface
0	Propulsor Station 0; Freestream Air Conditions
1	Propulsor Station 1; Propulsor Inlet
2	Propulsor Station 2; Fan Front Face / Rotor Inlet
22	Propulsor Station 22; Rotor Outlet
23	Propulsor Station 23; Stator Inlet
3	Propulsor Station 3; Compressor Discharge / Stator Outlet
8	Propulsor Station 8; Nozzle Throat / Nozzle Exit
ad	Adiabatic
alt	Altitude
A	Area
AC	Aircraft
c	Compressible
cent	Center
con	Constraint
cr	Cruise
crit	Critical
d	Disturbance
e	At Boundary Layer Edge
ec	Energy Conversion
exp	Experimental
E	Entrainment
f	Fuselage
f	Friction

---

ff	Fan Face
FF	Fuselage Fan
G	Gross
hi	Highlight
hub	Hub
i	Incompressible
i	Integrated
ing	Ingested
int	Intake
is	Isentropic
j	Downstream of Boundary Layer Ingesting Propulsor
L	Length
LE	Leading Edge
min	Minimum
max	Maximum
n	Normal
nac	Nacelle
ov	Overall
p	Point
p	Parallel
p	Propulsive
p	Profile
P	Propulsor
ph	Physical
pl	Planar
pol	Polytropic
pot	Potential
PS	Pressure Side
r	Relative
R	Required
ref	Reference
rev	Reversible
rot	Rotor
rot	Rotational
s	Shaft
s	Static
st	Stage
stat	Stator
sup	Supply
surf	Surface
SS	Suction Side
t	Stagnation / Total
thr	Throat
thr	Thrust
tip	Tip

---

tot	Total
tr	Transmission
T	Transpiration
TE	Trailing Edge
v	Viscous
vort	Vortex
w	Wake
w	Wall
wet	Wetted
'	Derivative
"	Non-Boundary Layer Ingestion
$\infty$	Freestream

# List of Abbreviations

Abbreviation	Description
AD	Actuator Disk
ADEC	Advanced Engine and Aircraft Configurations
AIP	Aerodynamic Interface Plane
ANSYS	ANalysis SYStem
AZ	Actuator Zone
BC	Boundary Condition
BFM	Body Force Model
BL	Boundary Layer
BLE	Boundary Layer Equation
BLI	Boundary Layer Ingestion
BWB	Blended Wing Body
CAD	Computer-Aided Design
CENTRELINE	ConcEpt validation sTudy foR fusElage wake-fILIng propulsioN intEgration
CFD	Computational Fluid Dynamics
CST	Class/Shape Transformation
CV	Control Volume
DisPURSAL	Distributed Propulsion and Ultra-high By-Pass Rotor Study at Aircraft Level
DNS	Direct Numerical Simulation
DoE	Design of Experiment
DPC	Disruptive Propulsive Concept
EC	European Commission
EIS	Entry Into Service
EMP	EMPIrical
EUL	EULer
EXP	EXPeriment
FANS	Favre-Averaged Navier Stokes
FDM	Finite Difference Method
FEA	Finite Element Analysis
FEM	Finite Element Methods
FF	Fuselage Fan
FL	Flight Level
FreeCAD	Free Computer-Aided Design
FV	Finite Volume
FVM	Finite Volume Method
GCI	Grid Convergence Index
GTF	Geared Turbo-Fan
HECARRUS	Hybrid ElectriC smAll commuteR aiRcraft conceptUal deSign
HiSA	High Speed Aerodynamic Solver
HPFVM	Hybrid Panel/Finite Volume Method
HTP	Horizontal Tail Plane
HWB	Hybrid Wing Body

---

HYPER-F	HYbrid electric Propulsion for Emission Reduction in Flight
IBL	Integral Boundary Layer
IBLE	Integral Boundary Layer Equation
iCST	intuitive Class/Shape function Transformation
ISA	International Standard Atmosphere
KED	Kinetic Energy Defect
L	Linear
LHS	Latin Hypercube Sampling
LWLOG	LOGarithmic Law of the Wall
LWSPALD	SPALding's Law of the Wall
MIDAP	Ministry-Industry Drag Analysis Panel
MTFLOW	Multielement Through-FLOW
NASA	National Aeronautics and Space Administration
NSE	Navier-Stokes Equation
NURBS	Non-Uniform Rational B-Spline
ODE	Ordinary Differential Equation
OGV	Outlet Guide Vane
OpenFOAM	Open Field Operation and Manipulation
ORFEC	Over- and Rear-Fuselage Engines Concept
P2	Second order Polynomial
PAX	Passengers
PBM	Power Balance Method
PCM	Parallel Compressor Model
PDE	Partial Differential Equation
PEGASUS	Parallel Electric-Gas Architecture with Synergistic Utilization Scheme
PFC	Propulsive Fuselage Concept
PM	Panel Method
RANS	Reynolds-Averaged Navier-Stokes
REG	REGression
RHS	Right Hand Side
RME	Rear Mounted Engine
RQ	Research Question
ShapePFC	Swift Hybrid numerical method for Aero-propulsive Performance Evaluation of Propulsive Fuselage Concepts
SDT	Source Diagnostics Test
SLR	SLenderness Ratio
ST	Source Term
STARC-ABL	Single-aisle Turboelectric AiRCraft with Aft Boundary Layer propulsion
SU2	Stanford University Unstructured
SUBLIME	Supporting Understanding of Boundary Layer Ingesting Model Experiment
SUGAR	Subsonic Ultra Green Aircraft Research
TDC	ThermoDynamic Cycle
TEPT	Turbo-Electric Power Train
TFM	Through-Flow Method
TLAR	Top Level Aircraft Requirement

TM	TurboMachinery
TRL	Technology Readiness Level
URANS	Unsteady Reynolds-Averaged Navier-Stokes
VTP	Vertical Tail Plane
WI	Wake Ingestion
WPCL	Wake Parameter calculated using CLauser pressure gradient
WPE	Wake Parameter calculated at Edge of boundary layer

# 1 Introduction

In 2018, aviation accounted for approximately 2.5% of global carbon dioxide (CO<sub>2</sub>) emissions, with consequences for climate change extending beyond this direct impact [1–3]. The aviation sector influences atmospheric gases and pollutants, resulting in complex radiative forcing effects. While emittants such as CO<sub>2</sub> or NO<sub>x</sub> directly contribute to warming, other factors like the short-term increase and long-term decrease in ozone, variations in methane, water vapor emissions, soot, sulfur aerosols, and water contrails introduce both warming and cooling effects. Overall, the warming effect dominates, and aviation’s contribution to effective radiative forcing accounted for 3.5% of all contributions to global warming in 2018 [1–3]. At the same time, air traffic volume, measured in revenue passenger kilometers, has increased 300-fold over the past seven decades and is anticipated to continue growing [2]. Despite this growth, emissions increased at a slower pace due to substantial efficiency improvements. These enhancements stem from various sources, including advancements in aircraft design and technology, larger aircraft sizes accommodating more passengers per flight, and an increased load factor, rising from approximately 60% in 1950 to 82% in 2018 [2].

However, these incremental improvements are reaching their limits, necessitating a multifaceted approach to reduce aviation’s environmental impact. Strategies include improving existing technology, operations, and infrastructure, implementing economic measures, adopting sustainable aviation fuels, and developing new-generation technologies [4, 5]. A pivotal aspect of this comprehensive strategy is improving and developing radical new aircraft technologies and concepts. While conventional aircraft configurations often feature a decoupled propulsion system, recent research suggests that a tightly coupled propulsor and airframe can enhance efficiency. Concepts like fuselage-embedded engines, engines with Boundary Layer Ingestion (BLI), or Wake-Ingestion (WI) demonstrate potential functional synergistic effects and reduction in required specific thrust, which can lead to decreased fuel consumption and reduced jet noise emissions, contributing to environmental sustainability [6].

The utilization of BLI to increase propulsive efficiency has been studied since the 1940s. In 2012, Steiner et al. identified the Propulsive Fuselage Concept (PFC) as the most promising application of BLI [6]. Subsequently, the concept has been studied in various projects, including the *Horizon 2020* project *CENTRELINE*. The turbo-electric *CENTRELINE* PFC, depicted in Figure 1.1, serves as the baseline for this dissertation. The PFC involves integrating a full annular propulsor concentrically around the



Figure 1.1: Rendering of the turbo-electric PFC developed in the *CENTRELINE* project [7].

aft section of the fuselage. The propulsor efficiently ingests and re-energizes the critical inner part of the fuselage Boundary Layer (BL), providing a highly coupled and efficient wake-filling propulsion integration strategy. PFC is particularly promising for large commercial tube-and-wing aircraft, as a significant portion of airframe drag is attributed to the fuselage [6]. Furthermore, unlike the aircraft's lifting surfaces, the fuselage will not decrease in size in the future due to constraints imposed by the required payload volume [8].

To understand and quantify the potential of PFCs, a thorough examination of the relationship between airframe aerodynamics, Fuselage Fan (FF) propulsion system, and the geometry of the involved aircraft components is essential. The initial phase of the aircraft design process, known as conceptual aircraft design, involves evaluating a variety of aircraft configurations within a predefined design space. The goal is to identify the aircraft design that best meets specified requirements [9]. This early stage of aircraft design is challenging, given the limited proven knowledge about the detailed performance and behavior of the involved systems. In the case of conventional systems and components, simple analytic or semi-empirical methods are typically employed to describe their multi-directional relationships [9]. BLI fans represent tightly integrated propulsion systems, inherently featuring a strong coupling between aircraft aerodynamics and propulsion system performance. Introducing a BLI device to an aircraft has profound implications for all aircraft systems and disciplines, including propulsion, aerodynamics, structure, and weights. Therefore, a multidisciplinary evaluation of the concept becomes imperative. However, the availability of empirical data is limited when it comes to aircraft concepts incorporating fuselage BLI propulsion. Consequently, achieving physically accurate modeling and analysis of PFC configurations proves challenging with conventional methods of aircraft conceptual design, as existing models often fall short in accuracy, computational efficiency, or applicability.

This dissertation addresses the need for a numerical model to predict the aero-propulsive performance of PFCs during the aircraft conceptual design phase. Additionally, it aims to revisit established metrics and thrust/drag bookkeeping methods, which are inadequate for determining the potential of aircraft concepts with a BLI propulsor.

Consequently, the research presented here aims to bridge the gap between fast and rapid conceptual aircraft design, commonly used for conventional aircraft configurations, and the aero-propulsive analysis of the highly coupled performance of airframe and propulsion systems inherent to fuselage BLI configurations. The primary goal is developing a fast-responding, sufficiently accurate numerical method that can be employed to evaluate the performance and determine the optimum design of a fuselage-installed propulsive device with BLI and can be employed for multi-disciplinary conceptual aircraft design. The development of the methodology follows a multi-step approach, which provides answers to the following Research Questions (RQs):

**Step 1:** Development of a universally applicable performance bookkeeping scheme for a consistent evaluation of concepts with fuselage wake-filling in aircraft conceptual design

**RQ 1:** What are the requirements for a universally applicable bookkeeping scheme, which addresses the incongruity between a drag/thrust-based conceptual aircraft design and a closely coupled airframe-propulsion integration? (Section 2.3)

**RQ 2:** Which bookkeeping scheme can adequately represent the tightly coupled effect of fuselage wake-filling and is at the same time compatible with conventional conceptual aircraft and propulsion system sizing tools? (Section 4.1)

**RQ 3:** Which universal figures of merit are best suited to quantify the performance of a propulsive fuselage within the early stages of aircraft conceptual design? (Section 4.2)

**Step 2:** Systematic identification of a most suitable simplified numerical method for the aero-propulsive assessment of propulsive fuselages with BLI

---

**RQ 4:** What are the requirements for a numerical method that captures the bi-directional effect of a fuselage-integrated propulsion system and the airframe with adequate accuracy and applies to the aircraft conceptual design phase, which requires fast response solutions to a broad design space? (Sections 3.1 - 3.3)

**RQ 5:** Which combination of existing methods and approaches can be employed to develop a most efficient simplified numerical tool, which captures the coupled aero-propulsive performance of a propulsive fuselage, can easily be integrated into a multi-disciplinary aircraft conceptual design framework and expanded with low effort to apply to other airframe-propulsion integration concepts? (Section 3.4)

**Step 3:** Development, validation, and application of a numerical method for the aero-propulsive assessment of propulsive fuselages with BLI in the context of aircraft conceptual design

**RQ 6:** Which specific models have to be combined for an automated, parametric, and validated, strongly coupled numerical approach for the analysis and design of PFCs in aircraft conceptual design? (Section 5)

**RQ 7:** How do the design parameters of the fuselage-propulsor configuration impact the figures of merit? (Sections 6 and 7.1)

**RQ 8:** What is the best approach to integrate the derived numerical methodology into an aircraft conceptual design framework? (Section 7.2)

The thesis structure is aligned with the above stated RQs.

Chapter 2 offers a comprehensive exploration of BLI theory, particularly emphasizing PFCs. This chapter reviews existing concepts and delves into multidisciplinary aircraft design approaches, the state-of-the-art modeling of aero-propulsive performance for PFCs, and various performance bookkeeping methods. It is the foundation for systematically identifying the most suitable simplified numerical method for the aero-propulsive assessment of PFCs in Chapter 3. Drawing from the insights gained in Chapter 2, Chapter 4 proceeds to derive a unified performance bookkeeping approach tailored explicitly for PFCs. At the core of the thesis, Chapter 5 unveils an innovative hybrid numerical method for the aero-propulsive assessment of fuselage-propulsor configurations within the context of aircraft conceptual design. The approach is developed and validated. Its applicability is showcased through a parameter study, with detailed results presented in Chapter 6. Derived from the study's findings, Chapter 7 delves into aircraft-level considerations before the thesis concludes with Chapter 8.



## 2 Conceptual Aircraft Design of Propulsive Fuselage Concepts

The conceptual aircraft design of PFCs deviates significantly from conventional aircraft design methodologies due to the tight coupling of airframe aerodynamics and BLI propulsion system. The theoretical background required to understand the potential benefit associated with BLI, particularly in PFCs, is outlined in Section 2.1. Following that, Section 2.2 provides a literature review on existing PFC studies with a particular emphasis on modeling the aero-propulsive interactions and the conduction of aircraft-level assessments. Section 4 outlines bookkeeping schemes and figures of merit, which are employed to evaluate the performance of BLI aircraft. Drawing from the insights of the literature review, Section 2.4 identifies gaps in current BLI research, paving the way for the formulation of RQs, which will be addressed in the subsequent chapters of this dissertation.

### 2.1 Boundary Layer Ingestion and Propulsive Fuselages

To exploit the BLI benefit for aircraft configurations, a full comprehension of the underlying physical mechanisms and the fundamentals of BL theory is essential. The following section focuses on the BL theory and a derivation of the BLI benefit. A promising aircraft configuration with BLI, the PFC is presented, and the associated aircraft design challenges are discussed.

#### 2.1.1 Boundary Layer Theory

In contrast to an ideal fluid, real flows are inherently viscous. A viscous flow resists a deformation rate with internal resistance, i.e., shear stresses; thus, tangential forces exist between adjacent fluid layers. Additionally, a real fluid adheres to solid walls (no-slip condition), further contributing to the tangential forces [10]. For flows with high Reynolds numbers the BL theory proposed by Prandtl identifies a thin layer of fluid that is in close proximity to a solid surface as the BL and an outer region. The BL is dominated by viscosity, in the outer, irrotational region viscosity can be neglected. The threshold between the viscous and potential flow region indicates the edge of the BL. Here, the velocity profile transitions to an asymptotic edge velocity  $u_e$ . Consequently, inside the BL, a typical BL velocity profile forms, where the velocity transitions from zero (at the wall) to  $u_e$  [10]. The fluid particles in the BL move in parallel layers and the thickness of the BL increases as the fluid flows over the surface. Here, the forces caused by viscosity may be similar in magnitude to those caused by the fluid's inertia even if the fluid has a low viscosity. Furthermore, the gradients of the fluid perpendicular to the surface are much more pronounced than the changes parallel to the surface [11].

In general, the development of the BL along a surface can be described in the following way: initially, the flow attaches near the front of the body, forming a laminar BL. Laminar BLs are characterized by smooth, orderly movement of fluid particles and are found in flows with low local Reynolds numbers ( $Re$ ). As the fluid moves along the body, more layers slow down, causing the BL to thicken. Simultaneously, small disturbances within the BL grow in scale and energy. At a critical point, these disturbances become unstable, leading to a transition from laminar to turbulent flow (see also Section 5.4.2.3). Turbulent BLs are characterized by chaotic, disordered movement of fluid particles and are found in flows with high local  $Re$ . These fluctuations enable mixing across layers perpendicular to the body's surface, causing the turbulent BL to grow faster than the laminar BL. The turbulent velocity profile is characterized by a more bulbous shape with a steeper velocity gradient at the wall. A thin viscous sublayer forms within

the turbulent BL close to the surface because the solid wall prevents transverse flow. This sublayer is dominated by viscous stresses rather than turbulent stresses. The transition between this sublayer and the main turbulent region is gradual. Once the BL detaches from the body it forms a viscous wake. If unfavorable (positive) pressure gradients occur locally, flow separation (and re-attachments) can occur prematurely while the flow travels along the surface [10, 12].

The BL thickness  $\delta$  is an artificial concept with little physical meaning. It is commonly defined as the distance from a surface at which the streamwise velocity component is  $0.99u_\infty$  [10]. Other more meaningful characteristics are derived from the integral momentum equation. Theoretically, an inviscid flow with a uniform velocity profile would require a thinner BL compared to a viscous flow to show the same mass flow around the body. The BL displacement thickness  $\delta^*$  indicates the theoretical body shape (displacement surface) for which the mass flow would be similar for an inviscid flow compared to a viscous flow around the original body [12]. The definition of the displacement thickness can be employed to calculate the potential (inviscid) flow solution on the body defined by the actual body shape enlarged by  $\delta^*$ . The surface applies a shear force on the fluid (skin friction), slowing the flow. This force generates an increasing momentum flux deficit within the BL. The increase in the momentum thickness in the streamwise direction is indicative of the momentum flux deficit [12]. Hence, the BL momentum thickness  $\theta$  measures the flux of momentum deficit due to the presence of the BL. It is defined as the distance by which a surface would have to be moved in an inviscid fluid of equal freestream velocity parallel to itself towards a defined reference plane to create the same total momentum as the momentum between the surface and the reference plane in a viscous fluid (see Figure 2.1, right). The evaluation of  $\theta$  can be useful for identifying laminar-turbulent transition (here,  $\theta$ , or  $Re_\theta$  is large). In an integral (planar) form,  $\delta^*$  and  $\theta$  depend only on the velocity  $u$  and density  $\rho$  distribution inside the BL and at the BL edge. They are calculated for compressible flows as provided in [12] (see also Figure 2.1):

$$\begin{aligned}\delta^* &= \int_0^\infty \left(1 - \frac{\rho u}{\rho_e u_e}\right) dy \\ \theta &= \int_0^\infty \frac{\rho u}{\rho_e u_e} \left(1 - \frac{u}{u_e}\right) dy\end{aligned}\tag{2.1}$$

For axisymmetric flows, the displacement and momentum deficit area  $\Delta^*$  and  $\Theta$  further depend on the local radius  $r$  and are calculated by the following equations presented in [13]:

$$\begin{aligned}\Delta^* &= \int_0^\infty \left(1 - \frac{\rho u}{\rho_e u_e}\right) r dy \\ \Theta &= \int_0^\infty \frac{\rho u}{\rho_e u_e} \left(1 - \frac{u}{u_e}\right) r dy\end{aligned}\tag{2.2}$$

Additionally, the physical displacement thickness  $\delta_{ph}^*$  as defined by Patel [14] is employed to calculate the actual physical displacement of the potential flow from the surface of an axisymmetric body:

$$\delta^* = \delta_{ph}^* \left(1 + \frac{1}{2} \frac{\delta_{ph}^*}{r_0} \cos \Phi\right)\tag{2.3}$$

$\Phi$  is the local angle between body contour and streamwise direction,  $r_0$  is the local body radius.

The BL shape factor  $H$  defined by Equation 2.4 is a dimensionless parameter that describes the shape of the BL velocity profile. It helps to understand how fast the fluid's velocity changes from an object's surface to its free stream velocity (the undisturbed flow away from the object), i.e. how the momentum deficit is distributed in the BL. A smaller shape factor indicates a BL that transitions relatively quickly from slow to fast velocity, which can signify a favorable pressure gradient. A higher shape factor denotes a slower transition indicative of an adverse pressure gradient [12]. The shape factor of the BL profile

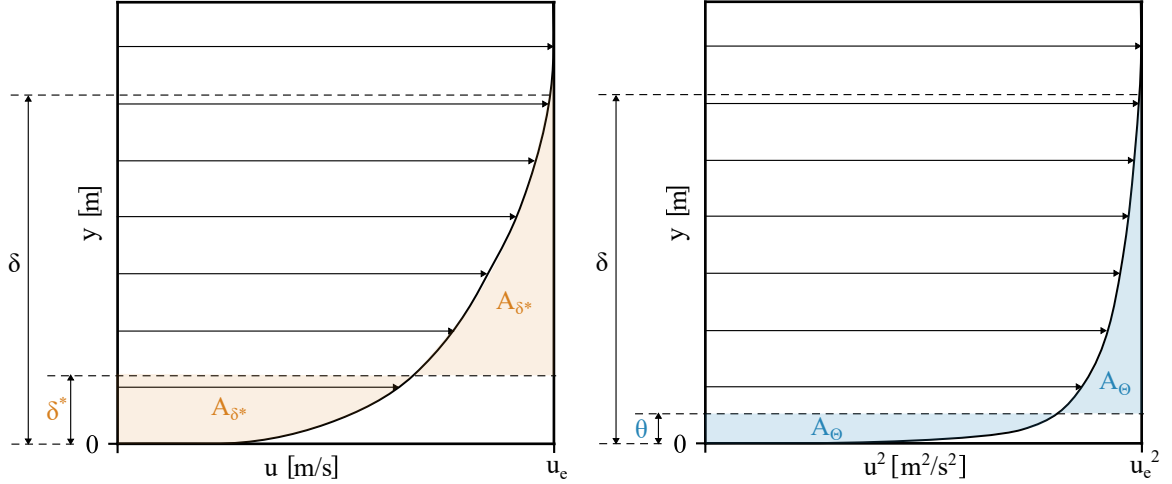


Figure 2.1: Relationship between BL thickness  $\delta$ , displacement thickness  $\delta^*$ , and momentum thickness  $\theta$ .

incident to a BLI propulsor can help decide on the size of the propulsor, i.e. how much of the momentum deficit should be ingested.

$$H = \frac{\delta^*}{\theta} = \frac{\Delta^*}{\Theta} \quad (2.4)$$

The BL theory can be employed to define viscous pressure and skin friction drag, which compose the total viscous drag of a moving body. Skin friction drag  $D_f$  directly results from the viscous effects in the BL, including viscosity and turbulence. Viscous pressure drag is due to the displacement effect of the BL. It contributes to a body's total pressure drag  $D_p$ , which further includes pressure drag caused by shocks or lift-induced drag. For streamlined bodies, the contribution of skin-friction drag to total drag dominates. The large wall velocity gradients of turbulent BLs especially contribute to the high friction drag [12]. For each aircraft surface,  $D_p$  and  $D_f$  can be calculated by integrating local fluid characteristics over the wetted surface as presented by [15]:

$$\begin{aligned} D_f &= \oint_S \tau_w \sin \Phi dS \\ D_p &= \oint_S p \cos \Phi dS \end{aligned} \quad (2.5)$$

$\Phi$  is the angle between the surface normal and the freestream velocity vector,  $\tau_w$  denotes the wall shear stress, and  $p$  the static pressure. The total drag is the sum of pressure and skin friction drag.

### 2.1.2 Boundary Layer Ingestion Benefit

Wake-filling aims at an efficient filling of a body's wake, which can be achieved through BLI or WI. BLI refers to the ingestion and acceleration of the slow velocity air in the vicinity of an aircraft body surface (a part of the BL) by a propulsor located on the body or directly behind it. Here, the pressure of the incident flow differs from the freestream pressure. In contrast, a WI propulsor ingesting the wake, which has recovered to freestream static pressure in a distance behind the body, is a rather academic wake-filling application [16]. In the following, the physical principles of BLI aircraft propulsion are discussed.

For typical civil transport aircraft, approximately 60 – 70% of the overall drag can be attributed to viscous and form drag, which is directly connected to the formation of the BL on the airframe's surfaces [17]. In steady-level flight, the airframe drag is balanced by engine thrust. For traditional tube and wing configurations, the airframe and propulsion system performance are mostly uncoupled. Thus, they

can be designed and analyzed independently. Two general approaches exist to decrease a conventional aircraft's propulsion energy demand: either airframe drag can be reduced, or the propulsion system efficiency can be improved. Reducing drag decreases the instantaneous thrust demand, directly affecting the propulsion power requirement. Improving propulsion system efficiency does not affect the propulsive power required to propel the aircraft but increases the efficiency of source energy to propulsion energy conversion. Consequently, the fuel consumption and the aircraft's local emissions can be reduced. The flow incident to conventional engines is considered to be mostly undisturbed with uniform velocity. In contrast, novel aircraft concepts with BLI feature propulsors, which ingest a part or all of the BL of an aircraft component and accelerate the low-velocity flow. Aircraft concepts with BLI aim to exploit the synergistic effects between airframe aerodynamics and propulsion system performance. As a result, airframe and propulsion system performance are tightly coupled, and they cannot be assessed independently of each other. Different approaches have been employed to explain the potential benefit of BLI for aircraft propulsion. Subsequently, they are presented in ascending order of the depth of comprehension regarding the underlying physical mechanisms.

Current research on civil aviation focuses mostly on a technology's potential to reduce mission energy or, in the case of conventional energy sources, on mission fuel burn reduction. Thus, the most intuitive approach from a top-down perspective is the comparison of mission energy or fuel consumption required by an aircraft with BLI and a non-BLI configuration without detailed knowledge of the involved mechanisms. Currently, no in-flight tests of BLI configurations have been performed and the approach remains theoretical. If a more detailed assessment of the BLI benefit is conducted, as explained in the following, it is possible to calculate the mission performance benefit using a bottom-up approach, where the aircraft or system performance alteration is translated to mission performance.

The overall aircraft performance of BLI configurations has been successfully compared to non-BLI configurations. In most cases, the propulsive power or the shaft power required to propel the aircraft in specific flight conditions is evaluated. Examples include numerical simulations [18–20] as well as wind tunnel tests [21, 22] of full aircraft configurations. An often-used metric is the Power Saving Coefficient (PSC), which was developed as one of the earliest BLI research activities by Smith [23]. It compares the propulsive power required by a BLI configuration to a non-BLI reference in the same flight conditions (see Section 2.3.2 for more details).

To gain an in-depth understanding of the underlying physical principles of BLI, the performance of individual aircraft components, such as the BLI propulsor or a fuselage-propulsor configuration, is analyzed. Often, a detailed flow field analysis of the relevant component is performed based on numerical simulation or experimental results. The different approaches employed to explain the potential BLI benefit apply to their own Control Volume (CV) and conserved quantity (see Section 2.3 for more details).

In the early BLI research, BLI benefit was mainly attributed to increased propulsion system performance. A simple examination of the net thrust  $F_N$  and propulsive efficiency  $\eta_P$  definition for a propulsor as given in the following equation by [24] reveals that  $\eta_P$  increases if the inflow velocity  $u_0$  decreases.

$$\begin{aligned} F_N &= \dot{m}(u_8 - u_0) + A_8(p_{s,8} - p_{s,0}) \\ \eta_P &= \frac{2}{1 + u_8/u_0} \end{aligned} \quad (2.6)$$

$\dot{m}$  is the air mass flow through the propulsor,  $p_s$  is the static pressure, and  $A_8$  is the nozzle exit area. All other mass flow-averaged flow characteristics at the nozzle exit are denoted by subscript 8. Compared to an undisturbed freestream flow, the mean velocity inside the BL, which is incident to the BLI propulsor, is reduced. This is depicted in Figure 2.2. For a given mass flow and thrust, the lower inlet velocity results in a lower propulsor exit velocity. Conversely,  $\eta_P$  increases. Thus, a BLI propulsor can produce the same thrust as a non-BLI propulsor with less expended power.

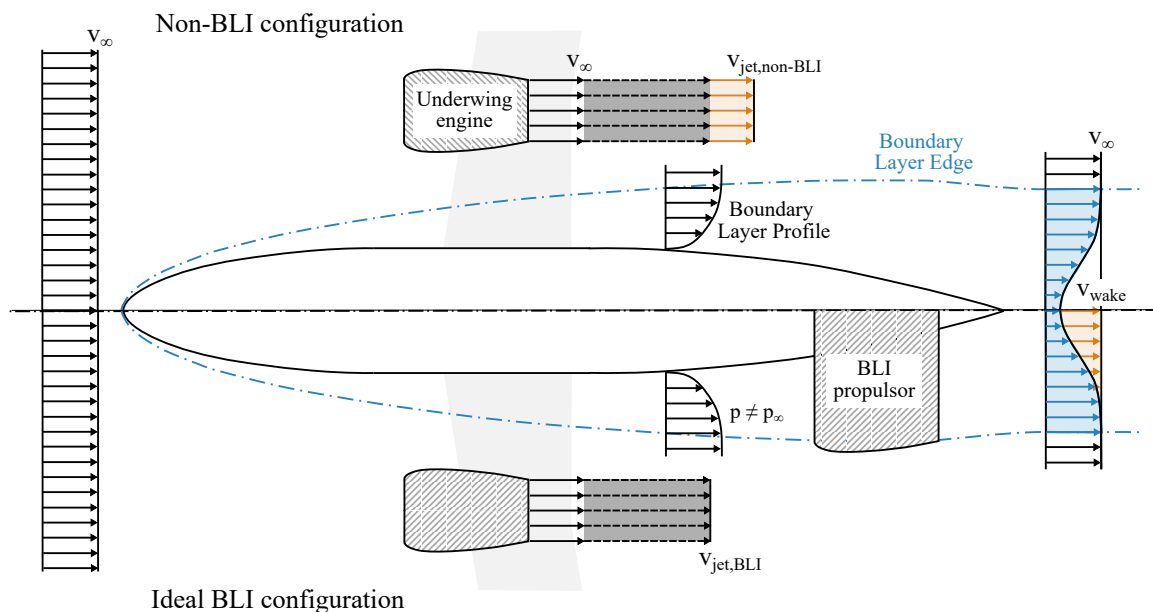


Figure 2.2: Exemplary comparison of non-BLI and ideal BLI configuration. Adapted from [25].

Further studies identified the BLI benefit as the reduction of ram drag, i.e. momentum flux in the BLI propulsor inlet streamtube in combination with a lower inlet total pressure recovery [26–28]. Inlet distortion additionally contributes to a degradation of fan efficiency [29].

Other approaches focused on the coupled aero-propulsive effect of BLI. From a momentum conservation perspective, the BLI benefit can be explained as an efficient (partial) recovery of the BL or wake momentum flux deficit, by re-energizing the aircraft BL or wake through a propulsor [23, 30]. The momentum deficit is induced by frictional dissipation in the BL and is indicative of the body’s viscous drag. The BLI propulsor accelerates the low velocity airflow and, thus, reduces the kinetic energy waste. To generate the same net axial force, less kinetic (propulsive) energy has to be generated compared to a non-BLI propulsor [31].

Based on the observation that the benefit of BLI manifests itself in a propulsive power reduction [32], power and exergy balance approaches [33, 34] became popular to investigate the underlying physical principles of the BLI benefit in more detail (see also Section 4).

The power balance approach introduced by Drela analyzes sources and sinks of mechanical energy in the flow field to identify the lost mechanical power terms (sources of dissipation), which are balanced by the mechanical flow power added to the flow by the propulsor [35]. Applying the approach to BLI configurations shows that the benefit of BLI quantified by a mechanical flow power reduction and described in terms of a reduction in lost power is mainly attributed to two mechanisms:

1. Reduction of propulsive jet dissipation. As the flow incident to the propulsor features a velocity lower than free stream velocity, the propulsor can produce the same force but with a lower jet velocity, i.e., less momentum excess in the downstream wake.
2. Reduction of viscous airframe dissipation (wake and surface dissipation). The wake kinetic energy defect downstream of the aircraft is reduced because energy is added to the wake flow through the propulsor. The presence of the propulsor can also affect the airframe performance, e.g., through suction effects, which change the flow characteristics of the respective component. Additionally, in some BLI cases, the total wetted surface area of the airframe can be reduced as a second-order effect, which contributes to a decrease in viscous surface dissipation.

In consequence, the propulsive efficiency, which is defined here as a function of mechanical flow power and jet dissipation, is increased [16, 29, 32, 33, 35–37].

Application of the exergy balance approach by Arntz to configurations with BLI lead to similar conclusions. Exergy analysis identifies two forms of energy: “useful” energy or exergy, which is (theoretically) fully convertible into mechanical work, and “useless” energy, i.e., anergy, which cannot be converted. Arntz showed that thermal exergy terms are negligible for BLI configurations compared to mechanical energy. Furthermore, the main contribution to the BLI benefit arises from decreased flow streamwise kinetic energy. Generally, a BLI propulsor produces less anergy to bring the wake or jet back to its thermodynamic equilibrium with the environment (i.e. freestream velocity) compared to an aero-propulsively uncoupled propulsor. In the latter case, the airframe and propulsion system are separated, and more viscous dissipation is generated. Thus, more anergy is produced [34, 38].

### 2.1.3 The Propulsive Fuselage Concept

In recent years, several aircraft concepts featuring BLI have been proposed. They range from small modifications to conventional tube-and-wing configurations by adding an additional BLI propulsor at the rear end of the fuselage (e.g. the *CENTRELINE* [17] or *NASA STARC-ABL* configuration [39]) to employing embedded BLI engines as the main propulsion source of unconventional airframes such as Blended Wing Bodies (BWBs) (e.g. *NASA N3-X* BWB [40]). BLI propulsors can be employed as the single source of the thrust of an aircraft (e.g. *VoltAir* [41]) or as an addition to the existing propulsion system (e.g. *DisPURSAL* [42]). They can ingest a part of the wing BL as proposed for various BWB concepts or a part of the fuselage BL [17, 40]. When located on the fuselage, a number of BLI propulsors can either be mounted side by side on the outside of the fuselage; they can be embedded in the fuselage to ingest only part of the BL, or encircle the fuselage in a full annular 360° configuration [6]. Furthermore, the BLI propulsors can be power and thrust generator at the same time or driven by a different power source such as in a turbo-electric configuration or by means of an added electrical energy source [17, 42, 43]. Further, the propulsors can be embedded, podded, or unpodded (e.g. [40, 42, 43]).

For large commercial tube-and-wing aircraft, 20–30% of the total cruise drag (e.g. [44]) can be attributed to the fuselage body, making it the most interesting airframe component for an application of BLI. A promising concept for a highly coupled wake-filling propulsion integration is the so-called Propulsive Fuselage Concept (PFC), first introduced by Steiner et al. [6]. Here, in addition to the underwing engines, a single, full annular propulsor concentrically encircles the aft section of the fuselage (360° installation). The propulsor ingests the inner, most crucial part of the fuselage BL and re-energizes the fluid. (see Figure 2.3). The BLI propulsor is located at the rear of the fuselage to maximize the BLI effect, i.e. to minimize wake dissipation.

### 2.1.4 Design Challenges of Aircraft Concepts with Boundary Layer Ingestion

The multidisciplinary conceptual design of an aircraft with a BLI propulsor poses several challenges. Even if the change in the aircraft configuration might seem small, introducing a BLI propulsor significantly affects a number of aircraft components and disciplines due to its tightly coupled nature. All first and second-order cascade effects on propulsion system performance, aerodynamics, structure, flight dynamics, etc. have to be captured and adequately quantified [29]. To arrive at an optimum PFC design, in which the BLI benefits outweigh the introduced disadvantages, aircraft-level compromises must be identified. For example, the highest BLI benefit can be achieved if the full BL is ingested by the BLI propulsor. However, for large commercial aircraft, the BL thickness can exceed 1 m at the rear part of the fuselage in cruise conditions. BLI propulsors with a large diameter are heavy and introduce a significant load to the fuselage structure. Reinforcing the fuselage structure leads to additional weight penalties, which in turn

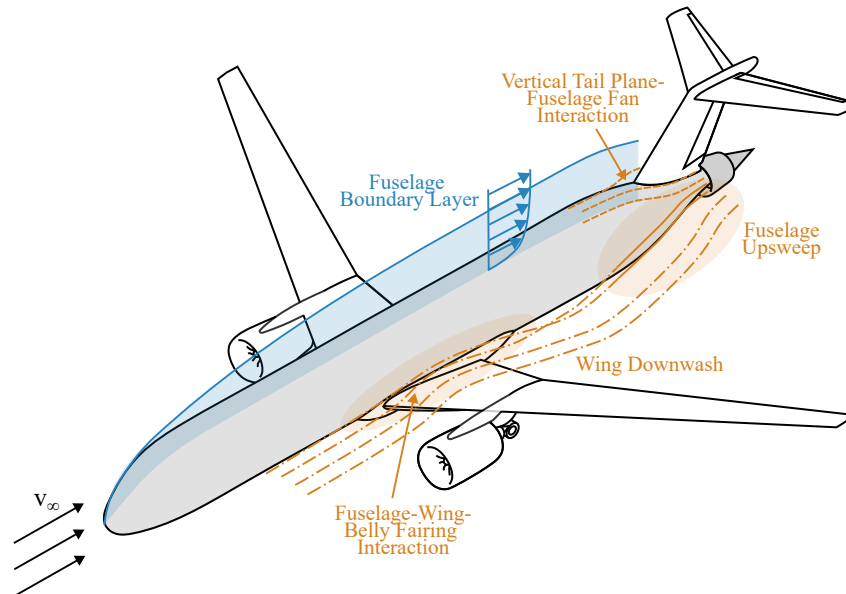


Figure 2.3: Sketch of a PFC with FF inlet distortion. Isolated fuselage-propulsor configuration colored in gray. Adapted from [45].

have a detrimental effect on the aircraft's performance. Here, a compromise has to be found between optimal BLI and minimum weight penalty.

The integration of BLI propulsion offers various potential synergistic advantages on the aircraft level beyond the BLI benefit itself, which was discussed in Section 2.1.2. One key advantage is the possibility of downsizing the main engines and their nacelles when the BLI propulsor is not the sole source of thrust. In such cases, the non-BLI engines have to provide less power. Consequently, the main engines and corresponding nacelles and pylons can be sized smaller, leading to a reduction in weight and the wetted area of the nacelles and pylons [46]. This nacelle wetted area is further decreased when the embedded BLI engines solely provide thrust. In this configuration, pylons are eliminated, further streamlining the aircraft's design [35]. Another advantage emerges from separating power and thrust generation if considered in the aircraft's configuration. This separation facilitates higher achievable by-pass ratios [47], allowing a higher degree of freedom in the overall aircraft design [40]. Moreover, noise emissions can be minimized through BLI integration. First, the jet velocities are decreased, which leads to lower airflow noise. Second, a tight integration with the airframe, especially for BWBs, enhances noise shielding [48]. Aircraft balance and stability also benefit from the adoption of BLI. By incorporating an additional propulsor at the rear of the aircraft and reducing the weight of the main engines, the downward pitching moment often associated with front-mounted engines can be mitigated, enhancing overall stability [46]. In summary, the aero-propulsive performance improvements brought about by BLI can trigger cascade effects that reduce the weight of energy sources such as fuel or batteries, further contributing to overall efficiency gains.

However, the realization of these advantages comes with notable challenges that can outweigh the aero-propulsive benefits of BLI integration. One significant challenge arises from introducing additional circumferential distortion due to the interaction of the body's BL with various aircraft components. This phenomenon is particularly evident in the PFC, where the radially distorted fuselage BL interacts with wing downwash, fuselage upsweep, Vertical Tail Plane (VTP), belly fairing, and FF cowling BLs [45] (see Figure 2.3). Moreover, adopting BLI propulsors, especially embedded propulsors with S-ducts, can reduce propulsive efficiency due to lower total inlet pressure recovery [35–37]. If a portion of the distorted inlet airflow is directed to the BLI core engine, this can further result in increased inlet total pressure

losses, which may negatively impact the engine's overall pressure ratio and thermal efficiency [49, 50]. Additionally, the possibility of BL separation and secondary flows inside the BLI propulsor duct, especially for embedded systems, is a concern [46]. Furthermore, inlet distortion can cause reductions in fan efficiency [36] and stall margin, increasing the risk of rotational stall, surge, and engine failure [51]. These issues are exacerbated by the circumferential inlet distortion, which can lead to a range of aero-mechanical and acoustic problems, including fan blade excitation, vibrations, and even structural failures of the propulsor blades [31, 51]. Incorporating BLI may necessitate additional structures for support, potentially introducing incremental weight [46]. This effect is particularly prominent for PFC, where the additional load on the fuselage structure requires increased structural reinforcement, leading to an increase in the overall weight of the aircraft [47]. Further components, such as additional propulsors, engines, nacelles, and electrical components (as seen in turbo-electric propulsion systems) contribute to the weight penalties. Additionally, the integration of the BLI propulsor into an aircraft component might require sizing of the hosting component to be larger, leading to an increase in the component's wetted surface area and weight [46]. The potential for foreign object damage during take-off rotation for aft-mounted propulsors also needs consideration, potentially requiring design modifications like introducing fuselage upsweep or an extended landing gear [45]. In addition, adopting embedded BLI engines could increase the complexity of engine maintenance and servicing [46].

In summary, while the potential advantages of BLI integration at the aircraft level are significant, they are accompanied by notable challenges and potential cascade effects that can pose significant hurdles to the holistic design of an optimal aircraft configuration with BLI and, thus, require sufficiently accurate modeling of the BLI performance.

## 2.2 Propulsive Fuselage Concept Studies in Literature

In recent multidisciplinary aircraft studies of PFCs, anticipated fuel burn reductions were projected within the one-digit range, spanning from 1% to 10% [42, 52–55]. Intriguingly, there have been instances where an increase in block fuel of 1.7% was reported [56]. However, these diverse outcomes are influenced by variations in aircraft and propulsion system configuration and geometry, Top-Level Aircraft Requirements (TLARs), and the specific modeling approaches adopted for each concept.

This section commences with an in-depth exploration of the literature on various PFC concepts and projects. Subsequently, an overview of conceptual aircraft design studies is presented, and the state-of-the-art aero-propulsive modeling for PFC configurations is outlined.

### 2.2.1 Aircraft Concepts

In the last years, several comprehensive review papers on BLI research activities have been published. Menegozzo and Benini reviewed the numerical modeling approaches for BLI and classified aircraft concepts with BLI as Propulsive Fuselage, Rear Engines Concepts, and Distributed Fans Concepts [57]. Diamantidou et al. derived a different classification and presented an overview of Hybrid Wing Body (HWB), Rear Mounted Engine(s) (RMEs), and PFCs with BLI [58]. An exhaustive review of the state of the art in BLI aircraft concepts and modeling approaches was presented by Moirou et al., who differentiated PFCs, Over- and Rear-Fuselage Engines Concepts (ORFECs) and Disruptive Propulsive Concepts (DPCs) [59]. They mapped and linked the literature on BLI by aircraft concept and study focus. In the following, a condensed outline of the history of PFCs is presented. For a more detailed discussion of the concepts, the reader is referred to the publications cited above.

The utilization of BLI as a means to increase the propulsive efficiency of an aircraft through wake-filling has been studied since the 1940's. A first patent for propulsion systems with BLI installed at the

trailing edge of the wing or the tail of a fuselage was submitted by *Armstrong Siddeley Motors Ltd.* and Heppner in 1941 (published in 1946) [60]. Figure 2.4 depicts the initially proposed aircraft configurations. According to Eckardt, Heppner was probably the first to use the term “boundary layer propulsion” for aircraft propulsion in a technical report in 1944 [61,62]. Soon after, Smith and Roberts (Douglas Aircraft Company, Inc.) conducted a first conceptual study comparing the performance of a large transport aircraft with reciprocating engines to a turbojet configuration with direct ramming inlets, and one with BL inlets. They demonstrated the potential to reduce fuel consumption in cruise due to the delay in BL transition, which they attributed to BLI [63].

In the following decades, only a small number of studies dealt with the theoretical benefit of wake-filling for aircraft application, i.e. propulsive efficiency improvements [64,65], or the performance of airships [66,67]. At the same time, research and development of BLI propulsion for marine application intensified [68–70].

In the aviation research community, the technology gained broader interest once Smith published his landmark study in 1993, which uncovered the advantages associated with unducted WI propulsion. Smith employed the actuator disk theory to analytically derive the potential power savings and propulsive efficiency improvements for an aircraft with wake-filling propulsion compared to a non-wake-filling configuration [23]. Subsequently, research in aircraft concepts featuring a variety of propulsive devices with BLI or WI intensified, especially over the last decade as depicted in Figure 2.5, which visualizes the number of publications on WI, BLI, and PFC over the last 30 years. It shows an overview of systematic literature research conducted with the abstract and citation database Scopus [71]. Noted examples of first concepts include the aft-FF concept *Fuse Fan* [72], the embedded BLI configuration of the *Silent Aircraft Initiative SAX-40* [73], the *MIT D-8* “double bubble” fuselage with BLI [74], and the *N3-X BWB* concept studied by NASA [75]. The *Propulsive Fuselage* was introduced by Steiner et al. in 2012. The concept resulted from a systematic downselection of several aircraft configurations with BLI propulsion [6]. In the same year, Boeing conducted the *SUGAR* project (Subsonic Ultra Green Aircraft Research), which explored advanced technologies for future transport aircraft. One concept featured a combination of truss braced wings, hybrid fuel cell and gas turbine propulsion system, and a fuselage mounted BLI engine [76].

The first multidisciplinary study for a large transport category PFC with a full annular fuselage BLI propulsor was performed as part of the *European Commission* (EC) funded research project *DisPURSAL* (Distributed Propulsion and Ultra-high By-Pass Rotor Study at Aircraft Level) [42]. *DisPURSAL*

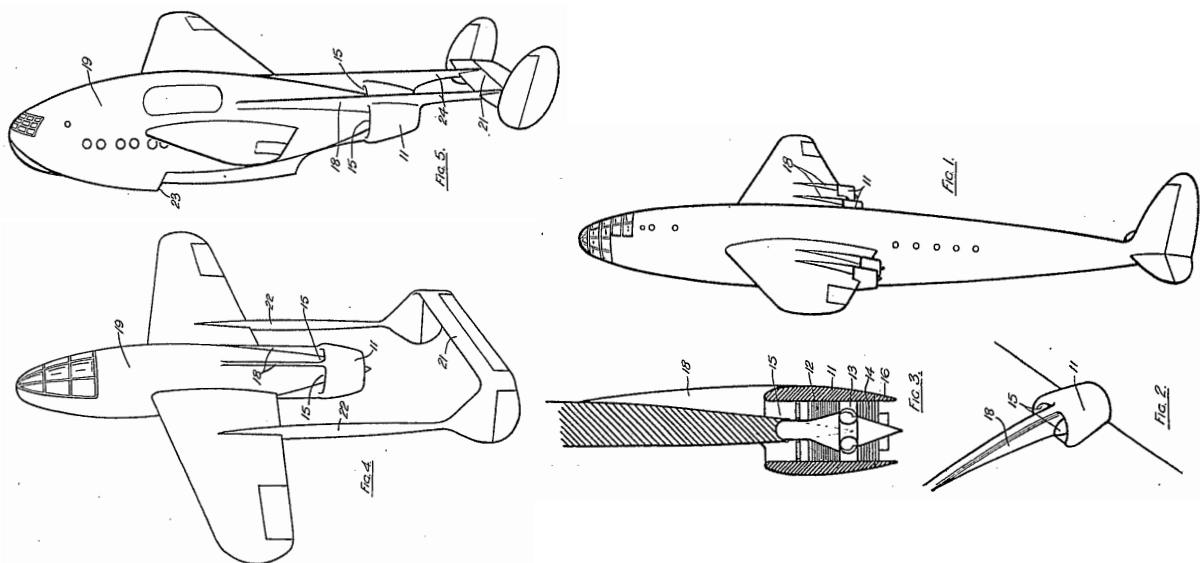


Figure 2.4: Sketch of first aircraft concepts with BLI propulsion. Source: [60].

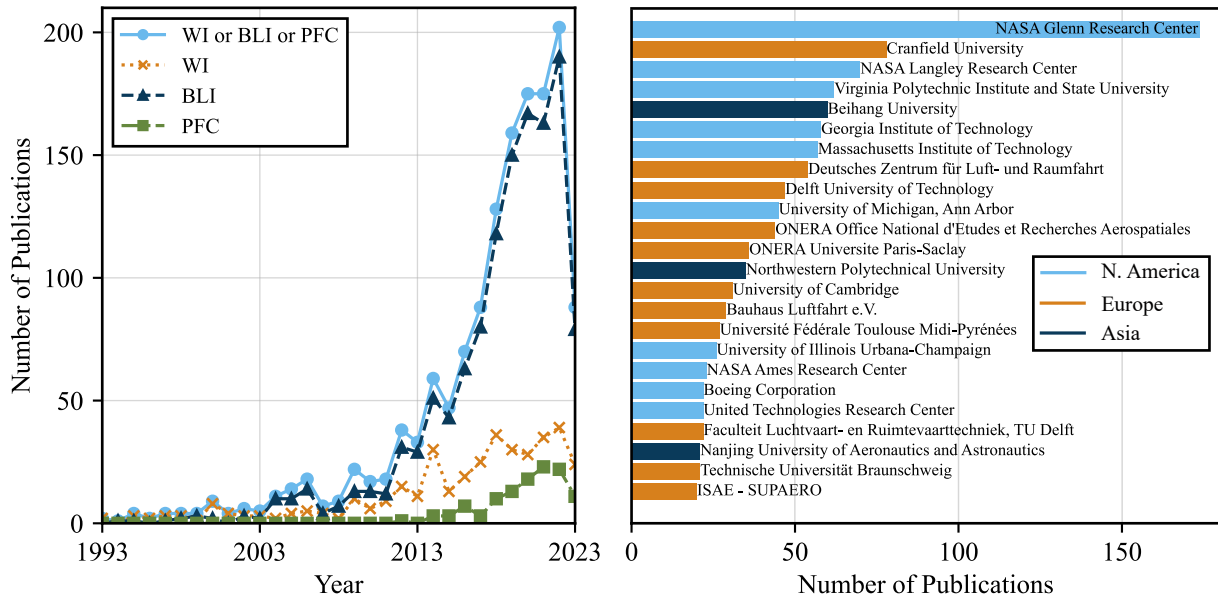


Figure 2.5: Publications regarding WI<sup>a</sup>, BLI<sup>b</sup>, PFC<sup>c</sup>, and a combination of all keywords<sup>d</sup> since 1993 (left). Publications affiliated with international research institutions since 1993<sup>d</sup> (right).

<sup>a</sup> Scopus search query: (ALL("wake-filling" or "wake ingestion") AND NOT TITLE-ABS-KEY(scramjet OR plasma) AND PUBYEAR > 1992)

<sup>b</sup> Scopus search query: (ALL("boundary layer ingestion") AND NOT TITLE-ABS-KEY(scramjet OR plasma) AND PUBYEAR > 1992)

<sup>c</sup> Scopus search query: (ALL("propulsive fuselage" or "propulsive fuselage concept") AND NOT TITLE-ABS-KEY(scramjet OR plasma) AND PUBYEAR > 1992)

<sup>d</sup> Scopus search query: (ALL("wake-filling" or "wake ingestion" OR "propulsive fuselage" OR "propulsive fuselage concept" or "boundary layer ingestion") AND NOT TITLE-ABS-KEY(scramjet OR plasma) AND PUBYEAR > 1992)

explored the multidisciplinary effects and mission fuel burn reduction potential of a widebody medium-to-long range tube-and-wing PFC based on an A330-type aircraft. In addition to the two underwing podded Geared Turbo-Fans (GTFs), the concept featured an additional core engine in the rear of the fuselage. The core engine is mechanically connected to a full annular FF that ingests the BL in front of the VTP. An S-duct is located inside the FF duct, ingesting the air required for the core engine. For the design mission (340 PAX, 4800 nmi,  $Ma_{cr} = 0.80$ ), a fuel burn reduction of 9% was estimated compared to a conventional aircraft with similar Entry Into Service (EIS) 2035 [42].

Subsequent PFC design studies included the turbo-electric *STARC-ABL* (Single-aisle Turboelectric Aircraft with Aft Boundary Layer propulsion) and *CENTRELINE* (ConcEpt validation sTudy foR fusElage wake-fILling propulsioN intEgration) configuration, both featuring a 360° fuselage propulsor [7, 17, 39, 52].

The *CENTRELINE* project aimed to advance research on BLI to TRL 3 (Technology Readiness Level) by a proof of concept study of a PFC with a Turbo-Electric Power Train (TEPT). The *CENTRELINE* configuration is based on the *DisPURSAL* concept. The reference configuration is similar to an A330-300 aircraft with 340 PAX, a design range of 6400 nmi, and a cruise speed of  $Ma_{cr} = 0.82$ . It features a full annular FF installed at the trailing edge of the VTP, which is driven by an electric motor. Generator off-takes from advanced GTF main engines provide electric energy. Results of numerical and experimental campaigns were incorporated into multi-disciplinary aircraft design studies, which derived a fuel burn reduction potential of 3.2% compared to a conventional aircraft with EIS 2035 [54] (see also Section 5.1).

Concurrently to the European Union-funded *CENTRELINE* project, NASA explored the potential benefit of a narrowbody aircraft (similar to a B737-800) with an electrically driven full annular FF. The FF is located at the trailing edge of the VTP and powered by electricity, which is generated by two underwing podded main engines [39]. Integrated aircraft design results for the *STARC-ABL* Rev B2.0 configuration

promised a design mission (150 PAX, 3500nmi,  $Ma_{cr} = 0.70$ ) block fuel reduction of 3.4% for an EIS 2035 with respect to a reference aircraft configuration [52].

Similar turbo-electric PFCs were investigated in the Clean Sky 2 project *HYPER-F* (HYbrid electric Propulsion for Emission Reduction in Flight) [55,77,78], and the *Horizon 2020 SUBLIME* project (Supporting Understanding of Boundary Layer Ingesting Model Experiment). Here, high-fidelity Computational Fluid Dynamics (CFD) studies were combined with wind tunnel testing to improve the understanding of the potential of PFCs [79–81]. Giannakakis et al. based their studies on the *STARC-ABL* configuration. They conducted an analytical design space exploration [82] and assessed the feasibility of the concept [56]. Independent of each other, Schnell et al. and Fernandez and Smith conducted CFD studies of a turbo-electric PFC based on an A320 aircraft [53,83]. Similarly, within the *ADEC* project (Advanced Engine and Aircraft Configurations), advanced aircraft configurations featuring an annular FF were explored [84]. Recently, Ahuja and Mavris studied the sensitivity of BLI performance on geometric changes in a Boeing 737-8-like fuselage with different FF configurations [37,85].

Most PFCs target the short- to long-haul market. Some studies, however, investigate thin haul commuters and regional aircraft with fuselage BLI. In 2012, Stückl et al. assessed the feasibility of a fully electric regional aircraft concept *VoltAir* with a single fuselage-propulsor [41]. Similarly, the 9 PAX fully electric regional aircraft concept, *TailWind*, is powered solely by one full annular fuselage propulsor [86,87]. Secchi et al. studied a TEPT system architecture with a BLI aft-fuselage propulsor on a regional Embraer E175-based aircraft configuration [88]. The *PEGASUS* (Parallel Electric-Gas Architecture with Synergistic Utilization Scheme) concept is a parallel hybrid-electric regional aircraft with a combination of wingtip propulsors, underwing propulsors, and an unducted BLI propulsor installed at the rear fuselage [43]. Stoll et al. analyzed the potential of BLI for a thin haul propulsive fuselage concept [89] and the *HECARRUS* (Hybrid ElectriC smAll commuteR aiRcraft conceptUal deSign) project explored the option to further reduce emissions of a hybrid-electric commuter aircraft through BLI [90].

In addition, aircraft concepts emerge, which employ the synergistic effects of combining the principle of BLI with other promising technologies. Two independent studies investigated the potential of distributed electric propulsion by arranging several BLI propulsors around the aft-fuselage of an aircraft [91,92]. Furthermore, synergistic effects of a closed non-planar wing with two embedded BLI engines installed at the rear of the fuselage are explored in the H-23 aircraft concept [93].

Lately, civil aviation research activities focus on employing hydrogen as an environmental friendly energy source. Due to hydrogen's low volumetric energy density compared to kerosene or batteries, the volume of aircraft components housing the hydrogen tanks increases. Consequently, friction losses are amplified, enhancing the potential of BLI. Druot et al. explored several hydrogen-powered aircraft concept options with BLI engines mounted on the rear of the fuselage and/or on the rear of externally mounted hydrogen tanks, using this synergistic effect [94].

### 2.2.2 Conceptual Aircraft Design

Conceptual aircraft design is the first stage of the aircraft design process. A range of aircraft configurations are evaluated within a pre-defined design space to identify an aircraft design that fulfills the design requirements best [9]. In modern civil aviation, the requirements mostly focus on reducing in-flight emissions, such as CO<sub>2</sub>, NO<sub>x</sub>, soot, water, or noise. The aircraft level performance of a configuration has to be determined at an early stage of aircraft design where there is little proven knowledge on the detailed performance and behavior of the involved systems. For conventional systems and components, simple analytic or semi-empirical methods describe their multi-directional relations [9]. BLI fans are tightly integrated propulsion systems, which inherently feature a strong coupling between aircraft aerodynamics and integrated propulsion systems. Consequently, installing a BLI device on an aircraft impacts all systems and disciplines, including the propulsion system, aerodynamics, structure, and weights, and

a multidisciplinary evaluation of the concept is imperative. However, limited empirical data exist for aircraft concepts with fuselage BLI propulsion. Thus, physically correct modeling and analysis of PFC configurations proves to be difficult with conventional methods of aircraft conceptual design. On the other hand, an analysis using high-resolution numerical simulation methods and wind tunnel testing is resource-demanding.

Multi-disciplinary studies on the aircraft level have been conducted for a number of the configurations with fuselage propulsion integration presented in Section 2.2.1. These include studies on the mechanical PFC investigated in *DisPURSAL* [42], the turbo-electric configurations *STARC-ABL* [39], *CENTRELINE* [54], *HYPER-F* [55], a regional PFC based on an Embraer 175-E1 [88], and other studies loosely based on the *STARC-ABL* configuration (e.g. [53, 56]). All studies compared the mission performance of an aircraft with an FF either against a state-of-the-art conventional reference configuration or against a conventional configuration with advanced conventional technologies projected to an EIS in the future.

The *DisPURSAL* project was a two-year project which started in 2013. It included a derivation of an appropriate bookkeeping scheme [25], 2D-axisymmetric RANS (Reynolds-Averaged Navier-Stokes) CFD studies of the fuselage-propulsor configuration with an Actuator Disk (AD) representing the influence of the FF [42], the integration of high-fidelity aerodynamic data into a propulsion system design model [95], the development of a conceptual framework for the cycle and flow path design of a FF [96], and the development of a quasi-analytical method for the evaluation of PFCs [97]. The first multi-disciplinary aircraft study of a PFC with EIS 2035 was conducted to conclude the project. The performance of all gas turbines (underwing and aft-fuselage) was modeled with a modified gas turbine performance tool. Regression models were derived from the CFD data to match the aerodynamic analysis with the 0D FF performance model. Additionally, a parallel compressor theory method was employed to account for the effect of radial inlet distortion on fan efficiency and surge margin. Aerodynamic and weight estimation was based on semi-empirical methods [42, 98]. Bijewitz continued the efforts of the *DisPURSAL* project and used its PFC geometry to demonstrate the applicability of a conceptual aircraft design framework for aircraft configurations with fuselage propulsion. The aerodynamic data from six different fuselage-propulsor geometries was employed to derive regressions as input to the thermodynamic cycle model. The aerodynamic data was derived from 2D-axisymmetric CFD simulations conducted within the project [42]. The propulsion system methodology was a critical part of the aircraft design framework, which included thermodynamic cycle design, flow path sizing, geometric dimensioning, and weight prediction for the main engines and the FF. The conceptual aircraft design framework was based on the methodology presented by Seitz [99]. It used semi-empirical methods to estimate aerodynamics and structural weights. The propulsion system's performance, design, and weights (underwing podded GTFs and FF) were fed to the aircraft design via a surrogate model [96]. Bi-directional aero-propulsive effects were considered in this study by including powered CFD data. However, the small number of studied geometries limits the design space for the configuration.

The aim of the *CENTRELINE* project was the proof of concept demonstration of a turbo-electric PFC. Therefore, all aircraft systems that are affected by introducing an FF were studied in detail. This included sizing and performance modeling of the propulsion system (underwing-podded GTFs and FF) [100, 101], the design of the TEPT components [102, 103], an FEA (Finite Element Analysis) aero-structural analysis of the aircraft structure [104, 105], 2D and 3D RANS CFD studies and wind tunnel experiments of the bare fuselage-propulsor configuration and the full aircraft geometry [21, 22, 106] (see also Section 2.2.3), and a combination of numerical and experimental studies for the design of the FF stage [107, 108]. Most of the results were incorporated into a multi-disciplinary assessment of the aircraft performance as depicted in Figure 2.6. For a given cabin geometry and design *FPR* (Fan Pressure Ratio), the fuselage-propulsor geometry was optimized, and its performance characteristics in different flight conditions of the flight envelope were calculated with 2D-axisymmetric RANS CFD simulations. A Body Force Model (BFM) modeled the effect of the FF on the fluid. A surrogate model was derived from the numerical results

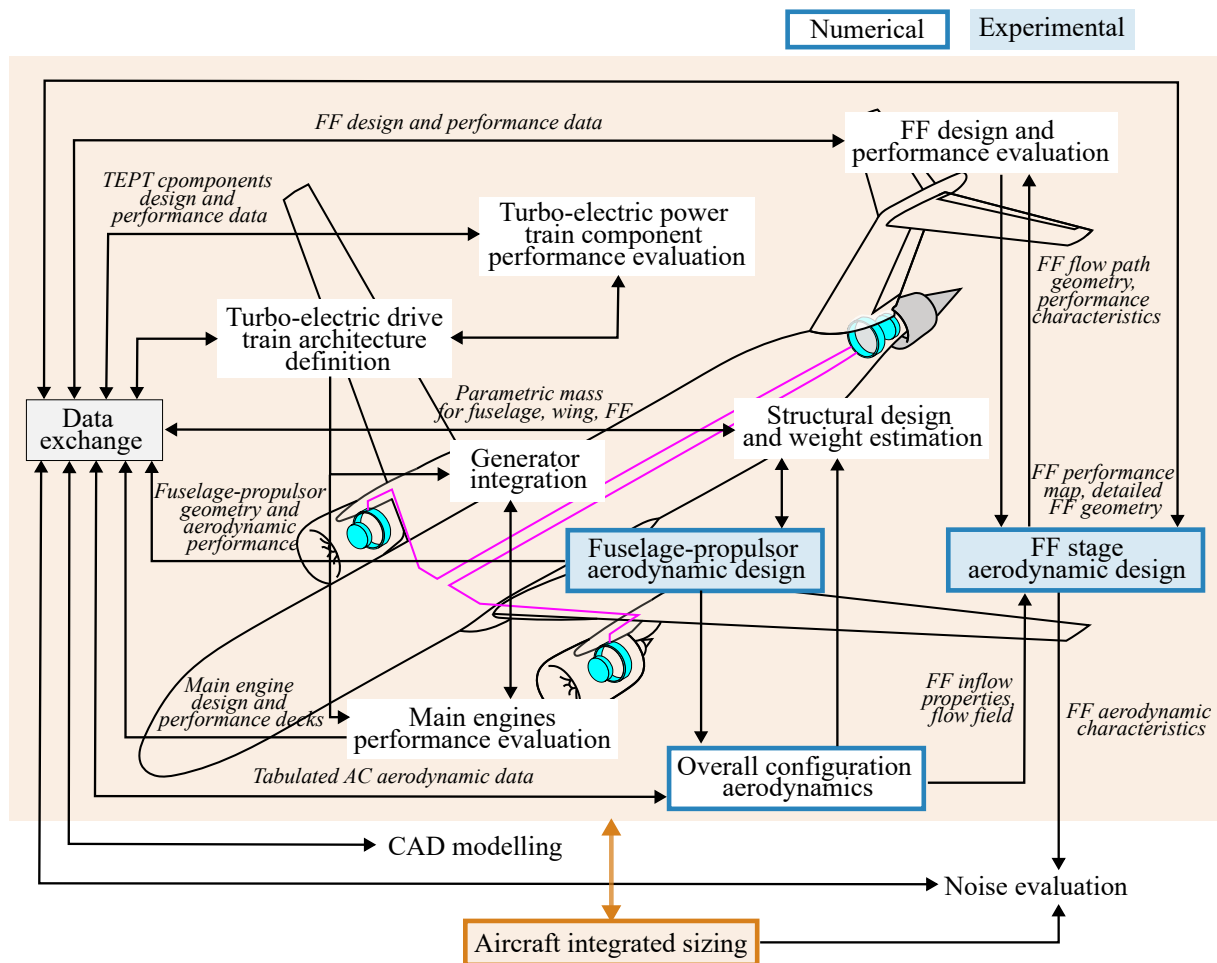


Figure 2.6: Design studies, which contributed to the integrated aircraft design in the *CENTRELINE* project. Adapted from [109].

covering FF design and off-design conditions. The aerodynamic performance map was integrated into the aircraft design process. 3D RANS CFD data of the full aircraft geometry served as an input to the combined numerical and experimental assessment of the FF. Results of the analysis were employed to derive an FF sizing and performance synthesis model, which was incorporated into the integrated aircraft design framework. Additionally, the fuselage and FF weights resulting from the FEA analysis, models for TEPT component weights and efficiencies, and the main engine performance deck were employed to derive the final PFC configuration [54, 109, 110]. The aircraft study considered the mutual effect of fuselage and fuselage-propulsor by including powered CFD data. However, the TLARs for the PFC were consolidated early in the project. Thus, the design space for the explored fuselage-propulsor geometry was limited to an optimization of the rear part of the fuselage and the FF nacelle at a given design cruise condition, FF *FPR*, and fuselage nose and center section geometry.

Comprehensive research activities focused on the design of individual systems of the *STARC-ABL* configuration. These included (but were not limited to) numerous 2D and 3D numerical studies aiming to optimize the coupled aero-propulsive performance of the fuselage-propulsor geometry by aerodynamic shape design [18, 20, 49, 50, 111–117] (see Section 2.2.3 for more details), structural integration studies for the FF [118], the efficient design of a BLI fan and Outlet Guide Vanes (OGVs) with inlet distortion [119, 120], a dynamic analysis of the aircraft's propulsion system [121], and the investigation of a

direct-drive electric motor for the FF [122]. The first conceptual design studies of the *STARC-ABL* configuration were published by Welstead and Felder in 2016. Their results served as a baseline for the detailed system-level studies cited above. No higher-order tools were employed to analyze the PFC analyzed in the multi-disciplinary study. However, CFD simulations of the aft section of the non-BLI *Boeing SUGAR Freeze* fuselage were used to estimate the BL profiles incident to the FF in take-off and at top-of-climb. A normalized average Mach number and total pressure at the FF inlet were derived from the profiles, which served as an input to the thermodynamic cycle analysis tool. The same tool modeled the main engine propulsion performance. Simplified methods were employed for aerodynamic and weight estimations [39]. The study followed a fully uncoupled approach, which did not consider any aero-propulsive coupling (see also Section 2.2.3). Additionally, Hall et al. assessed the mission fuel burn reduction potential of the *STARC-ABL* configuration with highly simplified models of all components and disciplines in an attempt to demonstrate their aircraft optimization framework based on signomial programming. Especially the limited fidelity of the propulsion performance models limits the meaningfulness of the results [123]. Giannakis et al. presented a preliminary design analysis of a turbo-electric PFC similar to the *STARC-ABL* concept. Results of powered 3D RANS CFD calculations were post-processed, and an equivalent inlet velocity was derived, which served as an input to the BLI propulsion performance modeling. Simulations for three aft-propulsor configurations with  $FPR = 1.3$  were carried out. The main and BLI engine performance was modeled using a propulsion system performance analysis. The masses of the turbofans and the BLI propulsor were derived from a mechanical analysis. Additional weight increments and efficiency losses by the electrical components were considered [56]. Computationally expensive 3D CFD simulations were carried out to model the bi-directional aero-propulsive effect of the FF. As elaborated in Section 2.2.3, the shape of the fuselage-propulsor geometry significantly impacts the performance of the BLI propulsor. In this study, the number of simulations was too small to identify an optimal fuselage-propulsor geometry and, thus, to adequately represent the propulsor performance for an aircraft-level optimization study.

Within the *HYPER-F* project, a combination of Level 0 (draft pre-design) and Level 1 (comprehensive pre-design) multidisciplinary investigation of a turbo-electric PFC based on an A320 configuration was conducted. A Vortex Lattice Method (VLM) combined with semi-empirical analysis was employed to estimate the drag of the lifting surfaces and all other aircraft components. An AD model, in combination with an approximation of the FF inlet BL, was employed to assess the *PSC* of the configuration. The estimated BLI benefit then served as an input to studying the TEPT. A thermodynamic cycle code was used for modeling the gas turbine performance [55]. The aircraft design method simplified the BLI effect and did not consider bi-directional aero-propulsive implications.

Finally, Secchi et al. investigated the potential of retrofitting a regional aircraft with a turbo-electric FF system. They assumed that wing size and structure, main engine diameter, and landing gear stayed unchanged compared to the reference aircraft. Conventional methods were employed to model aircraft aerodynamics. The characteristics of the BL flow incident to the FF was estimated with a (corrected) empirical 1D flat plate model for turbulent BLs. The electric fan was modeled with isentropic thermodynamic correlations, and the underwing-podded engines were modeled with a 0D thermodynamic cycle analysis in GasTurb [124]. It was taken into account that the addition of electrical propulsive components leads to an efficiency degradation of the propulsion chain and introduces weight. The weight of the main engines and the FF was estimated from semi-empirical correlations as a function of fan diameter [88]. The approach did not consider the mutual influence of fuselage-propulsor performance and fuselage aerodynamics.

To ascertain the potential reduction in fuel burn of PFCs on aircraft level, it is imperative to employ fast-responding methodologies. These methods should model the reciprocal influence of the BLI propulsor on the design and performance of all other aircraft components and aircraft-level parameters. Most existing multi-disciplinary PFC studies either hinge on a multitude of assumptions, simplifying the coupling

between airframe aerodynamics and propulsion system performance to a level at which the bi-directional influence of the propulsor on the airframe aerodynamics, and vice versa, is disregarded. Alternatively, they resort to high-fidelity 2D and 3D CFD simulations and/or wind tunnel testing results to optimize singular aircraft geometries for specific operating conditions. The aerodynamic performance of the fuselage and FF nacelle geometry is significantly affected by the operation of the FF and vice versa. At the aircraft level, block fuel burn estimations can vary by several percent if aero-propulsive coupling effects are omitted in the conceptual design of aircraft with BLI [85]. Recent studies attribute only a low-digit fuel burn reduction advantage to BLI. Consequently, neglecting the coupling effects substantially reduces confidence in aircraft-level results. Employing high-fidelity methods, on the other hand, is resource-intensive and time-consuming, rendering them impractical for swift integration into the iterative process of rapid conceptual aircraft design and analysis.

Hence, for a sufficiently adequate estimation of the potential emission reduction offered by PFCs in the initial phases of conceptual aircraft design, a rapid, responsive method is required. Such a method should provide aero-propulsive performance data of sufficient accuracy and seamless integration into conventional aircraft design frameworks.

### 2.2.3 Aero-Propulsive Methods

Compared to conventional aircraft configurations with underwing engines, PFCs inherently exhibit a strong coupling between airframe aerodynamics and propulsion system performance due to the closely coupled airframe-propulsor integration. Thus, achieving the optimal and efficient integration of a BLI propulsor at the aircraft level requires a comprehensive physical comprehension of local aero-propulsive effects arising from the multi-directional interaction of various aircraft components with the BLI propulsor. In the context of a PFC, the incident airflow directed towards the FF undergoes radial and circumferential distortion as it traverses along the fuselage and interacts with other aircraft components (refer to Figure 2.3). Thus, the geometric shape of the fuselage and the FF propulsion system assumes a crucial role in the multi-disciplinary performance optimization of a fuselage-propulsor concept. Consequently, it becomes imperative to undertake fuselage-propulsor shape optimization to maximize the benefit offered by a PFC. Optimizing the shape is inherently specific to each BLI concept and its associated design conditions.

Various approaches to modeling and evaluating the coupled aero-propulsive BLI performance have been developed over the last years. According to Hendricks, they can be categorized by two main characteristics: The type of model employed for modeling the airframe aerodynamics and propulsion system performance and the degree of coupling between the models [29]. The potential benefit associated with the PFC inherently stems from the interaction of the airframe aerodynamics with the BLI engine. Thus, the aerodynamic and propulsion system models require a sufficient degree of coupling to estimate the actual aero-propulsive effect of the configuration on the aircraft level. Hendricks classified the degree of coupling of a method as:

- Uncoupled – Isolated execution of aerodynamic and propulsion system model. One-dimensional data exchange between models.
- Weakly coupled – Bi-directional data exchange between models. Limited number of manual iterations.
- Strongly coupled - Bi-directional data exchange between models. High number of automated iterations until convergence.

Uncoupled approaches do not necessitate convergence of the solution and cannot capture complex interactions between aerodynamics and the propulsion system. According to Ahuja and Mavris, “Decoupled

approaches are particularly useful when there is limited design knowledge regarding the airframe and/or the propulsor, as is usually the case in conceptual design” [125, p. 3]. In contrast, weakly and strongly coupled methods capture the coupling effects through an iterative solution with varying numbers of iterations [29].

Several methods with varying degrees of fidelity can be employed to analyze the airframe aerodynamics. These include but are not limited to

- EMPirical methods (EMPs) or REGressions (REGs) based on numerical or experimental results,
- Panel methods (PMs),
- EULer CFD (EUL) coupled with Integral Boundary Layer (IBL) methods,
- 2D and 3D RANS CFD,
- Favre-Averaged Navier-Stokes (FANS) CFD,
- Unsteady RANS CFD,
- Direct Numerical Simulations (DNSs), and
- Wind tunnel EXPeriments (EXPs).

Analog, the BLI propulsion system performance can be modeled through

- EMPirical methods (EMP) or REGressions (REG) based on numerical or experimental results,
- Fixed mean station values assigned at the fan inlet and outlet, e.g. pressure, mass-flow, temperature calculated from fan efficiency or *FPR*,
- 0D and 1D ThermoDynamic Cycle (TDC) analysis,
- BFMs,
- Through-Flow Methods (TFMs),
- Parallel Compressor Models (PCMs),
- TurboMachinery (TM) CFD, and
- Fan rig experiments.

Figure 2.7 provides an overview of aerodynamic and propulsion system models, along with the level of coupling of the methods for PFCs discussed in the literature. No studies were identified that followed a weakly coupled approach, as defined by Hendricks [29]. Thus, a difference is made only between uncoupled and strongly coupled methods. Additionally, aerodynamic and propulsion system models are categorized based on increasing levels of model fidelity. Following the classification presented by Ahuja and Mavris [125], the approaches are further categorized as aerodynamic-, propulsion system-, or vehicle-centric.

In most numerical studies, the characteristics of the propulsion system, which are calculated in the propulsion system model, are transferred to the aerodynamic model either through a Boundary Condition (BC) or a Source Term (ST) interface. In the former case, the fan stage is treated as a black box in the aerodynamic simulation, with prescribed FF inlet and outlet conditions. These conditions can be constant parameters, such as mass flow, total pressure, or temperature, prescribed by the user or calculated with a 0D or 1D TDC model. Similarly, fan characteristics can be applied through STs. STs can be utilized for

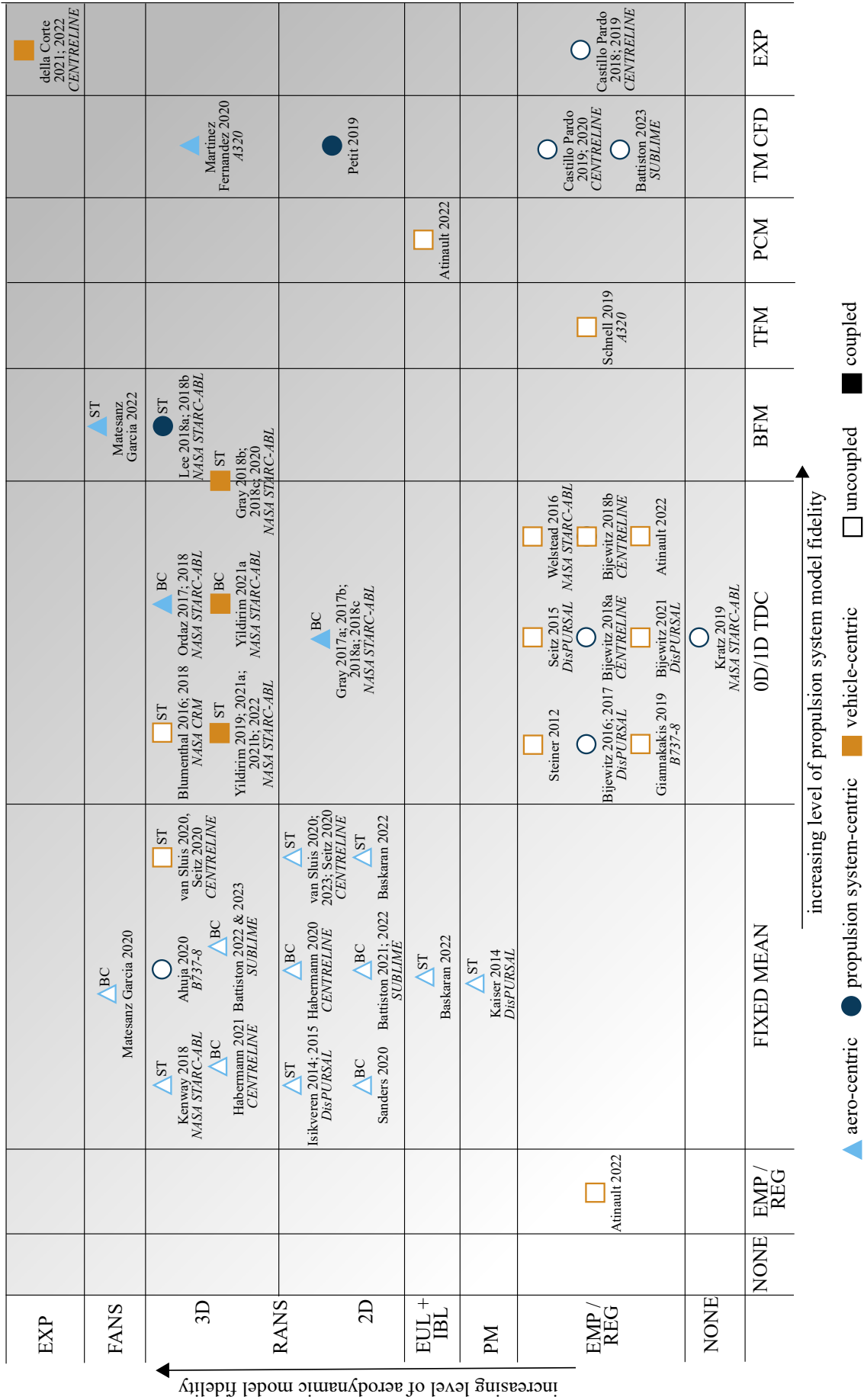


Figure 2.7: Methods employed for the aero-propulsive performance assessment of PFCs in literature. Adapted from [59, 125]. Some propulsion system models are introduced to the aerodynamic model through Source Terms (STs), such as Actuator Disks (ADs) or Actuator Zones (AZs), or through Boundary Conditions (BCs).

AD or Actuator Zone (AZ) models. BFM models constitute a special form of STs, which model the geometry of the fan stage, inherently featuring strong coupling of the propulsion system with the aerodynamic model.

The following literature review focuses on the specifics of the aerodynamic and propulsion system methods and the approach to couple the models. For a detailed review of the studies and a summary of important results, the reader is referred to existing comprehensive reviews of numerical BLI methods such as those presented by Menegozzo et al. [57] or Moirou et al. [59].

Initial in-depth analyses of BLI concepts concentrated on evaluating the performance of uninstalled propulsion systems. This assessment is inherently decoupled, as it does not consider interactions between the airframe and the propulsion system. Building upon Smith's theoretical approach [23], Plas et al. extended and applied the methodology to study the performance of embedded BLI engines in the *Silent Aircraft Initiative* [30,31].

To assess the potential of PFCs, initial aircraft-level studies employed fast and uncoupled models of low to medium fidelity to estimate the aero-propulsive performance. Exemplary, Steiner et al. derived BL characteristics from 2D RANS CFD simulations of a non-BLI fuselage, which served as input to a TDC model [6]. In a subsequent study, Seitz and Gologan followed the same approach [47]. Similarly, in the vehicle- and propulsion-system-centric studies of the *DisPURSAL* project and in the beginning of the *CENTRELINE* project, Bijewitz et al. employed RANS CFD results from the *DisPURSAL* fuselage-propulsor configuration. Regressions derived from 2D RANS CFD results of the bare fuselage-propulsor configuration [42] represented airframe aerodynamics and were used as input to the BLI TDC model [95,96,100,126,127]. The aerodynamic results were obtained through a 2D-axisymmetric RANS CFD simulation with ADs [42,98]. They were additionally used to (pseudo-)validate the results of a PM approach introduced by Kaiser et al. in 2014, combining a viscous-inviscid potential theory and Boundary Layer Equation (BLE) code with constant fan characteristics introduced through a 2D AD model [97]. The first aircraft-level study results of the *STARC-ABL* project were also based on regressions derived from 3D RANS CFD results from another project (*Boeing SUGAR Freeze*) [39]. Additionally, the aircraft-level study of a turbo-electric PFC configuration based on the *STARC-ABL* concept by Giannakakis et al. derived an equivalent velocity from powered CFD data to feed into a TDC model of the BLI engine [56]. In 2022, Atinault et al. presented a design process for BLI configurations, which employed models of different fidelity. At Level 0, an empirical model was used, which was replaced by a combination of a flat plate model and power law for BL characteristic prediction with a TDC model for Level 1 assessments. At the highest Level 2, an Euler CFD code was coupled with an IBL method to predict the BL characteristics required as an input for a PCM. All approaches featured no coupling between aerodynamic and propulsion system model [128]. Schnell et al. similarly focused more on the FF design and performance than on an accurate prediction of the FF inflow aerodynamics in their assessment of a turbo-electric A320-type PFC. They used an empirical method (flat plate assumptions combined with the  $1/7^{\text{th}}$  power law) to estimate the BL characteristics incident to the 2D TFM model of the FF [53].

Naturally, most studies that concentrate on assessing or optimizing the aerodynamics of the propulsive fuselage configuration employed aerodynamic models of higher fidelity. Within the *CENTRELINE* project, van Sluis et al. conducted a 2D design space exploration to optimize the isolated fuselage-propulsor configuration. Pre-defined FF characteristics were introduced to the flow field through an AZ in 2D RANS CFD simulations [19,106,129]. The same methodology was employed to assess the impact of wing downwash, VTP, belly fairing, and the 3D fuselage-propulsor shape in a 3D simulation [19,129]. In a similar approach, Battiston et al. conducted RANS CFD simulations as part of the *SUBLIME* project. Initial 2D simulations aimed at narrowing the design space for a subsequent parametric 3D shape optimization of the fuselage-propulsor configuration. In an iterative process, mass flow and fan outlet total temperature were prescribed through BCs to achieve a pre-defined *FPR* and polytropic fan efficiency  $\eta_{pol}$  [81,130,131]. 3D results additionally served as an input to the design of the concept's FF based on single-passage steady TM CFD [81]. Matesanz Garcia et al. similarly developed a methodology

for shape optimization of a fuselage-propulsor configuration through 2D FANS simulations. Initially, the impact of the FF on the flow field was modeled using a mass-flow BC at the rotor inlet and a pressure BC at the stator outlet station [132]. In a subsequent study, the FF model was replaced by a BFM, aiming for a stronger coupling of the models [133]. In 2020, Ahuja published a comprehensive study on the sensitivity of typical tube-and-wing airframe features on BLI performance for a B737-8 type aircraft with a distributed fans concept. Ahuja's studies focused on the propulsor design for a PFC configuration similar to the *STARC-ABL* concept. The FF effect was introduced to the 3D RANS CFD solver through fan BCs, with a uniform static pressure and temperature prescribed at the fan face, and a uniform total pressure and temperature prescribed at the fan stage outlet [134]. Baskaran et al. compared the results of a viscous-inviscid Euler/IBL code with an actuator volume model *MTFLOW* (Multielement Through-Flow) [135], to 2D RANS CFD simulations with an AD for an unducted propulsor installed at the fuselage trailing edge. The former method models the effect of the propulsor only in the inviscid flow field, necessitating a propulsor radius larger than  $\delta$ . Thus, partial BLI cannot be modeled by this approach [136]. Sanders and Laskaridis demonstrated the applicability of an energy-based force decomposition method to BLI configurations on 2D RANS CFD simulation data. They introduced the effect of the FF on the flow field through pre-defined fan BCs [137].

Although Rodriguez et al. presented a coupled approach to estimating the aero-propulsive performance of a BWB with BLI as early as 2001 [26], the first strongly coupled methodology for PFC was demonstrated by Gray et al. for the *STARC-ABL* configuration in 2017 [111]. Since then, the *STARC-ABL* concept has been comprehensively assessed through strongly coupled aero-propulsive numerical methods. Initial studies by Gray et al. introduced a coupled-adjoint approach for assessing and optimizing the fuselage-propulsor aerodynamics for a pre-defined *FPR* using a 1D TDC model coupled to 2D RANS CFD simulations through BCs in a multi-disciplinary design and optimization framework. Their work highlighted the significant contribution of both BLI propulsion and aerodynamics to the potential BLI benefit, emphasizing the importance of strongly coupled models for assessing the aero-propulsive performance of such configurations [50,111,112,138]. In a lower fidelity, uncoupled approach, Kenway and Kiris employed 3D RANS CFD with an AZ to analyze a simplified model of the *STARC-ABL* concept, focusing on the impact of wing downwash on the BLI performance. A uniform thrust was specified across the AZ. Their study involved a 3D adjoint-based aerodynamic shape optimization of the fuselage diffuser and nacelle inlet, aiming to minimize inlet distortion at the BLI propulsor and demonstrating the sensitivity of the design to flight conditions and wing downwash [117]. Based on these results, later studies of Gray et al. addressed the geometric optimization of the propulsor to achieve minimum FF shaft power in a 3D RANS CFD simulation of the full 3D aircraft geometry coupled with a 1D TDC model through a BFM [18,49,138]. Gray's BFM approach was further employed in comprehensive 3D design optimization studies by Yildirim et al. for the full *STARC-ABL* aircraft geometry [20,113,114,116]. Additionally, Yildirim compared the ST setup to a numerical simulation with BCs in his PhD dissertation, pointing out that the powered BC model is less accurate than the ST method as it cannot transfer the non-uniformities of the flow field as effectively [20]. Ordaz et al. proposed a similar strongly coupled adjoint-based numerical design and optimization approach for minimizing flow distortion at the BLI propulsor intake. They combined a 3D RANS CFD model with a TDC through BCs and applied it to an MTA450 business jet with an aft fan, as well as the *STARC-ABL* concept [139,140]. In contrast, Lee et al. focused on the aerodynamic design and optimization of the BLI propulsion system. They followed a multi-fidelity approach with a quasi-2D TFM for FF blade design, 3D TM CFD for fan design, and performance analysis coupled to a 3D RANS CFD flow field assessment through a BFM [119,120]. In a lower fidelity approach, Kratz and Thomas conducted a dynamic, nonlinear system analysis of the *STARC-ABL* propulsion system with a 1D TDC model of the BLI fan, neglecting interaction with the airframe aerodynamics [121]. Concurrent with the NASA STRAC-ABL project, Blumenthal et al. developed a numerical method based on 3D RANS CFD simulations on the *NASA Common Research Model* (CRM) geometry with an unducted fuselage propulsor. Results of a 1D TDC model of the BLI engine were introduced to the flow field through

an AD [46,141]. Other strongly coupled approaches include the combination of 3D TM CFD simulation with a 2D RANS simulation of the axisymmetric flow domain by Petit et al. to optimize the propeller of a BLI configuration [142]. Further, Martinez Fernandez and Smith investigated the forces and moments acting on the fuselage-propulsor geometry of a BLI concept based on an A320-type aircraft compared to a non-BLI fuselage. They employed a fully coupled approach, with a 3D RANS CFD simulation of the flow field and FF rotor [143].

Only a small number of experimental investigations of PFCs are documented in the literature. Two studies were conducted in the *CENTRELINE* project. In [107,144,145] Castillo Pardo et al. presented a BLI fan design study, which consisted of an experimental fan rig campaign in conjunction with 3D RANS CFD studies. Here, the inlet conditions to the FF stage were pre-imposed through distortion gauze and numerical BCs, respectively. The conditions were derived from RANS CFD simulations by van Sluis [19]. In contrast, the wind tunnel test campaign by della Corte et al. focused on the full aircraft configuration, including the coupled interaction of fuselage and fuselage propulsor in subsonic conditions with  $Ma_\infty < 0.12$  [21,22].

The literature review reveals a significant research gap in evaluating the aero-propulsive performance of PFCs within the context of aircraft conceptual design. While numerous aircraft-level studies have been conducted, most utilized simplified and decoupled approaches for appraising fuselage-propulsor performance, neglecting crucial aero-propulsive interactions. Recently, there has been an escalation in the fidelity of employed models and the degree of coupling. Results from aerodynamic-centric investigations emphasize the necessity for a strongly coupled approach to aptly model the aero-propulsive performance of PFCs. Decoupled approaches often lack the capacity to capture intricate interdependencies between airframe aerodynamics and BLI propulsion, resulting in inconsistent results and increased uncertainty in the conceptual design results. Strongly coupled methodologies utilizing high-fidelity aerodynamic and propulsion system models are more suitable for assessing BLI concepts. However, existing coupled approaches are deemed more suitable for post-conceptual design stages due to their inefficiency in conceptual design, requiring a substantial number of iterations between models and incurring high computational expenses.

In summary, despite the potential benefits of BLI, a noticeable deficiency exists in computational methods capable of efficiently and accurately evaluating PFC performance and enabling the parametric and coupled aero-propulsive design and analysis of PFCs during the conceptual aircraft design process. Such a methodology is essential for assessing the performance of BLI concepts, considering multiple flight conditions, and expediting rapid design space exploration for quick knowledge acquisition during the conceptual aircraft design stage.

## 2.3 Bookkeeping for Boundary Layer Ingesting Aircraft

*The following chapter provides a summary of the comprehensive review on “Performance Bookkeeping for Aircraft Configurations with Fuselage Wake-Filling Propulsion Integration”, which was published by the author as part of the thesis project [146].*

Assessing the emission reduction potential of unconventional aircraft configurations and comparing them to conventional concepts requires adhering to common standards. As such, a practical bookkeeping scheme should be consistent with the following criteria outlined by the *Ministry-Industry Drag Analysis Panel (MIDAP) Study Group* in 1979 [147, p. 27]

- "It must be free from ambiguity"
- "It must, so far as possible, provide for the separate study of engine and airframe performance [...], both in preliminary paper projects and in any subsequent model and/or flight testing"

- “It must include clear definition of the interfaces where engine and airframe responsibilities meet, and facilitate a proper understanding of any zones where responsibilities overlap”
- “It must assist in planning model and flight testing in such a way as to provide the information required for design and performance evaluation at minimum total cost.” (component-wise testing: airframe model, intake, nozzle, engine test bed)
- “It must recognize practical limitations in experimental and theoretical techniques”

However, BLI concepts involve closely integrated propulsion systems, resulting in strong coupling between airframe aerodynamics and propulsion system. In cases where propulsion systems are integrated into the aft fuselage, a significant interaction occurs between the fuselage flow field, surface pressure distribution, and the FFs internal aerodynamics. In consequence, defining conventional drag and thrust terms according to [147] becomes challenging due to this intricate coupling, rendering traditional simplifications and CV definitions ineffective. Various studies explored BLI potential using specific bookkeeping methods tailored to distinct configurations and objectives. Some focus on the potential of the BLI propulsion system [40, 148, 149] or on the integrated aircraft concept compared to conventional aircraft [33, 150]. However, these existing methods are limited in scope and applicability due to numerous assumptions or simplifications. A unified bookkeeping approach is essential to enable a meaningful comparison of different BLI concepts. This approach should cover initial aircraft sizing studies and subsequent more detailed design analyses, facilitating consistent performance analysis and identification of improvement. A unified bookkeeping approach is essential to enable a meaningful comparison of different BLI concepts during all multidisciplinary conceptual aircraft design stages (see [147]). In the following section, existing bookkeeping schemes and figures of merit for the performance evaluation of BLI concepts are reviewed and evaluated. Chapter 4 subsequently presents a unified bookkeeping scheme and accompanying figures of merit, which are based on the presented literature research and employed in the current study.

### 2.3.1 Bookkeeping Schemes

In 2018, Hendricks first approached the categorization of bookkeeping schemes for BLI configurations. He examined modeling approaches and performance metrics for various BLI concepts at NASA, highlighting the need for a unified modeling approach due to diverse methodologies existing within the same institution. Hendricks categorized approaches based on the propulsion system and vehicle aerodynamics modeling and the extent of coupling between the two disciplines [29] (see also Section 2.2.3). An alternative categorization of bookkeeping schemes is established in the following. It is summarized in Figure 2.8. It categorizes approaches based on the conserved quantity and CV approach. This classification of aircraft bookkeeping schemes stems from an extensive literature review. All methods integrate conserved quantities within a CV. Approaches based on integral momentum conservation differ from those based on integral kinetic or total energy conservation. CV perspectives vary, with most employing a body perspective, where parts of the CV boundary run along the model surface [8, 23, 26, 151, 152]. In the fluid-flow perspective, all CV boundary surfaces are situated in the aircraft’s far field [153]. Integral momentum conservation methods mostly analyze uninstalled propulsion systems or assess coupled airframe-propulsion systems. Conversely, all power and exergy balance methods consider bidirectional aero-propulsive effects.

#### 2.3.1.1 Integral Momentum Methods

In the traditional separation of airframe and propulsion system, many schemes employ momentum conservation on a body-centered CV, derived from Newton’s second law. The integral momentum equation

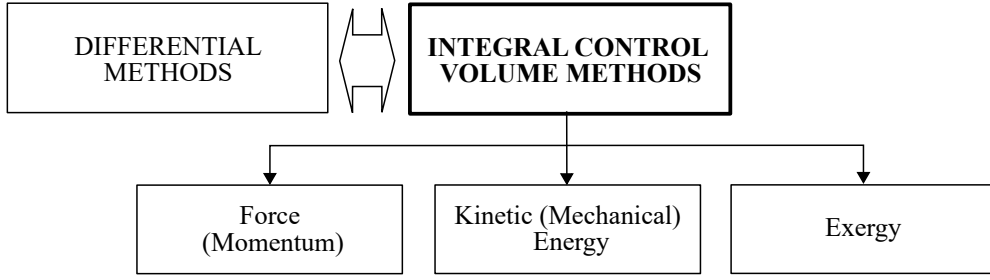


Figure 2.8: Classification of bookkeeping schemes. Adapted from [146].

as provided by [154] in Equation 2.7 accounts for momentum change inside the CV and efflux across its boundaries, balanced by pressure, viscous forces, and body forces.

$$\frac{d}{dt} \iiint_V \rho \mathbf{v} dV + \iint_A \rho (\mathbf{v} \cdot \mathbf{n}) \mathbf{v} dA = \iint_A -p \mathbf{n} dA + \iint_A \bar{\tau} dA + \iiint_V \rho \mathbf{g} dV \quad (2.7)$$

Momentum conservation methods are widely used for drag calculation, deriving drag components from wake properties or body forces. The classic drag/thrust bookkeeping, introduced by the *MIDAP Study Group* [147], assesses propulsion and airframe independently through predefined CVs. BLI configurations, however, inherently feature a strong coupling of airframe and propulsion system and, thus, require a more intricate definition of thrust, drag, and force terms. To apply the integral momentum approach, two main strategies emerge: assessing the uninstalled propulsion system or adopting a holistic view that considers the bi-directional impact of BLI on aerodynamics and propulsion system performance. Some approaches focus on fluid-flow perspectives, while most adhere to body-centered viewpoints. Fluid-flow methods typically use stream tubes enveloping the airframe or propulsion system, spanning from upstream of the fuselage nose/engine inlet to far downstream of the fuselage trailing edge/engine exit. Based on experimental or numerical data, this scheme effectively calculates drag components, including pressure, viscous, lift-induced, and wave drag [12, 153, 155].

Initially, detailed BLI concept assessments concentrated on uninstalled propulsion systems, which evaluated the propulsion system in isolation, ignoring airframe interaction. Plas, Hardin, and Goldberg furthered this approach, analyzing the *Silent Aircraft*, *NASA N3-X* BWB, and other concepts [8, 152, 156–159]. Meanwhile, a coupled approach, exemplified by Gray and Ordaz, examined installed systems, integrating drag and thrust forces over the aircraft’s surfaces [49, 111, 139, 140, 160, 161]. Employing bookkeeping schemes grounded in integral momentum conservation, particularly Smith’s advancements, helps grasp the fundamental principles of BLI. Directly integrating surface stresses provides clarity in understanding forces on the aircraft, especially when resolving flow fields through CFD. The calculation of forces acting on the aircraft components fosters consistency with the traditional multidisciplinary aircraft design based on a drag and thrust force definition. However, momentum conservation approaches often focus on propulsion perspectives and may neglect bi-directional influences, limiting their applicability. A comprehensive bookkeeping approach based on integral momentum conservation could bridge the gap between traditional aircraft design and the evaluation of unconventional propulsion-airframe integration benefits.

### 2.3.1.2 Integral Energy Methods

To address the complexities that arise from the tight aero-propulsive coupling, the power and exergy balance methods introduced by Drela and Arntz, respectively, offered alternative viewpoints for assessing aircraft configurations with BLI [8, 33, 150, 151]. Both methods utilize an integral energy conservation approach from a fluid-flow perspective. Drela’s power balance method analyzes kinetic energy conservation within a defined CV, accounting for the coupling of the propulsion system and aerodynamics.

The method conserves wake energy by incorporating kinetic energy deposited in the Trefftz plane and dissipated within the wake. The resultant power balance equation (Equation 2.8 [33]) equates total mechanical power supply, production and inflow into the CV (net propulsor shaft power  $P_S$ , net pressure volume  $P_V$ , and net propulsor mechanical energy flow rate into the CV  $P_K$ ) to mechanical power consumption and outflow due to processes within the CV (viscous dissipation rate  $\Phi$  and mechanical energy flow rate out of the volume  $\dot{\epsilon}$ ).

$$P_S + P_V + P_K = \dot{\epsilon} + \Phi \quad (2.8)$$

This approach has been widely applied in BLI concept studies [35, 46, 137, 141, 162–171]. The power balance method is especially useful for assessing the advantages of a BLI configuration over a conventional concept. It helps understand the individual mechanisms responsible for the overall benefit of BLI. To use the original method by Drela, in-depth knowledge of flow-field characteristics, obtainable from wind tunnel tests or CFD simulations, is required. Yet, optimizing single components based on the power balance method is difficult. Calculating forces, drag, or thrust, which conventional tools rely on, involves many simplifications.

Arntz introduced the exergy balance method in 2014 as a system-level framework for aircraft performance assessment, combining momentum balance and the first and second laws of thermodynamics [150]. The exergy supply by the propulsion system and its partial destruction within a thermodynamically open CV are evaluated. The exergy method considers mechanical and thermal energy, providing a comprehensive approach to aero-thermo-propulsive performance assessment. It aims at identifying designs with minimum waste and destruction of energy, which therefore require the least propulsive energy to compensate for the energy losses [34, 150, 171, 172]. Applications of the exergy balance method included unpowered airframe solutions, propulsor configurations, BWB with BLI, and heat exchanger integration [34, 150, 172–176].

In summary, the power balance and exergy balance methods offer insightful perspectives on BLI configuration benefits. However, both methods necessitate a fully resolved flow field, such as the results of high fidelity CFD simulations or highly resolved wind tunnel results in combination with customized flow field evaluation tools (e.g. *Epsilon* [177]). This limits their applicability to advanced stages of design analysis (see also Section 2.3.2).

## 2.3.2 Figures of Merit

All bookkeeping schemes applied to BLI concepts are accompanied by performance indicators, which quantify the potential of evaluated configurations. In the following, several important performance indicators are introduced and discussed regarding their relevance to conceptual aircraft design. The selection of figures of merit is based on the authors' discretion and is not exhaustive.

### 2.3.2.1 Conventional Performance Indicators

To facilitate understanding, conventional power and propulsion efficiency terms, drag, thrust, and force definitions are presented first. Commonly used system efficiency terms in propulsion performance analysis include core or energy conversion efficiency  $\eta_{ec}$ , transmission efficiency  $\eta_{tr}$ , and propulsive efficiency  $\eta_p$ , which collectively contribute to the overall efficiency  $\eta_{ov}$  (e.g. [99]):

$$\eta_{ov} = \eta_{ec}\eta_p\eta_{tr} = \frac{P_{thr}}{P_{sup}} \quad (2.9)$$

Degree of Universality	
Covered flow properties	Compressibility Non-uniform inflow Wave drag effects
Configurational properties	Applicability to ducted propulsors Flexibility in axial propulsor location
Included installed propulsion system effects	Drag and thrust interaction Wake and jet interaction Impact of propulsor upstream interaction effects with aircraft surfaces
Applicability to Conceptual Design Phase	
Reduce resource demand	Pre-processing time and effort Response time No CFD/numerical resolution required
Improve compatibility	... with standard propulsion system performance calculation ... with typical aircraft conceptual design tooling ... with physical testing e.g. wind tunnel/fan rig testing ... with methods of different fidelity (e.g. semi-empirical/fully resolved CFD) ... with typical drag and thrust decomposition
Improve design analysis capability	Component based resolution capability Indication of local design optimization

Table 2.1: Assessment criteria for BLI figures of merit. Source: [146].

Propulsive efficiency connects the useful power output  $P_{thr}$  to the propulsor power  $P_p$ . For maintaining steady level flight in given atmospheric conditions, the required thrust power is defined as the power required  $P_R$  and is related to the aircraft's total drag  $D$ :

$$\begin{aligned}
 P_p &= \frac{\dot{m}}{2} (u_9^2 - u_0^2) \\
 P_{thr} &= T u_0 \\
 P_R &= T_R u_0 = D u_0
 \end{aligned} \tag{2.10}$$

While defining drag and thrust is straightforward for conventional under-wing engine aircraft, it becomes more complex for BLI studies to conform with existing design tools. The *MIDAP Study Group's* publication [147] defines drag as the difference between integrated surface forces in real (viscous) flow and the potential flow buoyancy for the same body. When considering an entire body, the potential flow buoyancy is zero, making the drag equivalent to the sum of integrated skin friction and pressure forces over the full body surface. However, the potential flow buoyancy cannot be dismissed if only specific body parts are considered. Calculating drag terms necessitates knowledge of potential flow characteristics for the same body segments.

### 2.3.2.2 Assessment Criteria

A thorough evaluation was conducted to gauge the suitability of existing figures of merit for the application to the multidisciplinary conceptual aircraft design. The requirements for the suitability of the available figures of merit for BLI configurations stem from the multidisciplinary assessment of aircraft configurations during the conceptual design stage. Two key criteria are employed: the extent of the figure's universality and its applicability within the conceptual design phase. Detailed evaluation criteria are provided in Table 2.1. A comprehensive account of the assessment process and outcomes is presented in [146]. The summarized results of the assessment are depicted in Figure 2.9. Details on the reviewed performance indicators are presented in the following.

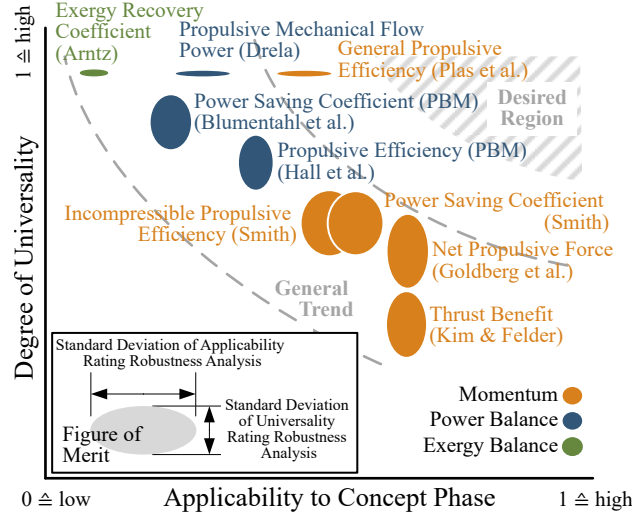


Figure 2.9: Rating of figures of merit. Source: [146].

### 2.3.2.3 Power Saving Coefficient and Propulsive Efficiency

As part of his initial studies on the potential of BLI, Smith introduced a non-dimensional  $PSC$  in 1993 [23]. It is a metric for evaluating the propulsion advantages of unducted, axisymmetric fans with BLI compared to a reference non-BLI configuration. The  $PSC$  relies on a body-centered momentum conservation evaluation. It is defined as the ratio of the difference in propulsive power between non-BLI and BLI configurations to the propulsive power required to propel the body without wake ingestion [23]:

$$PSC = \frac{P_{p,nonBLI} - P_{p,BLI}}{u_0^D / \eta_{p,nonBLI}} \quad (2.11)$$

For propellers with wake ingestion, the  $PSC$  is determined by fluid density  $\rho$ , freestream velocities upstream and downstream of a propulsor disk ( $u_0$  and  $u_j$ ), upstream and downstream wake velocities ( $u_w$  and  $u_{jw}$ ), wake momentum area  $\Theta_A$ , and propulsor disk diameter  $d_P$ . To differentiate between airframe drag and propulsion thrust effects of BLI, Smith calculates drag from wake properties by analyzing a CV boundary in the far field of the airframe [23]:

$$D = \rho u_0^2 \Theta_A \quad (2.12)$$

The  $PSC$  is an initial gauge for potential fuel savings when comparing BLI and non-BLI concepts. Simple power calculations for the  $PSC$  can be executed using standard propulsion system sizing tools. Nonetheless, its strict application, as outlined by Smith, remains confined to unducted, axisymmetric BLI designs and incompressible flow scenarios. The propulsor's impact on inlet flow non-uniformity is implicitly considered. In the context of conceptual design, a number of assumptions about BL properties or preliminary CFD outcomes are necessary when applying this metric. Individual drag and thrust computations ensure compatibility with conventional aircraft conceptual design methodologies.

Another performance indicator by Smith [23] is the (incompressible) propulsive efficiency:

$$\eta_{P,i} = \frac{2}{\frac{u_j}{u_0} + 1 - \frac{D}{T}(2 - R) \left( \frac{u_j}{u_0} - 1 + R(1 - K) \right)}, \quad (2.13)$$

Where  $\frac{u_j}{u_0}$  is the function of disk loading,  $K$  is the pseudoenergy factor, and  $R$  is the wake recovery, which remain the same for cases with and without wake ingestion. Substituting  $D$ ,  $T$ ,  $R$ , and  $K$ , and assuming  $u_{j,BLI} = u_0$  (ideal wake filling), yields:

$$\eta_{P,i} = f(\rho, A, d_P, u_0, u_w, u_j, u_{jw}, \Theta_A) \quad (2.14)$$

Plas et al. utilized Smith's propulsive efficiency definition along with the integral momentum equation and propulsive kinetic energy equation to derive a general propulsive efficiency definition applicable to compressible flow conditions. The relationship is provided in Equation 2.15. They assumed that changes in nacelle drag can be neglected and applied the metric to assess the benefits of an embedded, axisymmetric BLI concept [178].

$$\eta_{p,c} = \frac{1 + \beta}{\frac{H^*}{2} + \beta \left(1 - \frac{u_j - u_0}{2u_0}\right)} \quad (2.15)$$

$H^*$  is an energy factor, which depends on the profile of the BL,  $\beta$  is the ratio of uningested drag to ingested drag [178]. In an abstract sense, propulsive efficiency is the ratio of useful power to available mechanical power. If  $\beta$  approaches 0 in an ideal BLI case (full BL is ingested) and if  $H^*$  approaches 1 for specific BL profiles,  $\eta_p \rightarrow 2$ . Thus,  $\eta_p$  can exceed unity, and it is not an adequate metric to measure energy losses. Unlike Smith's definition, Plas et al.'s propulsive efficiency formula covers ducted propulsors and compressible flow scenarios. Nevertheless, this metric solely addresses the influence of BLI on the propulsion system, overlooking alterations in airframe aerodynamics, nacelle, and fuselage drag. Ideal BLI is assumed. To compute the "uningested drag," comprehensive resolution of BL properties at the fan face, often through detailed CFD analysis, is required.

#### 2.3.2.4 Thrust Benefit and Net Propulsive Force

Integration of physical properties over body surfaces facilitates the calculation of axial net forces, enabling a component-based characterization and evaluation of the aircraft's performance (e.g. [47]). Kim and Felder adopted the "internal volume" approach, mapping BL properties to a CV inlet within the propulsion system. They gauged propulsion system advantages using non-dimensional figures of merit such as the thrust-specific fuel consumption benefit and the Thrust Benefit ( $TB$ ). The latter is a percentage increment in net thrust for a BLI system compared to a free-stream propulsion system devoid of total pressure loss ahead of the inlet. The  $TB$  is formulated as [40]:

$$TB = \left( \frac{T - T_{(p_{t,1}/p_{t,\infty}=1)}}{T_{(p_{t,1}/p_{t,\infty}=1)}} \right) \cdot 100\% \quad (2.16)$$

The internal volume method encompasses the impact of the BL on propulsion system performance, however, it overlooks the reciprocal influence of the installed propulsion system on the BL at the fan face. Employing a conventional propulsion system sizing tool can yield the necessary net thrust  $T$ . Comparable to other methods grounded in momentum conservation, wave drag consequences, and the influence of propulsor upstream interaction with the aircraft surface remain beyond its scope. Goldberg et al. utilized the Net Propulsive Force ( $NPF$ ) as a performance metric for assessing BLI propulsion at the conceptual design stage. Unlike employing net thrust,  $NPF$  incorporates system integration aspects [158]. Originating from the *MIDAP Study Group's* work,  $NPF$  based on force accounting can be expressed as the disparity between intrinsic net thrust  $F_{G9} - F_{G1}$  and nacelle force  $\Phi_{nac}$  [147]:

$$NPF = F_{G9} - F_{G1} - \Phi_{nac} = F_{G9} - F_{G1} - D_{nac} - \tau_w S_{wet} \quad (2.17)$$

A portion of airframe propulsion drag (the region within about twice the inlet height ahead of the propulsor highlight) is considered for simplicity while acknowledging BLI's impact on airframe drag [158].  $\tau_w S_{wet}$  signifies skin friction drag from the airframe's wetted surface area [119]. In addition to  $NPF$ , Goldberg et al. assessed ingested drag,  $\eta_p$ , and  $PSC$  to explore the BLI advantage from various perspectives [158]. Subsequent studies applied this method to the *N3-X* BWB concept [158, 159, 176]. The direct impact of the BL on propulsion system performance remained unaddressed due to the inability to directly account for propulsor intake and fan efficiency losses caused by flow distortion.

Preliminary non-dimensional characteristics of the propulsion system were initially approximated using standard propulsion system sizing tools. Employing a semi-empirical approach allowed for determining skin friction and nacelle drag. Similar to *TB*, *NPF* necessitates minimal preprocessing and exhibits rapid responsiveness, aligning well with conceptual design needs.

### 2.3.2.5 Mechanical Flow Power, Power-Based Propulsive Efficiency, and Power Saving Coefficient

The power balance method employs the mechanical flow power,  $P_K$ , which is necessary to balance all dissipation sources in the flow field as a figure of merit to assess the potential of an aircraft configuration (see Figure 2.10). By re-arranging Equation 2.8, the benefit can be translated to a reduction in flow dissipation for BLI application [149]:

$$P_K = \dot{\epsilon} + \Phi - P_S - P_V \quad (2.18)$$

The power balance method is valuable for identifying significant factors and physical mechanisms affecting the aircraft's power requirements. Interference and build-up drag are covered better compared to force-based techniques [150]. It is especially practical for BLI configurations, as it does not mandate explicit thrust and drag definitions. However, most conceptual aircraft design studies employ standard tools requiring drag and thrust accounting. An independent evaluation of propulsion and airframe components, as is common practice in the early design stages, is difficult. Using the power balance method demands detailed configuration knowledge, leading to time-intensive analysis of multiple setups [158, 159]. Most studies employing the power balance method analyze configurations with a BLI propulsor installed at the fuselage's trailing edge. Applying it to the *CENTRELINE* concept (propulsor at  $\approx 93\%$  fuselage length) posed challenges due to the interaction of the FF jet with the fuselage surface aerodynamics if the method is employed using the assumptions stated in the literature [33, 35, 162, 179, 180]. Different from Hall et al.'s approach, which considered nacelle and aft body drag (fuselage behind propulsor duct exit), expressing the power balance formulation in terms of drag and thrust is not feasible. Moreover, an analysis of the kinetic energy deficit from the BL and wake properties would be required. Hall et al. derived the following equations for a ducted BLI configuration, where the propulsion system is a single propulsor at the trailing edge of the fuselage [35, 123].

$$\begin{aligned} \dot{m}(u_{jet} - u_0) &= (D'' - f_{BLI}D''_p) - F_x \\ P_K &= \frac{1}{2}\dot{m}(u_{jet}^2 - u_0^2) + f_{BLI}(1 - f_w)D''_p v_0 \end{aligned} \quad (2.19)$$

Here, the factor  $f_{BLI}$  is a function of kinetic energy defect at the propulsor inlet and the trailing edge of the fuselage, while  $f_w$  depends on the bare fuselage wake and surface dissipation.  $D''$  and  $D''_p$  represent the total and profile drag of the non-BLI reference configuration. Under cruise conditions (steady-state,

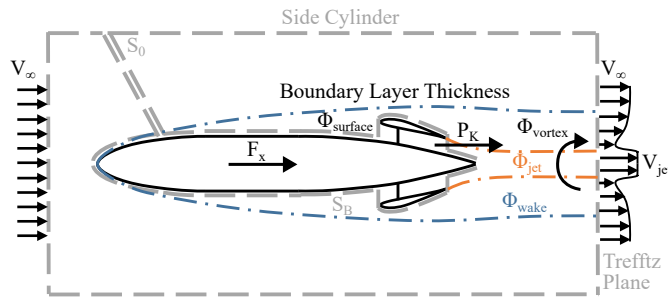


Figure 2.10: CV for the application of the power balance method. Source: [146] with original source [33].

level flight), the net streamwise force is  $F_x = 0$ , making the decrease in mechanical flow power  $P_K$  an adequate figure of merit for evaluating BLI benefit in terms of energy consumption and fuel efficiency [35]. The method is applied under several assumptions, including:

- Negligible volumetric flow power at low speeds (valid for compressible flow)
- Constant mass flow
- Steady, turbulent flow
- Trefftz plane positioned far downstream to ensure freestream conditions
- Propulsor has minimal effect on surface dissipation
- Negligible nacelle surface dissipation (i.e. nacelle drag)
- Propulsor has no impact on span-wise lift distribution and trailing vorticity mixing
- Thin shear layer assumption with constant static pressure across the shear layer
- Freestream static pressure just downstream of the propulsor

With the assumption of a uniform jet velocity, Hall et al. additionally introduced a novel propulsive efficiency definition for steady, level flight in both BLI and non-BLI configurations, formulated using power terms [35]:

$$\eta_{p,c} = \frac{P_K - \Phi_{jet}}{P_K} \quad (2.20)$$

Their study highlighted that the reduction in mechanical flow power due to BLI hinges on the extent of ingested BL and the mass flow through the propulsor. They identified two primary fuel consumption advantages of BLI: diminished wake dissipation, leading to lower airframe-required propulsive power, and reduced jet dissipation, yielding heightened propulsive efficiency. This underscored that aerodynamic performance alone is not sufficient as a sole performance indicator. Unlike the propulsive efficiency definitions by Smith or Plas et al. (Equations 2.13 and 2.15), Equation 2.20 does not necessitate the computation of drag and thrust components. Moreover, the propulsive efficiency remains bounded below unity, as jet dissipation is always positive. This figure of merit was effectively applied in CFD studies. The propulsor's  $P_K$  is calculated from an integration of properties across propulsor inlet and outlet planes, while the net streamwise force comprises summed pressure and viscous forces on the fuselage surface and the axial momentum flux across the propulsor inlet and outlet planes. Non-BLI dissipation is obtained from supplementary CFD results for an isolated fuselage. When applied to wind tunnel experiments, force measurements are not taken, the focus is solely on propulsor power. It can be determined by either numerically integrating pressure fields, velocity magnitudes, and flow directions at the propulsor inlet and outlet, or the mechanical flow power is indirectly calculated by measuring electrical power supplied to the FF motor, along with motor and fan efficiencies. To align the power balance approaches with the conventional aircraft sizing and design requirements, Marien et al. modified the approach presented by Hall et al. [35] to translate the power balance equation into the required terms for Equation 2.19 [181]. For a BLI concept with the propulsor situated at the fuselage's trailing edge during cruise, the necessary terms for assessing BLI benefits can be derived from total drag and profile drag of an isolated fuselage, and data from aerodynamics analysis, such as CFD results and propulsion system design tools. Additionally, an external aerodynamic performance figure of merit, the lift-to-drag ratio  $L/D$ , was defined based on lift, freestream velocity, and various dissipation terms (surface, wake, wave, and vortex dissipation) [181]:

$$L/D = \frac{Lu_0}{\Phi_{surf} + \Phi_{wake} + \Phi_{wave} + \Phi_{vort}} \quad (2.21)$$

Further figures of merit based on a power balance evaluation are the net propulsor power coefficient  $C_{PK}$  and the power balance saving coefficient  $PSC_{PBM}$  derived by Blumenthal et al. [46, 141]:

$$\begin{aligned} C_{PK} &= \frac{P_K}{q_0 v_0 S_{ref}} \\ PSC_{PBM} &= \frac{C_{PK,nonBLI} - C_{PK,BLI}}{C_{PK,nonBLI}} \end{aligned} \quad (2.22)$$

Blumenthal et al. aimed to demonstrate the beneficial impact of BLI on configuration performance rather than optimizing the design. They employed the PBM to assess the overall configuration benefit, rather than analyzing individual components. Consequently, the  $PSC$  derived from the power balance approach is less suitable for both conceptual sizing, due to the need for detailed flow field analysis, and design analysis, as it provides limited insights into component optimization potential.

### 2.3.2.6 Exergy-Recovery Coefficient

Arntz introduced the Exergy-Recovery Coefficient ( $ERC$ ) concept for evaluating aircraft's aero-thermal-propulsion performance. It quantifies the efficiency of exergy recovery achieved through BLI application for compressible and viscous mean steady flows as defined in Equation 2.23 [150]. It is assumed that energy is supplied through the propulsion system and heat is transferred via the aircraft's surfaces.

$$ERC = \frac{\dot{\epsilon}_{prop}^{ref} - \dot{\epsilon}_{prop}^{BLI}}{\dot{\epsilon}_{rev}} = \frac{\text{Exergy saving}}{\text{Recoverable exergy}} \quad (2.23)$$

The exergy method was designed to assess aircraft performance during the preliminary design phase. However, its application demands a detailed resolution of the flow field. Essential local properties like entropy or enthalpy are necessary for calculating exergy parameters. So far, the method has exclusively been employed as a post-processing tool for RANS CFD simulations and has not been linked to drag and thrust expressions. Arntz suggested that further advancements might be needed before aircraft designers readily adopt the method, yet it holds potential for alignment with conventional aircraft performance measures [150].

## 2.4 Synthesis and Research Questions

The potential of BLI lies in efficiently ingesting and accelerating slow-velocity air in the vicinity of an aircraft's body surface, specifically the BL, with a propulsive device. BLI presents an opportunity to reduce an aircraft's propulsion power demands, subsequently lowering energy requirements. The PFC emerges as particularly promising for large commercial tube-and-wing aircraft during cruise, as a significant portion of airframe drag is attributed to the fuselage. PFC involves integrating a full annular propulsor concentrically around the aft section of the fuselage, effectively ingesting and re-energizing the critical inner part of the fuselage BL, offering a highly coupled and efficient wake-filling propulsion integration strategy.

To address the challenges posed by the tight coupling between airframe aerodynamics and BLI propulsion systems in the conceptual aircraft design of PFCs, it is essential to develop a universally adaptable bookkeeping method. The literature review identified that several bookkeeping methods have been employed, which differ significantly and are mostly specific to the investigated aircraft configuration. Thus, a research gap for a universal bookkeeping scheme for concepts with BLI is identified. The following RQs have to be addressed:

**RQ 1:** What are the requirements for a universally applicable bookkeeping scheme, which addresses the incongruity between a drag/thrust-based conceptual aircraft design and a closely coupled airframe-propulsion integration?

**RQ 2:** Which bookkeeping scheme can adequately represent the tightly coupled effect of fuselage wake-filling and is at the same time compatible with conventional conceptual aircraft and propulsion system sizing tools?

Additionally, adequate metrics have to be derived for a meaningful evaluation of the performance of PFCs, answering the following RQ:

**RQ 3:** Which universal figures of merit are best suited to quantify the performance of a propulsive fuselage within the early stages of aircraft conceptual design?

The challenges of aircraft design of PFCs lie in the inherent tight coupling between airframe aerodynamics and BLI propulsion system, disrupting the conventional paradigm of independent design and analysis following a thrust-/drag-accounting approach. Accurate evaluation of the fuel burn reduction potential requires fast-responding methodologies that account for the reciprocal influence of BLI propulsors on the airframe, as current studies often oversimplify or overlook these coupled aero-propulsive interactions. Therefore, achieving precision and efficiency in designing and sizing aircraft concepts with BLI necessitates a responsive aero-propulsive BLI performance method seamlessly integrated into rapid conceptual aircraft design and analysis processes. The research gap in the aero-propulsive performance assessment of PFCs within aircraft conceptual design becomes evident in the literature review. While recent aircraft-level studies have increased model fidelity and aero-propulsive coupling, there remains a deficiency in computational methods tailored for conceptual design. The need for a parametric and coupled aero-propulsive methodology specifically designed for conceptual aircraft design is underscored, aiming to efficiently evaluate PFC performance under various conditions and address the current limitations in BLI assessment methods. The following RQs guide this endeavor:

**RQ 4:** What are the requirements for a numerical method that captures the bi-directional effect of a fuselage-integrated propulsion system and the airframe with adequate accuracy and applies to the aircraft conceptual design phase, which requires fast response solutions to a broad design space?

**RQ 5:** Which combination of existing methods and approaches can be employed to develop a most efficient simplified numerical tool, which captures the coupled aero-propulsive performance of a propulsive fuselage, can easily be integrated into a multi-disciplinary aircraft conceptual design framework and expanded with low effort to apply to other airframe-propulsion integration concepts?

**RQ 6:** Which specific models have to be combined for an automated, parametric, and validated, strongly coupled numerical approach for the analysis and design of PFCs in aircraft conceptual design?

**RQ 7:** How do the design parameters of the fuselage-propulsor configuration impact the figures of merit?

**RQ 8:** What is the best approach to integrate the derived numerical methodology into an aircraft conceptual design framework?

The identified research questions are addressed in the subsequent chapters of this dissertation.

# 3 Review of Numerical Methods for Boundary Layer Ingestion Aero-Propulsive Performance Evaluation

The complex interaction of BLs in the context of BLI, especially in the transonic flight regime of commercial aircraft with propulsive fuselages, introduces a multitude of intricate flow phenomena.

Section 3.1 explores the flow characteristics unique to BLI, emphasizing the challenges posed by viscous, compressible, and turbulent flows to address RQ 4. For a systematic derivation of the most suitable model for aero-propulsive performance evaluation in the context of aircraft conceptual design, Section 3.2 discusses the equations governing the flow, and Section 3.3 provides an overview of available numerical methods. The quest for the most suitable method for modeling BLI in transonic regimes posed by RQ 5, leads to the proposal of a hybrid numerical approach in Section 3.4.

## 3.1 Flow Characteristics of Boundary Layer Ingestion in Transonic Flow Conditions

A complex interaction of BLs characterizes BLI flow. PFCs in transonic cruises especially inherit several flow phenomena, which do not allow for a strong simplification of the occurring flow characteristics. The most noteworthy flow phenomena that occur in BLI are discussed below.

Viscosity plays a crucial role in the formation and behavior of BLs. Thus, viscous effects have to be modeled adequately. Furthermore, the interaction of the nacelle and fuselage BL leads to a complex flow in the vicinity of the FF. The flow field around the FF is further affected by the rotor and stator of the FF. It is generally assumed that for  $Ma > 0.30$ , compressibility effects have to be accounted for [154]. For the investigated aircraft configuration with  $0.75 < Ma_{cr} < 0.85$ , shocks can occur, for example, on the upper side of the FF cowling. Thus, an interaction of the shock with the nacelle BL must be considered. Further, it was shown that the transition from a laminar BL to a turbulent BL occurs at the fuselage nose at  $< 5\%$  fuselage length. Therefore, the following assumes that the BL flow incident to the FF is fully turbulent. Change in the fuselage diameter from its constant section diameter to the hub diameter of the FF leads to an adverse pressure gradient in front of the FF. The thickness of the BL increases (e.g. from 0.56 to 1.60m or from  $\delta/r_f = 20$  to 215% for the reference configuration) and the assumption of a thin BL with  $\delta \ll d$  does not hold. In addition, turbulent flow separation can occur in front of the FF, inside the FF duct, and at the rear fuselage.

Due to a combination of the occurring flow phenomena, the BL incident to the FF cannot be described unambiguously by the conventional definition of a BL as being a thin layer in the vicinity of a surface. Its radial extension in terms of  $\delta$  or  $\delta^*$  is also ambiguous. Thus, the common assumption that the static pressure of the BL is constant inside the BL does not hold either. Furthermore, the Prandtl BL theory, which distinctively divides the flow into an inviscid outer region and a viscous BL (see also Section 2.1.1), cannot practically be applied to the case at hand. The occurrence and strength of the phenomena are affected mostly by freestream flow characteristics, such as Reynolds number  $Re$  and Mach number  $Ma$ , the characteristics of the BL at the engine inlet, especially  $\delta$  and  $\delta^*$ , and the ratio of ingested fuselage BL  $\beta$ . The last parameter mainly depends on the position of the FF with respect to the fuselage and its geometry. For the presented application, the FF is fully immersed into the inner region of the flow, which can be attributed to the BL of the fuselage as depicted in Figure 3.1. To adequately model the

aero-propulsive effect of a propulsive fuselage, a combination of governing equations, which model the flow phenomena sufficiently accurately yet fast enough for the application in conceptual aircraft design, and an adequate method to numerically solve this system of equations is required.

In summary, the sought method is required to model a viscous, compressible, and turbulent flow with a complex BL and possible BL and shock interaction as well as turbulent separation and no possibility to distinctly divide the flow in the vicinity of the FF into a viscous BL and an inviscid outer region. To significantly reduce the required computational resources, the problem is, however, simplified to a steady fluid flow.

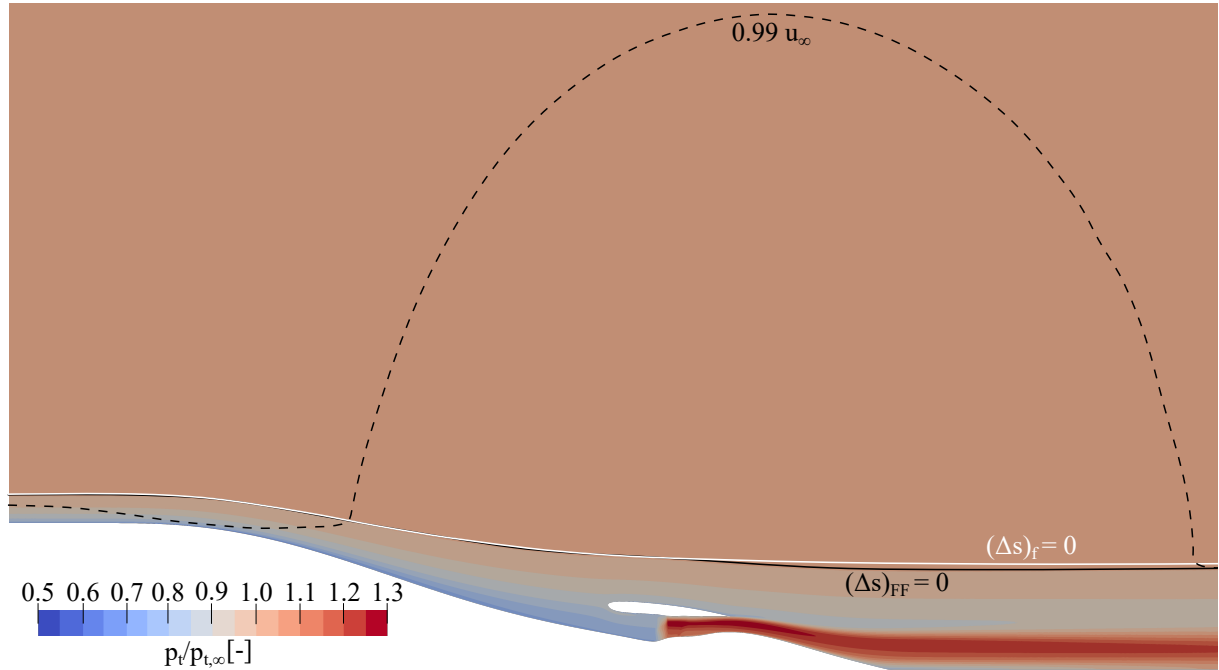


Figure 3.1: BL edge of the powered reference fuselage-propulsor configuration (black) and the bare fuselage (white) derived from RANS CFD results. The edge is estimated as the location with zero entropy generation  $\Delta s$ . Location of  $99\% u_{\infty}$  is additionally indicated.

## 3.2 Governing Equations

Governing equations are a set of mathematical equations that describe the behavior of a physical system. These equations are derived from the basic laws of physics and are used to predict the system's behavior under different conditions. The Navier-Stokes Equations (NSEs) are the governing equations describing a fluid's motion and the forces acting on it. The equations are based on the laws of mass and energy conservation and Newton's second law. They are used to predict the behavior of a fluid, including its velocity, pressure, and temperature distribution. They are generally written as a system of coupled, nonlinear Partial Differential Equations (PDEs), which are hyperbolic and elliptic, depending on the modeled physical conditions. The equations are based on the assumption that the stresses occurring in the fluid are the sum of a diffusing viscous term, which is proportional to the velocity gradient, and a pressure term. The NSEs generally apply to all fluid dynamic problems and are, thus, suitable for modeling BLI aerodynamics [182]. The numerical solution of the NSEs is, however, resource-intensive. For certain flow problems, the set of equations can be simplified to decrease computational costs. Figure 3.2 provides an overview of the most common simplifications of the NSEs. Turbulent flows are characterized

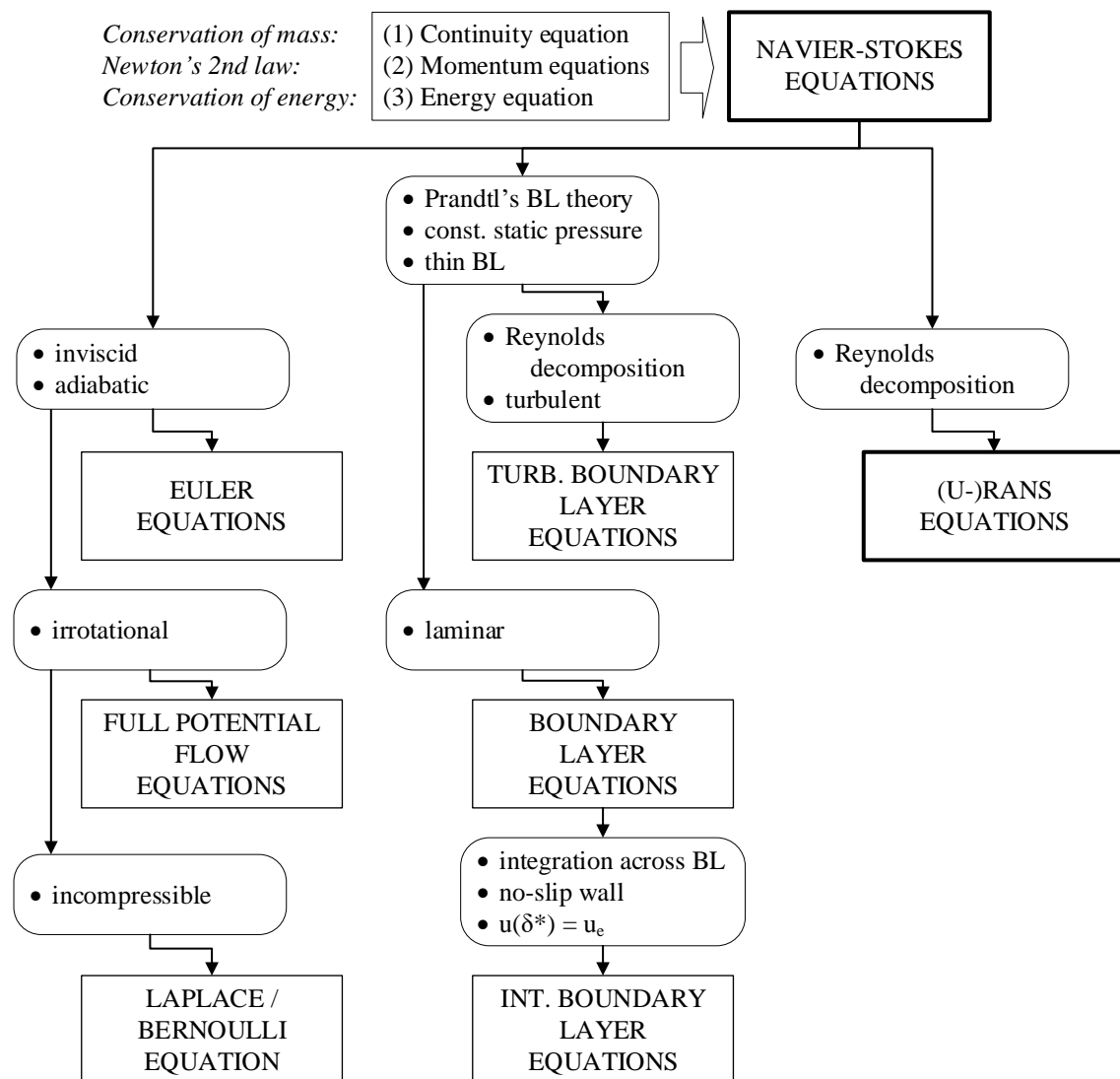


Figure 3.2: Governing equations and corresponding assumptions to describe the motion of fluids. Equations applicable to BLI flows marked with bold borders.

by a high degree of randomness and irregularity in the fluid motion, which are caused by small-scale eddies. The (U-)RANS equations can be employed to simplify the solution of turbulent flow fields. The derivation of the equations makes use of the Reynolds decomposition, which is a mathematical tool used to decompose a fluid velocity field into a mean (or average) component and a fluctuating (or turbulent) component [11]. RANS CFD solvers are widely employed to solve mostly turbulent flow fields of various kinds and are suitable for the present flow problem. The Euler equations are derived by assuming zero viscosity and adiabatic conditions. They are a set of nonlinear PDEs [182]. As viscous effects dominate the BL, they cannot be employed for the present case. The full potential flow equation is derived if the flow is additionally assumed to be irrotational (no vorticity). Potential flow is a fluid flow characterized by the fact that a scalar velocity potential function can describe the flow. This means that the velocity of the fluid at any point can be calculated from the gradient of the velocity potential function at that point. For incompressible flows, the equations that govern potential flow are the Laplace equation, which is a second-order linear elliptic PDE, and the Bernoulli equation, which is a first-order nonlinear Ordinary

Differential Equation (ODE) [183]. Prandtl's BL theory (see Section 2.1.1) is employed to derive the Boundary Layer Equations (BLEs) from the NSEs. It is assumed that the BL is thin ( $\delta \ll d$ ) and that the static pressure inside the BL equals the pressure at the edge of the BL independent of  $y$ . The BLEs can be employed for laminar flows. They are simplified for turbulent flows using the Reynolds decomposition described above. To further decrease the effort of solving the set of parabolic PDEs, the equations are integrated across the BL to arrive at the Integral Boundary Layer Equations (IBLEs). A no-slip condition is employed at the wall ( $u(y_{wall} = 0) = 0$ ), and the velocity at the edge of the BL can be calculated using inviscid methods as  $u(\delta^*) = u_e$ . The IBLEs can be employed to calculate integrated characteristics of the BL, such as  $\delta$ ,  $\delta^*$ , or  $H$ . Local flow characteristics, such as the velocity distribution inside the BL, are unresolved. Empirical models are used to estimate the BL profiles. Furthermore, the flow characteristics at the edge of the BL, such as the pressure gradient  $\frac{dp}{dx}$ , have to be known a priori to solve the BLEs [11]. In general, viscous flow problems can be solved by coupled viscous/inviscid codes, such as *MTFLOW* [135]. Here, the flow is divided into two regions in which either governing equations that model inviscid, i.e. potential flows, or governing equations, which model BL flow, are solved. The solution is converged by an iterative solution of both flow fields, including coupling effects [12]. For PFC, it is not possible to unambiguously identify the threshold between the inviscid and viscous region at the edge of the BL in the rear part of the fuselage because of the interaction of nacelle and fuselage BL and FF as derived in Section 3.1. The BL does not hold true to the assumption of being a thin layer, and the pressure is not constant across the BL. Thus, a coupled viscous/inviscid code employing the equations described in the above paragraphs cannot be employed here. However, in the front part of the fuselage up to the end of the constant radius section, the fuselage BL is undisturbed by the FF. Here, a viscous/inviscid code can be employed to estimate the characteristics of the fuselage BL.

### 3.3 Numerical Methods

For realistic, more complex flow problems, the governing equations cannot be solved analytically. Thus, numerical methods approximate solutions to the mathematical problems posed by the governing equations. In CFD, the following numerical methods are most notable: Finite Difference Methods (FDMs), Finite Element Methods (FEMs), Finite Volume Methods (FVMs), and Panel Methods (PMs) [182]. FDMs approximate the solutions to differential equations by dividing the domain into a grid of discrete points and approximating the derivatives at each point using finite differences. FEMs divide the domain into elements and approximate the solution within each element using a set of basis functions. FVMs approximate the solutions to differential equations by dividing the domain into small control volumes and integrating the equations over each volume. Each of the described methods has its own advantages and disadvantages, and the choice of method depends on the specific problem being solved, the required level of accuracy, and the available computational resources [182]. Recently, FVMs have been widely employed in fluid dynamics for several reasons. They enable high flexibility because they can be applied to a wide range of fluid flow problems, including both steady-state and unsteady-state problems and laminar and turbulent flows. They can also be used to model complex geometries and boundary conditions. In addition, they are based on the integral form of the governing equations, which ensures that the equations of conservation of mass, momentum, and energy are satisfied. This makes them a suitable method for solving problems in fluid dynamics, where the conservation of these quantities is important. FVMs are comparably easy to implement and are robust against small errors in discretization. They are also well-suited for parallel computing, which allows for efficient and accurate solution for problems involving large amounts of data. They can be easily extended to high-order accuracy using higher-order interpolation and integration methods [182]. In summary, FVMs can provide accurate solutions even with complex geometries and boundary conditions, which makes them very useful in practice. Several FVM codes are available, which serve as a framework to solve different sets of governing equations, focusing on

the solution of the RANS equations. While FDMs, FEMs, and FVMs represent a body as a set of discrete points or elements and discretize the domain around the body by grid points, elements, or volumes, PMs represent a body as a collection of line segments or “panels” and use the potential flow equations to determine the velocity and pressure fields around the body. Panel methods are particularly useful for solving problems with simple geometries, such as airfoils or streamlined bodies. They are highly accurate, efficient, and widely used in aerospace [182]. PMs can be employed as a basis for a viscous/inviscid code, which solves the potential flow around a simple geometry and combines it with an IBL method [12].

### 3.4 Most Suitable Method

In Section 2.2.3, it was established that in order to estimate the potential of a PFC on the aircraft level, the accurate modeling of the strongly coupled aero-propulsive performance of the fuselage and fuselage-propulsor geometry is crucial. Further, in Section 3.1 the requirements posed by conceptual aircraft design to an aero-propulsive model of a PFC were covered. In summary, the model, which describes the aero-propulsive performance of combined fuselage and fuselage-propulsor, is required to provide fast results with a sufficiently accurate representation of the flow characteristics. However, most existing methodologies either neglect the coupling of airframe and BLI propulsion system or employ computationally expensive approaches, which require a high number of iterations and are not practical for rapid aircraft conceptual design (see also Section 2.2.3). Thus, a simplified numerical model is required to predict the aerodynamic characteristics. Section 3.2 discussed the applicability of different governing equations to represent the flow phenomena and characteristics attributed to BLI. It was found that simplified equations and methods, such as viscous/inviscid codes, cannot be employed to model the prevailing fluid characteristics and flow characteristics in the vicinity of the FF without the availability of sound empirical data on the aerodynamics around a propulsive fuselage or without making bold assumptions, which can introduce errors. These errors could be in the same order of magnitude as the potential improvement attributed to optimizing the fuselage and nacelle geometry. Thus, numerical methods must be employed, which are more computationally expensive and can not be integrated directly into a practical conceptual aircraft design loop. To ensure sufficient accurateness while keeping the computational effort low, surrogate models can link the numerical solution of the PFC aerodynamics and the integrated conceptual aircraft design loop (see Section 7.2). A hybrid numerical aerodynamic method is proposed to rapidly generate the data to populate the surrogate model. It is visualized in Figure 5.1. The approach is inspired by a hybrid viscous/potential flow method for multi-element wings introduced by Dvorak and Woodward, who combined a PM with FD calculations [184–186]. The method developed in this thesis combines a viscous/inviscid panel code with the solution of the RANS equations by an FVM. The flow around the front part of the fuselage, which is not affected by the BL ingesting FF, can be interpreted as a simple flow around a streamlined body. Here, a PM is used to solve the inviscid potential flow around the displaced body. The viscous IBL equations calculate the expansion of the displaced body. The method is capable of predicting the transition point of the BL. The BL profile is estimated by using semi-empirical relations. Complex flow phenomena dominate the flow in the rear part of the fuselage near the FF. Here, an FVM is employed, which solves the RANS equations with a turbulent model. The flow is assumed to be fully turbulent. This constitutes an additional advantage to the suggested method. Instead of employing a computationally expensive transition model in the FV domain, the laminar region and transition point occurring in the front part of the fuselage are predicted and modeled by the computationally inexpensive IBL method. To further increase the speed of the solution, a two-equation turbulence model is used in conjunction with simplified modeling of the effect of the FF on the flow. The PM results at the interface are used as BCs at the FVM inlet. Due to the rapid solution of the PM (convergence is reached after a few seconds) and the reduction of the number of cells in the FV domain, the convergence of the hybrid method is 25% faster compared to an FVM

RANS solution of the full configuration. Considering the requirements posed by BLI on the method, which accurately models the aero-propulsive performance of a propulsive fuselage, the proposed method is the fastest numerical method with sufficient accuracy conceivable. Details on the employed numerical methods, their implementation, and validation are discussed in Chapter 5.

## 4 Unified Performance Bookkeeping Approach for Propulsive Fuselage Concepts

*This chapter provides a summary of the unified bookkeeping scheme presented in "Performance Bookkeeping for Aircraft Configurations with Fuselage Wake-Filling Propulsion Integration" by the author of this thesis [146]. Additionally, excerpts from the contribution of the author to the publications "Optimality Considerations for Propulsive Fuselage Power Savings" [129] and "Numerical Investigation of the Effects of Fuselage Upsweep in a Propulsive Fuselage Concept" [45] are included.*

The literature review presented in Section 2.3 revealed that a universally adaptable bookkeeping method is needed for consistently assessing and optimizing fuselage-propulsor geometries for rapid multidisciplinary initial sizing and local design analysis. The *MIDAP Study Group* defined general criteria for practical bookkeeping schemes (Section 2.3). They are well applicable to the design and sizing of traditional aircraft configurations, where the airframe and propulsion systems can be separated, allowing for thrust-/drag-bookkeeping. For closely integrated propulsion systems, such as fuselage propulsors, this assumption does not hold. Thus, responding to RQ 1, the criteria of the *MIDAP Study Group* are extended for the design and development of aircraft concepts with BLI:

- "[The bookkeeping scheme] must be free from ambiguity" [147]
- *It must be universally applicable to different aircraft configurations and throughout the whole aircraft design process*
- "It must, *so far as possible*, provide for the separate study of engine and airframe performance [...], both in preliminary paper projects and in any subsequent model and/or flight testing" [147]
- *It must allow for a strongly coupled assessment of tightly integrated propulsion systems*
- "It must include clear definition of the interfaces where engine and airframe responsibilities meet, and facilitate a proper understanding of any zones where responsibilities overlap" [147]
- "It must assist in planning model and flight testing in such a way as to provide the information required for design and performance evaluation at minimum total cost." (component-wise testing: airframe model, intake, nozzle, engine test bed) [147]
- "It must recognize practical limitations in experimental and theoretical techniques" [147]
- *It must be compatible with recognized aircraft design methodologies*

A practical integral momentum conservation approach is developed, which conforms to the derived criteria, and its applicability to integrated conceptual sizing and subsequent design analysis is assessed. The proposed scheme is universally applicable to coupled airframe-propulsion aircraft concepts and works well with standard aircraft and propulsion system sizing tools. It can be employed for both low- and high-fidelity aerodynamics methods. The development of the scheme addresses RQ 2. Lastly, a selection of suitable figures of merit is presented, encompassing various design aspects in BLI evaluation. Here, the performance indicators established in [146], and additional metrics are presented in response to RQ 3.

## 4.1 Control Volume and Forces Definition

In Section 2.3.1, it was established that energy and exergy conservation-based bookkeeping methods and figures of merit exhibit broad universality but limited applicability to the aircraft conceptual design phase, which requires the assessment of the aircraft in terms of forces instead of energy. Thus, an integral momentum approach is deemed more practical. Using this integral momentum approach and incorporating Seitz and Gologan's approach [25, 47], a bookkeeping scheme is developed to meet the requirements outlined above. This scheme focuses on a 2D-axisymmetric fuselage-propulsor configuration. Wing and empennage forces are assumed to have secondary effects on BLI benefits. The scheme employs a CV encompassing the body surface boundaries, thus enabling the computation of defined forces in line with multidisciplinary aircraft sizing tools. It is visualized in Figure 4.1. The CV definition presented in [146] is slightly adapted for the hybrid numerical method employed in the present study (see Section 5). However, the underlying assumptions remain the same. The developed method shows high flexibility, which can be employed for the hybrid method and pure RANS CFD results. Additionally, the 0D IBL method employed for calculating the BL characteristics in the front part of the fuselage 5.4.2 is consistent with momentum integration along the CV boundaries.

The comprehensive control volume CV0 is divided into eight adjacent CVs strategically selected to enable the computation of relevant parameters through a momentum conservation approach for the chosen numerical method. The inlet flow properties of CV1 match freestream conditions. The outlet of CV8 is positioned at the fuselage's trailing edge. The front part of the fuselage, calculated by the PM, is split into two CVs. The boundary between CV1 and CV2 corresponds to the BL displacement thickness. At the interface of the two calculation methods, the characteristics of the BL and the potential flow domain are projected onto the inlet of CV 4 and CV5, and CV3, respectively. The boundary between CV4 and CV5 follows the contour of the propulsion system streamtube. CV7 aligns with the surfaces of the propulsor duct. The FF volume force  $F_{FF}$  is introduced between the rotor inlet and stator outlet (thermodynamic stages 2 and 3), already accounting for the polytropic stage efficiency  $\eta_{pol}$ . Aerodynamic forces outside the propulsion stream tube are integrated into airframe force accounting. Thus, the nacelle force term encompasses all aerodynamic forces acting on the nacelle beyond the propulsion system stream tube.

The presented approach is universally applicable across various phases of conceptual design. During initial sizing, approximations and assumptions facilitate the quick evaluation of numerous configurations. In contrast, during detailed design analysis, higher-fidelity methods like CFD or experimental testing provide complex data for component-based force analysis. The coupling level depends on the analysis methods and tools used.

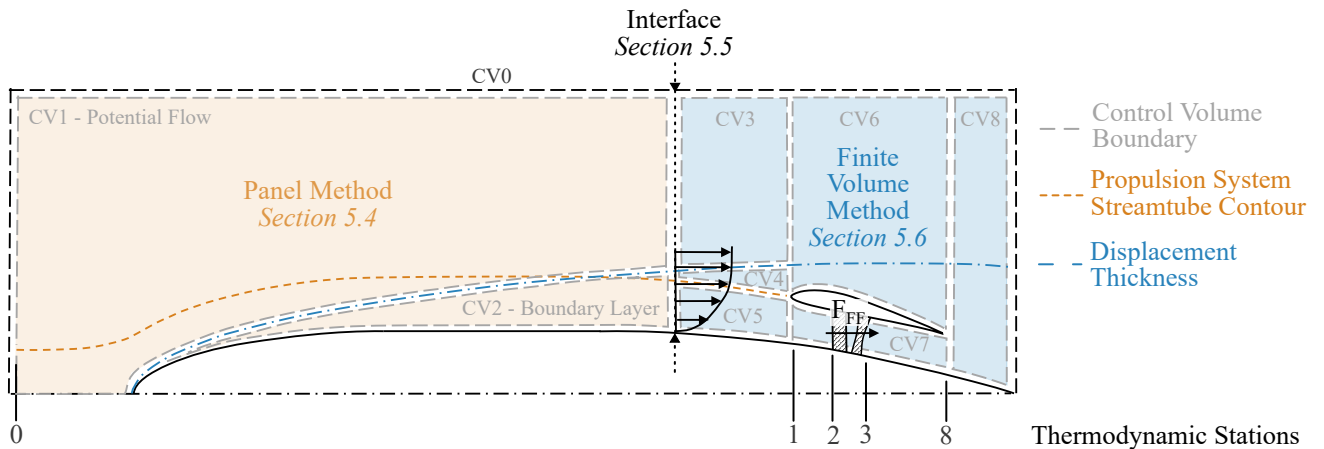


Figure 4.1: CV scheme employed in current study. Adapted from [146].

To comply with the definition of drag and thrust by the *MIDAP Study Group* (see Section 2.3.2.1), the presented bookkeeping approach is based on force instead of drag terms. This is required because the approach necessitates the assessment of streamwise forces of individual parts of components. In contrast to a complete and isolated body for which the potential flow buoyancy is zero and, therefore,  $D_{body} = F_{body}$ , the drag of a part of a closed body is defined as the difference of the integrated surface forces on that part of the body and its potential flow buoyancy  $\Phi_{pot}$  [147]:

$$D_i = \Phi_i - \Phi_{pot} = F_i - \int_A (p_{s,pot} - p_{s,\infty}) dA \quad (4.1)$$

## 4.2 Figures of Merit

Section 2.3.2 established that a universal figure of merit that accounts for all aircraft configurations and flow properties and is suitable for the aircraft conceptual design phase is not available. Consequently, employing a combination of performance indicators when analyzing different aspects of BLI performance is recommended.

### 4.2.1 Energy Specific Air Range

When the results of the aero-propulsive study are integrated into the multidisciplinary aircraft sizing, in addition to mission block fuel  $BF$ , the Energy Specific Air Range ( $ESAR$ ) can be employed to compare the aircraft level potential of different PFC with each other and to a reference (non-BLI) configuration [99]:

$$ESAR = \frac{dR}{dE} = \frac{\eta_{ov} L/D}{m_{AC} g} \quad (4.2)$$

$\eta_{ov}$  is the instantaneous overall propulsion efficiency,  $m_{AC} g$  is the instantaneous aircraft weight and  $L/D$  is the corresponding aircraft lift-to-drag ratio.

### 4.2.2 Power Saving Coefficient

The BLI benefit on the propulsion system level can be assessed using the  $PSC$  in its original form. This offers a convenient way to comparatively evaluate the BLI system-level benefit, comparing a PFC to a reference non-BLI configuration [23]. It can be employed in a broad range of aircraft configurations and aero-propulsive results based on varying levels of fidelity.

$$PSC = \frac{P_{ref} - P_{PFC}}{P_{ref}} \quad (4.3)$$

### 4.2.3 Net Propulsive Force and Boundary Layer Ingestion Efficiency Factor

Utilizing momentum conservation in the CV suggested in Section 4.1 results in the subsequent Equation 4.4 for the complete momentum outflow from CV0 in the streamwise direction. An analog derivation for a similar CV is detailed in [146].

$$\dot{I}_{out,CV8} = F_{p,in,CV1} - F_{p,out,CV8} + \dot{I}_{in,CV1} + F_{FF} + F_f + F_{aftbody} + F_{nac} + F_{duct} \quad (4.4)$$

The summation of streamwise pressure forces on the overall control volume is represented by  $F_{p,in,CV1} - F_{p,out,CV8}$ . The inlet momentum flow is denoted by  $\dot{I}_{in,CV1}$ .  $F_{FF}$  refers to the volume force of the FF imparted to the flow by, e.g., BCs or STs. Each surface force term summarizes the combined effect of

pressure and skin friction forces for specific components in streamwise direction:  $F_{duct}$  represents the collective force components acting on the tip and hub contours within the duct,  $F_{nac}$  corresponds to the force on the nacelle cowling,  $F_f$  signifies the force acting on the fuselage upstream of the propulsor inlet, and  $F_{aftbody}$  accounts for the force acting on the fuselage contour downstream of the propulsor outlet. Rearranging Equation 4.4 yields the expression for the net streamwise propulsive force acting on the bare PFC configuration ( $NPF_{PFC,bare}$ ) presented in Equation 4.5. It is the total effective net force acting on the fuselage-propulsor configuration without wing, empennage, etc., and without accounting for the interference of the fuselage-propulsor with the latter.

$$\begin{aligned}
NPF_{PFC,bare} &= \dot{I}_{out,CV8} - \dot{I}_{in,CV1} + F_{p,out,CV8} - F_{p,in,CV1} \\
&= F_{FF} - F_f - F_{aftbody} - F_{nac} - F_{duct} \\
&= F_{FF} - F_{PFC,bare} \\
&= \iiint_{V_{FF}} S_{u_x} dV_{FF} - \sum_i \iint_{S_i} (pn_x + \tau_w) dS_i
\end{aligned} \tag{4.5}$$

The BFM employed in this study allows to directly calculate the force imparted on the fluid by the FF stage in axial direction  $F_{FF}$  by integrating the momentum source terms  $S_{u_x}$  over the rotor and stator volumes (refer to Section 5.6.3.1).

$F_{PFC,bare}$  is the sum of integrated viscous and pressure forces on the fuselage-propulsor component surfaces. Surface forces pointing in the drag direction have a positive sign, and thrust forces are positive according to *MIDAP Study Group* conventions [147]. Thus, a negative  $NPF$  indicates a force in the drag direction.

The bare BLI efficiency factor  $f_{\eta,BLI,bare}$  is employed to evaluate the coupled aero-propulsive performance of the fuselage-propulsor configuration. It links the Net Propulsive Power (NPP) to the FF shaft power  $P_{FF,s,pol}$ :

$$f_{\eta,BLI,bare} = \frac{NPP}{P_{FF,s,pol}} = \frac{NPF_{PFC,bare}u_0}{P_{FF,s,pol}} \quad \forall P_{FF,s,pol} > 0 \tag{4.6}$$

Here, the actual, i.e. polytropic shaft power is employed. It is calculated on a CV, which encompasses the whole FF stage between station 2 and 3, including rotor and stator:

$$P_{FF,s,pol} = \dot{m}\Delta h = \dot{m}(h_3 - h_2) = \dot{m}c_p(T_3 - T_2) \tag{4.7}$$

The isentropic shaft power  $P_{FF,s,is}$  can be related to the actual shaft power through the polytropic fan efficiency  $\eta_{pol}$  using the following equation:

$$\eta_{pol} = \frac{P_{FF,s,pol}}{P_{FF,s,is}} \tag{4.8}$$

In aircraft conceptual design,  $f_{\eta,BLI,bare}$  can be applied in initial sizing and design optimization studies to compare various fuselage-propulsor designs.

#### 4.2.4 Kinetic Energy Defect

The kinetic energy defect area  $KED_A$  describes the reduction in kinetic energy in a fluid as it flows over a solid surface. In a BL, the fluid near the surface slows down due to shear stresses, causing a drop in kinetic energy.  $KED_A$  is the difference between the actual kinetic energy of the fluid and the ideal kinetic energy in the absence of viscosity. The reduction in kinetic energy due to viscosity results in an increase in the internal energy of the fluid, which can be associated with the work done by the fluid on the body, leading to a net increase in the total drag force. Thus, the  $KED_A$  is another important metric

that can be used to evaluate the aero-propulsive performance of a given fuselage-propulsor geometry. For an axisymmetric case, the impact of the BL shape on  $KED$  increases in the radial direction. To consider this, the Kinetic Energy Defect (KED) formulation by [33] is adapted. It is based on the kinetic energy area  $\Theta^*$  in the following manner:

$$KED_A = \rho_e u_e^3 \Theta^* = \int_0^{A_e} (u_e^2 - u^2) \rho u dA \quad (4.9)$$

$KED_A$  has the dimension  $W$ . In Section 3 it was derived, that the edge of the BL cannot be determined unambiguously for a fuselage-propulsor configuration. Here, the BL edge is defined at the location at which  $u(y) = 0.99u_\infty$ . For an ideal BLI case,  $KED_A = 0$  at the fuselage trailing edge. The BLI fan would have fully recovered the KED without generating excessive kinetic energy. To estimate the efficiency of the FF to recover the kinetic energy, a kinetic energy defect recovery factor  $R_{KED_A}$  is introduced in Equation 4.10. It relates the kinetic energy defect at the fuselage Trailing Edge (TE) to that at an Aerodynamic Interface Plane (AIP).

$$R_{KED_A} = \frac{KED_{A_{TE}}}{KED_{A_{AIP}}} \quad (4.10)$$

If  $R_{KED_A} > 0$ , the KED is not fully recovered. Excessive kinetic energy is generated if  $R_{KED_A} < 0$ . The smaller the absolute value of  $R_{KED_A}$ , the closer the setup is to an ideal BLI fan.

#### 4.2.5 Ingested Defect Ratio

The ingested defect ratio  $\beta$  quantifies the wake-filling potential of the configuration. The version of  $\beta$  employed in this study relates the momentum or kinetic energy defect area ingested by the FF to the total momentum or kinetic energy defect area at the AIP in the following manner:

$$\beta_{KED} = \frac{KED_{A_{ing}}}{KED_{A_{AIP}}} \quad \text{and} \quad \beta_{MD} = \frac{MD_{A_{ing}}}{KMD_{A_{AIP}}} \quad (4.11)$$

The area-based momentum defect ( $MD_A$ ) definition with dimension  $N$  is based on [33] with  $\Theta$  being the BL momentum area:

$$MD_A = \rho_e u_e^2 \Theta = \int_0^{A_e} (u_e - u) \rho u dA \quad (4.12)$$

The ingested area defects are calculated by integrating the defect at the AIP from the body surface to the height of the FF highlight.

#### 4.2.6 Radial Distortion

The inlet distortion quantifies the quality of the airflow incident to the FF. For practical, non-axisymmetric fuselage-propulsor configurations with fuselage-wing and -empennage interference, circumferential distortion is important. However, circumferential distortion does not exist for bare axisymmetric propulsor-fuselage configurations, and only radial distortion can be quantified. Here, the radial distortion intensity defined by the *Society of Automotive Engineers* in the *Gas Turbine Engine Inlet Flow Distortion Guidelines* [187] is calculated at the FF interface as:

$$\left( \frac{\Delta PR}{P} \right)_j = \frac{PFAV - PAV_j}{PFAV} \quad (4.13)$$

$\left( \frac{\Delta PR}{P} \right)_j$  is the radial intensity of ring  $j$ ,  $PFAV$  is the face average total pressure and  $PAV_j$  is the ring average total pressure [187]. The intensity is calculated for several concentric rings  $n$  of the fan face. The higher the deviation from the face average total pressure, the higher the inlet distortion.



## 5 Hybrid Numerical Method for Aero-Propulsive Boundary Layer Ingestion Assessment

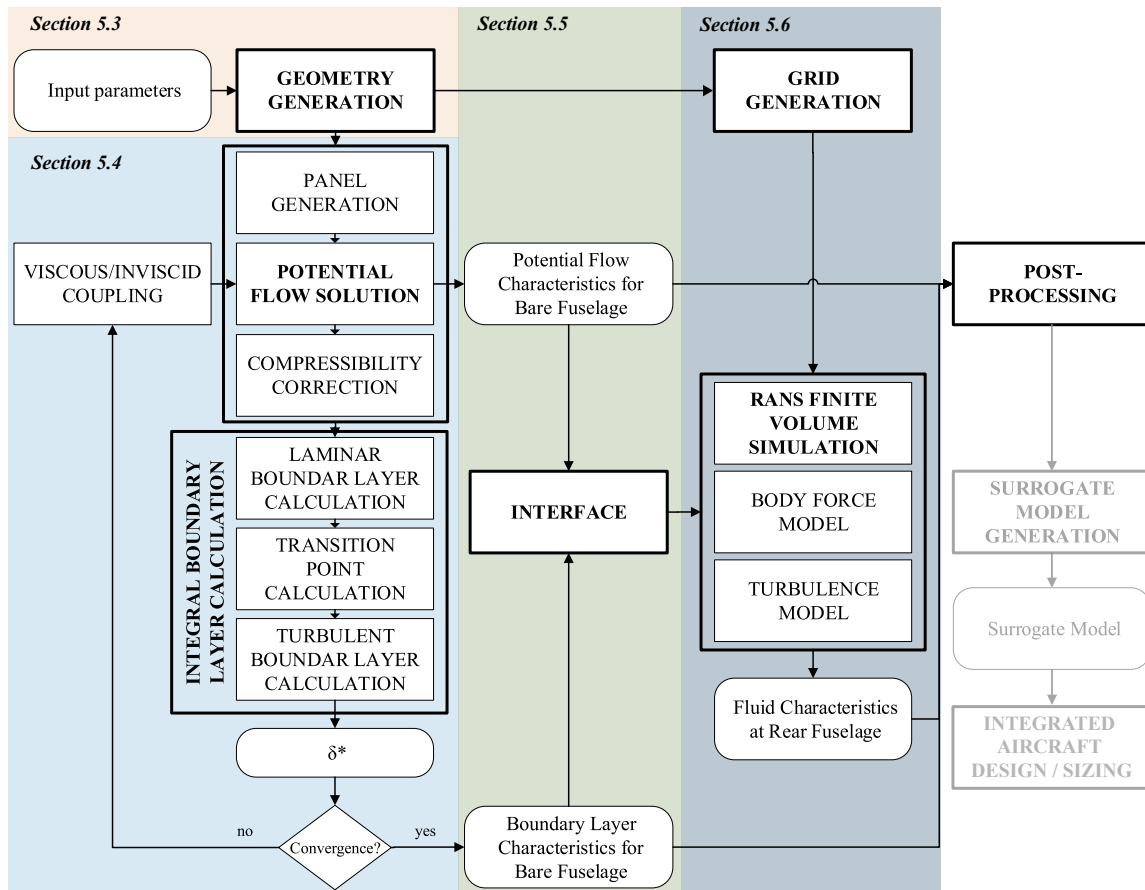


Figure 5.1: Overview of hybrid numerical method.

In this chapter, a combination of available methods for a hybrid numerical approach to automated modeling of the coupled aero-propulsive performance of PFC in aircraft conceptual design is proposed and validated as an answer to RQ6. Figure 5.1 depicts a flow chart of the hybrid numerical method.

An overview of the PFC, which serves as a reference for the present study, is provided in Section 5.1, and assumptions and limitations of the methodology are summarized in Section 5.2. Section 5.3 presents the chosen geometry parameterization strategy, including an overview of selected geometrical and operational design parameters. The generated geometries serve as an input to the IBL PM, which predicts the flow characteristics in the front part of the fuselage and at the IBL/FVM interface (Section 5.4). As described in Section 5.5, at the interface, 1D flow characteristics are translated to 2D characteristics, which are used as input to the FVM. The open source grid generator *Gmsh* [188] is employed to generate the FV mesh. A BFM is implemented in the RANS CFD *HiSA* solver, which is an open-source *C++* library of tools specifically developed for the solution of transonic and supersonic compressible flows within the *OpenFOAM* framework [189]. The selection and implementation of the FV methods and the simulation

setup are described in Section 5.6. IBL and FV methods' results are post-processed and can be employed to generate a surrogate model for integration in an aircraft conceptual design framework (see also Section 7.2).

All functions and scripts required to execute the method are publicly available in the *GitHub* repository *ShapePFC* (Swift Hybrid numerical method for Aero-propulsive Performance Evaluation of Propulsive Fuselage Concepts) [190]. Most methods, including geometry generation, PM, PM/IBL interface, post-processing, and automation of the approach, are implemented in *Python* version 3.8 [191].

## 5.1 Reference Aircraft Configuration

The current study is based on the PFC investigated in the *European Union Horizon 2020* project *CENTRELINE* [7]. Results are limited to configurations similar to this concept.

A sketch of the *CENTRELINE* concept is depicted in Figure 5.2. The tube-and-wing configuration was derived from the Airbus A330-300 wide-body aircraft. Its EIS is specified as the year 2035. Project-specific TLARs define a design range of 6500nmi for 340 passengers in a 2-class seating arrangement for the baseline family member. Design cruise conditions are  $Ma_{cr}=0.82$  at an initial cruise altitude of FL330 (ISA+10K) [7]. The turbo-electric PFC is based on the results of a mechanically driven FF concept previously studied in the *DisPURSAL* project [42]. Two advanced GTFs are installed as underwing podded engines on the main wing. Electric generator off-takes of the GTFs are employed to power the full annular BLI FF. The TEPT required to transmit the electricity from the main engines to the FF consists of the main generator, power electronics, the FF drive motor, cabling, and a cooling system. It contributes significantly to the weight penalties introduced by the FF [7]. A T-tail arrangement was chosen to minimize the distortion incident to the FF, located at the aft fuselage at the root trailing edge of the VTP [192]. For the final configuration, the fuselage propulsor is designed to require around 7MW

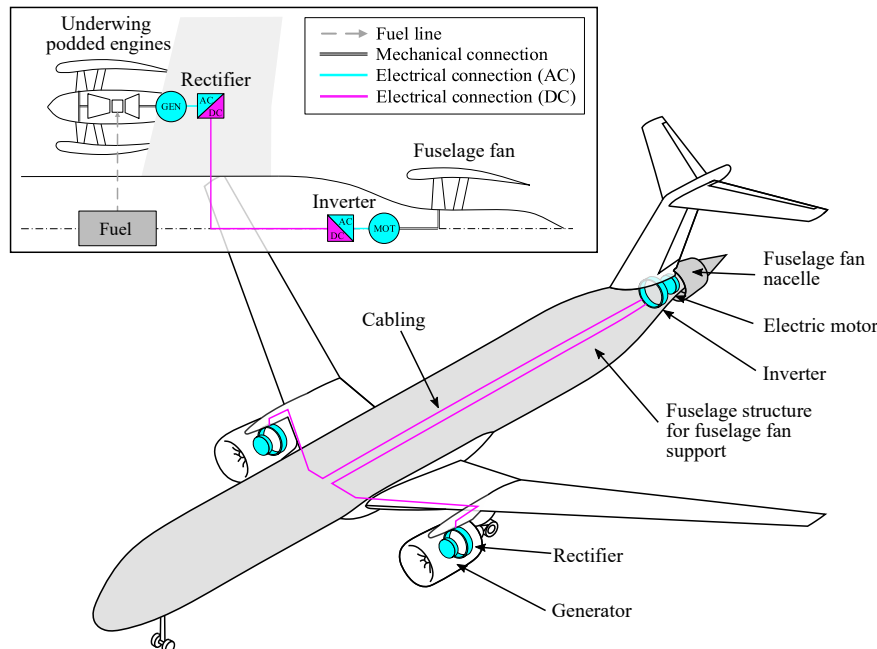


Figure 5.2: Sketch of the *CENTRELINE* aircraft configuration and turbo-electric propulsion system.

shaft power in take-off conditions. Mid-cruise requires less than 5 MW. Each GTF provides 35.5 kN net thrust in mid-cruise conditions. At the same time, the  $NPF_{FFC,bare}$  is  $\approx -2$  kN [110] (a negative  $NPF$  denotes a force in drag direction). More details on the configuration can be found in [7, 17].

## 5.2 Assumptions and Limitations

The aircraft conceptual design phase is dedicated to exploring a wide design space to assess the potential of a specific aircraft concept or technology. Numerous configurations are investigated using models of limited fidelity. Models of components and disciplines, which cover the whole design space, are usually limited in the number of input and output variables and rely on simplifying assumptions and limitations.

This study's primary focus of investigation is the rear part of the fuselage, where the full annular FF is located. In cruise conditions (at an angle of attack of  $0^\circ$ ), the distortion of the flow incident to the fan is more significantly affected by its interaction with the fuselage than with other aircraft components [117]. Consequently, this study omits the impact of the wings, VTP, and HTP (Horizontal Tail Plane) on the BL distortion. The fuselage-propulsor geometry is simplified to a 2D-axisymmetric body, neglecting the effect of an asymmetric fuselage nose, elliptic center section, fuselage upsweep, and wing/fuselage/belly-fairing interaction. Experimental assessments on a conventional fuselage geometry demonstrated that deviations from symmetry result in some flow deviation; however, the overall trends in flow characteristics are maintained [193]. Hence, the distortion incident to the FF is assumed to be axisymmetric, considering only radial distortion due to the BL. Further, the assumptions imply that the FF does not significantly affect the aircraft's lift.

The methods and flow-solving techniques employed further narrow the applicability of the presented approach.

The chosen shape parameterization strategy, describing fuselage and nacelle geometry by their physical characteristics, inherently reduces the geometrical design space.

The Hybrid Panel/Finite Volume Method (HPFVM) assumes steady flow conditions.

Additionally, limitations arise from the IBL method applied to the front part of the fuselage. The flow domain is divided into two distinct regions, separated by the BL edge: an inner viscous BL region and a potential region. The potential flow solution is based on linearized potential flow theory, suitable for small angles of attack and perturbations in the flow. The compressibility correction is valid only for flows without shock waves, limiting the local edge Mach number  $Ma_e$  to not surpass the critical Mach number  $Ma_{crit}$ . The transition model simplifies the laminar to turbulent flow transition to a punctiform event. Laminar separation is detected within the laminar flow region. However, instead of modeling a laminar separation bubble, it is assumed that at the point of laminar separation, the BL immediately re-attaches as a turbulent BL and transition occurs. Inside the turbulent BL, flow separation caused by adverse pressure gradients is identified but cannot be modeled by the IBL method. However, turbulent separation does not occur for any geometry in the front part of the fuselage.

The RANS CFD solver, used for the rear part of the fuselage, including the FF, has different limitations. The fully turbulent simulation relies on turbulence models to represent the effects of turbulence, which can introduce errors. Further, the solution's accuracy depends on the computational mesh's quality and resolution, especially near the body surfaces. It may also have limitations in accurately predicting separated flows, particularly under strong adverse pressure gradients [194].

An uncalibrated BFM, which models the effect of the FF on the flow, simplifies the impact of the rotor and stator to 2D-axisymmetric and is valid only for steady flows. For the study, the fan stage geometry of the *CENTRELINE* project is employed and scaled according to the geometrical constraints. The fan

is expected to not perform optimally for all studied configurations. Further, without knowledge of the off-design performance of the fan stage, the study is constrained to cruise design conditions.

Comprehensive validation and verification studies of the individual methods and the full HPFVM are conducted and documented in the following section to ensure accurate modeling of the aero-propulsive performance despite the presented assumptions and limitations. Grid convergence studies are additionally performed to minimize the impact of grid resolution on results.

## 5.3 Geometry Parameterization

Choosing an adequate shape parameterization strategy is decisive for aerodynamic design and optimization. By constraining the parametric description of the aerodynamic geometry to several design parameters and applying a specific parameterization method, the design space and, thus, the optimum achievable result is limited [195]. Consequently, design parameters, constraints, and the applied parameterization method must be chosen deliberately. For the presented application, the parameterization of the geometry should allow the representation of a wide variety of fuselage and fuselage-propulsor geometries. At the same time, the number of design parameters, that describe the geometry using physical characteristics, should be limited. Thus, a combination of Bezier curves and intuitive Class/Shape function Transformation (iCST) [195] is employed. The most important design parameters are presented in the following subsections, and the applied iCST method is described.

### 5.3.1 Design Parameters

Simplifying the 3D geometry to a 2D-axisymmetric fuselage-propulsor geometry confines the number of design parameters. However, to describe the complex 2D aerodynamic shape, a minimum number of design parameters is required. Table A.1 presents all parameters, which serve as an input to the parameterization. Figure 5.3 provides a sketch of the geometry. It is described by 25 parameters in total. These include lengths, radii, angles, relevant factors, and ratios, which define the relations of several parameters.

The strategy allows for a flexible shape variation while limiting the number of physical design parameters. The following assumptions are made, which can impact the result of the design optimization:

- Haack series shaped fuselage nose
- Constant fuselage center section
- Pointed fuselage aft-end
- FF stage aspect ratios similar to original *CENTRELINE* Fan B stage (see also Section 5.6.3.5)
- Fan cowling represented by a round-nosed airfoil with pointed aft-end
- Maximum fuselage nozzle radius coincides with nacelle trailing edge
- The upper nacelle leading edge radius is proportional to the distance of the nacelle leading edge to the point of maximum nacelle radius

The Haack minimum drag nose function introduced by Haack in 1946 (as cited in [196]) defines the fuselage nose shape:

$$\begin{aligned}
 r &= \frac{r_{f,cent}}{\sqrt{\pi}} \sqrt{\theta - \frac{1}{2} \sin^2 2\theta + C_{Haack} \sin^3 \theta} \\
 \theta &= \arccos \left( 1 - \frac{2z}{l_{nose}} \right)
 \end{aligned} \tag{5.1}$$

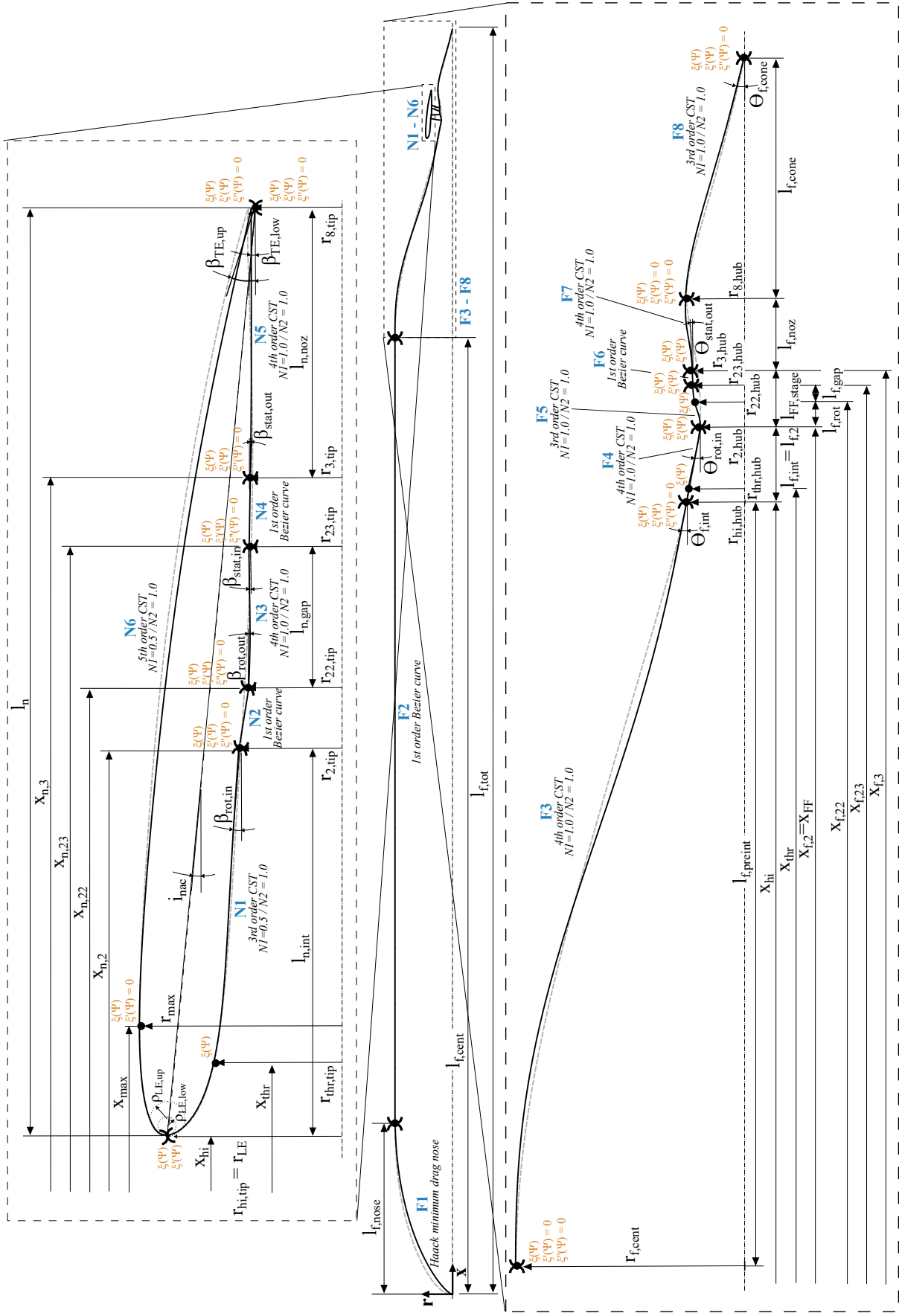


Figure 5.3: Geometry parameterization. Dashed gray lines indicate original *CENTRELINE* geometry [19]. Solid black lines indicate reference geometry employed in the current study.

$r_{f,cent}$  is the maximum radius of the fuselage. The fuselage nose length of the reference geometry is  $l_{nose}$  is  $1.65 \cdot d_{f,cent}$ , similar to the *CENTRELINE* reference geometry [19], which is close to the factor of  $1.2 - 1.6 \cdot d_{f,cent}$  proposed by Howe [197].  $C_{Haack} = \frac{2}{3}$  is chosen to ensure a smooth transition between the fuselage nose and center section (Haack 1946 as cited in [196]).

As a result of the chosen parameterization strategy, some parameters result from the geometry generation instead of serving as an input. These include the fuselage angle at the nacelle highlight  $\theta_{f,int}$ , the total fuselage length  $l_{f,tot}$  and, correspondingly, the fuselage SLR, as well as the nacelle incidence angle  $i_{nac}$  and the nacelle chord length  $c_{nac}$ . Similarly, the length of the FF stage  $l_{FF,stage}$  and the ratios of the station areas, such as  $A_3/A_2$  are dependent parameters. Figure 5.3 visualizes the geometry and essential design parameters. In addition, three operational parameters serve as design parameters, describing cruise operating conditions ( $Ma$ ,  $h_{alt}$ , and  $\Omega_{rot}$ ). The rotor rotational speed  $\Omega_{rot}$  determines the fan operating conditions. It is calculated from the rotor tip speed  $U_{tip}$  of the original configuration and the rotor tip diameter  $d_{2,tip}$ .

The reference fuselage-propulsor geometry of the current study is based on the *CENTRELINE* Rev 07 geometry presented in [19]. Reference design parameter values are provided in Table A.1 (Appendix A.1).

### 5.3.2 Intuitive Class/Shape Function Transformation

According to [198, 199] and summarized by [195], a suitable parameterization method requires the following properties:

1. "high flexibility to cover the potential optimal solution in the design space,
2. small number of key design variables,
3. smoothness and realizability of the shapes, and
4. intuitiveness of the design parameters for geometrical and physical understanding by the design engineers in exploring the design space and setting up optimization constraints." [195, p. 17].

The Class/Shape Transformation function method (CST) was initially introduced by Kulfan in 2006 [200]. Compared to other parameterization methods, which are widely used in aerodynamic design and optimization, such as Bezier polynomials, B-splines, Non-Uniform Rational B-spline (NURBS), PARSEC [201] or Bezier-PARSEC [202], CST also satisfies properties 1-3 but is universally applicable to a wider range of geometries [195]. Even though its purpose is to represent the diverse geometry of complex aircraft configurations, it is especially suitable for 2D airfoil shapes with a round nose and a pointed aft end. For these shapes, it already includes intuitive parameters like leading edge curvature radius, boattail angle, and trailing edge thickness [199]. However, the parameterization of airfoils using CST requires defining non-intuitive parameters. To overcome this limitation, iCST was introduced by Zhu and Qin in 2014 [195]. iCST combines the advantages of CST (universally applicable, flexible airfoil design) and PARSEC (intuitive parameter description). Since its development, iCST has been adapted and applied successfully to the aerodynamic design and optimization of 2D airfoils (e.g., [195]), 2D and 3D engine nacelles (e.g., [203–205]) and 2D-axisymmetric propulsive-fuselages (e.g., [132, 206]). The derivation of the employed functions follows the explanation by [203], which is based on [195, 200]. All equations, which are presented in the following, can be found in [203].

Any geometry represented by CST is described by the following mathematical expression, which is the product of a class function  $C(\psi)$  and a shape function  $S(\psi)$  and a term, which accounts for the offset of the curves at the endpoint ( $\psi \Delta \xi_{TE}$ ):

$$\xi(\psi) = S(\psi)C(\psi) + \psi \Delta \xi_{TE} \quad (5.2)$$

$\xi = \frac{y}{c}$  and  $\psi = \frac{x}{c}$  are the non-dimensional y- and x-coordinates, respectively, with  $c$  being the curve length in x-direction. The class function  $C(\psi)$  defines the general class of the geometry, and the shape function  $S(\psi)$  specifies the shape of the geometry class. A set of class functions can be defined by the following function, where different combinations of the exponents  $N1$  and  $N2$  define various general geometric shape classes.

$$C_{N2}^{N1}(\psi) = \psi^{N1}(1-\psi)^{N2} \quad (5.3)$$

For example, *NACA* type round-nosed and pointed aft-end airfoils can be represented with  $N1 = 0.5$  and  $N2 = 1.0$ . The shape function  $S(\psi)$  used here employs  $n + 1$  Bernstein polynomials  $BP$  of order  $n$  and Bernstein polynomial coefficients  $bp$ , which weigh the influence of the individual polynomials. They are defined as:

$$\begin{aligned} BP(\psi) &= \sum_{i=0}^n [K_{i,n} \cdot (\psi^i \cdot (1-\psi)^{n-i})] \\ K_{i,n} &= \frac{n!}{i!(n-i)!} \\ S(\psi) &= \sum_{i=0}^n [bp_i \cdot K_{i,n} \cdot (\psi^i \cdot (1-\psi)^{n-i})] \end{aligned} \quad (5.4)$$

To employ the shape function for geometry parameterization, the Bernstein polynomials have to be manipulated through identification of the Bernstein polynomial weighting coefficients. Zhu and Qin proposed a method to analytically calculate the coefficients from intuitive design variables [195], which was extended by Christie et al. to a generic method applicable to arbitrary constraints [203]. For a number of constraints  $N_{con}$ , the order of the CST curve is  $N_{con} - 1$ . Constraints can specify positions, gradients, and derivatives up to the  $k^{th}$  degree as well as curvature, radii of curvatures, and their derivatives. Each constraint is defined by its  $\psi$ -coordinate and its magnitude  $\xi^k(\psi)$  (a derivative of the  $k^{th}$  degree of the CST function):

$$\xi^{(k)}(\psi) = [S(\psi)C(\psi) + \psi \Delta \xi_{te}]^{(k)} \quad (5.5)$$

The derivatives of the  $k^{th}$  degree of the  $BP$  are polynomials of degree  $k - 1$  and can be written as a linear combination of Bernstein polynomials in the following form:

$$BP'_{i,n}(\psi) = n[BP_{i-1,n-1}(\psi) - BP_{i,n-1}(\psi)] \quad (5.6)$$

The combination of all linear equations, each representing one designer imposed constraint, forms a linear system of equations with the coefficient matrix  $\mathbf{A}$ , the vector of inhomogeneous terms  $\mathbf{b}$  and the vector of  $bp_i$   $\mathbf{x}$  (Equation 5.7), which can be solved for  $\mathbf{x}$ .

$$\mathbf{A} \cdot \mathbf{x} = \mathbf{b} \quad (5.7)$$

The application of the CST method follows a multi-step approach:

1. Split geometry into individual curves
2. Identify curves, which shall be represented by CST
3. Define class function for each curve ( $N1$  and  $N2$ )
4. Define main design parameters for each curve
5. Derive constraints and order of CST
6. Analytically calculate leading edge and trailing edge  $bp_i$ , if applicable
7. Set up and solve linear system of equations for remaining  $bp_i$
8. Derive complete CST function and solve for  $0.0 < \psi < 1.0$

### 9. Scale results with $c$ to original size

The propulsive-fuselage geometry is represented by a combination of 1st order Bezier splines for straight lines, a B-spline for the fuselage nose, and CST for more complex geometries as depicted in Figure 5.3. Two types of class functions are employed for the nacelle geometry, which defines airfoils with a round nose and pointed aft end ( $N1 = 0.5$  and  $N2 = 1.0$ ) and biconvex airfoils with a pointed nose and pointed aft end or ogive bodies ( $N1 = 1.0$  and  $N2 = 1.0$ ). CST curves with  $N1 = 1.0$  and  $N2 = 1.0$  are used for the fuselage geometry. The order of the curves depends on the number of imposed constraints and varies from  $n = 3$  to 4. Design parameters and derived constraints are presented for nacelle and fuselage in Tables A.2, A.3, and A.4 (Appendix A.2). The type, corresponding derivative, normalized x-coordinate  $\psi$ , and magnitude  $\xi^k(\psi)$  are provided for each constraint. In addition, their influence on the weighting coefficients is identified. According to [200],  $bp_0$  and  $bp_n$  can be calculated analytically for class functions with  $N1 = 0.5$  and  $N2 = 1.0$  from airfoil geometry variables. The non-dimensional leading edge radius  $\rho_{LE} = \frac{r_{LE}}{c}$  and the trailing edge boattail angle  $\beta_{TE}$  can be used as following [200]:

$$bp_0 = \sqrt{2 \cdot \rho_{LE}} \text{ and } bp_n = \tan(\beta_{TE}) + \xi_{TE} \quad (5.8)$$

If trailing edge and leading edge angle are defined,  $bp_0$  and  $bp_n$  can similarly be calculated for class functions with  $N1 = 1.0$  and  $N2 = 1.0$ :

$$bp_0 = \tan(\beta_{LE}) - \xi_{TE} \text{ and } bp_n = -\tan(\beta_{TE}) + \xi_{TE} \quad (5.9)$$

For all other constraints, the corresponding linear equation is defined and the function coefficients  $a_{m,n}$  and constant terms  $b_m$  are derived to populate matrix  $\mathbf{A}$  and vector  $\mathbf{b}$ , which are defined as:

$$\mathbf{A} = \begin{bmatrix} a_{1,1} & a_{1,2} & \cdots & a_{1,n} \\ a_{2,1} & a_{2,2} & \cdots & a_{2,n} \\ \vdots & \vdots & \ddots & \vdots \\ a_{n,1} & a_{n,2} & \cdots & a_{n,n} \end{bmatrix} \text{ and } \mathbf{b} = \begin{bmatrix} b_{1,0} \\ b_{2,0} \\ \vdots \\ b_{n,0} \end{bmatrix} \quad (5.10)$$

The coefficients and terms can be derived from re-arranging Equation 5.5 to the Equations 5.11 for positional arguments with  $k = 0$ , to Equations 5.12 for gradients with  $k = 1$ , and to Equations 5.13 for  $k = 2$ .

$$a_{x,m} = BP_{m,n} \cdot C(\psi) \quad (5.11)$$

$$b_{x,0} = \xi(\psi) - \Delta\xi_{te}\psi - C(\psi) \cdot (bp_0 \cdot BP_{0,n} + bp_n \cdot BP_{n,n})$$

$$a_{x,m} = [BP_{m,n}]' \cdot C(\psi) + BP_{m,n} \cdot C'(\psi) \quad (5.12)$$

$$b_{x,0} = \xi'(\psi) - \Delta\xi_{te} - C(\psi) \cdot (bp_0 \cdot [BP_{0,n}]' + bp_n \cdot [BP_{n,n}]') \quad (5.12)$$

$$- C'(\psi) \cdot (bp_0 \cdot BP_{0,n} + bp_n \cdot BP_{n,n})$$

$$a_{x,m} = [BP_{m,n}]'' \cdot C(\psi) + 2[[BP_{m,n}]' \cdot C'(\psi)] + BP_{m,n} \cdot C''(\psi) \quad (5.13)$$

$$b_{x,0} = \xi''(\psi) - C(\psi) \cdot (bp_0 \cdot [BP_{0,n}]'' + bp_n \cdot [BP_{n,n}]'') - 2C'(\psi)[bp_0 \cdot [BP_{0,n}]' + bp_n \cdot [BP_{n,n}]'] - C''(\psi) \cdot (bp_0 \cdot BP_{0,n} + bp_n \cdot BP_{n,n})$$

Based on the presented parameterization strategy and the design parameters introduced in Section 5.3.1, a variety of geometries is generated. Geometries, which violate global constraints due to an unfavorable or unphysical combination of design parameters are automatically identified and discarded from the sample.

## 5.4 Panel Method

The PM used to predict the BL in the undisturbed front part of the fuselage is based on a combination of a potential flow solution and an IBL method, as depicted in Figure 5.1. Hence, the 2D-axisymmetric problem is reduced to a 1D problem. The solution of the IBL equation requires the characteristics of the BL edge provided by the solution of the potential flow domain. The incompressible potential flow solution is corrected for compressibility. An equivalent body approach is employed to model the viscous/inviscid interaction. Convergence is reached after a few seconds when the displacement thickness along the fuselage converges. The model is limited to steady and compressible 2D-axisymmetric flows without shockwaves. Flow separation due to adverse pressure gradients is detected and handled by the method. Characteristics of the BL along the fuselage length and the potential flow solution are used to predict the flow characteristics at the PM/FVM interface and calculate the skin friction and pressure force of the front part of the fuselage. The implementation of the method is based on [207] and [208].

### 5.4.1 Potential Flow Solution

The solution of the inviscid flow region follows the Hess-Smith PM proposed by Hess and Smith for incompressible flows [209, 210]. The body's surface is treated as a distribution of singularities along the length of the body. For a streamlined body such as the fuselage, the distribution of fluid sources and sinks represents the flow perturbation caused by the body. To account for compressibility effects, the Karman-Tsien compressibility correction is employed.

#### 5.4.1.1 Hess-Smith Panel Method

In a potential flow region, the flow is assumed to be inviscid and incompressible, leading to the following relations for dynamic viscosity  $\mu$  and density  $\rho$ :

$$\begin{aligned}\mu &= 0 \\ \rho &= \text{const} , \text{ thus } \frac{D\rho}{Dt} = 0\end{aligned}\tag{5.14}$$

The continuity equation reduces to the zero-divergence condition:

$$\nabla \cdot \mathbf{V} = 0\tag{5.15}$$

For a potential flow along a body surface, the total velocity  $\mathbf{V}$  can be expressed as the sum of the freestream velocity  $\mathbf{V}_\infty$  and the disturbance velocity  $\mathbf{V}_d$ , which is induced by the body on the flow [211].

$$\mathbf{V} = \mathbf{V}_\infty + \mathbf{V}_d\tag{5.16}$$

Under the assumption that  $\mathbf{V}_d$  is irrotational ( $\nabla \times \mathbf{V}_d = 0$ ) and that it can be expressed as the negative gradient of a scalar function, the velocity potential  $\varphi$  [210], it can be expressed as:

$$\mathbf{V}_d = -\nabla\varphi\tag{5.17}$$

Combining Equation 5.15 and 5.17 leads to Laplace's equation, which is the governing equation for the incompressible potential flow:

$$\nabla^2\varphi = 0\tag{5.18}$$

In addition it is assumed that the body contour forms a streamline and that no flow enters the external body surface  $S^+$  (kinematic flow condition):

$$\mathbf{V} \cdot \mathbf{n}|_{S^+} = 0 , \text{ thus } \nabla\varphi \cdot \mathbf{n}|_{S^+} = \left. \frac{\delta\varphi}{\delta n} \right|_{S^+} = \mathbf{V}_\infty \cdot \mathbf{n}|_{S^+}\tag{5.19}$$

Further, the disturbance velocity vanishes at infinity (regularity condition)

$$\lim_{r \rightarrow \infty} \nabla \varphi = 0 \quad (5.20)$$

The combination of Equations 5.18 through 5.20 forms the Neumann problem [212]. For some specific problems, the Neumann problem can be solved analytically [210]. For complex geometries, numerical methods are employed.

Laplace's equation is a linear PDE. Therefore, the solution of  $\varphi$  at any point of interest can be constructed as a sum of elementary solutions  $\varphi_i$  with weighting factors  $C_i$  (superposition principle) [212]:

$$\nabla^2 \varphi = \sum_i C_i \cdot \nabla^2 \varphi_i \quad (5.21)$$

Elementary solutions can be singularities such as sources, vortices or doublets located on the body surface. For non-lifting surfaces, such as streamlined bodies, the flow is modeled by a continuous distribution of source singularities with source strength  $\sigma_j^*$  located along the body surface [210]. The disturbance potential  $\varphi_{\sigma,ij}$  is expressed by:

$$\varphi_{\sigma,ij} = \iint_S \frac{\sigma_j}{r_{ij}} dS \quad (5.22)$$

$r_{ij}$  is the distance between points  $i$  and  $j$  and  $\sigma_j = \frac{\sigma_j^*}{4\pi}$  is the scaled source strength. For an arbitrary point  $i$  on the surface of the body, a combination of Equations 5.21 and 5.22 yields a Fredholm integral equation, which features a near field term  $2\pi\sigma_i$  and an integral far-field term [211]:

$$\pm 2\pi\sigma_i - \iint_S \frac{\delta}{\delta n} \frac{\sigma_j}{r_{ij}} dS = -\mathbf{V}_\infty \mathbf{n}_i \quad (5.23)$$

The near field term expresses the influence of the source on the field point. If the surface is approached from the external flow, it requires a positive sign; if approached from the internal flow, it requires a negative sign. In the presented implementation, the kinematic flow condition is satisfied in the external flow, and thus, a positive sign is required. Equation 5.23 can be solved by approximation. The body surface is divided into  $N$  line segments or panels and  $N+1$  defining points, one at the beginning and one at the end of each panel. The panel source strength is assumed to be constant along the panel. The surface integral of Equation 5.23 can then be replaced by the sum of  $N$  finite sources [213]:

$$\pm 2\pi\sigma_i - \sum_{j=1}^N \sigma_j \iint_{S_j} \frac{\delta}{\delta n} \frac{1}{r_{ij}} dS = -\mathbf{V}_\infty \mathbf{n}_i \quad (5.24)$$

A system of  $N$  linear equations with  $N$  unknowns can be derived in the following matrix notation

$$\mathbf{A}\boldsymbol{\sigma} = -\mathbf{V}_\infty \mathbf{n} \quad (5.25)$$

which can be written in component notation as

$$\sum_{j=1}^N A_{i,j} \sigma_j = \mathbf{V}_\infty \mathbf{n}_i \quad (5.26)$$

The normal influence coefficients  $A_{i,j}$  represent the normal velocities at the control points of the panels  $i$ , which are induced by a source sheet with unitary strength  $\sigma_j = 1$  on panel  $j$  [210]. General information on calculating the normal influence coefficients for axisymmetric source panels is provided in [209, 210]. Detailed information on their implementation for the present study are found in [207, 208]. The linear system of Equations 5.25 is solved for the source strengths of all panels  $\sigma_j$ . They are then employed

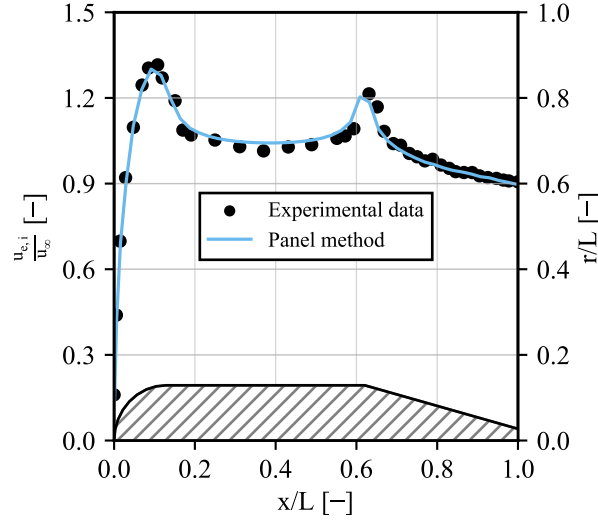


Figure 5.4: Incompressible BL edge velocity distribution for *Fuselage* geometry (Appendix A.3). Comparison to experimental data by [214].

to calculate the velocity at any arbitrary point  $(x_p, y_p)$  in the flow field by multiplication of the panel velocity disturbances  $W_{ij}$  with their respective source strengths  $\sigma_j$  [211]:

$$\mathbf{V} = \mathbf{V}_\infty + \sum_{j=1}^N W_{ij} \sigma_j \quad (5.27)$$

To obtain the incompressible edge velocity distribution  $u_{e,i}$ ,  $N$  points with coordinates  $(x_0, r_0 + \delta^*)$  are distributed along the edge of the BL, which serve as points of interest ( $\delta^* = 0$  for the first iteration).

Figures 5.4 and 5.5 show the results of applying the incompressible PM to different streamlined geometries. Additional validation results can be found in [207]. The trend of the incompressible BL edge velocity  $u_{e,i}$  is matched well. However, in regions of high velocities, the incompressible edge pressure coefficient  $C_{p,e,i}$  is slightly underpredicted.

#### 5.4.1.2 Compressibility Correction

Compressibility models by Prandtl-Glauert [216], Karman-Tsien [217], Myring [218] and Laitone [219] were implemented and tested (see [207] for more details). All models are derived from the linearized potential equation and are restricted to fully subsonic flows. As depicted exemplarily in Figure 5.5, validation cases with compressible freestream conditions showed that the Karman-Tsien model performed best in predicting the compressible pressure coefficient  $C_{p,c}$  and could improve the accuracy of the solution compared to the incompressible calculation. Thus, it was employed in the current solver.

The method is based on manipulating the compressible and incompressible stream functions combined with isentropic relations for an ideal gas and an additional assumption that the quantity  $(1 - Ma^2)/\rho^2$  is constant. This leads to a relation between compressible and incompressible pressure coefficient  $C_{p,c}$  and  $C_{p,i}$ , which can be employed to correct the incompressible edge pressure coefficient  $C_{p,e}$  and velocity  $u_e$  for compressibility [217].

$$C_{p,c} = \frac{C_{p,i}}{\sqrt{1 - Ma_\infty^2} + \frac{Ma_\infty^2}{1 + \sqrt{1 - Ma_\infty^2}} \frac{C_{p,i}}{2}} \quad (5.28)$$

In the transonic flow regime, sonic or supersonic regions can occur on the body surface even if  $Ma_\infty < 1$ . It is assumed that for  $Ma_\infty > Ma_{crit}$ , local sonic regions occur. Here, the compressibility correction is

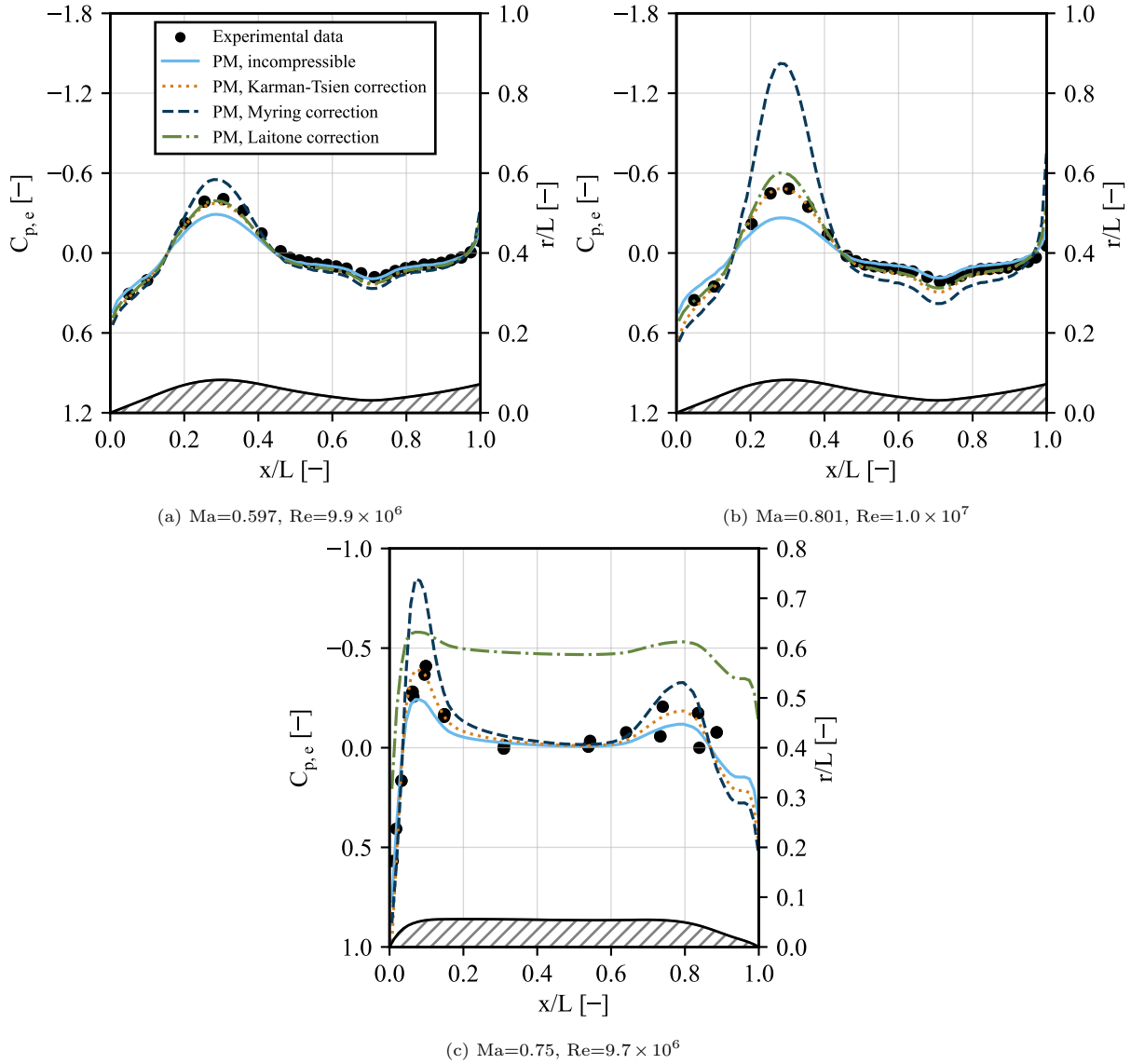


Figure 5.5: Pressure coefficient distribution at edge of BL for *Waisted Body* (top) and *Equivalent Fuselage* (bottom) (see also Appendix A.3). Comparison of the results of different compressibility correction models against experimental data by [215] and [193].

not valid. However, for the present case, pre-studies showed that pronounced supersonic regions only occur at the upper surface of the nacelle, which is located in the RANS FVM domain and, thus, the compressibility correction is valid for the PM domain.

#### 5.4.2 Integral Boundary Layer Prediction Method

The potential theory does not hold true near the body's surface, as elaborated in Section 3.1. The BLEs are solved in this region to determine the local flow characteristics. The current method focuses on evaluating the BL on a simplified 2D-axisymmetric body. Thus, the BL is conveniently evaluated on a curvilinear, axisymmetric coordinate system as depicted in Figure 5.6.  $x$  measures the distance along the body's contour and  $y$  the distance normal to the body contour.  $r$  is the distance normal to the axis of symmetry.  $u$  and  $v$  are the tangential and normal velocities in the BL.

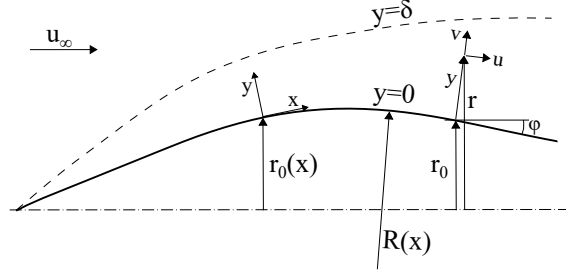


Figure 5.6: Curvilinear and axisymmetric coordinate system employed for IBL method. Source: [220]

BL characteristics at the body's surface and the BL's edge are indicated with index 0 and  $e$ , respectively. With  $R$  being the curvature radius and  $\Phi$  being the slope angle, the following geometrical relationships hold [220]:

$$\begin{aligned}
 r &= r_0 + y \cos \Phi \\
 \frac{dr_0}{dx} &= \sin \Phi \\
 \frac{d\Phi}{dx} &= -\kappa = -\frac{1}{R} \\
 \frac{\delta r}{\delta y} &= \cos \Phi \\
 \frac{\delta r}{\delta x} &= (1 + \kappa y) \sin \Phi
 \end{aligned} \tag{5.29}$$

Patel [220] provided a derivation of the following thin axisymmetric BLEs (Equations 5.30) from the NSEs under the assumptions that

- In a BL a high gradient exists perpendicular to the surface, thus:  $\frac{\partial}{\partial y} \gg \frac{\partial}{\partial x}$
- Based on experiments:  $\overline{u'v'} \ll uv$  and  $\overline{v'^2} \ll v^2$  [14]
- Time-averaging:  $v \ll u$
- Thin BL, i.e. the BL thickness is small compared to all other relevant length scales:  $\delta \ll L$  (body length),  $\delta \ll R$  (curvature radius),  $\delta \ll r_0$  (transverse radius)

$$u \frac{\partial u}{\partial x} + v \frac{\partial u}{\partial y} + \frac{\partial}{\partial x} \left( \frac{p}{\rho} \right) + \frac{\partial}{\partial y} (\overline{u'v'}) - \nu \frac{\partial^2 u}{\partial y^2} = 0 \tag{5.30a}$$

$$\frac{\partial}{\partial y} \left( \frac{p}{\rho} + \overline{v'^2} \right) = 0 \tag{5.30b}$$

$$\frac{\partial u}{\partial x} + \frac{\partial u}{\partial y} + u \frac{1}{r_0} \frac{dr_0}{dx} = 0 \tag{5.30c}$$

Due to the simplifications, the former hyperbolic-elliptic governing equations become parabolic. Thus, the solution of one point in the domain does not depend on the solution of the entire domain, and Equations 5.30a through 5.30c can be solved by simple forward-marching schemes.

The IBL method is based on integrating the momentum equation in stream-wise direction (Equation 5.30a) over the BL thickness  $\delta$ . A series of substitutions and algebraic manipulations described for example in [12, 220] lead to the von Karman momentum integral equation for incompressible flows

$$\frac{d\theta}{dx} = \frac{C_f}{2} - \frac{\theta}{u_e} \frac{du_e}{dx} (H + 2) \tag{5.31}$$

and for compressible flows (e.g. [221])

$$\frac{d\theta}{dx} = \frac{C_f}{2} - \frac{\theta}{u_e} \frac{du_e}{dx} (H + 2 - Ma_e^2) \quad (5.32)$$

Equation 5.32 is a more compact form of Equation 5.30a and depends directly on several BL-related parameters, which were defined in Section 2.1.1. Derived from the momentum integral equation, a range of integral techniques for predicting laminar and turbulent boundary layers has been formulated, collectively referred to as integral methods. The methods employed in the current study are elaborated in the following subsections.

#### 5.4.2.1 Laminar Boundary Layer

Due to the high Reynolds numbers in cruise conditions, it is expected that transition will occur in the nose region of the investigated fuselage configuration. Thus, the laminar BL region will extend only over a small percentage of the total fuselage surface area and contribute only minorly to  $NPF_{FC,bare}$ . In addition, its impact on the BL characteristics at the IBL/FV interface will be small. Consequently, a simplified, explicit calculation method based on the Thwaites integral method is employed for calculating the laminar BL characteristics. Here, the Thwaites method, as described by Cebeci and Bradshaw [222] and extended to compressible flows by Rott and Crabtree [223], is implemented. Thwaites' approach is based on empirical observations, which indicate a linear correlation between the development of the laminar BL and the pressure-gradient parameter  $\lambda$ .

$$\lambda = \frac{\theta^2}{\nu} \frac{du_e}{dx} \quad (5.33)$$

$\nu$  is the kinematic viscosity. This correlation leads to the following formulation, which enables the determination of the axisymmetric momentum thickness:

$$\theta^2 = 0.45\nu_t \left(\frac{T_t}{T}\right)^3 r_0^{-2} u_e^{-6} \int_0^x \left(\frac{T}{T_t}\right)^{1.5} r_0^2 u_e^5 dx \quad (5.34)$$

Here,  $\nu_t$  represents the stagnation kinematic viscosity. Unless explicitly specified otherwise, all integrals are computed employing Simpson's rule throughout this study. Moreover, derivatives are assessed utilizing a first-order forward finite differences approximation. This approach extends to expressions applicable to the turbulent region as well.

Skin friction coefficient  $C_f$  and incompressible shape factor  $H_i$  are calculated with:

$$C_f = \begin{cases} \frac{2}{Re_\theta} (0.225 + 1.61\lambda - 3.75\lambda^2 + 5.24\lambda^3), & 0 \leq \lambda \leq 0.1 \\ \frac{2}{Re_\theta} \left(0.225 + 1.472\lambda + \frac{0.0147\lambda}{0.107+\lambda}\right), & -0.1 \leq \lambda \leq 0 \end{cases} \quad (5.35)$$

$$H_i = \begin{cases} 2.61 - 3.75\lambda + 5.24\lambda^2, & 0 \leq \lambda \leq 0.1 \\ 2.472\lambda + \frac{0.0147}{0.107+\lambda}, & -0.1 \leq \lambda \leq 0 \end{cases}$$

The compressible shape factor  $H$  is computed by:

$$H = \frac{T_t}{T} H_i + \frac{T_t}{T} - 1 \quad (5.36)$$

Assuming that close to the body's nose the BL length-scales are small compared to the geometrical length-scales, it is assumed that the flat-plate equation by Kays and Crawford is sufficiently accurate to calculate the laminar BL thickness [224]:

$$\delta = 4.64 \sqrt{\frac{\nu x}{u_e}} \quad (5.37)$$

### 5.4.2.2 Turbulent Boundary Layer

Mendoza assessed two integral methods for turbulent BLs [207]. The approach by Patel and Nakayama [225, 226] is specifically tailored to evaluating thick boundary layers. The lag-entrainment method by Green et al. [227] models the entrainment from the turbulent kinetic energy equation. Validation studies found that although both methods can accurately predict the BL characteristics, Patel et al.'s method predicts the flow at the tails of axisymmetric bodies and in regions of concave curvature better than Green's approach. These fuselage parts are of special interest for the presented method, as the interface between IBL and FVM will be located in this region. Furthermore, Patel et al.'s approach estimates the BL thickness and the distribution of the skin friction coefficient along the body better. In consequence, Patel et al.'s method is employed in the current study.

The approach is based on insights that the authors gained from experimental investigations [14]. They found that especially in the rear part of axisymmetric bodies the turbulent BL grows fast and the thin BL theory does not hold true. Here, the flow is strongly affected by curvature and pressure gradient effects. Consequently, they derived the following momentum integral equation without assuming a thin BL. It accounts for the longitudinal curvature and pressure variation across the BL height through the curvature integral  $I_k$  and the pressure integral  $I_p$ , respectively [13]:

$$\begin{aligned} \frac{d\theta}{dx} + (H+2) \frac{\theta}{u_e} \frac{du_e}{dx} &= \frac{C_f r_0}{2} + I_k + I_p \\ I_k &= \kappa \int_0^\delta \frac{uv}{u_e^2} dx \\ I_p &= \frac{1}{u_e^2} \int_0^\delta \frac{\partial}{\partial x} \left( \frac{p-p_e}{\rho} - \frac{v_e^2}{2} \right) dx \end{aligned} \quad (5.38)$$

To account for compressibility effects, Equation 5.38 was modified by Mendoza according to the definition of the compressible momentum integral equation by Green [221] provided in Equation 5.32 to finally yield the following equation:

$$f(x, \theta) = \frac{d\theta}{dx} = \frac{C_f r_0}{2} - (H+2 - Ma_e^2) \frac{\theta}{u_e} \frac{du_e}{dx} + I_k + I_p \quad (5.39)$$

A predictor-corrector algorithm (modified Euler FD equation) is employed to solve Equation 5.39 [207, 228].

The entrainment theory by Head [229] provides closure for the solution of the system of equations. Here, entrainment relates to mass influx from the potential flow region into the turbulent BL, which leads to the growth of the BL. The mass influx is modeled through an entrainment function  $\frac{dQ}{dx}$ . According to Nakayama et al. [13] for a body of revolution it is defined as:

$$\frac{dQ}{dx} = C_E u_e (r_0 + \delta) (1 + \kappa \delta) \quad (5.40)$$

Patel's method uses an analytical expression by Dvorak [230] to determine the entrainment coefficient  $C_E$ :

$$C_E = e^{-3.512 - 0.617 \ln(H_{pl}^* - 3)} \quad (5.41)$$

The planar entrainment shape factor  $H_{pl}^*$  is approximated by [231]:

$$H_{pl}^* = 3.3 + 1.535 (H_{pl} - 0.7)^{-2.715} \quad (5.42)$$

The solution of the following Equations 5.43 in combination with Equation 5.42 [14] yields the planar boundary characteristics indicated by index  $pl$  as a function of the axisymmetric characteristics.

$$\begin{aligned}\Delta^* &= \left( H_{pl} + \beta \frac{\beta_{pl}}{2r_0} (H_{pl} + 1) \right) r_0 \theta_{pl} \\ \theta &= \left( 1 + \beta \frac{\theta_{pl}}{r_0} \right) r_0 \theta_{pl} \\ \beta &= \frac{1}{2} \cos \Phi \frac{2H_{pl}^2 (H_{pl} + 1)}{(H_{pl} - 1)(H_{pl} + 3)}\end{aligned}\quad (5.43)$$

As planar and axisymmetric flows are similar in nature [14], the planar flow characteristics can easily be translated to axisymmetric characteristics through the following equations by Patel [225] combined with Equation 5.41 and the friction law by Thompson [232] fitted by Head and Patel [233] and provided in Equation 5.45:

$$\begin{aligned}H &= \frac{\delta^*}{\theta} \\ \frac{Q}{u_e} &= r_0(\delta - \delta^*) + \frac{1}{2}\delta^2 \cos \phi \\ n &= \frac{2}{H_{pl} - 1}\end{aligned}\quad (5.44)$$

$$\begin{aligned}C_f &= e^{aH_{pl}+b} \\ a &= 0.019521 - 0.386768c + 0.028345c^2 - 0.000701c^3 \\ b &= 0.191511 - 0.834891c + 0.062588c^2 - 0.001953c^3 \\ c &= \ln Re_{\theta,pl}\end{aligned}\quad (5.45)$$

To evaluate the integrals  $I_p$  and  $I_k$ , a linear velocity profile is assumed and the following expressions are solved according to [13]:

$$\begin{aligned}u_e^2 I_k &= \kappa \delta \left( \frac{n}{2n+1} r_0 + \delta \frac{n}{3n+1} \cos \Phi \right) u_e v_e \\ u_e^2 I_p &= \frac{d}{dx} \left( \frac{p_0 - p_e}{\rho} \right) \delta^2 \left( \frac{2r_0}{3\delta} + \frac{1}{4} \cos \Phi \right) + \frac{p_0 - p_e}{\rho} \delta \frac{d\delta}{dx} \left( \frac{2r_0}{3\delta} + \frac{1}{2} \cos \Phi \right) + v_e \frac{dv_e}{dx} \delta^2 \left( \frac{r_0}{\delta} + \frac{1}{2} \cos \Phi \right)\end{aligned}\quad (5.46)$$

Here, the static pressure distribution at the BL edge is defined as:

$$\frac{p_0 - p_e}{\rho} = \frac{n}{2n+1} u_e \delta^2 \frac{d}{dx} \left( \frac{v_e}{\delta} \right) + \frac{1}{2} v_e^2 - \kappa \delta \frac{n}{3n+1} u_e \delta^2 \frac{d}{dx} \left( \frac{v_e}{\delta} \right) - \kappa \delta \frac{2}{n+2} u_e^2 \quad (5.47)$$

From Equations 5.45 and 5.47, the skin friction and pressure distribution along the body are calculated, which serve as an input to the skin friction and pressure force estimation for the front part of the fuselage.

Initial conditions at the transition point are obtained from the solution of the laminar BL upstream of the turbulent flow region. The momentum thickness at the beginning of the turbulent region is taken as the momentum thickness at the end of the laminar region. The shape factor, however, will follow a step change if the transition is assumed to be punctiform (see Section 5.4.2.3). Following Zedan and

Dalton's [234] application of Nash and Macdonald's [235,236] empirical approach, the shape factor at the beginning of the turbulent BL is calculated by an iterative solution of the following equations:

$$\begin{aligned}
\Pi &= -\frac{2H}{C_f} \frac{\theta}{u_e} \frac{du_e}{dx} \\
G &= 6.1 \sqrt{\Pi + 1.81} - 1.7 \\
\frac{2}{C_f} &= 5.75 \log_{10}(H Re_\theta) + 1.5G + \frac{2110}{G^2 + 00} - 14.8 \\
H &= \frac{1}{1 - F \sqrt{C_f/2}}
\end{aligned} \tag{5.48}$$

$\Pi$  is a modified pressure gradient parameter,  $G$  is the velocity-defect form factor. A shape factor of  $H = 1.4$  and the solution of the skin-friction law by Ludwig and Tillmann [237] given in Equation 5.49 serve as an initial guess to the solution of the system of equations.

$$C_f = 0.246 \left( 10^{-0.678H} Re_\theta^{-0.268} \right) \tag{5.49}$$

The solution of the turbulent BL is iterated until the distribution of  $\theta$  along the body converges.

### 5.4.2.3 Transition Prediction

A laminar BL is a smooth and orderly fluid motion in parallel layers adjacent to a solid surface. It is governed by viscous forces, which dominate over inertial forces. In a laminar BL, fluid particles move in well-defined layers without significant mixing or turbulence. Small disturbances or fluctuations appear in the initially smooth laminar flow when the flow travels along the body for a certain distance. These disturbances grow over time due to the amplification of instabilities caused by the nonlinear interactions between the fluid layers. As the amplitude of these disturbances increases, the flow becomes more chaotic and turbulent, leading to enhanced mixing. The disturbances become unstable, and the laminar flow transitions to a turbulent flow. Turbulent flows are characterized by irregular and chaotic fluctuations in velocity, pressure, and other flow properties due to the dominance of inertial versus viscous forces. In reality, the laminar-turbulent transition is not a singular event but a gradual process unfolding over a region. However, the simplified transition models explored for the IBL method identify distinct transition locations  $x_{tr}$  by evaluating if the local flow properties cross a defined threshold.

The Preston criterion assumes that a flow is turbulent, whenever its local momentum thickness based Reynolds number  $Re_\theta$  becomes bigger than 320 [238]. Crabtree identified a universal transition curve as a threshold for transition, which depends on local  $Re_\theta$  and the pressure gradient parameter  $\lambda$  [239]. Similarly, the Michel-e<sup>9</sup> method by Cebeci et. al. [240] defines a  $Re_\theta$  and  $Re_x$  dependent threshold curve, which identifies if a BL flow is locally laminar or turbulent. All methods were employed to calculate the transition location of the *Akron Airship* and the *Low-Drag F-57 Body*, and the results were compared against experimental data provided in [241] (see Table 5.1).

	$Re_L$	$x_{tr}/L$			
		Experimental	Preston	Crabtree	Michel-e <sup>9</sup>
<b>Akron Airship</b>	$1.7 \times 10^7$	0.06 - 0.07	0.075	0.260	0.610
<b>Low-Drag F-57 Body</b>	$1.2 \times 10^6$	0.475	0.468	0.202	0.630

Table 5.1: Comparison of transition location prediction compared against experimental data provided by [241].

Results indicate that the Preston criterion best predicts the transition point for the evaluated axisymmetric bodies. However, when employing the criterion for bodies with  $Ma_\infty > 0.3$ , the assumption of a

punctiform transition from laminar to turbulent flow can lead to unphysical behavior of the flow characteristics, such as a discontinuity in the edge velocity distribution near the transition location. This is because solving the turbulent BL necessitates using the solution of the laminar BL at the transition point as a boundary condition. If the point of transition is predicted too far upstream, the laminar BL characteristics at the transition point differ significantly from the characteristics of the turbulent BL at the panel downstream of the transition location. The model is refined to "smoothen" the transition and foster convergence. The Preston criterion determines the transition location, but the laminar BL characteristics, provided as an input to the turbulent BL prediction, are taken from a location further downstream, determined from the more conservative Michel-e<sup>9</sup> threshold. Mendoza showed that this approach does not alter the BL characteristics downstream of the transition location [207]. In the following studies, this modified Preston approach is employed.

#### 5.4.2.4 Handling of Separation and Shock Waves

If the laminar BL separates before reaching the point of transition, it is assumed that the BL reattaches instantaneously as a turbulent BL [184]. The laminar separation point is, thus, used as the transition point, and the turbulent flow starts at the separation point. Laminar separation is detected by evaluating the local skin friction coefficient. If at any point  $C_f < 0$ , this point is assumed to be the point of laminar separation [242, 243]. For integral methods, the value of the shape factor  $H$  increases as the turbulent flow approaches the point of separation [244]. Thus, turbulent BL separation is detected by evaluating the local shape factor  $H$ . In accordance with Green et al. [227], a simplified approach is applied, which assumes that turbulent flow separation occurs at  $H > 2.8$ . As indicated by Olson and Dvorak [242], experimental observations showed that the static pressure is nearly constant within a separated flow. In consequence, it is assumed that the edge velocity  $u_e$  is constant and equal to the velocity at the point of separation along the remaining length of the body. The displacement thickness in the separated zone is obtained by linear extrapolation from the point of separation, similar to the procedure proposed by [242]. The turbulent BL does not re-attach. If turbulent separation is detected, the IBL calculation is terminated.

The compressibility correction for the potential flow solution derives from the linearized potential equation. However, a fluid exhibits nonlinear behavior in regions where  $Ma$  locally exceeds unity. Here, shock waves can form, which are inherently highly nonlinear as they are defined as abrupt and discontinuous changes in flow properties, such as pressure, temperature, and density, across a narrow region. Therefore, the PM is limited to  $Ma < Ma_{crit}$  because it cannot capture nonlinear effects.

Pre-studies of the fuselage-propulsor configuration showed that regions with  $Ma > 1$  only occur on the upper side of the FF nacelle and not on the fuselage itself. Furthermore, no laminar flow separation is exhibited, and turbulent separation regions are occasionally present inside the FF duct. Thus, the restriction of the applicability of the PM to fully subsonic flows without separation is valid for the present study, where its usage is limited to the front part of the axisymmetric fuselage (see also Section 5.5).

#### 5.4.2.5 Viscous/Inviscid Coupling

The most straightforward method to couple the viscous and inviscid flow solution is to iteratively recalculate the potential flow about an equivalent body. The equivalent body equals the original body surface offset by the physical displacement thickness  $\delta_{ph}^*$ , calculated by the IBL method.

An alternative coupling method is more suitable for multi-body configurations similar to the PFC, using a transpiration velocity [186, 245]. Instead of adapting the geometry of the body used for potential flow calculation, the displacement effect is simulated by modifying the normal boundary condition of the

potential flow solution [212]. An incremental transpiration velocity  $V_{T,i}$  is added to the normal boundary condition:

$$\sum_{j=1}^N A_{i,j} \sigma_j = \mathbf{V}_\infty \mathbf{n}_i + V_{T,i} \quad (5.50)$$

For an axisymmetric body,  $V_T$ , which is specified as a flow through the panel surface, is calculated by [246]:

$$V_T = -\frac{1}{4\pi(r_0 + \delta \cos \gamma)} \frac{d}{ds} (r_0 u_e \delta_{ph}^*) \quad (5.51)$$

$\gamma$  is the local panel angle with respect to the axis of symmetry. Here, the body geometry does not change between the iterations, and multiple bodies in close proximity can be simulated. The potential flow is calculated based on the updated BL characteristics and vice versa. Convergence is reached once the displacement thickness distribution converges.

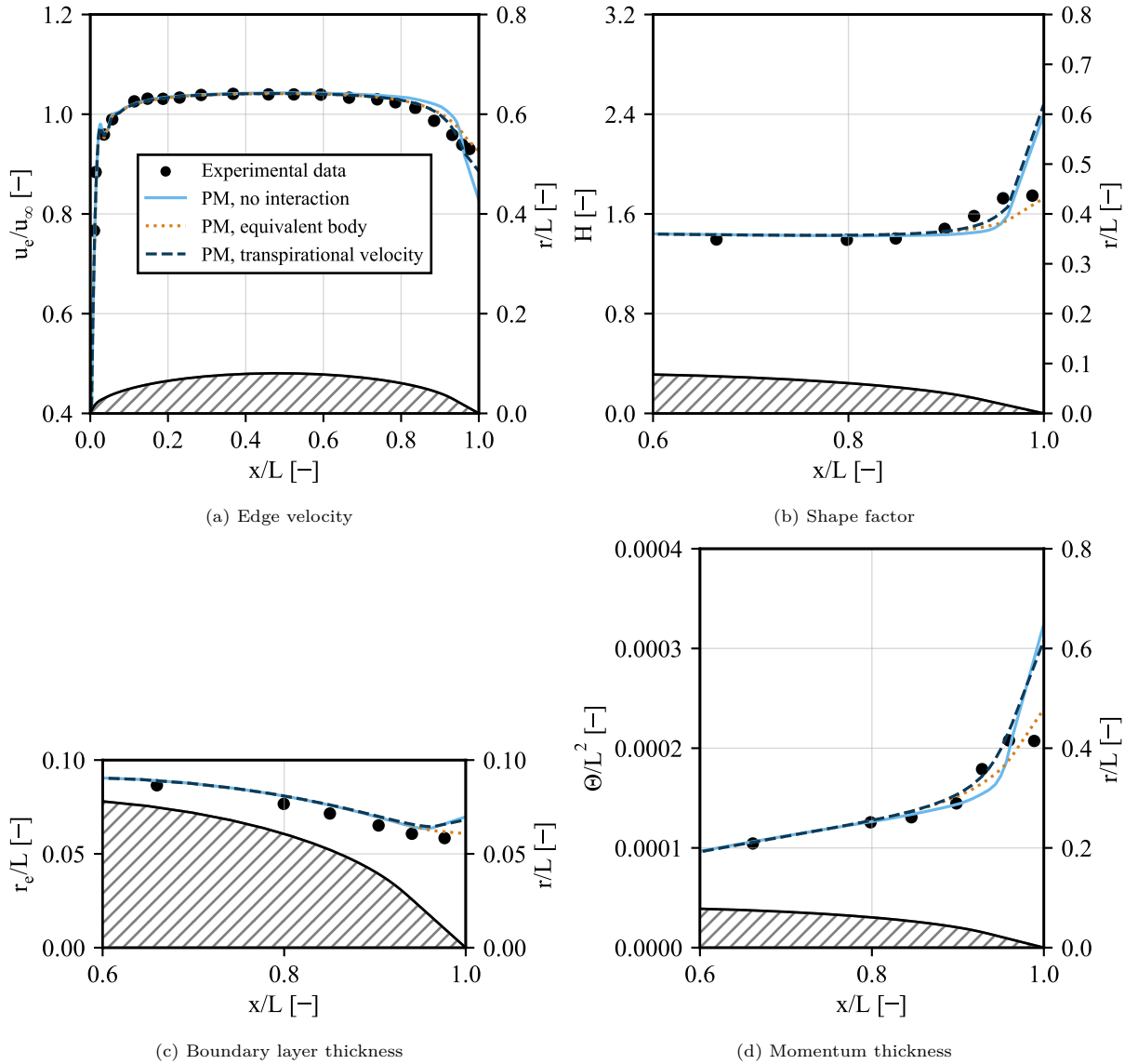


Figure 5.7: BL characteristics for the rear part of the 6:1 *Spheroid* (see also Appendix A.3). Comparison of the different viscous/inviscid coupling method results to experimental data by [14].

Figure 5.7 presents the numerically calculated BL characteristics with and without viscous/inviscid coupling compared to experimental data of the *6:1 Spheroid*. Without coupling the methods,  $\delta$  is overpredicted at the rear end of the geometry, which influences the bad prediction of  $H$  and  $\theta$ . Furthermore,  $u_e$  is underestimated. Both coupling methods can improve the accuracy of the prediction. However, the equivalent body approach performs significantly better than the transpiration velocity method. The current study evaluates only a single body with the IBL method. Therefore, the better-performing equivalent body approach is employed.

### 5.4.3 Validation

In addition to validating the individual methods in the preceding sections, the full PM is validated. A comprehensive validation study is provided in [207]. Figure 5.8 depicts the results of one exemplary validation for the *Waisted Body* geometry at  $Ma_\infty = 0.597$ . IBL results are based on a combination of the following selected methods as described above: Hess-Smith PM with Karman-Tsien compressibility correction, modified Preston method for transition prediction, Thwaites integral method for the laminar and modified Patel method for the turbulent BL region, and coupling of viscous and inviscid solution through the equivalent body approach. Results show that the BL characteristics predicted by the IBL method agree with experimental data, qualitatively and quantitatively. Furthermore, the IBL approach achieves higher accuracy in predicting  $\delta$ ,  $\delta^*$ , and  $\theta$  than the FV simulation method (see Section 5.6.2). As  $H$  is very sensitive to small variations of  $\delta^*$  and  $\theta$  near unity, its underestimation by the IBL method directly results from the small deviations of those BL characteristics. The IBL method in the front part of the body predicts  $C_f$  better than the FV approach. The transition prediction method predicts the transition point too far downstream. Thus, the first validation point is not matched by the IBL method. However, the agreement downstream of the transition point is better because the IBL approach differentiates between a laminar and a turbulent BL region, whereas the FV method assumes fully turbulent flow conditions in the whole domain. Near the waist of the body, the IBL method performs better for favorable pressure gradients and worse for adverse pressure gradients.

A pre-study of the reference fuselage geometry showed a need to adapt the calculated pressure distribution at the body's surface for post-processing. When comparing IBL results of the isolated fuselage to data obtained by a RANS CFD simulation, the surface pressure coefficient distribution  $C_{p,w}$  differs in the fuselage nose region (see Figure 5.9). This discrepancy significantly impacts the pressure force calculation for the fuselage body. However, in the fuselage region where  $\delta$  increases rapidly, i.e., behind the fuselage center section,  $C_{p,w}$  compares well to the FVM solution. The surface pressure is obtained from Equation 5.47 under the assumption that the BL thickness is relatively large compared to the body's size, represented by its maximum radius  $r_{max}$ . However, near the leading edge of the body, this assumption does not hold. Instead, the BL is thin, and the pressure gradient inside the BL is negligibly small. Thus, it should be assumed that the wall static pressure  $p_w$  equals the BL edge static pressure  $p_e$ . For the pressure force calculation, it is therefore assumed that the BL is thin for regions where  $\delta \leq 0.1r_{max}$  with  $C_p = C_{p,e}$ . For regions with  $\delta > 0.1r_{max}$ ,  $C_p = C_{p,w}$  is calculated with Equation 5.47, which is valid for thick BLs. As the surface pressure calculation is uncoupled from the calculation of the BL characteristics in the IBL method, this does not affect the IBL solution and the parameters that are provided to the FVM at the interface. The difference in fuselage pressure force in drag direction is, thus, reduced from 381% to 22% (see also Table 5.5).

In summary, the implemented IBL method predicts the characteristics of the BL on a streamlined body with sufficient accuracy and low computational costs. Thus, it is a suitable method for calculating the BL of a fuselage with BLI in the front part of the fuselage, where it is not affected by the FF propulsor.

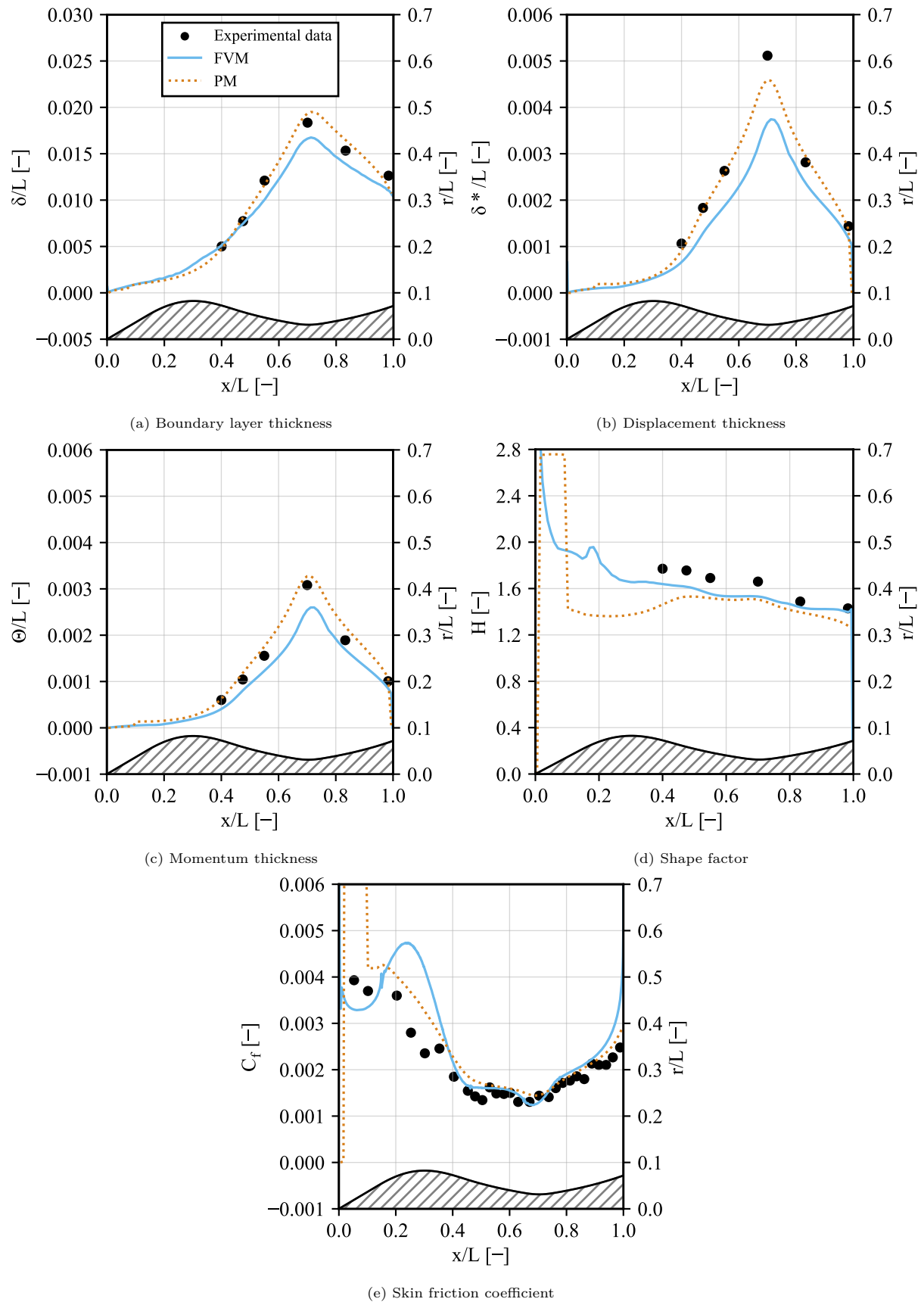


Figure 5.8: BL characteristics for the *Waisted Body* at  $Ma=0.6$  (see also Appendix A.3). Comparison of the numerical PM results to experimental data by [215] and numerical FV results ( $k-\omega$ -SST, fully resolved BL, see Section 5.6.2).

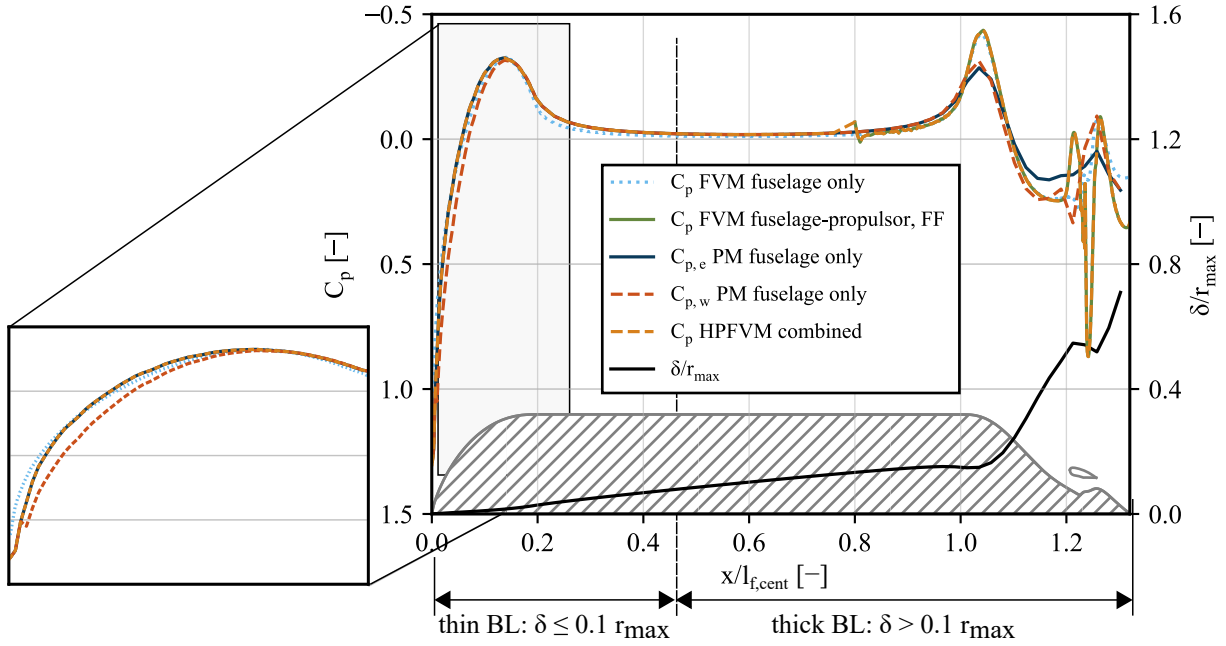


Figure 5.9: BL edge and wall pressure coefficient of the reference geometry obtained by FVM, PM, and HPFVM.

## 5.5 Interface

The location of the PM/FVM interface is determined from qualitative considerations and results of FVM pre-studies. The interface between the panel and FV domain is split into an inviscid and a viscous part, separated at the BL edge by  $\delta$ . The PM described in Section 5.4 is used to calculate the potential flow and the BL characteristics of the isolated fuselage.

### 5.5.1 Interface Location

It has to be ensured that the transfer of flow characteristics from PM results to the inlet of the FV domain does not alter the solution of the FV calculation. The interface must be located at a position that ensures that...

1. The influence of the nacelle on the flow field is part of the FV calculation. As the interaction of nacelle and fuselage BL cannot be adequately modeled by the PM (see Section 5.4), the interface has to be located at least upstream of the nacelle leading edge.
2. The occurrence of shocks on the geometry is simulated by the FVM because the PM implementation cannot capture shocks accurately (Section 5.4.2.4). Shocks might occur for non-optimal geometries, e.g., on the nacelle cowling or the fuselage aft curvature.
3. The occurrence of separation regions on the geometry is simulated by the FVM. Even though the PM can detect laminar and turbulent separation, its influence on the flow cannot be modeled accurately (Section 5.4.2.4). Separation might occur inside the FF duct or at the fuselage tail.
4. The influence of the FF on the flow field, but especially on the wall shear stress and pressure distribution on the fuselage, is negligible, because the PM does not model this influence.

- The upstream impact of the nacelle on the fuselage pressure and shear stress distribution can be neglected.

Figure 5.10 visualizes the stated considerations.

An FVM pre-study determines an adequate location for the PM/FVM interface. Figure 5.12 shows the  $C_p$  and  $C_f$  distribution on the reference fuselage-propulsor geometry. Three cases are calculated: the fuselage without nacelle and without FF, the fuselage-nacelle geometry without the effect of the FF, and the full fuselage-propulsor geometry with FF ( $FPR = 1.4$ ). The difference between local pressure and skin friction is evaluated, and the threshold is identified where the difference is smaller than 2%. The influence of both nacelle and FF on the wall shear stress extends further upstream than the surface pressure. Nacelle and FF impact local flow characteristics only downstream of the constant radius center section of the fuselage.

Similar behavior is observed for a variation of fuselage length and center section radius geometries and an artificial  $FPR$  variation by alteration of the  $\Omega_{rot}$ . Figure A.1 in Appendix A.4 shows the pressure and skin friction difference between a fuselage-propulsor with FF and bare fuselage for different  $FPR$ . The 2% threshold for pressure and wall shear stress is reached for all configurations downstream of the constant radius center section of the fuselage.

However, for non-optimal geometries with a steep curvature between the constant radius section and the inlet of the FF, shocks can occur at the beginning of the curvature, which impacts the flow field incident to the FF significantly. Thus, it is decided to locate the interface upstream of the start of the curvature. Velocity and temperature BL profiles (see also Section 5.5.3) are estimated by the PM and calculated by the FVM and compared for different locations at the fuselage center section. Exemplary results for the reference geometry in Figure 5.11 and Figure A.2 (Appendix A.4) show that the relative error at locations  $< 80\%l_{f,cent}$  is smaller than 4% and smaller than  $\pm 1\%$  for the velocity and temperature profile, respectively. Based on these results, the interface location is defined as  $80\%l_{f,cent}$ .

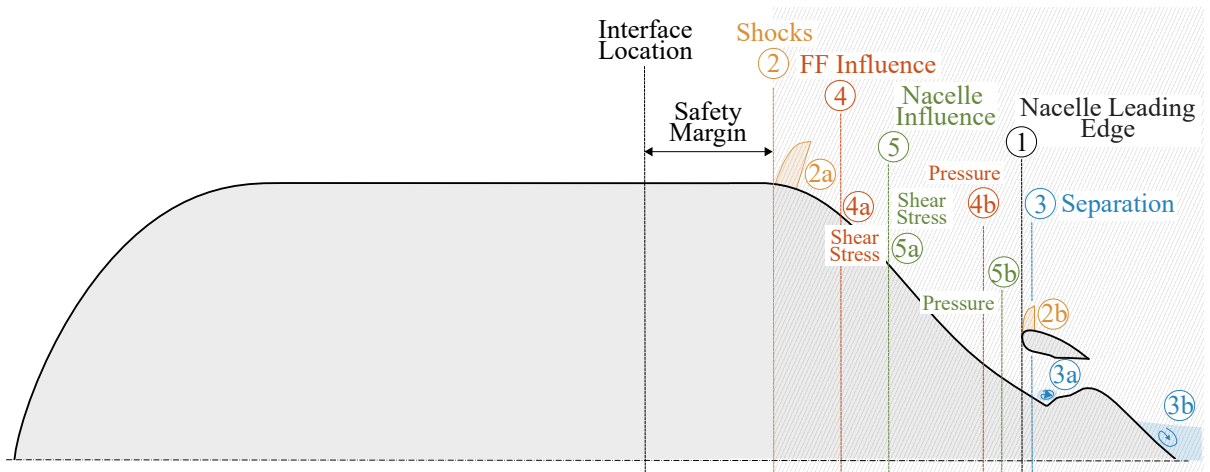


Figure 5.10: Interface location considerations.

## 5.5.2 Potential Flow Interface

In the inviscid part, the potential flow solution of the PM is imposed on the FV domain at the interface. The source strengths  $\sigma_i$ , determined for each singularity, are employed to calculate the velocity potential at the coordinates of the FV domain inlet above the BL edge. The resulting incompressible velocity

components  $V_r$  and  $V_z$  are corrected for compressibility effects with the Karman-Tsien compressibility correction.

### 5.5.3 Boundary Layer Interface

For the viscous part, the 0D results of the IBL calculation must be transformed into 2D flow characteristics before they can be imposed on the FV domain. At the interface, the BL is fully turbulent. Turbulent BLs can be divided into an inner (law of the wall) and an outer (law of the wake) region. Inside the inner region, the flow is dominated by viscous effects. Three regions characterize the mean velocity profile inside the inner region with increasing distance from the surface: the viscous sublayer, in which the velocity profile is nearly linear; a buffer layer in which the velocity profile blends from the linear sublayer to the logarithmic region and a log-law layer in which turbulence dominates, but the flow is not yet fully turbulent. Here, the mean velocity profile can be characterized by a logarithmic law of the wall [12]. Figure 5.13 sketches the turbulent BL regions.

A number of expressions exist that describe the different regions of the turbulent BL.

In the viscous sublayer ( $0 \leq y^+ \leq 5$ ) the mean velocity profile is assumed to be nearly linear and can be described by [10, 12]:

$$u^+ = y^+ \quad (5.52)$$

$u^+$  is the dimensionless wall velocity and  $y^+$  is the dimensionless wall distance. The logarithmic overlap law is valid for the overlap region of the inner region, which was empirically estimated to extend between  $y = 30\nu/u_\tau$  and  $y = 0.2\delta$  [10, 247]:

$$u^+ = \frac{1}{\kappa} \ln(y^+) + C^+ \quad (5.53)$$

The power law velocity profile can additionally describe the overlap region. Its exponent  $n$  can be determined from the local planar shape factor  $H_{pl}$  [225]:

$$u = u_e \left( \frac{y}{\delta} \right)^{\frac{1}{n}} = u_e \left( \frac{y}{\delta} \right)^{\frac{H_{pl}-1}{2}} \quad (5.54)$$

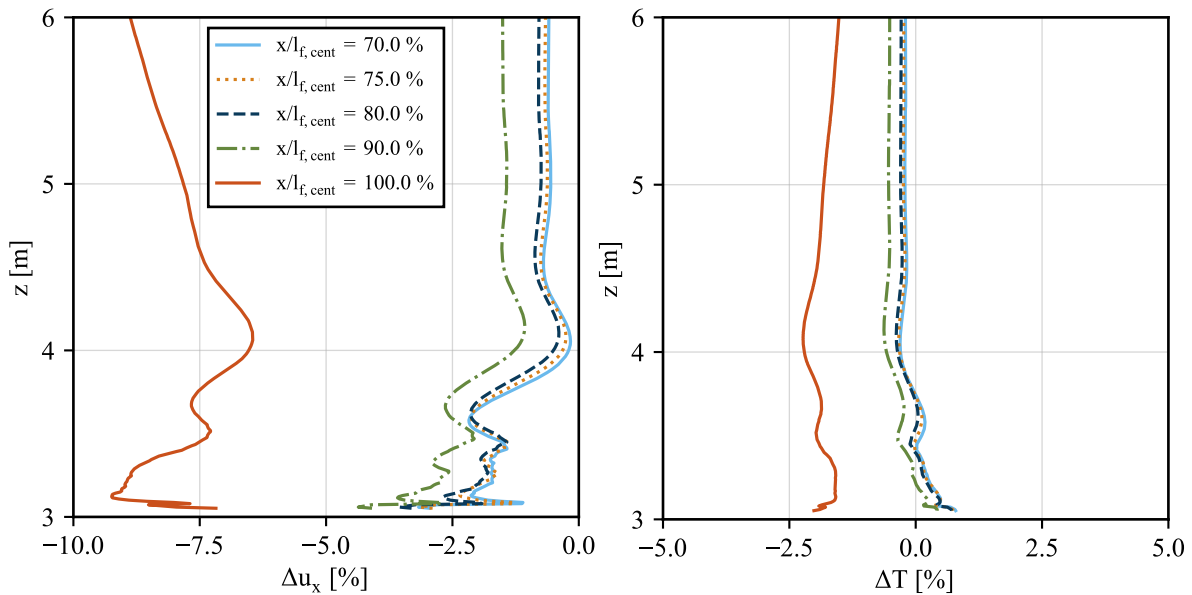


Figure 5.11: Velocity and temperature profile difference between PM and FVM results at different fuselage locations for the reference geometry.

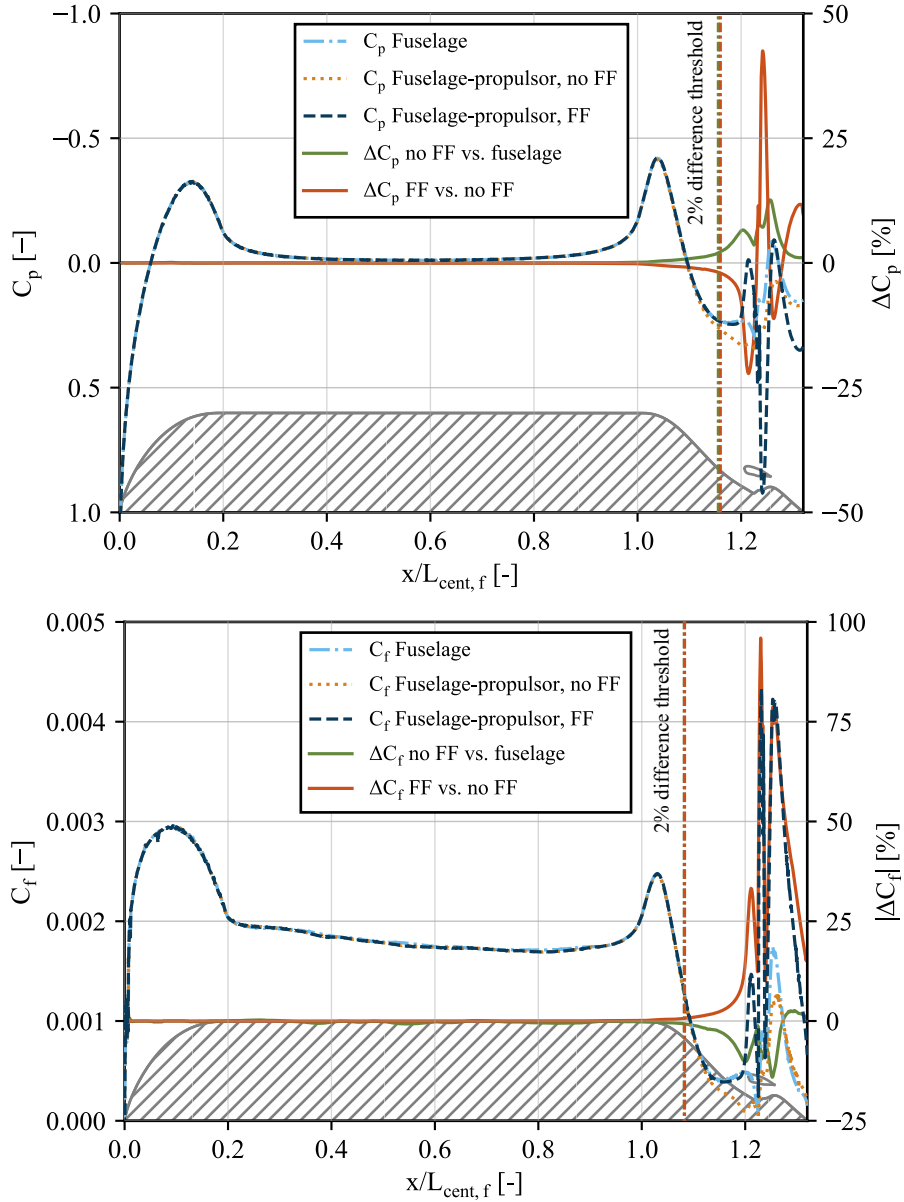


Figure 5.12: Skin friction and pressure coefficient distribution of the reference geometry for the identification of an adequate PM/FVM interface location.

Several approaches exist that aim to unify the individual sublayers' description in the turbulent BL's inner region to one unified law of the wall.

As such, Spalding's law of the wall describes the relationship between  $y^+$  and  $u^+$  in the entire law-of-the-wall region of the BL ( $0 \leq y^+ < 350$ ) [248]:

$$y^+ = u^+ + e^{-\kappa C^+} \left( e^{-\kappa u^+} - 1 - \kappa u^+ - \frac{(\kappa u^+)^2}{2} - \frac{(\kappa u^+)^3}{6} \right) \quad (5.55)$$

$\kappa = 0.40$  is the von Karman constant, the coefficient  $C^+$  is 5.1 for smooth walls [10].

Equation 5.55 is numerically solved for  $u^+$  and the velocity distribution can be determined from

$$u(y) = \frac{u^+(y)}{u_\tau} \quad (5.56)$$

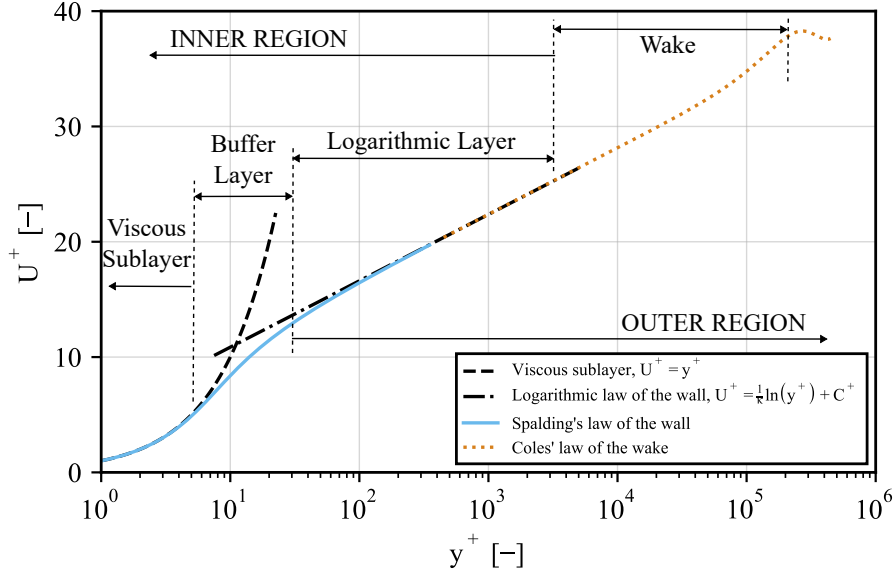


Figure 5.13: Exemplary velocity profile of a turbulent BL. Approximation with Spalding's law of the wall and Coles' law of the wake with  $\kappa = 0.40$  and  $C^+ = 5.1$ . Adapted from [10, 12].

Friction velocity  $u_\tau$ , is derived from the IBL characteristics  $C_f$  and  $u_e$ :

$$u_\tau = u_e \sqrt{\frac{C_f}{2}} \quad (5.57)$$

Coles' "law of the wake" further predicts the mean velocity distribution in the inner and outer region of the BL for flows with and without pressure gradient [249]:

$$u^+ = \Phi_1(y^+) + \frac{\Pi}{\kappa} W\left(\frac{y}{\delta}\right) \quad (5.58)$$

$W\left(\frac{y}{\delta}\right)$  is the law of the wake, which was fit by [250] to the following expression:

$$W\left(\frac{y}{\delta}\right) = 2 \sin^2\left(\frac{\pi y}{2\delta}\right) \quad (5.59)$$

The logarithmic law of the wall function given in Equation 5.53 can be used to calculate  $\Phi_1(y^+)$ , if the viscous sublayer and buffer layer are excluded from the calculation, i.e.  $y^+ \leq 30$  [11]. Functions, which employ Equation 5.53 are denoted LWLOG in the following figures. To include the lower layers of the BL, the Spalding law of the wall Equation 5.55 can be employed for  $\Phi_1(y^+)$  instead (LWSPAL).

The wake parameter or wake strength  $\Pi$  can be calculated in different ways. For instance, the Clauser pressure gradient parameter  $\beta$  can be used to calculate  $\Pi$  as proposed by White [251] (denoted by WPCL):

$$\beta = \frac{\delta^*}{\tau_w} \frac{dp_e}{dx} = 0.42\Pi^2 + 0.76\Pi - 0.4 \quad (5.60)$$

Else,  $\Pi$  can be determined from the difference between the law of the wall and the actual velocity at the BL edge [12]. Therefore, Equation 5.58 is evaluated at the BL edge with  $W(1) = 2$  and solved for  $\Pi$  using the characteristics at the BL edge calculated with the IBL method (WPE) [11]:

$$\frac{u_e}{u_\tau} = \frac{1}{\kappa} \ln \delta^+ + C^+ + \frac{2\Pi}{\kappa} \quad (5.61)$$

Instead of employing Spalding's law of the wall, Coles' equation can be extended to include the region  $0 \leq y^+ \leq 30$  in the following manner proposed by Thompson [11, 252]:

$$u^+ = \begin{cases} y^+, & y^+ \leq 4 \\ 1.0828 - 0.414 \ln y^+ + 2.2661 (\ln y^+)^2 - 0.324 (\ln y^+)^3, & 4 < y^+ < 30 \\ \text{Equation 5.58}, & y^+ \geq 30 \end{cases} \quad (5.62)$$

As Equation 5.58 leads to a non-zero  $\delta u/\delta y$  at the edge of the BL, Granville [253] modified Coles' law:

$$u^+ = \Phi_1(y^+) + \frac{1}{\kappa} \left[ \Pi \left( 1 - \cos \left( \pi \frac{y}{\delta} \right) \right) + \left( \left( \frac{y}{\delta} \right)^2 - \left( \frac{y}{\delta} \right)^3 \right) \right] \quad (5.63)$$

For Granville's equation, the following function is solved at the BL edge [11]:

$$\frac{\delta^*}{\delta} = \frac{u_\tau}{\kappa u_e} \left( \frac{11}{12} + \Pi \right) \quad (5.64)$$

An accurate prediction of the mean velocity distribution in the turbulent BL is crucial for the analysis of BLI. Thus, the most suitable model for predicting the interface's velocity profile must be determined. Results from the IBL validation on the *Waisted Body* are compared against experimental data from [215] as well as results from the FVM validation (see also Sections 5.4.3 and 5.6.2).

Velocity profiles are generated from the 0D IBL data at specified locations along the body using the abovementioned models. All results are presented in Figures A.3 and A.4.

As is evident from Figure A.3, the power law and Spalding's law of the wall hold only for their relevant sublayers and cannot be employed for describing the whole BL.

If the logarithmic overlap law is employed as the law of the wall in the inner region (e.g., Granville-LWLOG/WPE, Coles-LWLOG/WPCL), the velocity profile of the viscous sublayer is not represented correctly (see Figure A.3).

Usage of the Clauser pressure gradient parameter for calculation of  $\Pi$  leads to a deviation of the BL edge velocity to the edge velocity calculated by the IBL, especially for regions with a favorable pressure gradient ( $x/L \leq 0.55$ , Figure A.4).

Based on this first evaluation, the most suitable models are selected and compared against the experimental results (Figure 5.14).

For the upper part of the BL, the difference in  $u/u_e$  between experimental and numerical IBL results is smaller than 5% for all velocity profile modeling methods. The biggest discrepancy exists for the inner region. However, accurately measuring the velocity profile close to a surface is difficult and, thus, experimental measuring errors cannot be ruled out. Furthermore, the average error of the IBL profiles is smaller than the FV results (k- $\omega$ -SST, fully resolved BL) for all locations, where the velocity profile is measured.

Even though the velocity profile prediction methods based on IBL results perform slightly differently for different pressure gradients, they perform similarly well on average. Thus, to ensure a zero pressure gradient at the BL edge and to ensure a smooth transition between all sublayers, the Granville function (Equation 5.63) in combination with Spalding's law of the wall (Equation 5.55) is selected for the following study.  $\Pi$  is calculated using the edge condition provided in Equation 5.64.

Further, a temperature profile is calculated at the interface. McLean provides the following formula for the temperature profile of laminar and turbulent flows and adiabatic walls [12].

$$\frac{T}{T_e} = 1 + \frac{\gamma - 1}{2} r M a_e^2 \left( 1 - \frac{u^2}{u_e^2} \right) \quad (5.65)$$

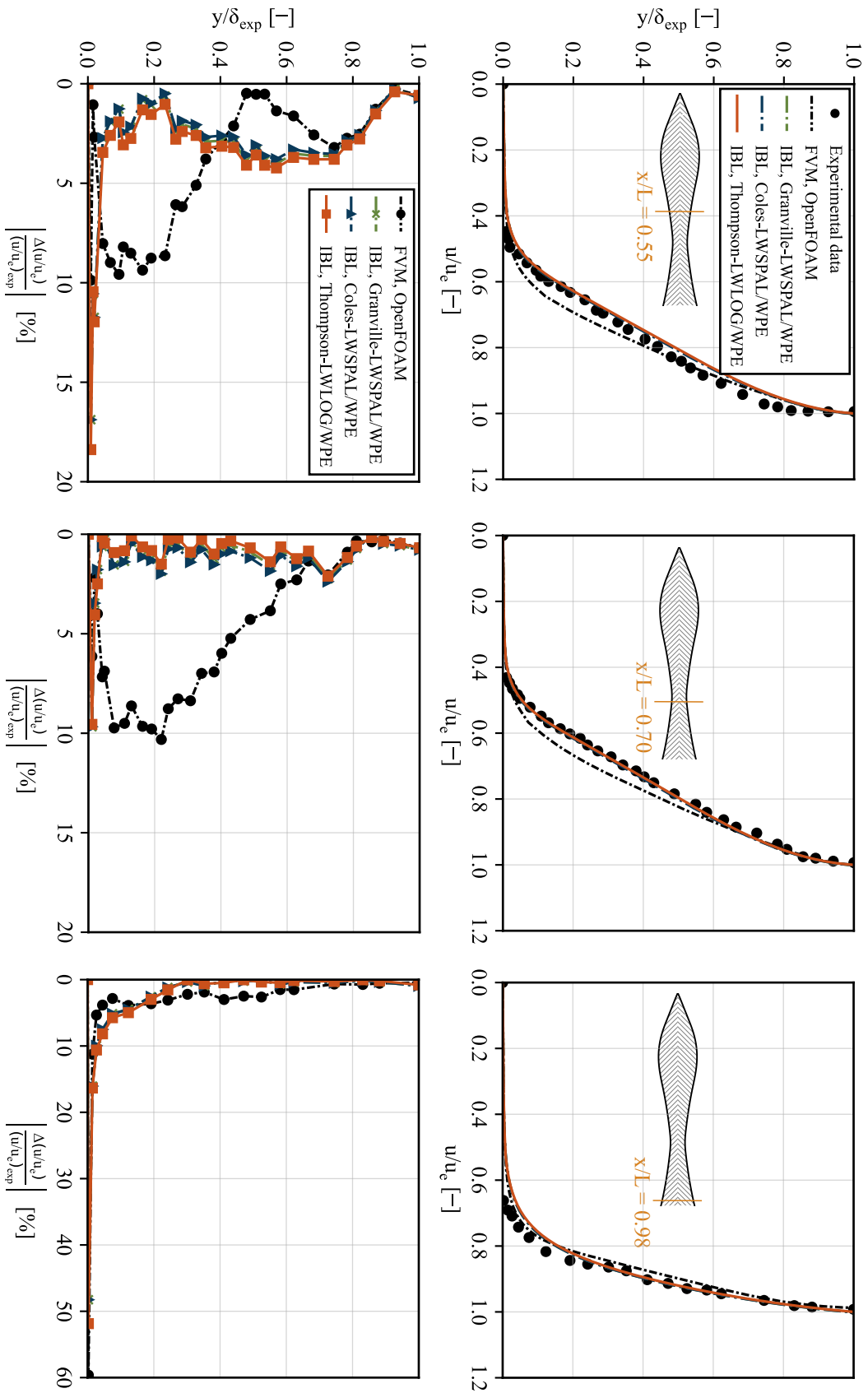


Figure 5.14: Validation of velocity profile prediction for IBL method. Compared against experimental data for *Waisted Body* by [215]. Velocity profile (top). Relative error compared to experimental data (bottom).

Here,  $r$  is the adiabatic recovery factor, which is calculated from the Prandtl number  $Pr$  for turbulent air flows as follows:

$$r \approx Pr^{1/3} \approx 0.89 \quad (5.66)$$

The BL edge temperature is approximated to be equal to the freestream temperature. Additionally, the static pressure is assumed to be constant inside the BL for the temperature profile prediction.

#### 5.5.4 Verification

To verify the PM/FVM interfacing strategy, velocity and temperature profiles at different locations along the powered reference fuselage-propulsor downstream of the interface are compared for full FVM and HPFVM simulation results in Figures 5.15 and A.2. For the HPFVM, a laminar BL is present near the fuselage leading edge, whereas the FVM solution is fully turbulent. Thus, a difference in velocity and temperature profiles downstream of the laminar region is expected. Further, the boundary layers profiles predicted by PM and FVM differ slightly, as discussed in Section 5.5.3. Figure 5.15 (right) shows that the relative temperature agrees sufficiently well with a difference of less than  $\pm 1.5\%$  at all locations. The difference is higher near the fuselage surface and reduces to less than  $-0.5\%$  far from the wall. The PM predicts a slightly more favorable, i.e., more negative, pressure gradient at the wall of the interface location compared to the full FVM calculation (see Figure A.2). This small difference in the velocity profile, which is imposed at the interface, leads to a difference of HPFVM and FVM results exceeding  $+6$  and  $-8\%$  near the wall as depicted in Figure 5.15 (left). The biggest difference occurs at  $x/l_{f,cent} = 110\%$ , i.e., at the location where the fuselage contour contracts from the center section diameter to the FF inlet and the BL disperses. Inside the FF duct at stations 1 (highlight) and 2 (rotor inlet), the difference is less than  $-5\%$ . Far from the wall, the deviation is smaller than  $-1\%$ . In addition, Figure A.2 (right) shows that the temperature and velocity distribution trend is in good agreement for FVM and HPFVM results further downstream of the interface. In conclusion, employing a different prediction methods in the front part of the fuselage and imposing the solution of the PM onto the FVM at  $x/l_{f,cent} = 80\%$  leads to acceptable differences in the velocity and temperature profiles incident to the FF. A subsequent comparison of integrated FF results confirms this conclusion (see Section 5.7).

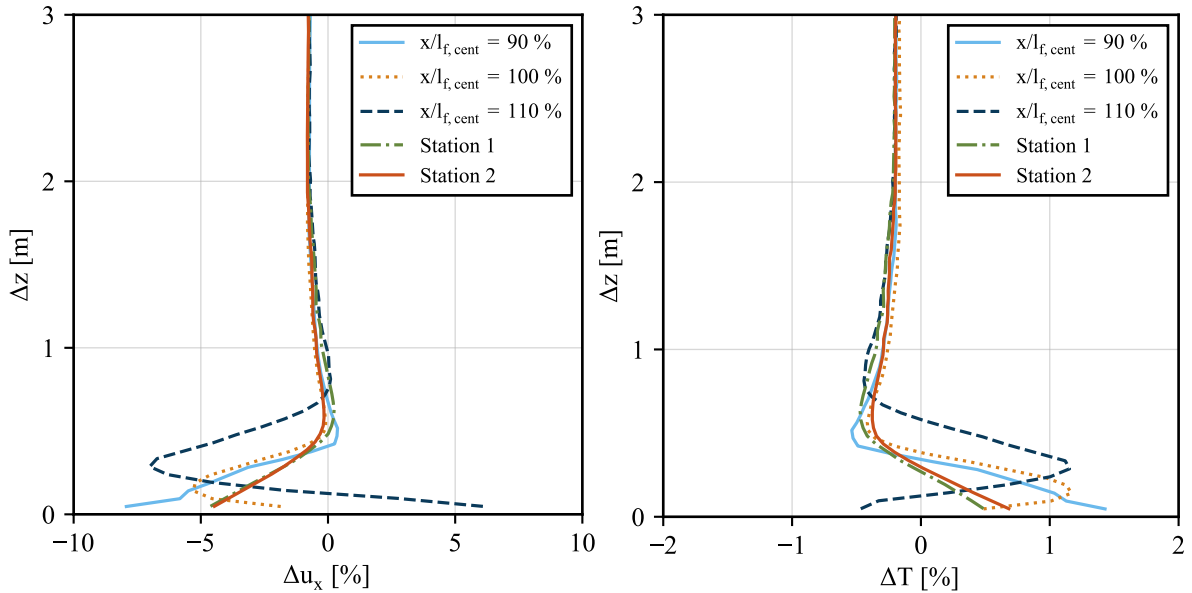


Figure 5.15: Velocity and temperature profile difference between FVM and HPFVM results at different fuselage and duct locations for the reference geometry.  $\delta z = z - z_w$ .

Figure 5.9 and 5.16 visualize the pressure and skin friction distribution along the isolated fuselage geometry obtained by FVM and PM. Further, results for the FVM part of the HPFVM method and the combination are visualized. Due to the boundary conditions applied at the FV domain interface, skin friction and pressure distribution vary from the expected result directly behind the interface. The relative error is negligible for the pressure distribution and small for skin friction. However, the latter affects the calculation of the body's forces minorly. Therefore, for the calculation of the viscous fuselage force, the skin friction coefficient obtained by the PM is employed beyond the interface until up to  $95\%l_{f,cent}$  as depicted in Figure 5.16.

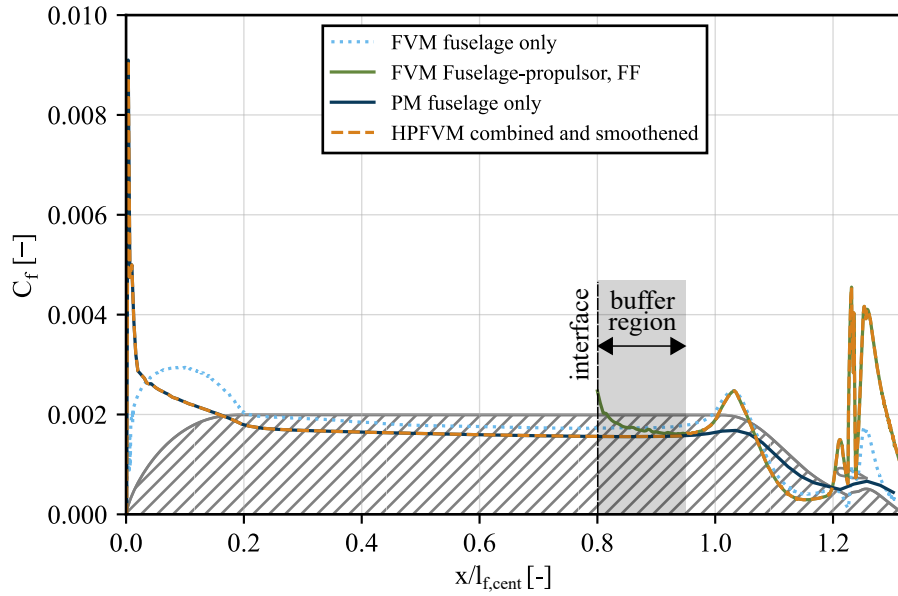


Figure 5.16: Skin friction coefficient of the reference geometry obtained by FVM, PM, and HPFVM.

## 5.6 Finite Volume Reynolds-Averaged Navier-Stokes Method

The High Speed Aerodynamic Solver (*HiSA*) of the CFD framework *OpenFOAM-v2206* (Open Field Operation and Manipulation) is employed to simulate the flow around the rear part of the fuselage including the FF. *OpenFOAM* is a free and open-source CFD software package, written primarily in the programming language *C++* and based on FVM. It provides a flexible and modular framework for solving a wide range of fluid flow problems, from laminar and turbulent flows to multiphase and reacting flows. Fluid flows are modeled by solving the NSEs. The highly customizable framework allows users to tailor the simulation setup and solver settings to their specific needs and requirements [254].

### 5.6.1 HiSA Solver

*HiSA* is an open source *C++* library of tools, specifically developed for the solution of transonic and supersonic compressible flows within the *OpenFOAM* framework [189]. In high-speed external flows, regions of high velocity can be accompanied by local numerical discontinuities such as the formation and propagation of shock waves. To appropriately model these discontinuities, a density-based solver, such as *HiSA* is required [189]. The applicability of the solver to model the external aerodynamics of aircraft in transonic flows has been extensively validated [45, 255]. The original system of conservative governing equations for unsteady, compressible viscous flow, which are solved by the *HiSA* solver [189],

is customized to accommodate the source terms  $S_i$  on the RHS (Right Hand Side) of the equations [256], which are required for modeling the FF (see Section 5.6.3.2):

$$\begin{aligned} \frac{\partial(\rho)}{\partial t} + \frac{\partial(\rho u_i)}{\partial x_i} &= S_\rho \\ \frac{\partial(\rho u_i)}{\partial t} + \frac{\partial(\rho u_i u_j)}{\partial x_j} &= -\frac{\partial p}{\partial x_i} + \frac{\partial}{\partial x_j} \sigma_{ij} + S_{u_i} \\ \frac{\partial(\rho E)}{\partial t} + \frac{\partial(\rho E u_j)}{\partial x_j} + \frac{\partial(u_j p)}{\partial x_j} &= \frac{\partial(u_i \sigma_{ij})}{\partial x_j} + k \frac{\partial T}{\partial x_j} + S_E \end{aligned} \quad (5.67)$$

Here,  $u_i$  is the velocity in the Cartesian direction  $i$ ,  $E$  is the specific total energy,  $h_t$  is the specific total enthalpy,  $k$  is the thermal conductivity, and  $\sigma_{ij}$  are the components of the viscous stress tensor  $\sigma_{ij}$  with the Kronecker delta  $\delta_{i,j}$ :

$$\begin{aligned} \sigma_{ij} &= \mu \left( \frac{\partial u_i}{\partial x_j} + \frac{\partial u_j}{\partial x_i} - \lambda \frac{\partial u_k}{\partial x_k} \delta_{i,j} \right) \\ \lambda &= -\frac{2}{3} \mu, \end{aligned} \quad (5.68)$$

In this study, the source terms  $S_i$  are employed to account for the external forces of the fan on the fluid. They are specified in Section 5.6.3.1.

## 5.6.2 Simulation Setup

To reduce the computational effort, (quasi)-2D-axisymmetric steady simulations are carried out (Section 5.6.4). Solution of one fuselage-propulsor geometry requires approx. 200 CPU hours. For sufficient

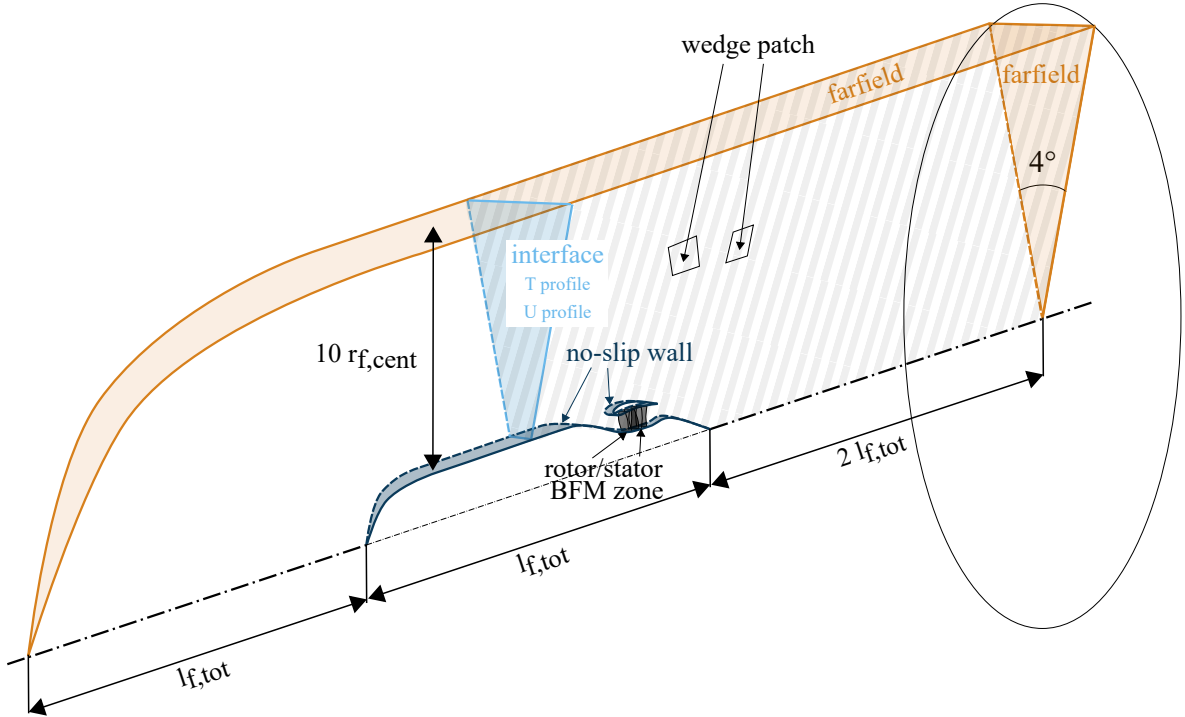


Figure 5.17: Sketch of the 2D-axisymmetric FVM domain for the reference geometry. Boundaries and corresponding boundary conditions are marked. The domain for the HPFVM is indicated in gray. Sketch not to scale.

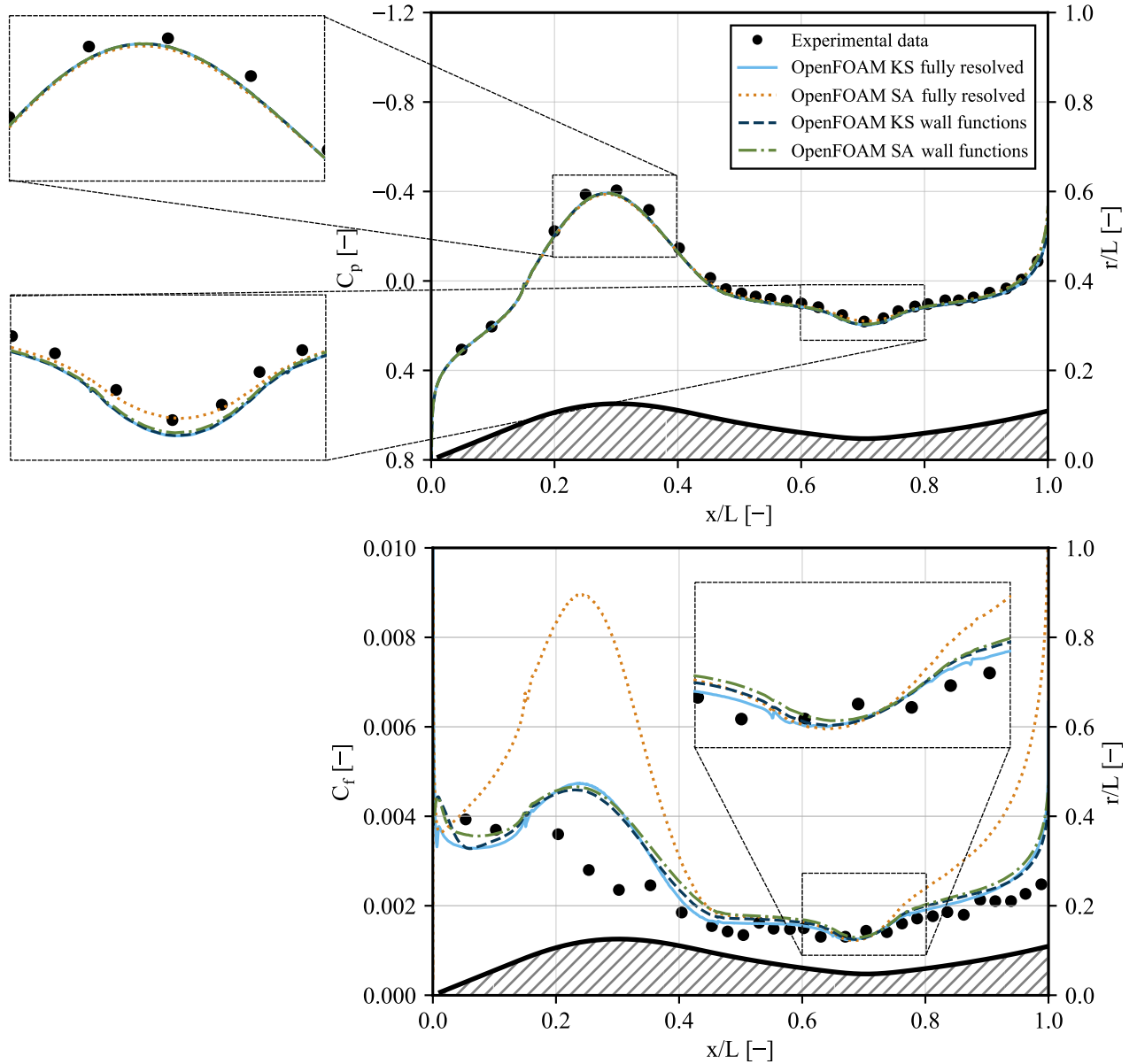


Figure 5.18: FV CFD setup validation. Distribution of pressure coefficient (top) and skin friction coefficient (bottom). Comparison of results for different turbulence models and BL resolution against experimental data of a *Waisted Body* at  $Ma_\infty = 0.597$  and  $Re_\infty = 9.98 \times 10^6$  provided in [215]. KS: k- $\omega$ -SST, SA: Spalart-Allmaras. See also Appendix A.3.

accuracy of the results, the BL is fully resolved (Section 5.6.4.2). The thermodynamic behavior of the air is assumed to follow the ideal gas law. Sutherland's Law is used to model the temperature-dependency of the viscosity.

The BCs employed for the simulation of the full fuselage-propulsor configuration and the rear part of the configuration required for the HPFVM are depicted in Figure 5.17. The customized velocity and temperature BCs at the PM/FVM interface are described in Section 5.6.5. Additionally, Section 5.6.3 gives details on the implemented fan model.

To validate the FV simulation setup, the flow around the *Waisted Body* geometry described and employed in Sections 5.4.3 and 5.5.3 is simulated for four different cases. The Spalart-Allmaras [257] and k- $\omega$ -SST [258] turbulence models are compared. Additionally, two different grid types are tested, where the

BL is fully resolved or the number of cells near the wall is reduced and wall functions are employed. A comparison of the results against experimental data from Winter et al. [215] is provided in Figure 5.18. The resulting pressure distribution matches experimental results well for both turbulence models and BL resolutions. However, the fully resolved Spalart-Allmaras results agree slightly better in the concave region of the body. The numerical simulation is fully turbulent; thus, the laminar region near the body's nose cannot be represented accurately. As a result, the skin friction coefficient is predicted wrongly in the nose region but aligns well with experimental results in the center and rear parts of the body. Here, the fully resolved  $k\text{-}\omega\text{-SST}$  case matches best with experimental results. When combined with wall functions, the Spalart-Allmaras turbulence model predicts similar friction data compared to the  $k\text{-}\omega\text{-SST}$  turbulence model. However, when combined with a fully resolved BL grid, the wall shear stress is overpredicted in regions with a convex curvature. Similar to the BFM validation study (see Section 5.6.3.4), it is found that the implementation of the Spalart-Allmaras model in *OpenFOAM* does not perform more efficiently compared to the  $k\text{-}\omega\text{-SST}$  implementation. As the Spalart-Allmaras model leads to high discrepancies in skin friction coefficient for the presented validation case, the  $k\text{-}\omega\text{-SST}$  turbulence model is employed for all fuselage-propulsor studies.

### 5.6.3 Fan Model

Reduced order models have been widely employed to efficiently model the effect of turbomachinery on the air flow streaming through the blade rows. Thollet proposed a categorization of reduced order throughflow models by dimension: 2D, 3D, 3D + wakes, and universally applicable [259]. For each dimension, several methods with differing levels of fidelity are applicable. 3D TFMs for example can be clustered into the following categories: Explicit, physics-based BFMs; interpolation-based models; semi-explicit models; and implicit approaches based on deviation and loss correlations. A detailed description of historic and state-of-the-art models, their advantages, and disadvantages is presented in [259].

#### 5.6.3.1 Body Force Model

The Hall-Thollet BFM, employed in the current study, falls in the category of physics-based models. These approaches are based on deriving a physics-based model for the blade forces, resulting in the computation of deviation and losses. They compute blade forces locally, relying on the local blade geometry and local flow conditions. Thus, they inherently capture the effect of inlet distortion, which is advantageous for the numerical study of configurations with BLI [259, 260]. Further, BFMs ensure a strong coupling between the aerodynamic and BLI propulsion system model (see also Section 2.2.3).

BFMs employ the source terms of the governing equations to introduce local force and work generated by the rotor and stator blades. An axisymmetric volume that covers the meridional span of the blades to represent the blading geometry is utilized. The method derives its name from the fact that the external force is treated as a body force acting on the entire volume of each element. This volume contains distributions of momentum and energy source terms that produce flow turning, pressure rise, and temperature rise, similar to those produced by the actual blading geometry. The absence of blades enables using a coarser computational mesh compared to fully resolving the blading geometry. Unsteady effects are disregarded due to the low reduced frequency of the BLI distortions being examined [260]. Additionally, no mixing plane is required to distinguish between rotating and stator blade rows, which further decreases computational costs [261]. Even though, the model requires knowledge on the geometric shape of the rotor and stator blades (specifically camber and blockage), it can be easily used in a conceptual design phase as it does not require calibration for design conditions.

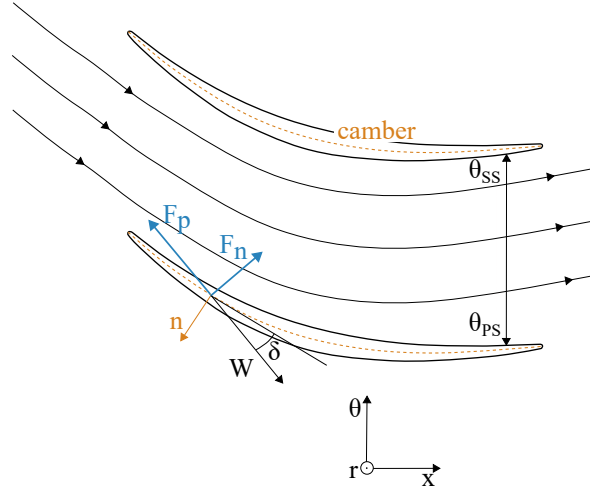


Figure 5.19: Exemplary *NASA R4* rotor cross section. Derivation of blockage parameter, normal and parallel force decomposition. Adapted from [259].

BFM s represent the effect of turbomachinery in non-uniform inflow conditions at an adequate accuracy, yet comparably small computational costs [259, 260, 262]. Thus, they are capable of modeling the FF in the current study.

Several BFM s exist, which have different ranges of applications. The Hall-Thollet model is suitable for the present study because it captures the aero-propulsive interaction of BLI configurations, accounts for compressibility effects and flow path blockage due to the presence of the blades (*metal blockage*), and does not require calibration based on blade computations. In addition, it is robust and can be integrated into an existing CFD solver [259].

The original inviscid and incompressible BFM by Hall was constrained to modeling flow turning only and did not include terms for loss generation or flow obstruction resulting from the thickness of the blades [260].

Thollet extended Hall's model by adding metal blockage terms and compressibility effects. The blade force was decomposed into a force parallel to the relative flow  $F_p$ , which generates the losses, and a force normal to the relative flow field  $F_n$ , which accounts for the turning of the flow [263] (see Figure 5.19).

The normal force  $F_n$  expression by Thollet accounts for compressibility and blockage effects [259]:

$$F_n = K_{Mach} 0.5 W^2 2\pi \delta \frac{1}{sb|n_\Theta|}$$

$$K_{Mach} = \begin{cases} \min\left(\frac{1}{\sqrt{1-Ma_r^2}}, 3\right), & \text{if } Ma_r < 1 \\ 3, & Ma_r = 1 \\ \min\left(\frac{4}{2\pi\sqrt{1-Ma_r^2}}, 3\right), & \text{if } Ma_r > 1 \end{cases} \quad (5.69)$$

$K_{Mach}$  is a compressibility coefficient based on the Prandtl-Glauert compressibility correction for subsonic flows and the Ackeret formula for supersonic flows,  $W$  is the local relative velocity magnitude,  $Ma_r$  is the relative local Mach number,  $\delta$  is the local deviation angle,  $s$  is the local blade pitch, and  $\mathbf{n}$  is the vector locally normal to the camber surface with components  $\mathbf{n} = (n_x, n_r, n_\Theta)$ . As depicted in Figure 5.19, the geometric blockage factor  $b$  is defined as [259]:

$$b = \frac{\Theta_{SS} - \Theta_{PS}}{2\pi/N_{blades}} \quad (5.70)$$

Loss generation is modelled by the parallel force  $F_p$ , which was derived by Thollet as [259]

$$\begin{aligned} F_p &= \frac{0.5W^2}{sb|n_\Theta|} (2C_f + 2\pi K_{Mach}(\delta - \delta^{\eta_{max}})^2) \\ C_f &= 0.0592 Re_x^{-0.2} \\ Re_x &= \frac{\rho W x}{\mu} \end{aligned} \quad (5.71)$$

$C_f$  is the local friction coefficient,  $Re_x$  is the local chordwise Reynolds number. A reference flow deviation angle  $\delta^{\eta_{max}}$  must be provided in off-design conditions. For the BLI application, off-design conditions are not considered, and thus, the off-design term  $2\pi K_{Mach}(\delta - \delta^{\eta_{max}})^2$  is neglected.

The definition of the body forces yields the source terms of the governing equations, which were defined in Equation 5.67:

$$\begin{aligned} S_\rho &= -\frac{1}{b} \left( \rho u_i \frac{\partial b_i}{\partial x_i} \right) \\ S_{u_i} &= \rho f_j - \frac{1}{b} \left( \rho u_i \frac{\partial b_i}{\partial x_i} \right) u_j \\ S_E &= \rho \Omega r f_\Theta - \frac{1}{b} \left( \rho h_t u_i \frac{\partial b_i}{\partial x_i} \right) \end{aligned} \quad (5.72)$$

$\mathbf{f}$  is the vector of the blade forces  $f_i$ ,  $\frac{\partial b_i}{\partial x_i}$  is the blockage gradient in the Cartesian direction  $i$ ,  $r$  is the local radius, and  $\Omega$  is the rotational speed of the rotor.

The Hall-Thollet method has been successfully employed for incompressible Euler and compressible RANS CFD simulations within the CFD frameworks *elsa* [263,264], *SU2* [261,265], and *ANSYS Fluent* [133].

### 5.6.3.2 Implementation

*OpenFOAM* allows the user to not only utilize existing features but it is possible to modify them and to develop customized models. Several fan models of different levels of complexity are readily available for 2D and 3D simulations. They can be categorized in ascending order of complexity as BCs (e.g., *fan*, *fanPressure* [266] or a custom BC [45]); ST representation (e.g., AD method by [267] or BFM by [268,269]); and full 3D blade representation. The available BFMs were implemented for the incompressible, turbulent *simpleFoam* solver [268,269] and an implementation for a compressible solver is not available. Thus, the *HiSA* solver is adapted so that the STs of the governing equation system (see Equations 5.67) can be manipulated at run time through user-specified explicit finite volume options – *fvOptions* [270]. In general, *fvOptions* can add source or sink terms, impose constraints to the field variables, or apply corrections [270]. The user can customize run-time compiled scalar and vector source terms with the *codedSource* option. The implementation of Hall-Thollet’s BFM for the incompressible *simpleFoam* solver using *fvOptions* by Saini [268] is adapted and extended to the compressible *HiSA* solver. The fields required for the calculation of the body forces, blockage, and blockage gradient, and a body force field are added. All source files and an exemplary study case are provided in [190]. As explained in Section 5.6.3.1, for each iteration, the forces parallel and normal to the relative flow velocity are calculated according to Equations 5.69 and 5.71 and transformed to the  $x, r, \Theta$  coordinate system. Axisymmetric flow conditions are assumed and, thus, the radial force is neglected. However, the influence of turning on the force in the x-direction is taken into account by the approach. An ST distribution is calculated in blade chord and span direction for all rotor and stator region cells. This ensures that the radial effect of the BL incident on the fan is represented. However, due to the axisymmetric flow conditions, any circumferential distortion is not represented. For the calculation of the STs, information on the local flow field characteristics, such as  $\rho, U, T$  is directly provided by the solver. In addition, the geometric characteristics of the blades are required, which are

derived in a pre-processing step using the CAD software *FreeCAD* [271] and *Python* [191]. Figure 5.20 exemplary depicts the derivation of the blade characteristics for the *NASA SDT* fan stage validation case (see Section 5.6.3.4). From the original 3D geometry, one blade of the *NASA R4* rotor geometry is extracted. Cross-sections of the blade reveal the 2D profiles, which are used to calculate the camber normal and blockage distribution along the chord lengths at different spanwise locations. The data is saved inside the *OpenFOAM* case directories so that it can be accessed during the simulation. In the first iteration, the extracted blockage and camber normal distribution are interpolated on those cells, which form the rotor and stator grid region. As there is no adequate *C++* library available for a cubic interpolation of the scattered data on the grid, an interpolation scheme of the *Python* library *Scipy* is employed [272]. The *Python* code is accessed through the *C++* library *pybind11*, which provides a bridge between *C++* and *Python* [273].

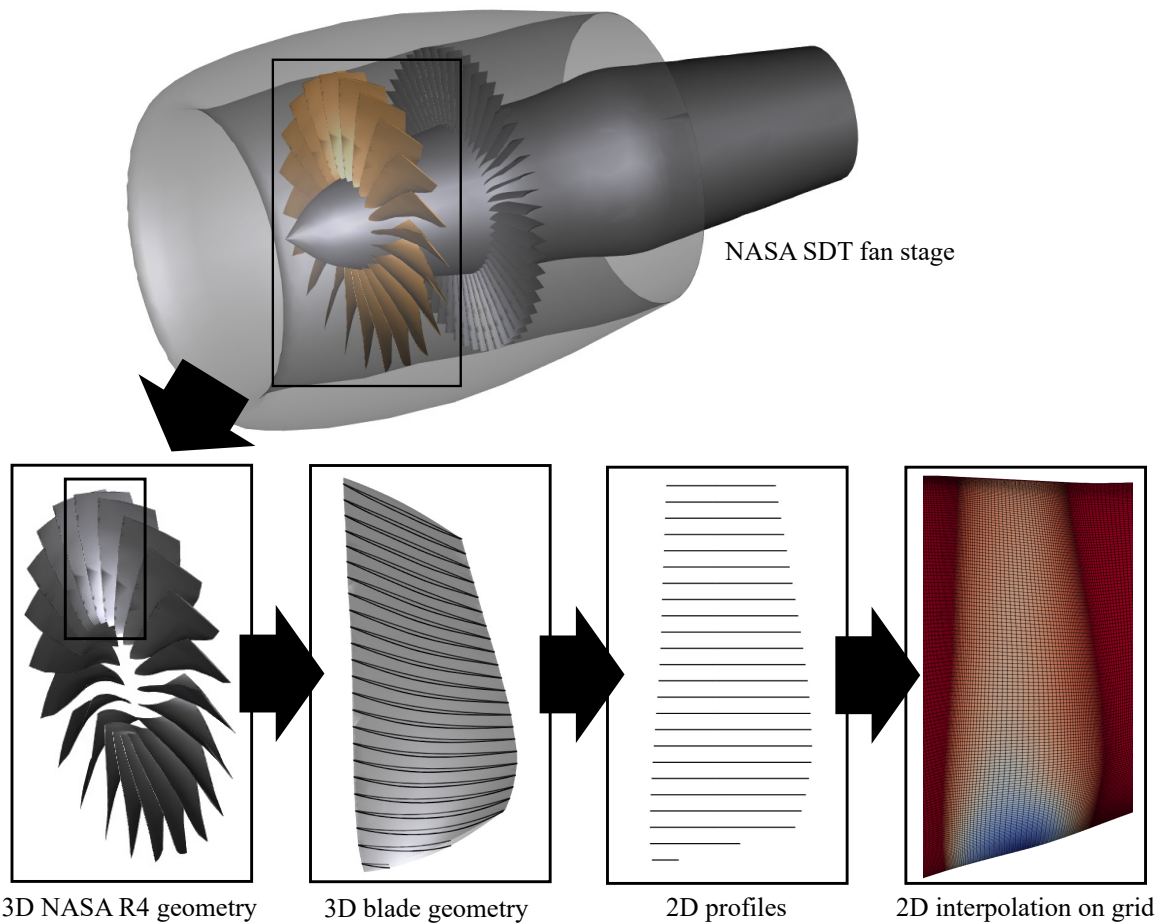


Figure 5.20: Extraction of rotor blade camber and blockage distribution and interpolation of data on the computational grid. Shown exemplary for *NASA SDT* fan stage. The *SDT* fan stage geometry was provided by *NASA Glenn Research Center*.

### 5.6.3.3 Verification

The correct implementation of the BFM is verified against a blade computation, following the approach presented by [261], where the Hall-Thollet model was implemented in the numerical solver *SU2*. The adapted *HiSA* solver is employed. The case setup including boundary and freestream conditions is provided in [190].

The two original meshes from [274] are used. Mesh 1 is a 2D-axisymmetric BFM computational domain, and Mesh 2 is a 3D stator blade computational domain as depicted in Figure 5.21.

Only the contribution of the parallel force to the STs is introduced to the governing equations to verify the parallel force implementation. The resulting area-averaged parallel force distribution along the blade chord is compared against the area-averaged parallel force and entropy gradient presented by [261]. Results are shown in Figure 5.22. The coefficient of determination  $R^2$  is  $> 0.99$  when comparing  $F_p$  against the entropy gradient.

To verify the blockage term implementation, the results of the 2D BFM computation with force and blockage terms on Mesh 1 are compared against the results of the 3D blade computation (Mesh 2). The area-averaged chord-wise  $Ma$ , mass flux  $\rho U_x$ , and normalized pressure distribution  $p_s/p_{t,inlet}$  are compared in Figure 5.23. The coefficient of determination  $R^2$  is  $> 0.99$  for all shown distributions.

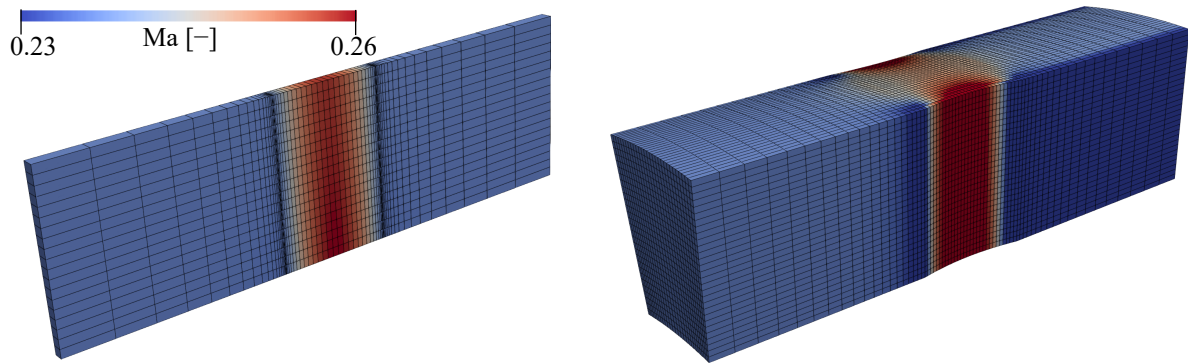


Figure 5.21: Mesh 1 (left) and Mesh 2 (right) with corresponding  $Ma$  distribution. Original grids from [274].

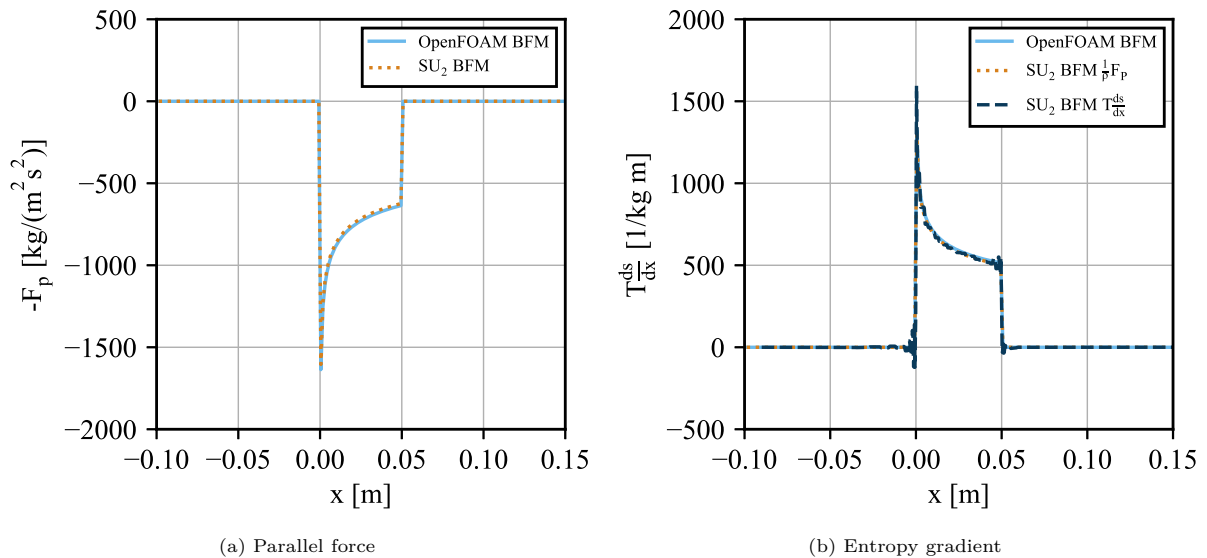


Figure 5.22: Parallel force verification.  $SU2$  results adapted from: [261, 274].

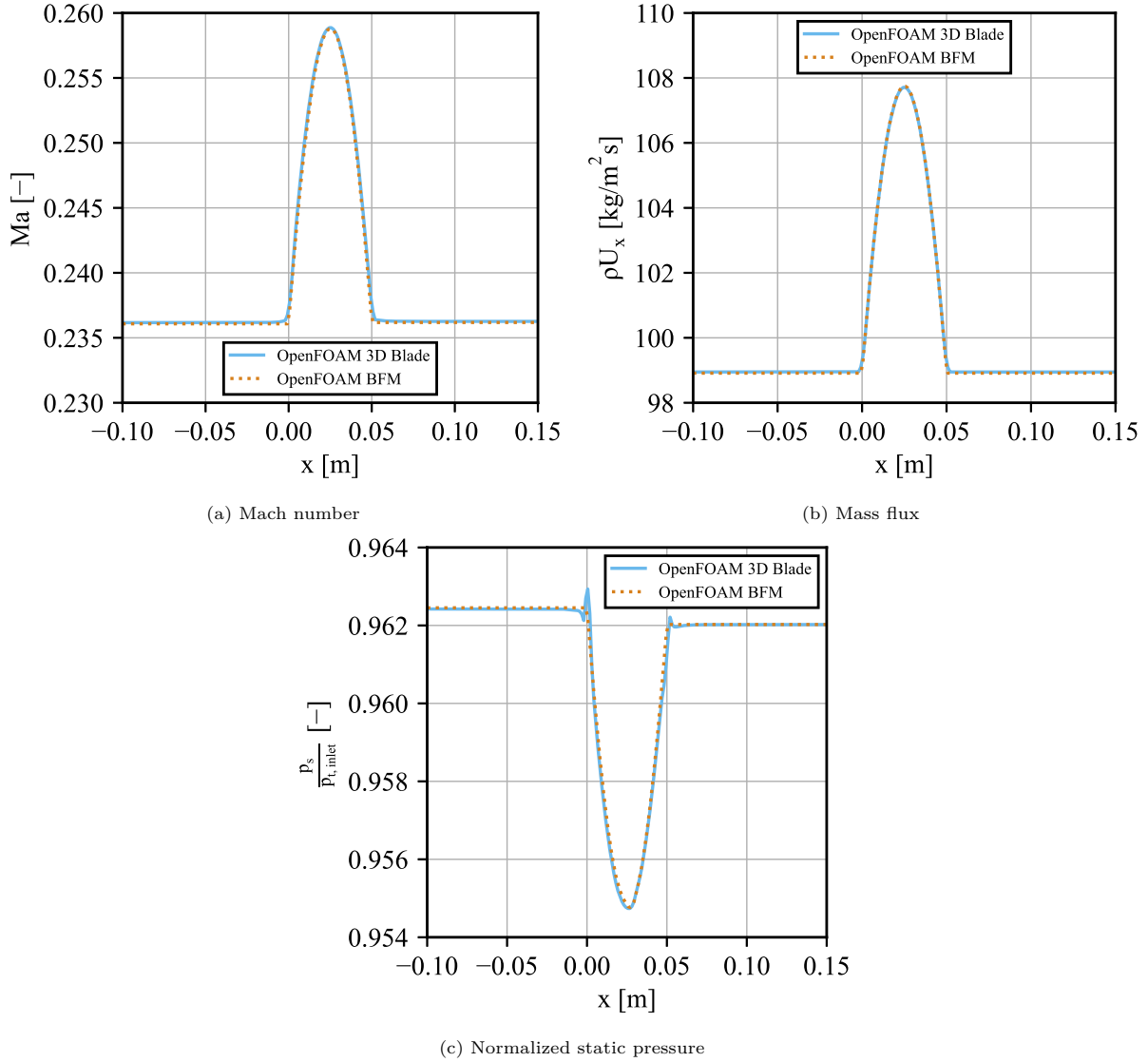


Figure 5.23: Blockage term verification. Adapted from: [261,274].

### 5.6.3.4 Validation

To validate the full BFM setup, a parameter variation study is performed for the *NASA SDT* (Source Diagnostic Test) fan stage (e.g., [275,276]). Figure 5.20 (top) visualizes the isolated single-stage ducted fan. The rotor is the *NASA R4* rotor. For the stator, the baseline OGV of the *NASA SDT* study is employed. It has a design stage pressure ratio of 1.47, similar to the BLI study. The *SDT* fan stage geometry was provided by *NASA Glenn Research Center*.

Results of a fan speed and mass-flow rate study are compared against experimental data [275,276] and computational results of a similar 2D-axisymmetric Hall-Thollet BFM implementation in *ANSYS Fluent* [133,277].

Figure 5.24 shows a side view of the wedge-shaped, 2D-axisymmetric computational domain. The single-layer wedge has an angle of  $4^\circ$  and the front and back planes feature *wedge* BCs to account for the rotational symmetry [254]. The fan stage geometry is reduced to a simulation of the duct with a stream tube inlet and a clean, i.e., undisturbed, inlet flow. The rotor has a casing/blade tip gap of 0.5mm [275].

As indicated, wind tunnel reference conditions are prescribed at the inlet of the domain [275]. Thus, fan speed and mass flow rate do not have to be corrected [275]. Sea level conditions are assumed with  $c = 340.3 \text{ m/s}$  and  $\rho = 1.225 \text{ kg/m}^3$ . Furthermore, a low turbulence intensity of 0.4% is assumed to calculate the transported values required for the turbulence models [278].

Specific mass-flows are enforced by prescribing static pressure values at the domain outlet (see Figure 5.24). The resulting mass-flow rate  $\dot{m}$  at the duct inlet is employed to calculate the flow capacity  $Q = \frac{\dot{m} \sqrt{T_{t,ref}}}{p_{t,ref} A_{ff}}$  according to [133] using the reference values provided in Table 5.2.

The mass-flow rate is varied for three different rotor rotational speeds  $\Omega/\Omega_{max} = \{50.0, 87.5, 100.0\}\%$ .

In alignment with [275], the stage pressure ratio is calculated from the area-averaged total pressure at the stator exit and the reference total pressure. Stage adiabatic efficiency  $\eta_{ad,st}$  is calculated from the same total pressure ratio and the area-averaged total temperature ratio at the rotor exit:

$$\eta_{ad,st} = \frac{\left(\frac{p_{t,stat}}{p_{t,ref}}\right)^{\frac{\gamma-1}{\gamma}} - 1}{\frac{T_{t,rot}}{T_{t,ref}} - 1} \quad (5.73)$$

Area-averaged results are calculated at the stations indicated in Figure 5.24 by extracting the flow characteristics at the same measurement stations employed by [275, 276] and integrating over the respective station area.

The swirl angle  $\alpha$  is defined by [279] as

$$\alpha = \arctan \frac{u_{\theta}}{u_x} \quad (5.74)$$

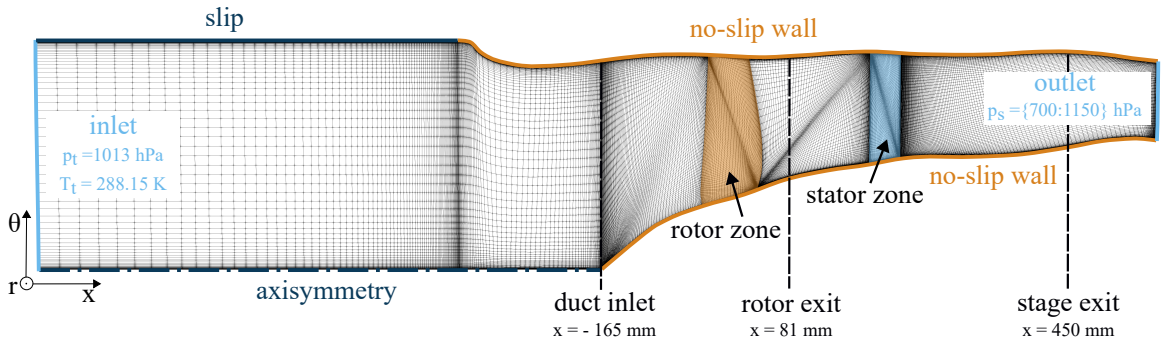


Figure 5.24: Side view of the coarse mesh with full BL resolution for *NASA SDT* fan stage validation. Boundaries and corresponding boundary conditions are indicated.

Parameter	Value
Reference temperature $T_{t,ref}$	288.15 K
Reference pressure $p_{t,ref}$	1013 hPa
Fan face area $A_{ff}$	0.223339 m <sup>2</sup>
Specific heat ratio $\gamma$	1.4
Maximum rotor rotational speed $\Omega_{max}$	12657 rpm

Table 5.2: Reference values for *NASA SDT* fan stage validation. Source: [275].

Two studies are performed. First, the BFM is employed without consideration of the off-design term  $2\pi K_{Mach}(\delta - \delta^{\eta_{max}})^2$  (see Section 5.6.3.1). Subsequently, the BFM design case is chosen for each studied  $\Omega$ , with  $\eta_{ad}$  closest to the maximum efficiency, which is reported for the experimental results by [275]. The deviation angle distribution  $\delta$  of the BFM design case is extracted and provided as the  $\delta^{\eta_{max}}$  distribution

to the relevant off-design cases. Results for both studies, with and without off-design term consideration, are presented at the end of this section.

A systematic grid convergence study is conducted to determine and report the grid discretization error. The Grid Convergence Index (GCI) approach described by Celik et al. is employed [280]. It is based on calculating the grid-independent solution ( $h \rightarrow 0$ ) by Richardson extrapolation.

The reference case for all studies is the  $\eta_{max}$  (design BFM) case for  $\Omega/\Omega_{max} = 87.5\%$  with  $p_{out} = 897\text{hPa}$ . Four different studies are conducted to explore the applicability of wall functions for  $30 < y^+ < 150$  compared against a fully resolved BL with  $y^+ < 1$  as well as a comparison of the k- $\omega$ -SST and the Spalart Allmaras turbulence model. For the *NASA SDT* fan stage, the error of the variables  $\Phi$ , mass flow rate, the area-averaged stage pressure ratio, and adiabatic efficiency are evaluated. The grid refinement factor  $r = 1.5$  is employed for all studies and grids.

Table 5.3 summarizes the results of the grid convergence studies.  $N_i$  is the total number of grid cells for each grid  $i$ . The number of cells decreases with  $i$ .  $\Phi_i$  is the solution of the variable  $\Phi$  on the  $i$ th grid.  $p$  is the apparent order of the method. For  $r = const$ ,  $\epsilon_{32} = \Phi_3 - \Phi_2$ ,  $\epsilon_{21} = \Phi_2 - \Phi_1$ , and  $r_{21} = r$  it is defined as

$$p = \frac{1}{\ln r_{21}} |\ln |\epsilon_{32}/\epsilon_{21}|| \quad (5.75)$$

The extrapolated values  $\Phi_{ext}$  for  $h \rightarrow 0$  are:

$$\begin{aligned} \Phi_{ext21} &= (r_{21}^p \Phi_1 - \Phi_2) / r_{21}^p - 1 \\ \Phi_{ext32} &= (r_{32}^p \Phi_3 - \Phi_2) / r_{32}^p - 1 \end{aligned} \quad (5.76)$$

The approximate relative error  $e_a^{21}$ , the extrapolated relative error  $e_{ext}^{21}$ , the fine-grid and medium-grid convergence index  $GCI_{fine}^{21}$  and  $GCI_{medium}^{32}$  are calculated as [280]:

$$\begin{aligned} e_a^{21} &= \left| \frac{\Phi_1 - \Phi_2}{\Phi_1} \right| \\ e_{ext}^{21} &= \left| \frac{\Phi_{ext}^{21} - \Phi_2}{\Phi_{ext}^{21}} \right| \\ GCI_{fine}^{21} &= \frac{1.25e_a^{21}}{r_{21}^p - 1} \\ GCI_{medium}^{32} &= \frac{1.25e_a^{32}}{r_{32}^p - 1} \end{aligned} \quad (5.77)$$

Figure 5.25 visualizes the data provided in Table 5.3. Here, the normalized grid spacing  $h/h_1$  relates the representative cell size  $h$  of grid  $i$  to the representative cell size of the finest grid  $h_1$ . For the 2D calculations,  $h$  is calculated from the total number of cells  $N$  and the area of the  $i$ th cell  $\Delta A_i$  as [280]

$$h = \left[ \frac{1}{N} \sum_{i=1}^N (\Delta A_i) \right]^{1/2} \quad (5.78)$$

BL resolution	$\Phi: Q [-]$				$\Phi: FPR_{st} [-]$			
	FR		WF		FR		WF	
$N_1, N_2, N_3$	100264, 45430, 20514		46288, 20216, 8679		100264, 45430, 20514		46288, 20216, 8679	
Turb. model	KS	SA	KS	SA	KS	SA	KS	SA
$\Phi_1$	0.03114	0.03114	0.03108	0.03107	1.31648	1.31654	1.31583	1.31558
$\Phi_2$	0.03112	0.03112	0.03109	0.03107	1.31540	1.31529	1.31538	1.31504
$\Phi_3$	0.03107	0.03105	0.03106	0.03103	1.31323	1.31275	1.31376	1.31343
$\Phi_{ext21}$	0.03116	0.03116	0.03108	0.03107	1.31751	1.31775	1.31601	1.31586
$p$	1.9029	2.1659	4.3258	7.0356	1.7904	1.7954	3.0473	2.6476
$e_a^{21} [\%]$	0.06	0.09	0.02	0.01	0.08	0.09	0.03	0.04
$e_{ext}^{21} [\%]$	0.12	0.15	0.02	0.01	0.16	0.19	0.05	0.06
$GCI_{medium}^{32} [\%]$	0.15	0.19	0.02	0.01	0.20	0.23	0.06	0.07
$GCI_{fine}^{21} [\%]$	0.07	0.08	0.00	0.00	0.10	0.11	0.02	0.03
$\Phi: \eta_{ad,st} [-]$								
BL resolution	fully resolved				wall function			
$N_1, N_2, N_3$	100264, 45430, 20514				46288, 20216, 8679			
Turb. model	KS	SA	KS	SA	KS	SA	KS	SA
$\Phi_1$	0.86973	0.87051	0.86492	0.86349				
$\Phi_2$	0.86749	0.86752	0.86369	0.86201				
$\Phi_3$	0.86286	0.86105	0.86043	0.85868				
$\Phi_{ext21}$	0.87184	0.87306	0.86565	0.86466				
$p$	1.8309	1.9558	2.3636	1.9645				
$e_a^{21} [\%]$	0.26	0.34	0.14	0.17				
$e_{ext}^{21} [\%]$	0.50	0.63	0.23	0.31				
$GCI_{medium}^{32} [\%]$	0.62	0.79	0.27	0.37				
$GCI_{fine}^{21} [\%]$	0.30	0.37	0.11	0.17				

Table 5.3: Results for *NASA SDT* fan stage grid discretization error study. KS: k- $\omega$ -SST, SA: Spalart-Allmaras. FR: Fully Resolved, WF: Wall Functions.

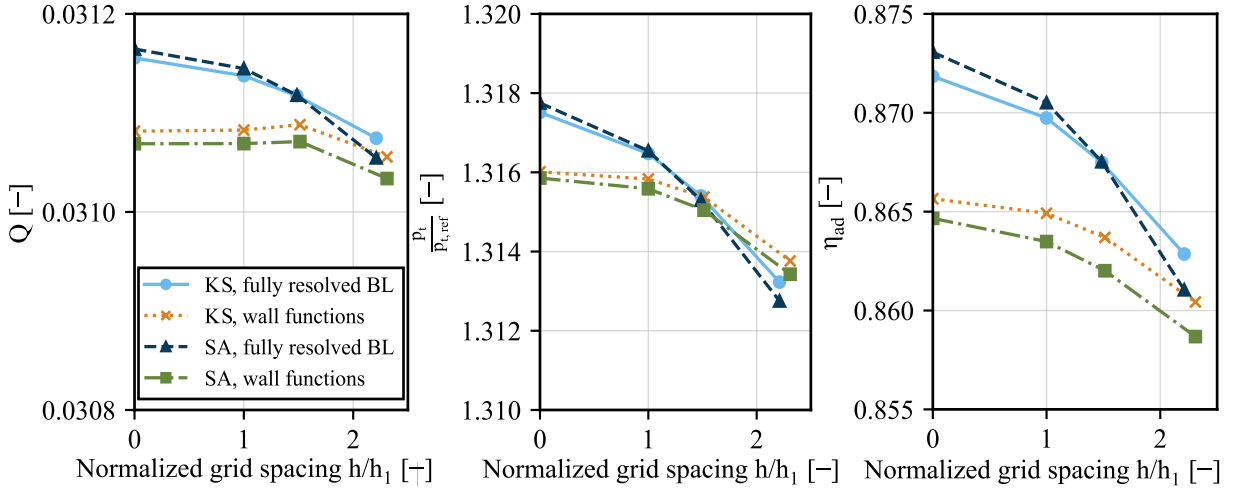


Figure 5.25: Grid convergence results for *NASA SDT* fan stage validation. BL resolution and turbulence model study. KS: k- $\omega$ -SST, SA: Spalart-Allmaras.

Figure 5.26 exemplarily depicts the  $\eta_{ad,st}$  distribution at the stator exit station for the different grids. Differences are visible, especially near the duct and hub walls. However, for all studies and all studied parameters, a  $GCI_{fine}^{21} < 0.4\%$  is achieved. Furthermore,  $GCI_{medium}^{32}$  is smaller than 0.8% for all cases (see Table 5.3). Thus, the grid discretization error is deemed sufficiently small, and grid 2 with medium cell size is employed for the subsequent validation study.

When comparing the results of the cases with a fully-resolved BL against the cases with wall functions and  $30 < y^+ < 150$ , the difference in  $\eta_{ad,st}$ ,  $Q$  and  $\frac{p_t}{p_{t,ref}}$  is similar for both turbulence models (see Table 5.3 and Figures 5.25 and 5.26). The results of the fully resolved BL are in better agreement with the experimental data by Hughes [275] and the numerical results by Matesanz-Garcia [133]. Based on this result, the validation study is further conducted on grids with a fully resolved BL.

Turbulence models provide closure for the RANS equations by approximations representing the Reynolds stresses. Several types of turbulence models exist, which are suitable for different application cases. One- and two-equation models are widely employed to predict external, transonic flow characteristics. The Spalart-Allmaras model, for example, introduces a single semi-empirical transport equation to model the eddy viscosity [257]. The  $k-\omega$ -SST turbulence model, on the other hand, is a two-equation turbulence model, which combines the  $k-\epsilon$  and  $k-\omega$  models to provide improved accuracy in predicting flow separation and complex turbulent flows. It uses two transport equations, one for turbulent kinetic energy ( $k$ ) and one for the specific dissipation rate ( $\omega$ ), and incorporates a blending function, that transitions between the  $k-\omega$  and  $k-\epsilon$  models near the wall and in the free stream, respectively [258]. One-equation models generally feature a higher computational efficiency. However, two-equation models show a higher accuracy at predicting complex flows with strong adverse gradients and separated flows [281]. The absolute results of the studied parameters (capacity, fan stage pressure ratio, and adiabatic efficiency) differ by less than 0.1% between the turbulence models (see Table 5.3). Furthermore, the distribution of parameters across the rotor exit station depicted exemplarily in Figure 5.27 shows only small differences. For the grid convergence study, the computational speed of each iteration of the cases employing the Spalart-Allmaras turbulence model is not significantly faster than the  $k-\omega$ -SST turbulence model. Additionally, the number of iterations required for convergence differs only slightly between the turbulence models ( $\sim 1\%$ ). Thus, the  $k-\omega$ -SST turbulence model is employed for the BFM validation study.

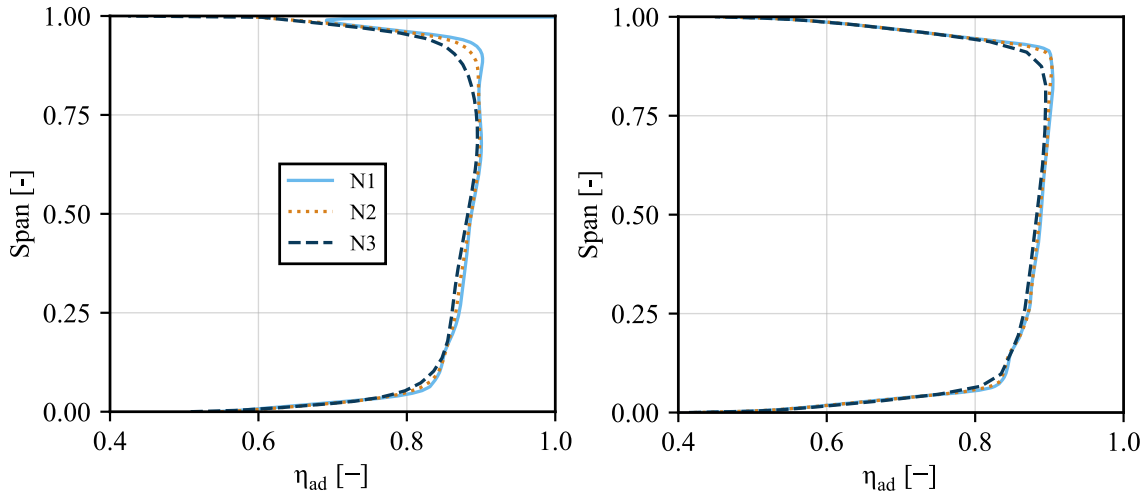


Figure 5.26: Fan stage adiabatic efficiency distribution for BFM design case ( $p_{out} = 897$  hPa,  $\Omega = 87.5\% \Omega_{max}$ ) and  $k-\omega$ -SST turbulence model for *NASA SDT* fan stage grid convergence study. Left: fully resolved BL, right: wall functions.

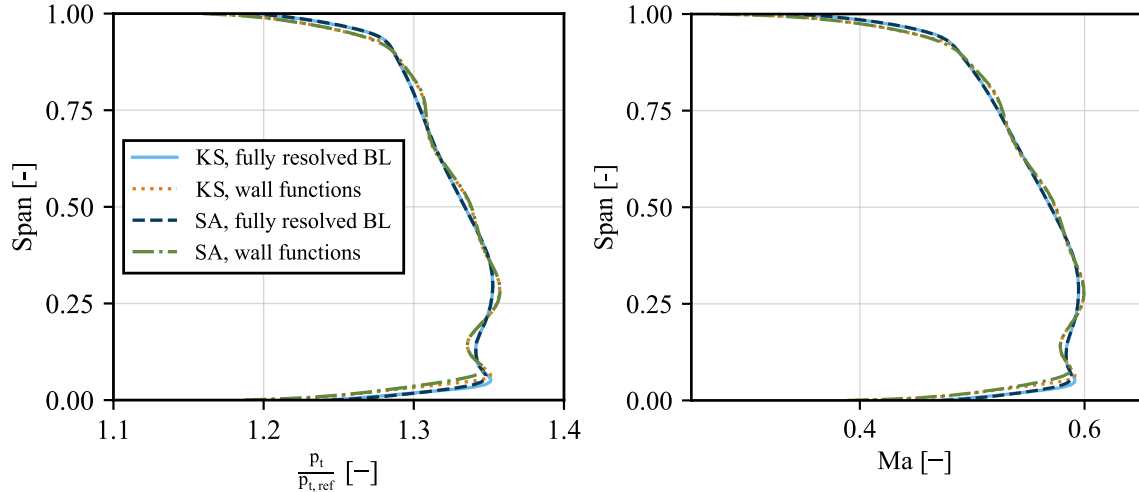


Figure 5.27: Fan stage pressure ratio (left) and Mach number distribution (right) at stator exit station for  $87.5\% \Omega_{max}$  BFM design case ( $p_{out} = 897 \text{ hPa}$ ,  $\Omega = 87.5\% \Omega_{max}$ ) for grid 1 with BL resolution and turbulence model variation for *NASA SDT* fan stage grid convergence study. KS: k- $\omega$ -SST, SA: Spalart-Allmaras.

Figure 5.28 shows an overview of the stage performance results of the *NASA SDT* fan stage validation study. For each  $\Omega$ , an initial mass-flow variation design study is performed. Here, the off-design term of the BFM is neglected. For operating points between the choke limit and the point of maximum efficiency, the trend and absolute values of  $FPR$  and  $\eta_{ad}$  compare well to the experimental results. However, the difference increases significantly when moving from the point of maximum efficiency toward the choke limit.  $\eta_{ad}$  is overpredicted for all  $\Omega$  variations. For each studied  $\Omega$ , the flow capacity for which the experimental adiabatic efficiency is maximum is chosen as the BFM design point. These points are indicated by a black contour in Figure 5.28. For the design points, the difference in  $FPR$  is smaller than 1.2% and the difference in  $\eta_{ad}$  is lower than 0.5% compared to the experimental results by Hughes [275]. The deviation angle distribution of the BFM design cases is employed to calculate the BFM off-design terms. Results of the off-design study are depicted in the same Figure. Using the off-design terms improves the accuracy of the results significantly. Between the peak maximum efficiency and the surge limit,  $\eta_{ad}$  is reduced for all studies, similar to the experimental results. Consequently, the coefficient of determination  $R^2$ , which is calculated for the *OpenFOAM* results compared against the experimental results, increases, and the Root Mean Square Error  $RMSE$  decreases for  $\Omega = 50\%$  and  $87.5\%$  (see Figure 5.28). With  $R^2 = 0.998$ , the  $FPR$  results compare well against the experimental results. However, off-design results for the adiabatic efficiency show the same trend but differ in absolute numbers. Choosing the correct BFM design point impacts the off-design results. Thus, the used approach might cause the observed errors. The operating line for maximum rotational speed visibly differs from both the experimental and computational validation data. The choke limit is reached for higher flow capacities, closer to the point of maximum efficiency. A pronounced separation region near the stator hub indicates the surge condition. The addition of the BFM off-design terms moves the surge limit even further toward the point of peak efficiency and decreases the range of operating conditions for maximum rotational speed. Consequently,  $RMSE$  and  $R^2$  deteriorate when off-design terms are considered. Figure 5.29 depicts the radial profiles of total pressure and temperature ratios, adiabatic efficiency, and swirl angle measured at the rotor exit station at the nominal operation point for  $87.5\% \Omega_{max}$ . The radial distributions compare well to the experimental results by Hughes [276]. Similarly to the computational results by Matesanz-Garcia [133], the biggest discrepancies occur in the tip region at  $> 80\%$  blade span. Tip losses are not captured accurately, leading to an overprediction of the stage adiabatic efficiency.

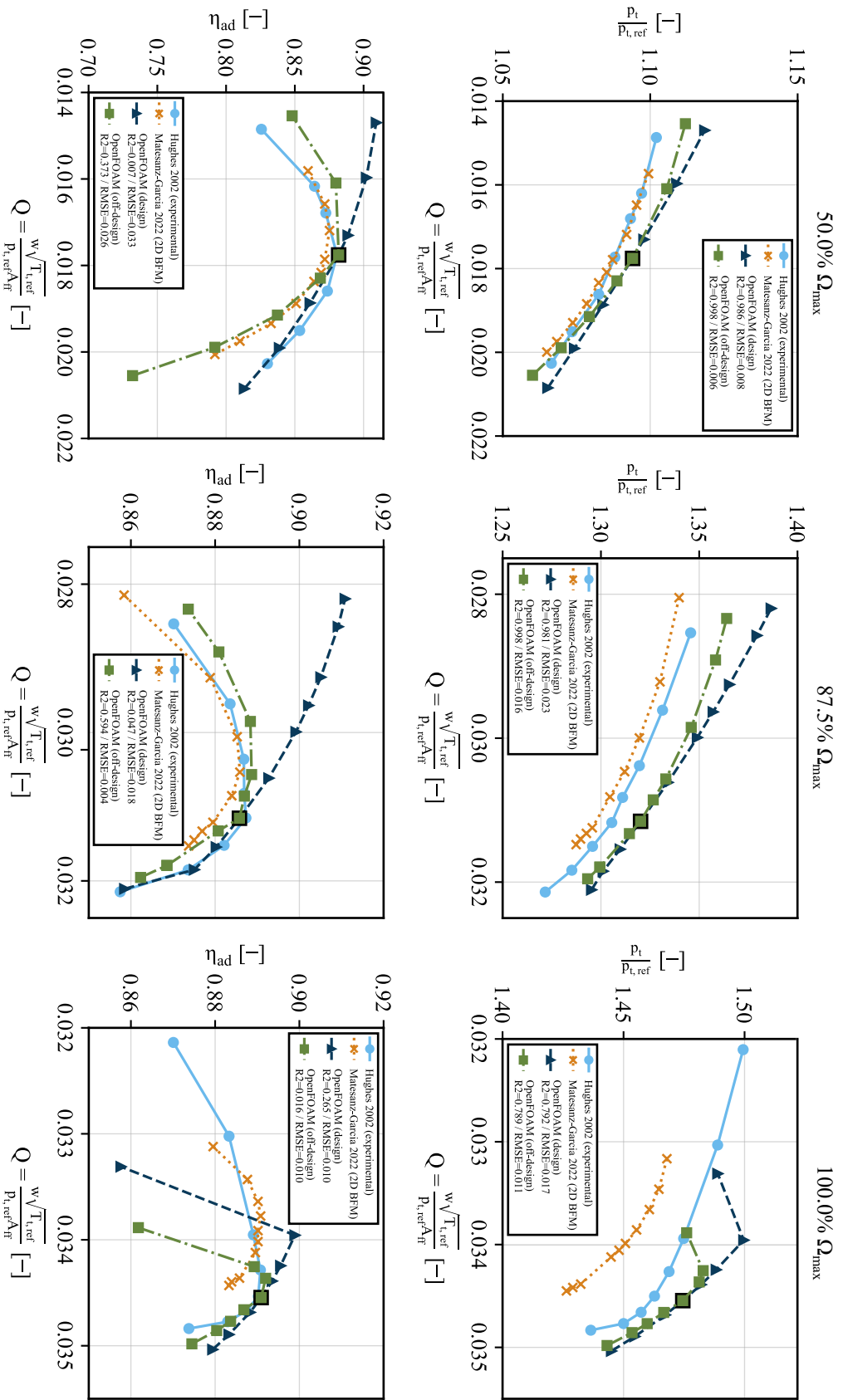


Figure 5.28: Fan stage pressure ratio (top) and adiabatic efficiency results (bottom) for the NASA SDT validation study. Study results considering and neglecting off-design terms are compared against experimental results by Hughes [275] and computational results by Matesanz-Garcia [133]. BFM design cases employed for the off-design terms are highlighted by a black contour in each diagram.

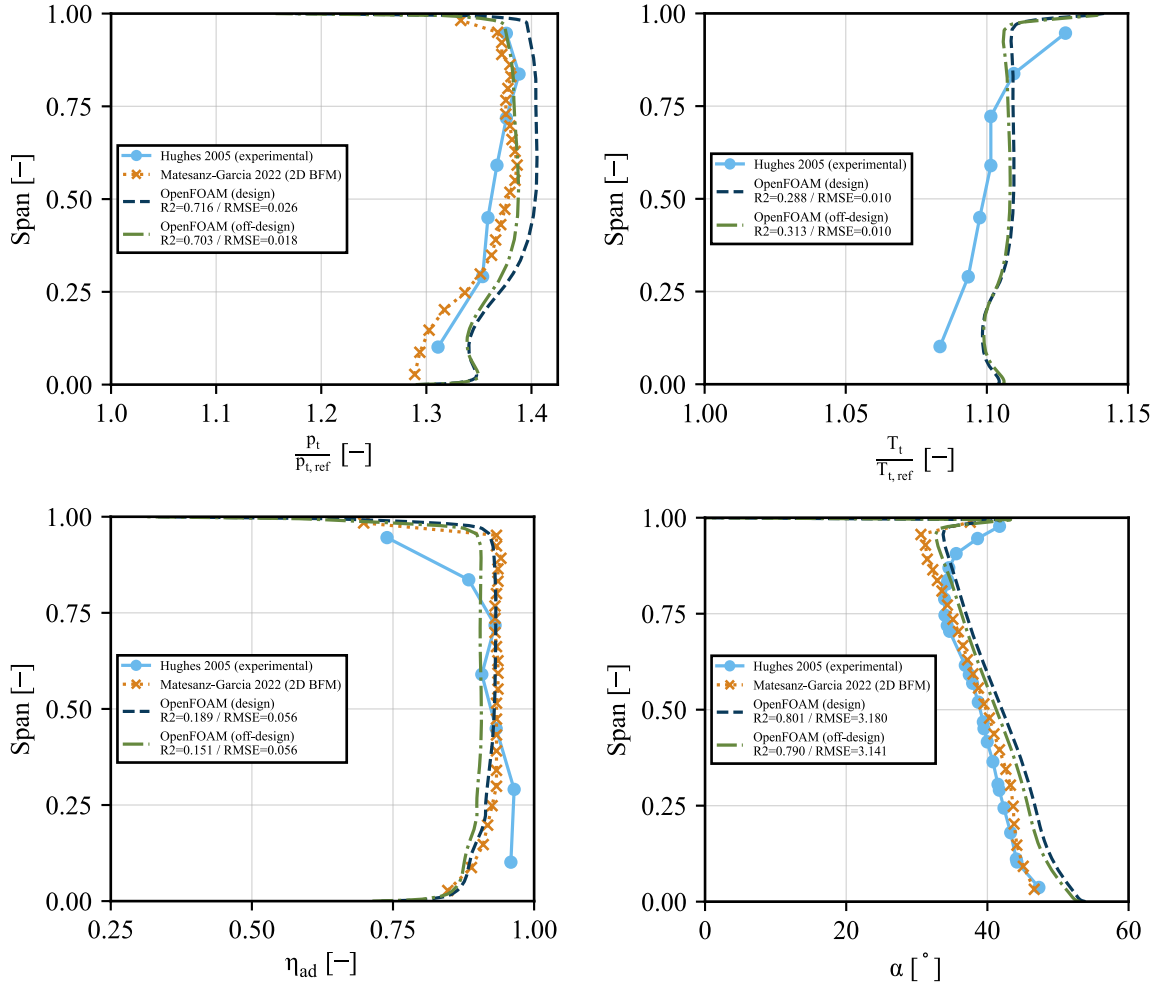


Figure 5.29: Spanwise radial profiles measured at the rotor exit station for the nominal operation point of  $87.5\% \Omega_{max}$  ( $Q = 0.02845$ ). Study results considering and neglecting off-design terms are compared against experimental results by Hughes [276] and computational results by Matesanz-Garcia [133].

The *NASA SDT* fan stage is a suitable validation case for the implementation and usage of the Hall-Thollet BFM as it features a similar operating *FPR* compared to the BLI study. The number of possible error sources for comparing the computational and experimental results is manifold. They include unknown errors in the experimental setup and the preparation of the experimental results, inaccuracies due to the derivation and interpolation of the blade geometries (especially blockage and camber distributions), and loss of accuracy due to the inherent simplifications of the employed BFM. Nevertheless, the discussed results for the fan design points show an adequate agreement with the experimental results, especially for lower rotational speeds. In the current BLI study, the focus will be placed on investigating optimum fuselage-propulsor geometries for design conditions only, and off-design terms will be neglected. Thus, using the low-order Hall-Thollet BFM to represent a fan in transonic flow conditions at low computational costs is deemed adequate for the current study. Based on the verification and validation results, its implementation for the *HiSA* solver is considered successful.

### 5.6.3.5 Scaling of CENTRELINE Fan Stage

To ensure optimal comparability between the results, optimizing the turbomachinery geometry for every studied design condition and fuselage-propulsor geometry would be necessary. However, this would require

coupling the CFD simulation with a fan rotor and stator optimization tool, leading to a higher complexity of the setup and, thus, to a significant increase in computational effort. A scaled fan stage is used for all studies to reduce the computational effort. A fan stage, specifically designed for a PFC application within the *CENTRELINE* project, is employed for a first estimation of the aero-propulsive effect.

As the investigated fuselage and fan stage geometries differ in size, the original fan stage has to be scaled accordingly. Conventional scaling methods for turbomachines follow the similitude approach [282, 283]. To achieve similarity in the device's performance, geometric, kinematic, and dynamic similitude has to be ensured. This implies that the linear dimensions of the scaled and original geometry, the ratios and directions of the acting forces, and velocities correspond. A common approach uses a dimensional analysis based on the definition of problem-specific dependent and independent parameters. In the case of a compressor in compressible flow, Dick defined the following independent parameters: gas properties at reference temperature, the initial state of the flow at the compressor inlet ( $p_{t,0}$ ,  $T_{t,0}$ ), the operating point ( $\dot{m}$ ,  $\Omega_{rot}$ ) and the characteristic diameter  $d_{rot,tip}$  [283]. The parameters are used to derive the independent dimensionless groups: heat capacity ratio, dimensionless viscosity, dimensionless mass flow rate, and dimensionless blade speed. The dependent parameters, such as the fan stage isentropic efficiency or total pressure ratio, can then be expressed as functions of the independent dimensionless groups [283].

For the BLI study, the conventional similitude approach is not applicable. Firstly, it is difficult to determine the compressor inlet conditions and the fan stage mass flow a priori for a BLI application. The parameters depend not only on the freestream conditions and the fan's rotational speed but are significantly affected by the specific BL flow characteristics at the FF inlet, which are determined by the upstream fuselage geometry and the suction effect of the FF. Furthermore, a variation of fuselage-propulsor geometries will be studied, including the variation of the rotor inlet duct height and the rotor hub-to-tip ratio. Consequently, kinematic and dynamic similitude cannot be ensured, and the fan's performance will vary for the different designs. Geometric similitude can be ensured by scaling the fan stage with the rotor duct height while keeping the stage aspect ratio, i.e.  $AR_{st} = h_{duct}/l_{FF,st}$ , the rotor and stator blade aspect ratios  $AR_{rot,blade} = b_{rot}/c_{rot,root}$  and  $AR_{stat,blade} = b_{stat}/c_{stat,root}$  and their thickness-to-chord ratio distributions along the chord and span  $(t/c)_{rot}$  and  $(t/c)_{stat}$  constant. Here,  $b$  denotes the blade span/height,  $c_{root}$  the root chord,  $h_{duct}$  the duct height at station 2, and  $l_{FF,st}$  the axial distance between station 2 and 3 (Figure 5.30). It is expected that scaling  $(t/c)$ , in reality, might follow a nonlinear approach, which focuses more on the structural integrity of the blades and the rotor or stator disk compared to the aerodynamic performance. However, this study assumes that  $(t/c)$  scales linearly with rotor duct height and is constant along the blade span. Consequently, the total stage length, the area ratio of stage exit and inlet, the blade chord ratios, blockage, and blockage gradients vary among the studied designs. Furthermore, the fan rotational speed is scaled to ensure a constant dimensionless blade speed  $\Pi$  with

$$\Pi = \frac{\Omega_{rot} d_{rot,tip}}{\sqrt{\gamma R T_{t,\infty}}} \quad (5.79)$$

The original blade speed of the Fan B is  $\Omega_{rot} = 5518 \text{rpm}$  at a rotor inlet tip diameter of  $d_{rot,tip} = 1.159 \text{m}$  in cruise conditions ( $Ma_\infty = 0.82$ , *FL350*, *ISA+10K*). The original corrected tip speed of  $355.76 \text{m/s}$  is maintained throughout the study. For the reference geometry, which is based on the *CENTRELINE* Rev 07 geometry, this leads to  $\Omega_{rot} = 293 \text{rad/s}$  at  $d_{2,tip} = 2.29 \text{m}$ .

The BFM allows for varying the number of rotor and stator blades. However, choosing the optimal number of rotor and stator blades and an optimal ratio thereof, is a complex task, because it affects the aerodynamics, acoustics, and aeroelastics of the turbomachine [284]. To limit the design space, these parameters are kept constant across the study ( $N_{rot} = 20$ ,  $N_{stat} = 43$ ). The rotor and stator blade geometry of the *CENTRELINE* Fan B stage provided by Castillo Pardo [107, 108, 145] are scaled according to the scaling laws provided above. Camber, blockage, and blockage gradients are then derived following the same approach described for the *NASA SDT* Fan Stage in Section 5.6.3.4. In contrast to the

validation study, only design conditions are considered, and thus, the BFM off-design term is neglected. Furthermore, the original *CENTRELINE* Rev 07 geometry is slightly altered to accommodate a design *FPR* of 1.4 for the calculated rotational speed. This is achieved by slightly reducing the fan nozzle area  $A_8$  as depicted in Figure 5.3.

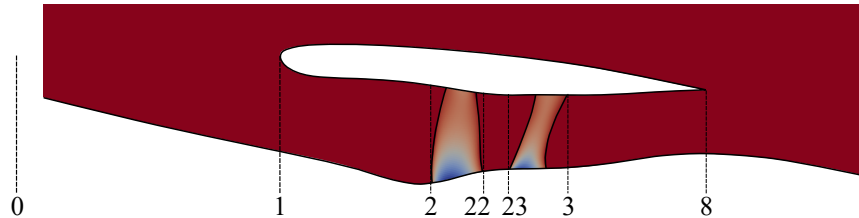


Figure 5.30: PFC geometry with scaled *CENTRELINE* Fan B. Color shading indicative of blockage distribution in rotor and stator region. Indication of FF stations in accordance with ARP755C [285]. Freestream air conditions are defined upstream of the fuselage nose (not shown here).

## 5.6.4 Grid

*Gmsh* is used to automatically generate the FV grids. Further, grid convergence studies are conducted to ensure an adequate mesh quality throughout the study.

### 5.6.4.1 Grid Generation

The FV mesh required for the RANS CFD simulation is generated using the open-source grid generator *Gmsh* [188]. *Gmsh* provides a scripting interface that automates the mesh generation process and ensures similarity between meshes of different geometries. The automated mesh generation process is provided in [190].

*OpenFOAM* requires a 3D computational domain even for 2D-axisymmetric simulations. Thus, the domain is a 3D wedge with an angle of  $4^\circ$  and a single cell width in the circumferential direction. For the simulation of the full configuration, the domain extends to  $1 \cdot l_{f,tot}$  in front of the fuselage leading edge. For all configurations, the domain extends to  $2 \cdot l_{f,tot}$  behind the fuselage trailing edge. Further, it stretches out by  $10 \cdot r_{f,cent}$  in the radial direction. Figure 5.17 depicts the domain.

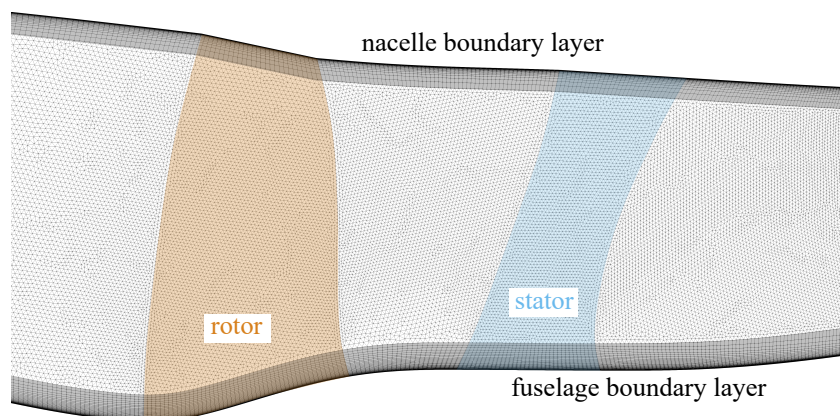


Figure 5.31: Grid inside the FF duct for the reference geometry.

For the HPFVM, the turbulent BL is fully resolved by a structured grid with  $y^+ \leq 1$  on all surfaces (see Section 5.6.4.2). The rest of the domain features an unstructured grid. Figure 5.31 exemplarily depicts the grid in the FF duct.

The FV grids employed for the HPFVM study feature less than 600,000 cells each.

#### 5.6.4.2 Grid Convergence

Two grid convergence studies are conducted using the approach described in Section 5.6.3.4. Both studies use a setup with a  $k-\omega$ -SST turbulence model and simulate the flow around the fuselage-propulsor reference geometry with  $FPR$  close to 1.4.

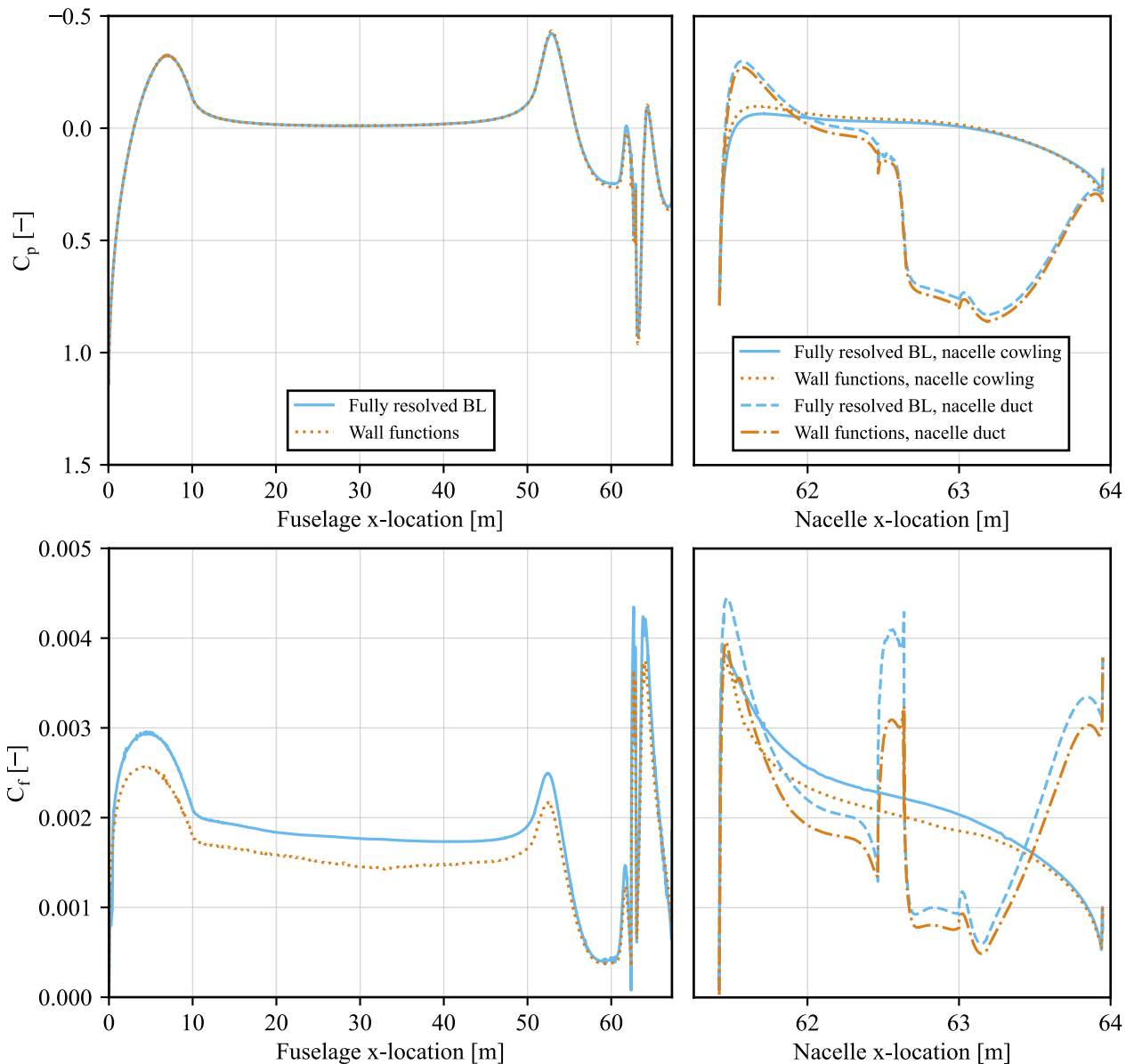


Figure 5.32: Comparison of pressure and skin friction coefficient distribution along fuselage (left) and nacelle (right) surface for a grid with full BL resolution compared to wall functions. Full FV domain with the finest grid resolution and  $k-\omega$ -SST turbulence model. Reference fuselage-propulsor configuration.

The first study validates the full FV domain grid, which is employed for the determination of the interface location (see Section 5.5) and the verification of the hybrid approach compared to the full FV approach (see Section 5.7). It compares different resolutions of a grid with fully resolved BL against using wall functions on grids with  $30 < y^+ < 150$ . Detailed results of this grid convergence study are provided in Appendix A.6. In contrast to the conclusion of the *Waisted Body* validation study (Section 5.6.2), integrated data of the fuselage-propulsor show that the application of wall functions leads to an underprediction of the wall shear stress, especially in the nose region of the fuselage (see Figure 5.32). The difference in wall shear stress is not recovered along the fuselage center section. Similarly, shear stresses at the nacelle surface are estimated too low. Consequently, the friction force in the drag direction of the fuselage-propulsor body is underestimated by  $\approx 15\%$ . Viscous drag contributes to  $\approx 70\%$  of the fuselage-propulsor bodies total force in streamwise direction, which is crucial in determining the aero-propulsive performance of the configuration (see Section 4.2). Therefore, it is critical to accurately predict the wall shear stresses. The study aims at a rapid, but sufficiently accurate prediction of the aero-propulsive characteristics of a fuselage with BLI. Thus, a coarse grid with wall functions would be beneficial as it reduces the required computational costs. However, based on the results of the validation study, wall functions cannot be employed, as they might lead to severe modeling errors and, therefore, for all subsequent simulations, the BL is fully resolved ( $y^+ \leq 1$ ), making the usage of wall functions unwarranted.

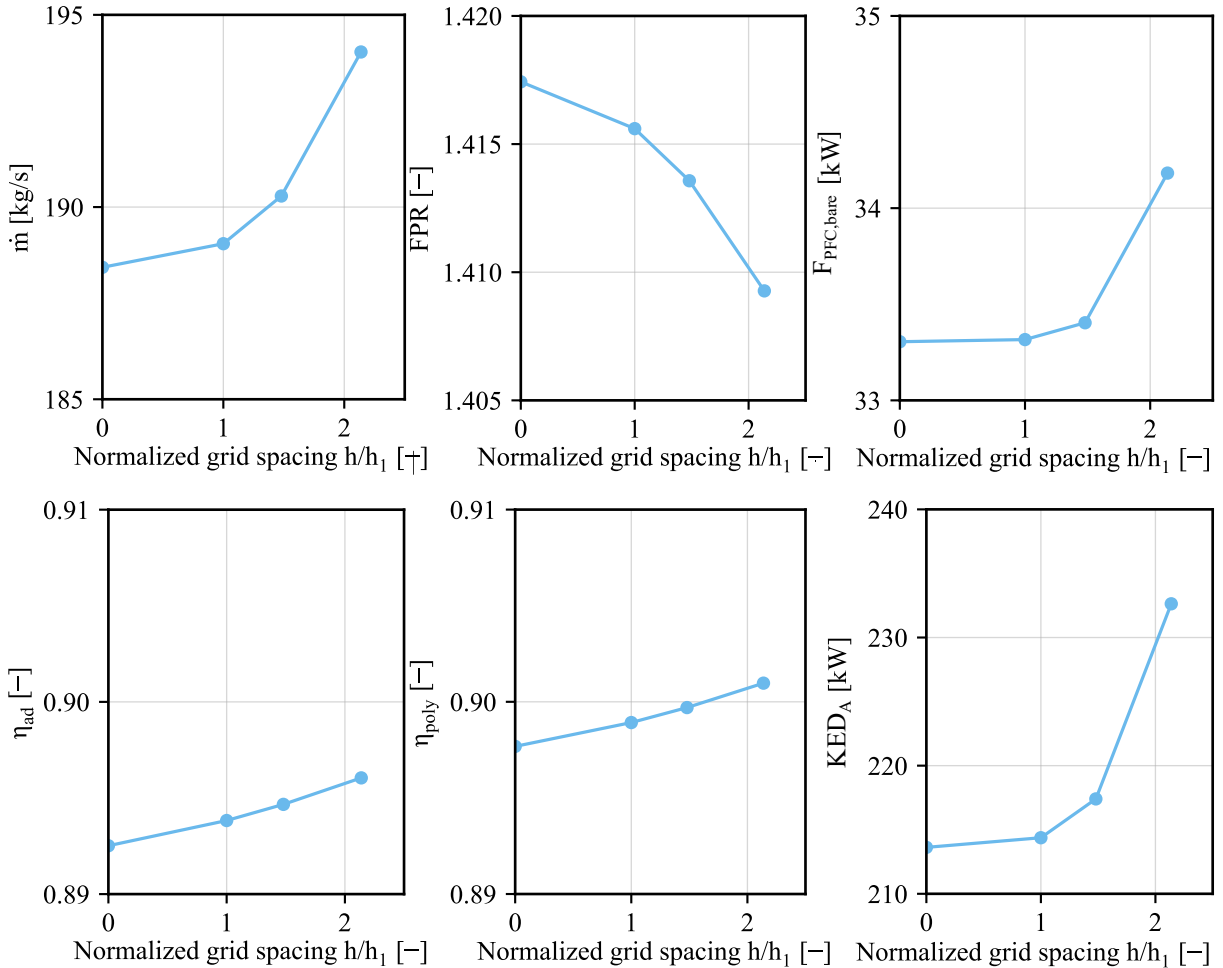


Figure 5.33: Grid convergence results for hybrid BLI FV domain with  $k-\omega$ -SST turbulence model and fully resolved BL. Reference fuselage-propulsor configuration.

	$\Phi: \dot{m} \left[ \frac{\text{kg}}{\text{s}} \right]$	$\Phi: \text{FPR}_{\text{st}} [-]$	$\Phi: \text{F}_{\text{PFC,bare}} [\text{kN}]$	$\Phi: \eta_{\text{ad,st}} [-]$	$\Phi: \eta_{\text{pol,st}} [-]$	$\Phi: \text{KED}_A [\text{kW}]$
$N_1, N_2, N_3$	577589, 263738, 126319					
$\Phi_1$	189.04682	1.41560	33.31622	0.89383	0.89892	214.37540
$\Phi_2$	190.28739	1.41357	33.40375	0.89467	0.89970	217.40426
$\Phi_3$	194.03402	1.40927	34.18235	0.89605	0.90097	232.63171
$\Phi_{\text{ext}^{21}}$	188.43270	1.41743	33.30513	0.89252	0.89768	213.62334
$p$	2.8199	1.9087	5.5757	1.2624	1.2447	4.1202
$e_a^{21} [\%]$	0.66	0.14	0.26	0.09	0.09	1.41
$e_{\text{ext}}^{21} [\%]$	0.98	0.27	0.30	0.24	0.23	1.77
$\text{GCI}_{\text{medium}}^{32} [\%]$	1.35	0.37	0.43	0.33	0.30	2.46
$\text{GCI}_{\text{fine}}^{21} [\%]$	0.41	0.16	0.04	0.18	0.17	0.44

Table 5.4: Results for grid discretization study for hybrid FV BLI domain with  $k\text{-}\omega\text{-SST}$  turbulence model and fully resolved BL. Reference fuselage-propulsor configuration.

An additional grid convergence study is performed for the FV grid of the rear part of the fuselage, which is used for all subsequent hybrid simulations. Results are provided in Table 5.4 and Figure 5.33. Based on a  $\text{GCI}_{\text{fine}}^{21} < 0.5\%$  for all studied variables, the finest grid is chosen for the HPFVM method.

### 5.6.5 Interface Boundary Condition

At the inlet boundary,  $U$  and  $T$  BCs are prescribed with the *OpenFOAM* function *codedFixedValue* [286]. Similar to the approach described in Section 5.6.3.2, the temperature and velocity profile, which were calculated with the PM (Section 5.5), are interpolated to the FVM nodes with *Python* functions through the *C++* library *pybind11* [273]. The BCs can be found in [190].

## 5.7 Verification and (Pseudo-)Validation of Hybrid Method

Verification of the hybrid numerical method involves comparing HPFVM to full FVM results for the powered reference fuselage-propulsor geometry. Due to methodological disparities, particularly the incorporation of a laminar region transition prediction in the IBL method, variations in results are anticipated. Figure 5.35 visualizes the skin friction and pressure coefficient distribution along the axisymmetric surfaces of the fuselage, nacelle cowling, and nacelle duct. Here, the differences of the coefficients  $C_i$  are defined as  $\Delta C_i = \frac{C_{i,\text{HPFVM}} - C_{i,\text{FVM}}}{\max(C_{i,\text{FVM}}) - \min(C_{i,\text{FVM}})}$ . The highest discrepancy in pressure is observed at the fuselage LE, where the pressure coefficient is overestimated by 21% by the HPFVM. However, for  $x/l_{f,\text{cent}} > 2.5\%$ , the difference is smaller than  $\pm 2.5\%$ . Near the FF hub, it is  $< \pm 1.8\%$ . Due to the small differences in the BL profile incident to the nacelle cowling (see Section 5.5.4 and Figure 5.34), the pressure coefficient at the nacelle highlight is 7.2% higher and 5.3% lower for the hybrid method at the top and bottom side of the nacelle, respectively.

At the fuselage LE, the HPFVM overpredicts the skin friction coefficient compared to FVM results. In the fuselage nose region downstream of  $x/l_{f,\text{cent}} > 3.3\%$ , the predicted skin friction coefficient is up to 18% smaller. The difference decreases to less than 5.5% downstream of the beginning of the constant center section. These results align well with the FV simulation setup validation findings of the *Waisted Body* geometry presented in Section 5.6.2. Here, the FVM overpredicted the skin friction coefficient compared to experimental data, especially in the convex region of the body. In the region of the FF, the discrepancy is less than  $\pm 2.3\%$ . Similarly to the pressure coefficient, the skin friction coefficient at the nacelle highlight differs significantly. Along the duct tip contour, the difference is smaller compared to the nacelle cowling.

Pressure and skin friction coefficient distributions are employed to calculate the axial surface forces in the streamwise direction (see Table 5.5). The smoothed HPFVM post-processing results show that

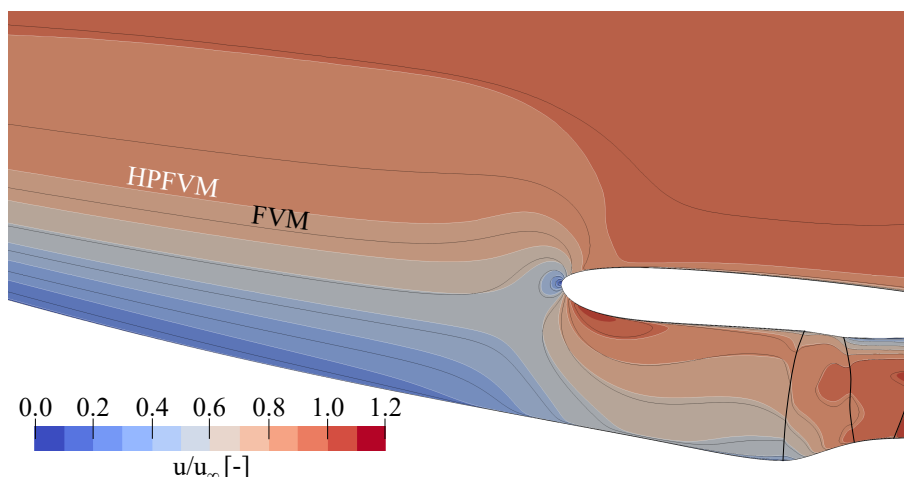


Figure 5.34: Normalized velocity distribution of the HPFVM simulation in the vicinity of the nacelle LE for the reference geometry. White contour lines indicate HPFVM results, Black contour lines indicate FVM results.

pressure and viscous forces of the nacelle (cowling and duct combined) differ by less than 3%. For the nacelle, the pressure force dominates on both sides, the outer cowling and the inner duct. The 22% difference in fuselage pressure force  $F_{f,p}$  is mainly attributed to the pressure coefficient deviation at the fuselage nose. However, the viscous force  $F_{f,v}$  dominates over  $F_{f,p}$  for the fuselage. The underprediction of  $C_f$  along the major part of the fuselage almost cancels out the overprediction of  $F_{f,p}$ . In summary,  $F_{PFC,bare}$  matches by  $-2.3\%$ .

Force in drag direction [kN]	Fuselage			Nacelle			Total		
	$F_{f,v}$	$F_{f,p}$	$F_{f,tot}$	$F_{nac,v}$	$F_{nac,p}$	$F_{nac,tot}$	$F_{tot,v}$	$F_{tot,p}$	$F_{PFC,bare}$
<b>FVM</b>	23.06	7.17	30.23	1.00	1.80	2.80	24.06	8.97	33.03
<b>Orig. HPFVM (unsmoothened)</b>	21.04	34.52	55.56	1.03	1.81	2.84	22.07	36.33	58.40
<b>HPFVM (smoothened)</b>	<b>20.68</b>	<b>8.74</b>	<b>29.41</b>	<b>1.03</b>	<b>1.81</b>	<b>2.84</b>	<b>21.71</b>	<b>10.55</b>	<b>32.26</b>
<b>Orig. HPFVM vs. FVM [%]</b>	-9	381	84	3	1	1	-8	305	77
<b>HPFVM vs. FVM [%]</b>	-10	22	-3	3	1	1	-10	18	-2

Table 5.5: Comparison of integrated surface forces for the reference geometry obtained with FVM, original HPFVM, and with combined pressure (Section 5.4.3) and smoothed skin friction distribution (Section 5.5.4).

Important FF metrics discussed in Section 4.2 are compared in Table 5.6 based on the smoothed HPFVM post-processing results.  $F_{FF}$  and  $F_N$  show the highest discrepancies. The small difference in FF mass flow is multiplied by the freestream velocity and leads to a 1.6% deviation of  $F_N$ . The decrease in  $F_{FF}$  results from the slight difference in velocity and density profile incident to the rotor inlet.

	$P_{FF,s,is}$ [MW]	$F_{FF}$ [kN]	$F_{PFC,bare}$ [kN]	$F_G$ [kN]	$F_N$ [kN]	$\dot{m}$ [kg/s]
<b>FVM</b>	5.53	22.80	33.03	54.39	7.89	191.24
<b>HPFVM (smoothened)</b>	5.57	23.18	32.26	54.40	8.02	190.72
<b>CENTRELINE Rev 07</b>	5.53 <sup>^</sup>	32.44 <sup>^</sup>	33.17 <sup>^</sup>	59.57 <sup>*</sup>	7.85 <sup>*</sup>	207.9 <sup>^</sup>
<b>HPFVM vs. FVM [%]</b>	0.7	1.7	-2.3	0.0	1.6	-0.3
<b>HPFVM vs. CENTRELINE [%]</b>	0.7	-28.5	-2.7	-8.7	2.2	-8.3

Table 5.6: Comparison of integrated FF variables for reference geometry with  $FPR=1.4$ .

<sup>^</sup> CENTRELINE Rev 07 [19].

<sup>\*</sup> CENTRELINE Rev 07 calculated from mass flow averaged station data [19].

Additionally, a (pseudo-)validation is carried out by comparing HPFVM results against the numerical simulation of the CENTRELINE Rev 07 geometry presented in [19]. The original data was obtained

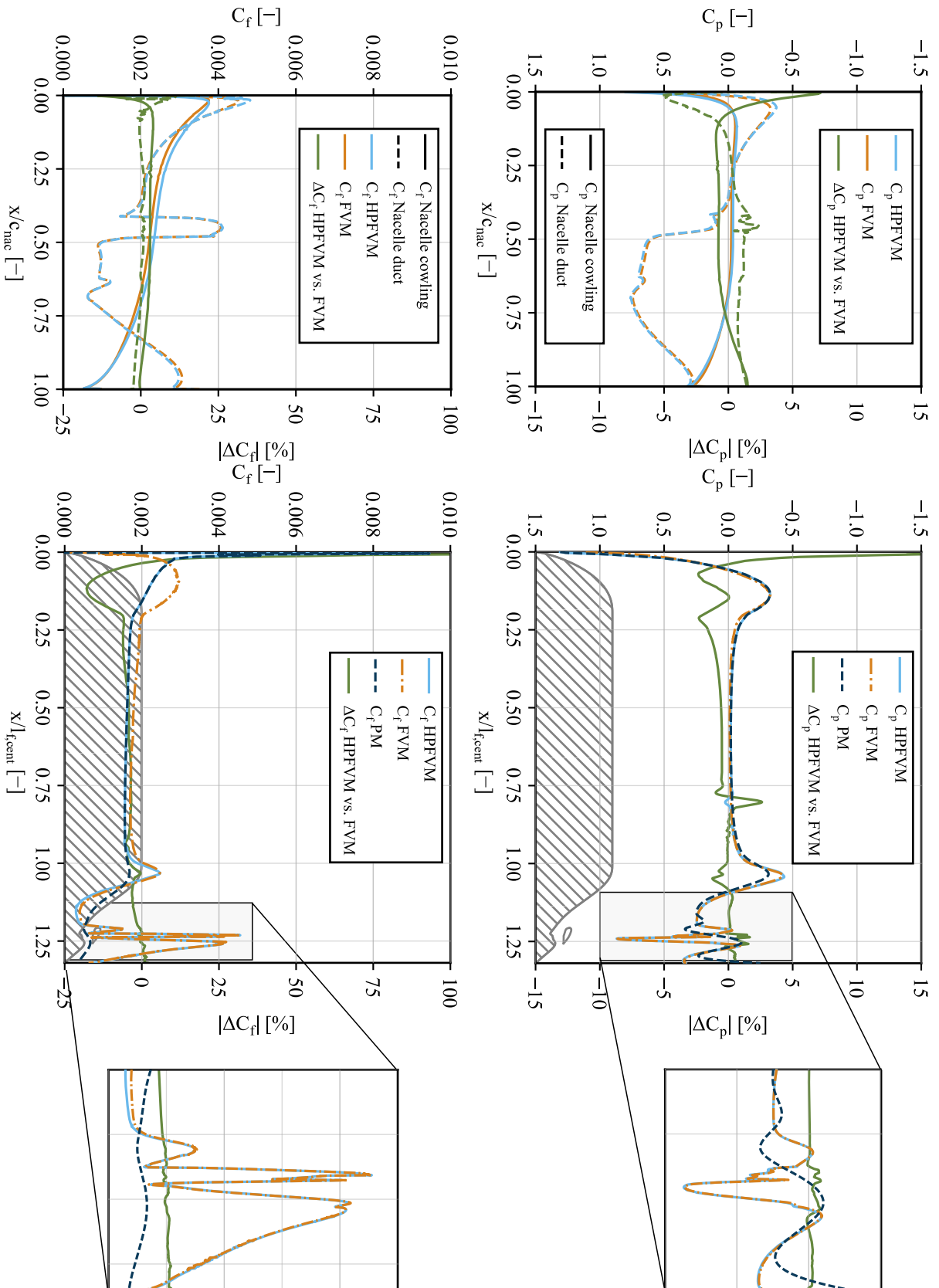


Figure 5.35: Skin friction and pressure coefficient distribution for the reference geometry for PM (fuselage only), full FVM, and HPFVM. Left: nacelle, right: fuselage

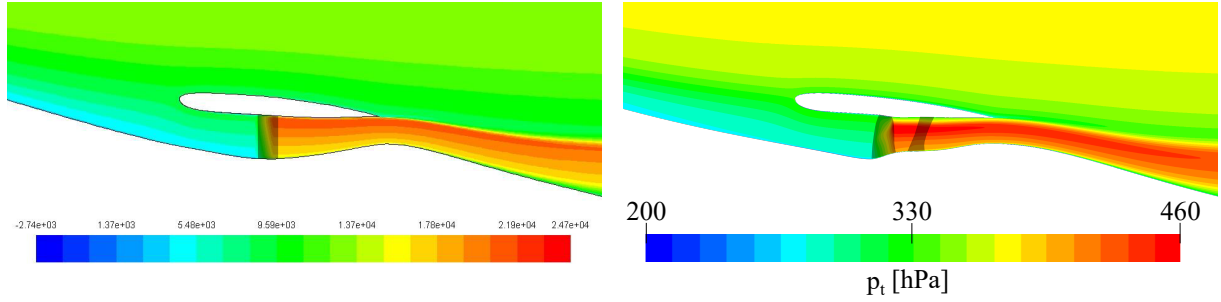


Figure 5.36: Comparison of total pressure distribution for the reference geometry. Left: *CENTRELINE* Rev 07, adapted from [19]. Right: HPFVM. Fan volumes are indicated in gray. Scales differ.

through steady RANS CFD simulations using *ANSYS Fluent*. Here, the effect of the FF on the fluid was modeled with a BFM, introducing axial momentum density and energy STs in a defined fan disk volume. The model employed a single volume, neglecting the effects of swirl and radial momentum terms. STs were manipulated iteratively to achieve the required *FPR* [19]. As discussed in Sections 5.3.1 and 5.6.3.5, the reference fuselage-propulsor geometry is based on the same *CENTRELINE* Rev 07. However, modifications are made to the FF duct to accommodate the *CENTRELINE* Fan B stage [108]. Consequently, mass flow-averaged station data and FF metrics are expected to exhibit differences. Figure 5.36 illustrates the discrepancy in FF duct geometries and the FF stage. The shaft power is directly linked to the *FPR*, resulting in only a 0.7% difference in  $P_{FF,s, is}$  for the same *FPR* (Table 5.6). The mass flow through the duct is 8.3% smaller for the HPFVM due to the lower mean velocity in the FF inlet. Consequently,  $F_G$  is reduced by 8.7%, even though the net thrust is increased. The most significant difference is observed in the FF volume force  $F_{FF}$ . For both HPFVM and *CENTRELINE* Rev 07,  $F_{FF}$  is calculated by integrating the STs over the FF volume. However, the fan modeling approaches and FF stage geometry differ significantly. Although both geometries feature the same station 2 area, the duct area reduction between the rotor inlet and stator outlet is 13.3% for the HPFVM geometry compared to 2.4% for the *CENTRELINE* Rev 07 geometry. Consequently, the duct area contraction in the HPFVM geometry contributes significantly more to achieving the required *FPR*, requiring less momentum introduction by the FF and resulting in a lower  $F_{FF}$ . The disparity in surface forces closely mirrors the comparison between FVM and HPFVM outcomes.

In conclusion, the validation and comparison of HPFVM against full FVM results for the powered reference fuselage-propulsor geometry reveal expected variations stemming from methodological differences. Despite slight differences in skin friction and pressure distribution near the fuselage nose and the nacelle LE, HPFVM demonstrates reasonable agreement with FVM, especially in the FF region. Additional validation against the *CENTRELINE* Rev 07 geometry further supports the method's credibility. Deviations in FF metrics can be attributed to the distinct fan modeling approaches and FF stage geometries. In summary, although some deviations are present, HPFVM exhibits reasonable validity in capturing complex aerodynamic interactions, establishing a promising foundation for its current application.



## 6 Parameter Study

The effectiveness of the hybrid numerical approach introduced in Section 5 is demonstrated by an exemplary sensitivity study. Each parameter is systematically varied around the reference value by  $\pm 1\%$  or  $\pm 1^\circ$  to evaluate its isolated impact. For each parameter, five geometry variations are simulated. The findings from this study provide initial insights into the influence of geometric and operational parameters on the performance of the fuselage-propulsor configuration, addressing RQ 7. Where possible, results are benchmarked against existing literature. However, given the prevalent focus on multi-parameter optimization in existing research, which seldom breaks down sensitivity analysis results (refer to Section 2.2.3), comparative data are scarce.

To facilitate the creation of comparable geometries, the method for geometry parameterization outlined in Section 5.3 is marginally modified to lessen the dependency on other geometric variables. Specifically, certain relative variables are substituted with absolute parameters, as listed (see also Table A.1, Appendix A.2):

- $r_{max}$  instead of  $f_{r,max}$
- $l_{nac}$  instead of  $f_{l,nac}$
- $x_{FF}$  instead of  $f_{x,FF}$

Nonetheless, certain dependencies persist, affecting the results discussed in the following.

The aggregated outcomes of all examined cases (except for variations in operational parameters  $Ma$  and  $h_{alt}$ ) are illustrated in Figures 6.1 and 6.2. For the studied configurations, an almost linear relationship is observed between the isentropic FF shaft power ( $P_{FF,s,pol}$ ) and the FF force ( $F_{FF}$ ), with higher  $F_{FF}$  correlating to increased  $P_{FF,s,pol}$ . Furthermore,  $FPR$  shows a correlation with both  $F_{FF}$  and  $P_{FF,s,pol}$ . While a higher  $F_{FF}$  enhances the aero-propulsive efficiency through a reduction in total streamwise force in drag direction ( $NPF_{PFC,bare}$ ), an increase in  $P_{FF,s,pol}$  triggers adverse cascade effects at the aircraft level, such as a bigger gas turbine or main engine power off-takes and an increase in the weight of the (turbo-electric) power train components. Thus, a compromise of both has to be found on the aircraft level.

Figure 6.2 indicates no direct relationship between  $NPP$  and  $P_{FF,s,pol}$ . Further, even for small, isolated parameter variations, geometries exist, which show an improved aero-propulsive performance compared to the reference geometry indicated by "x". For instance, for the best-performing geometry denoted as "+",  $f_{\eta,BLI,bare}$  sees a 0.05 improvement (the closer  $f_{\eta,BLI,bare}$  to 0, the closer is the configuration to an ideal BLI case). Although  $P_{FF,s,pol}$  worsens by 7.6%, the 2.7% enhancement in  $NPF_{PFC,bare}$ , amplified by the freestream velocity, translates to an overall  $f_{\eta,BLI,bare}$  improvement of 3.6%. These findings imply that further geometry optimization holds promise for enhancing the aero-propulsive performance of the fuselage-propulsor configuration for the specified operating conditions.

The effect of the individual design parameters on the aero-propulsive performance indicators presented in Section 4.2 is summarized in Figures A.6 to A.14 in Appendix A.7. Definitions of the design parameters can be found in Appendix A.2, Table A.1. The curves are fitted using simple linear regressions or regressions with 2nd-order polynomial terms if  $R^2 > 0.8$  is achievable.

Several geometric design parameters, most describe the geometry of the FF duct and nacelle cowl, minimally affect the aero-propulsive performance of the fuselage-propulsor configuration. These parameters include  $f_{x,max}$ ,  $l_{nac}$ ,  $f_{l,int}$ ,  $f_{\rho LE}$ ,  $f_{A_{thr},A_2}$ ,  $\Delta\beta_{TE}$ ,  $\Theta_{f,int}$ ,  $\Theta_{rot,in}$ , and  $f_{l,nose}$ . Modifying these parameters within  $\pm 1\%$  leads to variations of less than  $\pm 1\%$  in most performance metrics, except  $NPF_{PFC,bare}$ ,

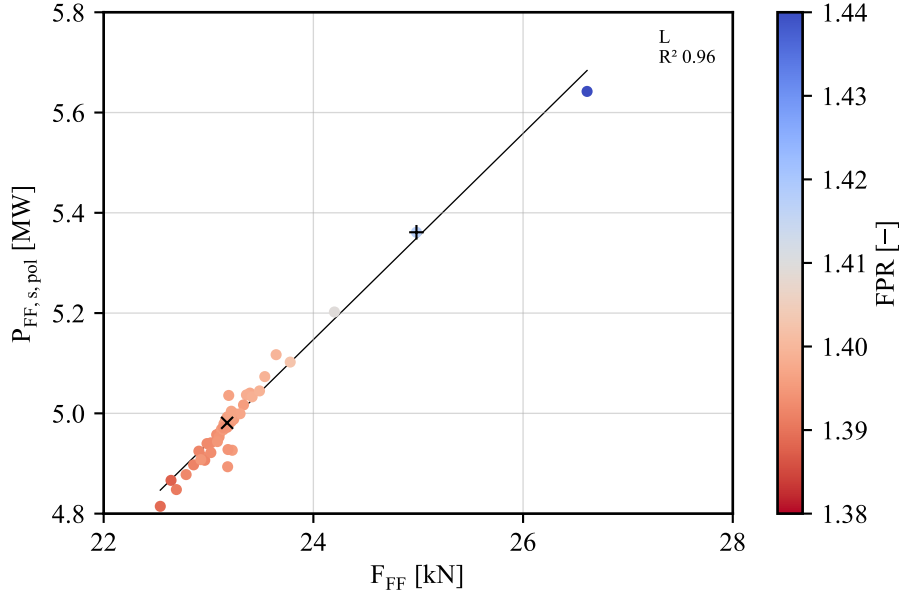


Figure 6.1: Relationship between FF force, FF shaft power, and  $FPR$ . Geometric parameters only.

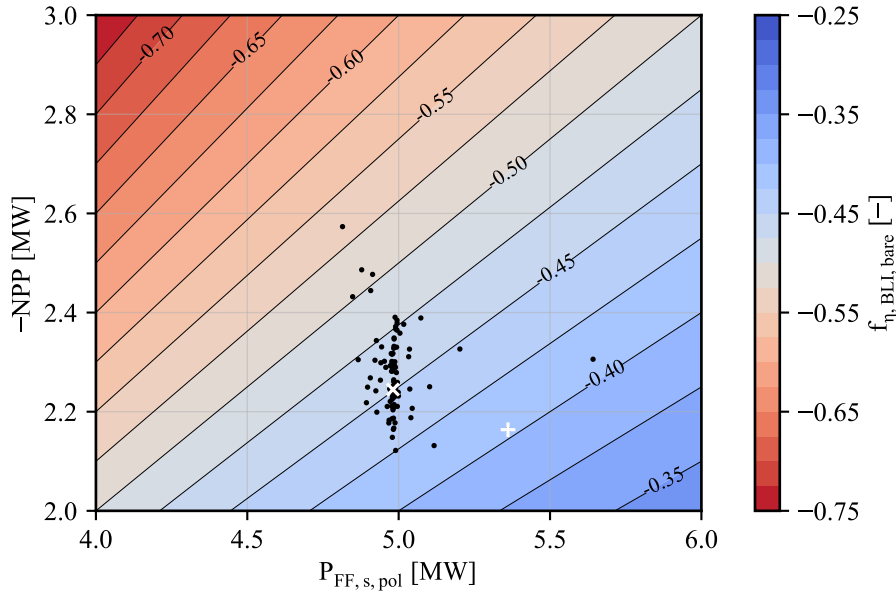


Figure 6.2: Relationship between NPP, FF shaft power, and  $f_{\eta,BLI}$ . Geometric parameters only.

where alterations of up to 2% can occur due to pressure force changes driving surface force variations. Further, the impact on the total fuselage surface force  $F_{f,tot} = F_f + F_{f,duct} + F_{aftbody}$  outweighs that on the nacelle force  $F_{nac,tot} = F_{nac} + F_{f,duct}$ . However, compared to other design parameters, the variation in  $NPF_{PFC,bare}$  is small.

Parameters like  $r_{max}$ ,  $x_{FF}$ ,  $r_{f,cent}$ ,  $l_{f,cent}$  and,  $f_{l,thr}$  exert minimal influence on the FF performance (altering performance metrics by less than  $\pm 1\%$ ), but their effect on  $NPF_{PFC,bare}$  is substantial. Parameter variations of  $\pm 1\%$  induce an  $NPF_{PFC,bare}$  alteration of up to  $\pm 10\%$ .

$r_{f,cent}$  and  $l_{f,cent}$  define the geometry of the fuselage center section. An isolated increase of  $r_{f,cent}$  leads to a fuselage surface area increase, which results in a rise in  $F_{f,tot}$ . At the same time, the contraction of

the fuselage geometry in front of the propulsor is stronger, i.e., the steepness of the slope of the fuselage contour incident to the FF increases. This leads to an increase in the local adverse pressure gradient and  $\delta$ , which modifies the local flow conditions at the FF inlet and in the vicinity of the cowling.  $F_{n,tot}$  rises, further contributing to the deterioration of  $NPF_{PFC,bare}$  for increasing  $r_{f,cent}$ . The change in flow characteristics incident to the FF does not significantly impact the FF performance. However,  $\beta_{MD}$  and  $\beta_{KED}$  decrease because of the lower velocity flow incident to the FF. Attention has to be paid to the limiting cases of the isolated  $r_{f,cent}$  variation (see Figure 6.3). When  $r_{f,cent}$  reaches 4.00m, the steep fuselage curvature upstream of the FF induces a shock that occurs at the convex end of the fuselage center section (Figure 6.4). This shock wave triggers flow separation downstream. The FF ingests the disrupted flow, and its performance deteriorates. Conversely, at a reduced  $r_{f,cent}$  of 1.75m and an unchanged FF cowling geometry, the flow velocity adjacent to the cowling intensifies, leading to the formation of a shock on the nacelle cowling (Figures 6.4 and A.14).

The isolated alteration of  $l_{f,cent}$  yields similar outcomes. Due to the chosen parameterization approach, the total fuselage length, nacelle, and FF geometry and position remain unchanged. When  $l_{f,cent}$  increases, the distance between the end of the fuselage center section and the FF inlet reduces. Thus, the steepness of the fuselage contour incident to the FF increases. Consequently, an increase in  $l_{f,cent}$  results in a rise in fuselage pressure force, while the average velocity entering the FF inlet diminishes slightly. Although this has a minor effect on FF performance, it contributes to a rise in  $R_{KEDA}$ . If the fuselage contour adjacent to the FF becomes excessively steep with higher values of  $l_{f,cent}$ , areas of sonic flow may develop at the terminus of the fuselage's constant center section, introducing nonlinearities in the trends of surface forces (Figure A.12).

In aircraft conceptual design,  $r_{f,cent}$  and  $l_{f,cent}$  are typically regarded as aircraft-level requirements stemming from cabin design considerations rather than parameters optimized for fuselage-propulsor performance. Consequently, determining whether a larger or smaller  $r_{f,cent}$  and  $l_{f,cent}$  is more advantageous remains inconclusive. Nevertheless, optimizing the curvature downstream of the fuselage center section is crucial for ensuring optimal flow characteristics at the FF inlet.

Variations in the positioning of the FF rotor inlet, denoted as  $x_{FF}$ , evoke similar effects when all other parameters remain constant. Despite the overall increase in fuselage length and, consequently, the expansion of fuselage surface area, the total fuselage force  $F_{f,tot}$  diminishes by 1.5% with an increase in  $x_{FF}$  of 1%. For the viscous surface force, the increase in surface area leads to a rise in viscous force of  $\approx 100\text{N}$ , regardless of the small decrease of  $C_f$  between the end of the fuselage center section and the FF caused by the reduced steepness of the fuselage contour. However, the decrease in fuselage pressure force of  $\approx -500\text{N}$ , driven by the reduction in  $C_p$ , outweighs the rise in viscous force. The altered flow characteristics at the FF inlet, coupled with the marginal alteration in FF performance leads to a nonlinear effect on  $F_{nac}$ , which translates to a nonlinear  $NPF_{PFC,bare}$  and  $f_{\eta,BLI,bare}$  behavior (see also Appendix A.7, Figure A.15). Nevertheless, owing to the predominant influence of fuselage force variation, there appears to be a tendency for the aero-propulsive performance measured by  $f_{\eta,BLI,bare}$  to enhance with higher  $x_{FF}$  values. For extreme cases of  $x_{FF}$ , nonlinear effects manifest, as depicted in Figure 6.3. Analogous to the behavior observed with  $l_{f,cent}$ , when  $x_{FF} = 0.85$ , the fuselage contraction becomes excessively steep, leading to a shockwave at the rear end of the constant-radius fuselage center section, prompting flow separation upstream of the FF inlet. Conversely, for  $x_{FF} = 0.95$ , the increase in viscous fuselage force surpasses the decrease in fuselage pressure force. Consequently, for the configuration under consideration, the results suggest that an optimal aero-propulsive performance is attainable close to the reference value  $x_{FF} = 92.8\%$ .

The parameter  $r_{max}$  primarily influences the geometry of the nacelle cowling, as illustrated in Figure 6.5. Its variation has a minimal direct impact on FF performance but yields significant effects on  $NPF_{PFC,bare}$  due to alterations in surface forces. When  $r_{max}$  increases, a noticeable rise in pressure force is exerted in the drag direction on the nacelle cowling. The geometric change of the nacelle cowling

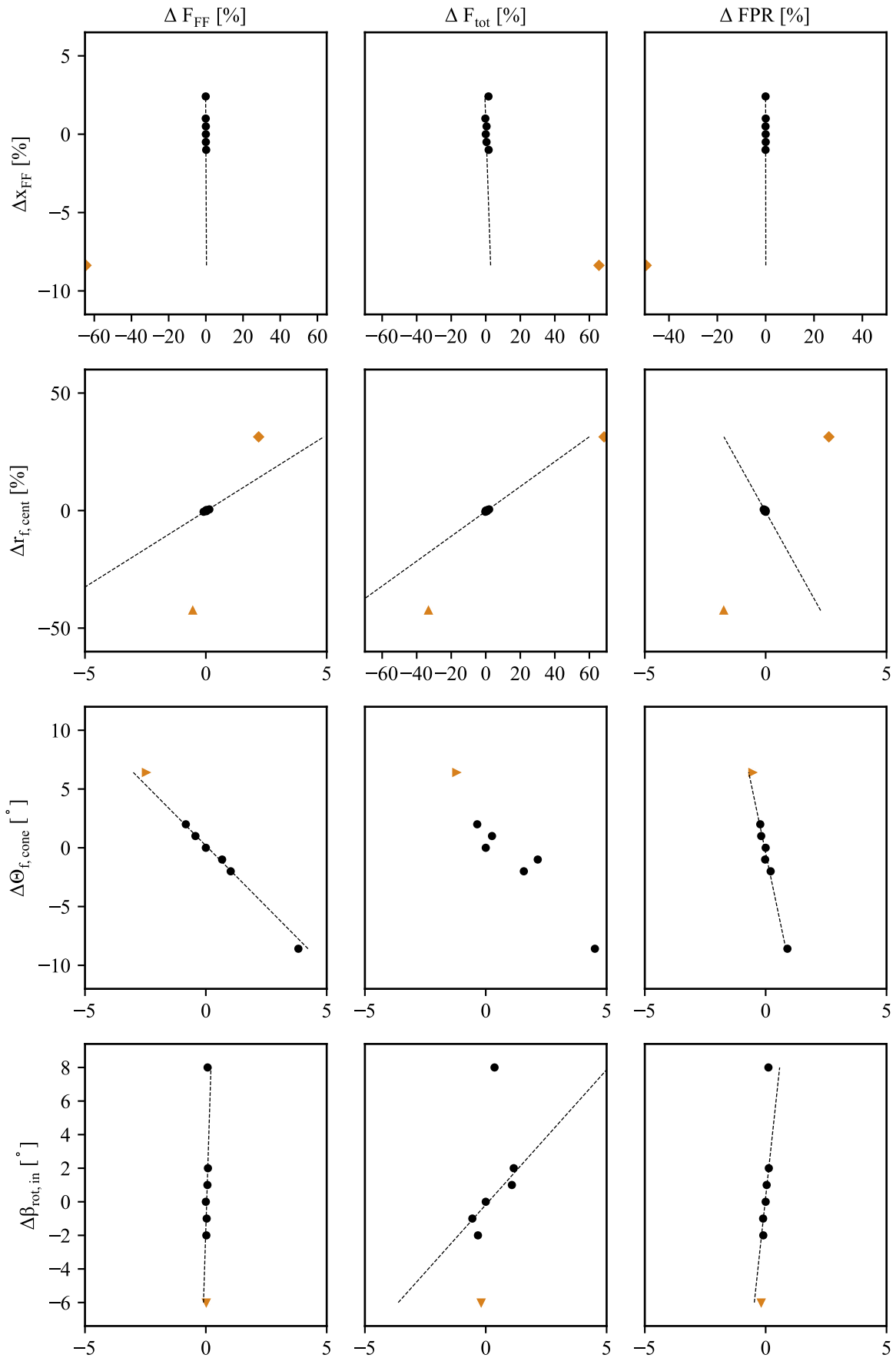


Figure 6.3: Extended parameter exploration study results. Regressions derived from sensitivity study results indicated (Figures A.6 - A.14, Appendix A.7).

- ▲ Shock on nacelle cowling; ▼ Shock inside FF duct; ► Shock on fuselage in front of FF; ◀ Shock on fuselage behind FF;
- ◆ Shock on fuselage body and flow separation incident to FF

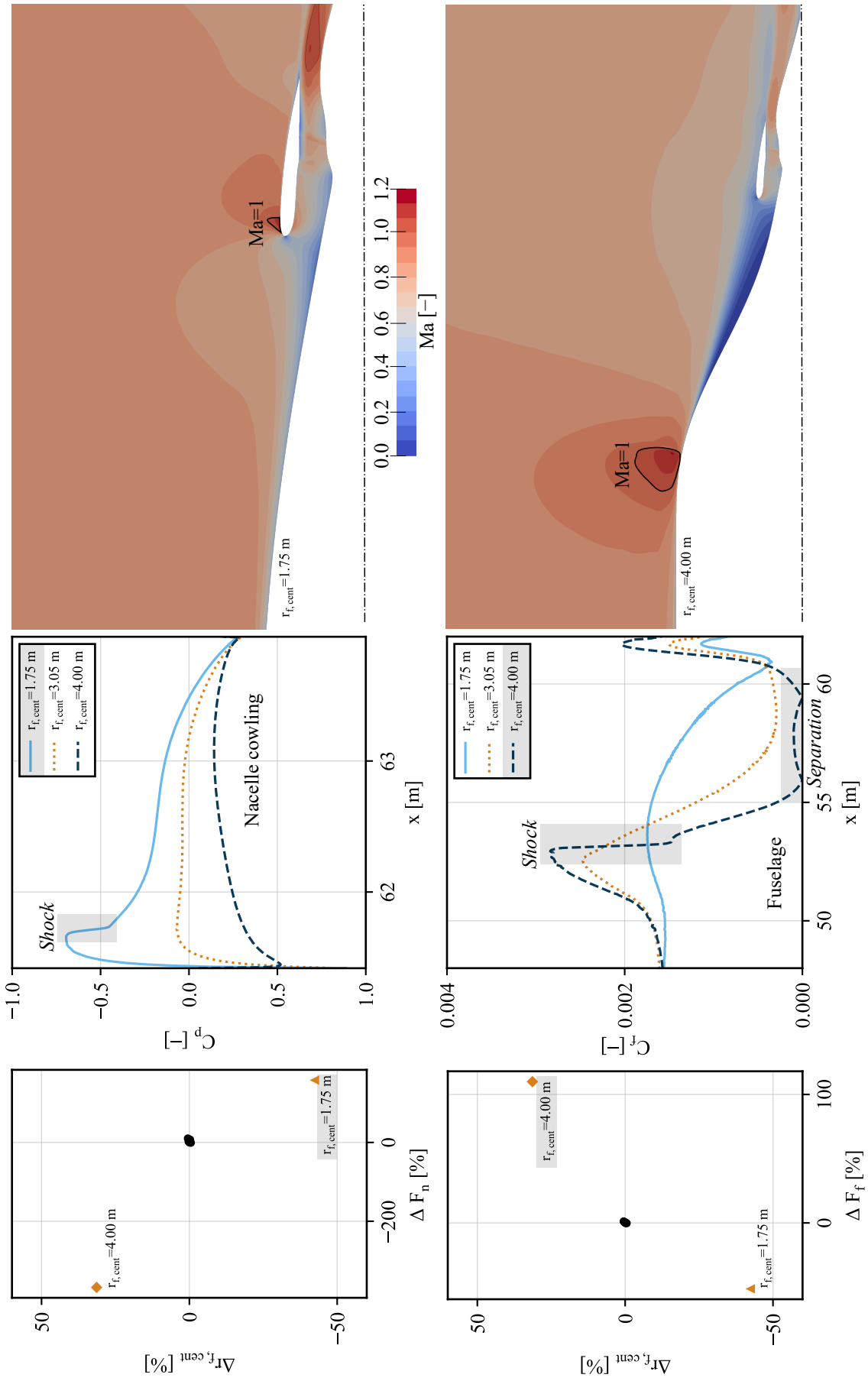


Figure 6.4: Nonlinear aerodynamic behavior for  $r_{f,cent}$  parameter variation.  
 ▲ Shock on nacelle cowling; ◆ Shock on fuselage body and flow separation incident to FF

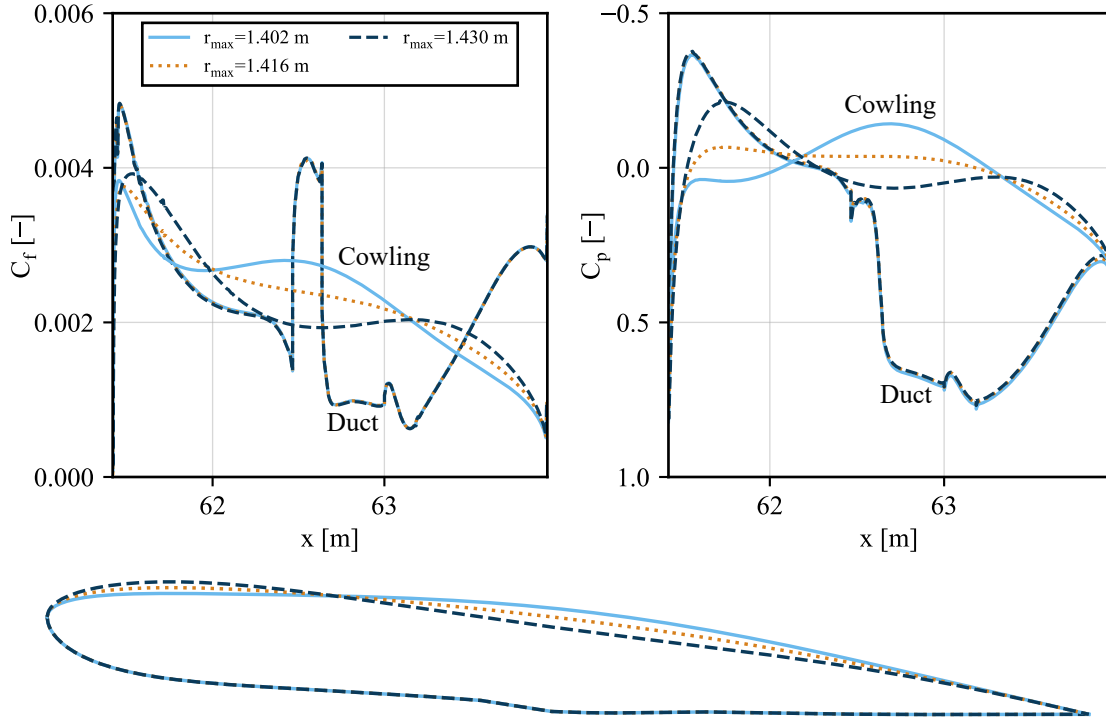


Figure 6.5:  $C_p$  and  $C_f$  distribution (top) along nacelle contour (bottom) for  $r_{max}$  variation.

further influences the local distribution of  $C_p$  and  $C_f$  along the fuselage aftbody and inside the FF duct near the nozzle, subsequently leading to a decrease in surface force acting on the FF duct. In most cases, the modification in the surface force of the duct dominates over the cowling force alteration. However, the interaction between the flow along the nacelle cowling, the flow characteristics at the FF inlet, and the flow downstream of the FF outlet, all of which impact FF performance, results in a nonlinear relationship between  $r_{max}$  and  $F_{PFC,bare}$  (see Appendix A.7, Figures A.12 and A.15). Consequently, no trend for the aero-propulsive performance can be derived for  $r_{max}$ .

$f_{l,thr}$  relates the distance of the FF throat to the FF highlight to the distance of the rotor inlet to the highlight. Despite inducing minor changes in the geometry of the FF duct, it exerts a notable influence on the pressure force acting on the upper side of the FF duct. Therefore, its adjustment requires careful consideration to optimize the aero-propulsive performance of the configuration.

Conversely, slight modifications in  $f_{A_{hi},A_{thr}}$ ,  $\beta_{TE,low}$ ,  $f_{r_{8,hub}}$ , or  $f_{r_{thr,tip}}$  result in significant alterations in the fuselage-propulsor geometry, because of the inherent interdependency due to the chosen parameterization strategy. Consequently, their impact on the aero-propulsive performance is substantial but follows nonlinear trends, making it challenging to define these parameters for optimal performance.

Increasing  $f_{A_{hi},A_{thr}}$  while keeping other parameters fixed leads to an expansion of the highlight area at a constant throat area. As a result,  $r_{hi,hub}$  increases, causing a slight steepening of the fuselage contour incident to the FF. This, in turn, reduces the mass flow-averaged velocity and density at the FF, resulting in a decrease in mass flow through the duct. Simultaneously, there is an increase in the average static temperature at the FF and rotor inlet, leading to a rise in  $P_{s,FF,pol}$ . Furthermore, alterations in the nacelle cowling contour contribute to a nonlinear variation in total surface forces and  $NPF_{PFC,bare}$  (see Appendix A.7, Figure A.15).

$\beta_{TE,low}$  defines the angle of the lower nacelle trailing edge. Its variation affects the upper duct contour in the nozzle area and the cowling contour downstream of  $x_{max}$ . These contour changes induce nonlinear variations in the fuselage and nacelle surface forces. Moreover, they impact the static pres-

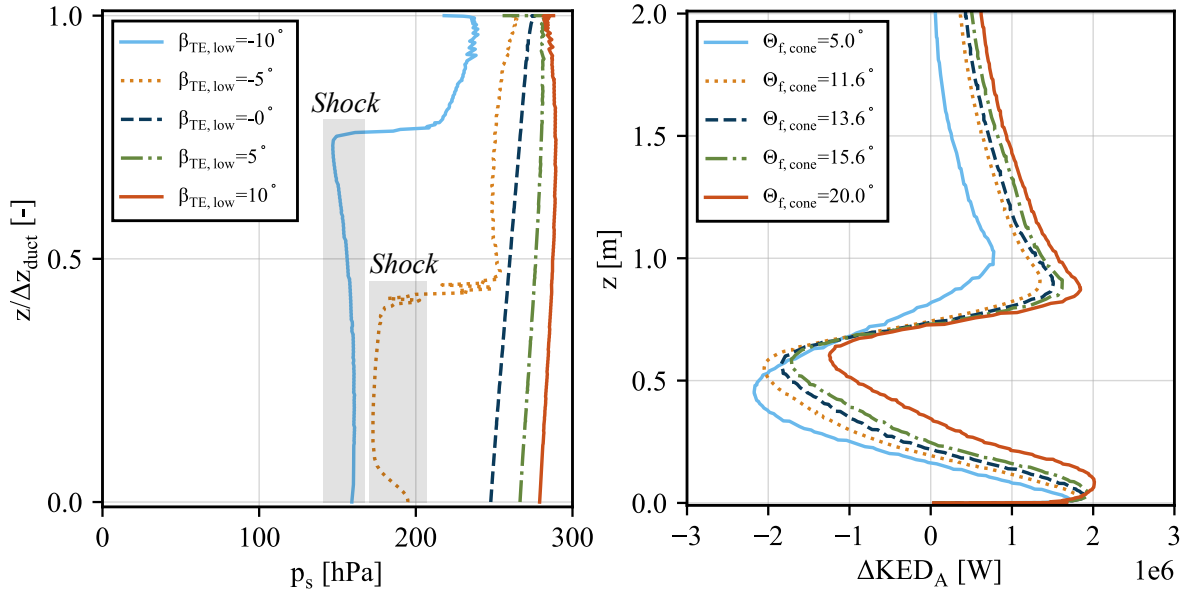


Figure 6.6: Static pressure at FF outlet (station 8) for  $\beta_{TE,low}$  variation (left) and  $KED_A$  difference between trailing edge and AIP station for  $\Theta_{f,cone}$  variation (right).

sure downstream of the FF exit (Figure 6.6, left), influencing FF performance. The geometry with  $\beta_{TE,low} = 10^\circ$  features the best aero-propulsive performance of the sample with  $NPF_{PFC,bare} = -8.90$  kN and  $P_{FF,s,pol} = 5.36$  MW resulting in  $f_{\eta,BLI,bare} = -0.40$ . For cases where  $\beta_{TE,low}$  is small ( $< -5^\circ$ ), the nozzle assumes a convergent-divergent profile, leading to the appearance of a sonic region inside the FF nozzle (see Figure 6.6, left). This sonic region prompts nonlinear behavior in FF performance.

Figure 6.7 provides a detailed depiction of the variation in  $f_{r_{8,hub}}$ , representing the ratio between the hub radius at the nozzle exit and the hub radius at the stator outlet. A larger  $f_{r_{8,hub}}$  results in a more pronounced "bump" at station 8. With  $\Theta_{f,cone}$  held constant, the total fuselage length and, consequently, the fuselage surface area increase. Simultaneously, changes occur in the nacelle cowling and duct contour. As a result, there is an alteration in the static pressure at the FF outlet, directly impacting FF performance. Furthermore, the reduction in velocity immediately downstream of the stator outlet (station 3) contributes to the variation in FF performance. The combination of these effects gives rise to nonlinear behavior in surface forces and FF performance concerning variations in  $f_{r_{8,hub}}$ , as illustrated in Appendix A.7, Figures A.13 and A.15. When  $f_{r_{8,hub}}$  reaches its maximum value of 1.3, a supersonic region emerges inside the nozzle duct near the fuselage surface.

Similarly, the variation of  $f_{r_{thr,tip}}$  exhibits a pronounced nonlinearity stemming from the chosen parameterization strategy. An alteration in  $f_{r_{thr,tip}}$  induces changes in the geometry of the fuselage upstream of the FF, the duct upstream of the rotor inlet, and the nacelle cowling, as depicted in Figure 6.8. The combination of geometric modifications leads to flow alterations, which interact. Consequently, both  $F_{nac,tot}$  and  $F_{f,tot}$  demonstrate nonlinear behaviors (refer also to Appendix A.7, Figures A.6-A.8, and A.15). Concurrently, variations in the FF inlet conditions occur, further influencing FF performance.

Minor variations in  $f_{r,2}$ ,  $\Theta_{f,cone}$ ,  $f_{A_8,A_3}$  or  $\beta_{rot,in}$  exert a considerable influence on the aero-propulsive performance of the fuselage-propulsor configuration, yet their effects do not exhibit a clear trend due to the nonlinear behavior of  $NPF_{PFC,bare}$ .

When  $f_{r,2}$  increases while  $h_{duct}$  is held constant, the hub and tip radius at the rotor inlet increase, resulting in a larger fan face area. Consequently, there is an increase in the mass flow, leading to a rise in  $P_{FF,s,pol}$ . Simultaneously, adjustments to the FF stage geometry, as per the scaling laws outlined in

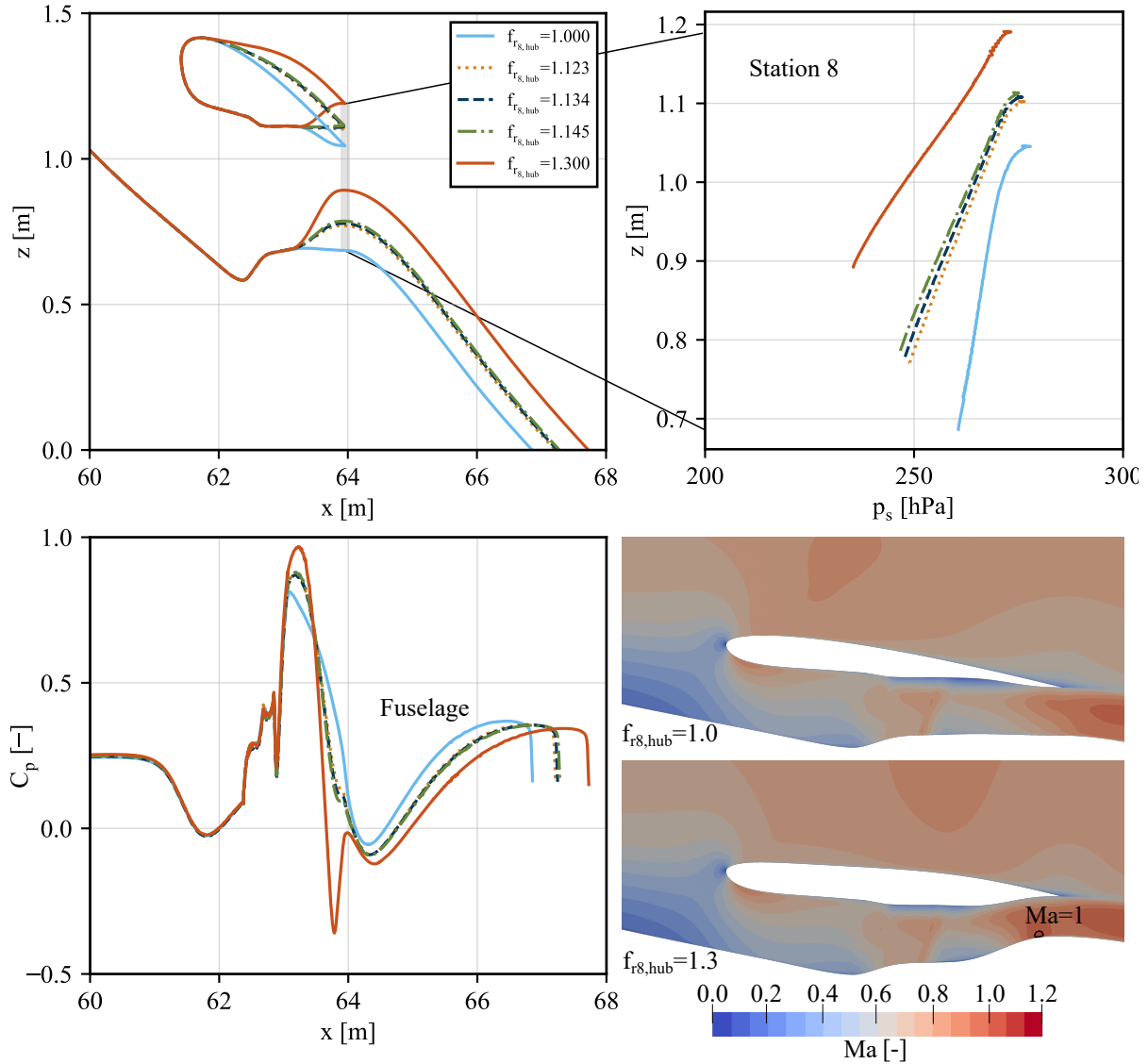


Figure 6.7: Nacelle and fuselage geometry (top left), static pressure at the nozzle exit (top right), pressure distribution along the fuselage contour (bottom left), and  $Ma$  distribution near the nacelle (bottom right) for  $f_{r8,hub}$  variation.

Section 5.6.3.5, contribute to a rise in  $FPR_{FF}$ , thereby augmenting shaft power and  $F_{FF}$ . Variations in fan performance subsequently impact local surface forces, causing an increase in fuselage pressure force on duct and boattail, which drives the rise in  $F_{PFC,bare}$ . In some cases, the surface force alteration dominates over the  $F_{FF}$  and vice versa. Thus, no definitive tendency for  $NPF_{PFC,bare}$  and  $f_{\eta,BLI,bare}$  can be derived.

For  $\Theta_{f,cone}$ , an increase in the boattail angle reduces  $F_{f,tot}$  due to decreases in surface area and improvements of the local  $C_p$  and  $C_f$  distribution. Notably, raising  $\Theta_{f,cone}$  from  $5^\circ$  to  $20^\circ$  reduces the total fuselage surface force by 10%. However, beyond a certain threshold, shock phenomena occur downstream of the nozzle exit (see Figure 6.3). Additionally, variations in boattail geometry influence the flow upstream of the nozzle exit by altering static pressures at the FF outlet and inlet. A  $15^\circ$  increase in  $\Theta_{f,cone}$  results in a modest rise in  $F_{nac,tot}$ , which is small compared to the reduction in fuselage surface force ( $\Delta F_{nac,tot} = 1.3\text{kN}$ ,  $\Delta F_{f,tot} = 3.2\text{kN}$ ). In combination, there is a tendency of decreasing  $F_{PFC,bare}$  with increasing  $\Theta_{f,cone}$ , albeit with a nonlinear behavior. Simultaneously, the decrease in

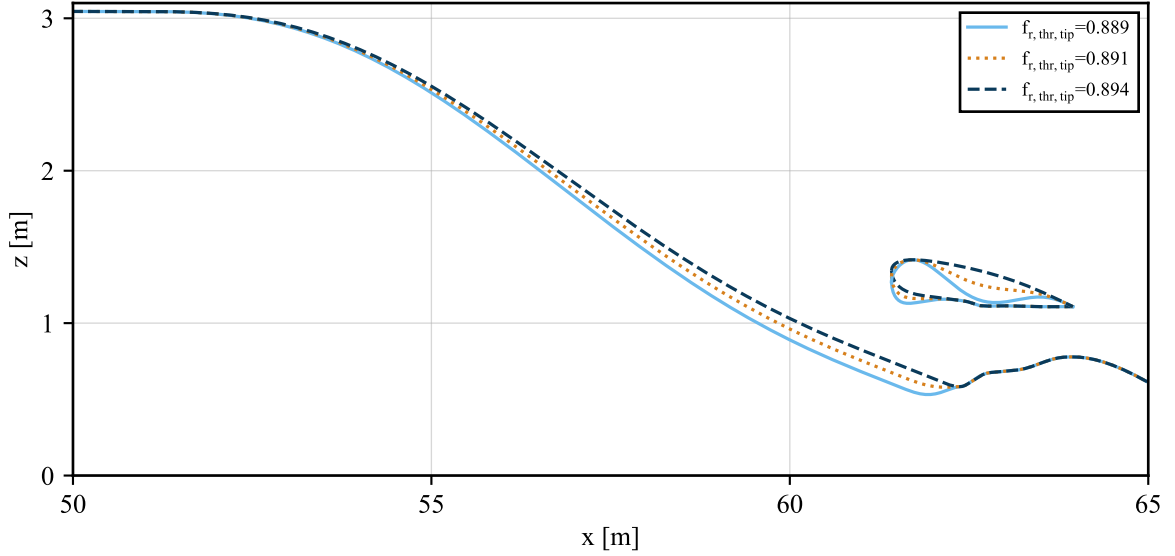


Figure 6.8: Nacelle and fuselage geometry for  $f_{r,thr,tip}$  variation.

mass flow-averaged static pressure at the FF outlet induces a reduction in  $FPR$ ,  $F_{FF}$ , and  $P_{FF,s,pol}$  by  $-6.1\%$  and  $-5.6\%$ , respectively. The increase in  $\Theta_{f,cone}$  precipitates an almost linear decrease in  $P_{FF,s,pol}$  and  $F_{FF}$ . Moreover, the steeper the boattail angle, the higher  $R_{KEDA}$ . Although the  $KEDA$  at the AIP remains relatively constant, the  $KEDA$  at the trailing edge surges by approximately  $18\%$  per  $1^\circ$  increment in  $\Theta_{f,cone}$ , because the excess kinetic energy inside the FF duct is reduced, while the  $KEDA$  outside of the FF increases (Figure 6.6, right). The kinetic energy recovery is diminished. The nonlinear behavior observed in performance indicators like  $f_{\eta,BLI,bare}$  stems from a combination of the effects discussed above.

Variations in  $\beta_{rot,in}$  solely affect the duct tip contour, influencing surface forces on the hub and tip contour, while  $F_{nac,tot}$  remains largely unchanged. Further,  $F_{FF}$  is mostly unaffected. Consequently, the nonlinear  $NPF_{PFC,bare}$  variation stems from the nonlinear behavior of  $F_{PFC,bare}$  (see also Appendix A.7, Figure A.15). When  $\beta_{rot,in}$  becomes too small, the FF throat shifts downstream toward the fan face, leading to a reduction in the throat area and inducing sonic flow within the throat, as depicted in Figure 6.9. Increasing  $\beta_{rot,in}$  from  $-10^\circ$  to  $4^\circ$  results in a  $15\%$  increase in  $P_{FF,s,pol}$  (Figure 6.3). This increment is attributed to a combination of increased mass flow and a change in the static temperature at the rotor inlet, induced by the duct contour upstream of the fan face (Figure 6.9). Although the change in shaft power is significant, the small nonlinear variation of  $NPF_{PFC,bare}$  is amplified when multiplied by the freestream velocity, leading to nonlinear behavior of  $f_{\eta,BLI,bare}$  (Figures A.9 - A.11, and A.15). In summary, even minor adjustments in  $\beta_{rot,in}$  can profoundly impact the required FF shaft power, thus exerting significant influence on the aircraft level through cascade effects.

The ratio of nozzle exit to stator outlet area,  $f_{A_8,A_3}$ , directly affects  $FPR$ . As  $f_{A_8,A_3}$  increases, the nozzle exit area  $A_8$  expands, leading to a decrease in  $FPR$ . Consequently,  $P_{FF,s,pol}$  and  $F_{FF}$  exhibit a linear decrease. The change in  $A_8$  influences the tip duct contour in the nozzle region and the nacelle cowling contour downstream of  $x_{max}$ , subsequently altering  $C_p$  and  $C_f$  along these surfaces (Appendix A.7, Figures A.9 - A.11, and A.15). In summary,  $f_{\eta,BLI,bare}$  tends to improve with decreasing  $f_{A_8,A_3}$ , primarily because the influence on surface forces outweighs the impact on FF performance.

Variation of the fan face duct height  $h_{duct}$  is similarly coupled to the FF performance through a linear relationship. Incrementing  $h_{duct}$  by  $0.5\%$  results in an increase in the mass flow through the FF duct, which translates to a rise in  $P_{FF,s,pol}$  by  $2.8\%$  and  $F_{FF}$  by  $2.0\%$ , respectively. Conversely, the relationship

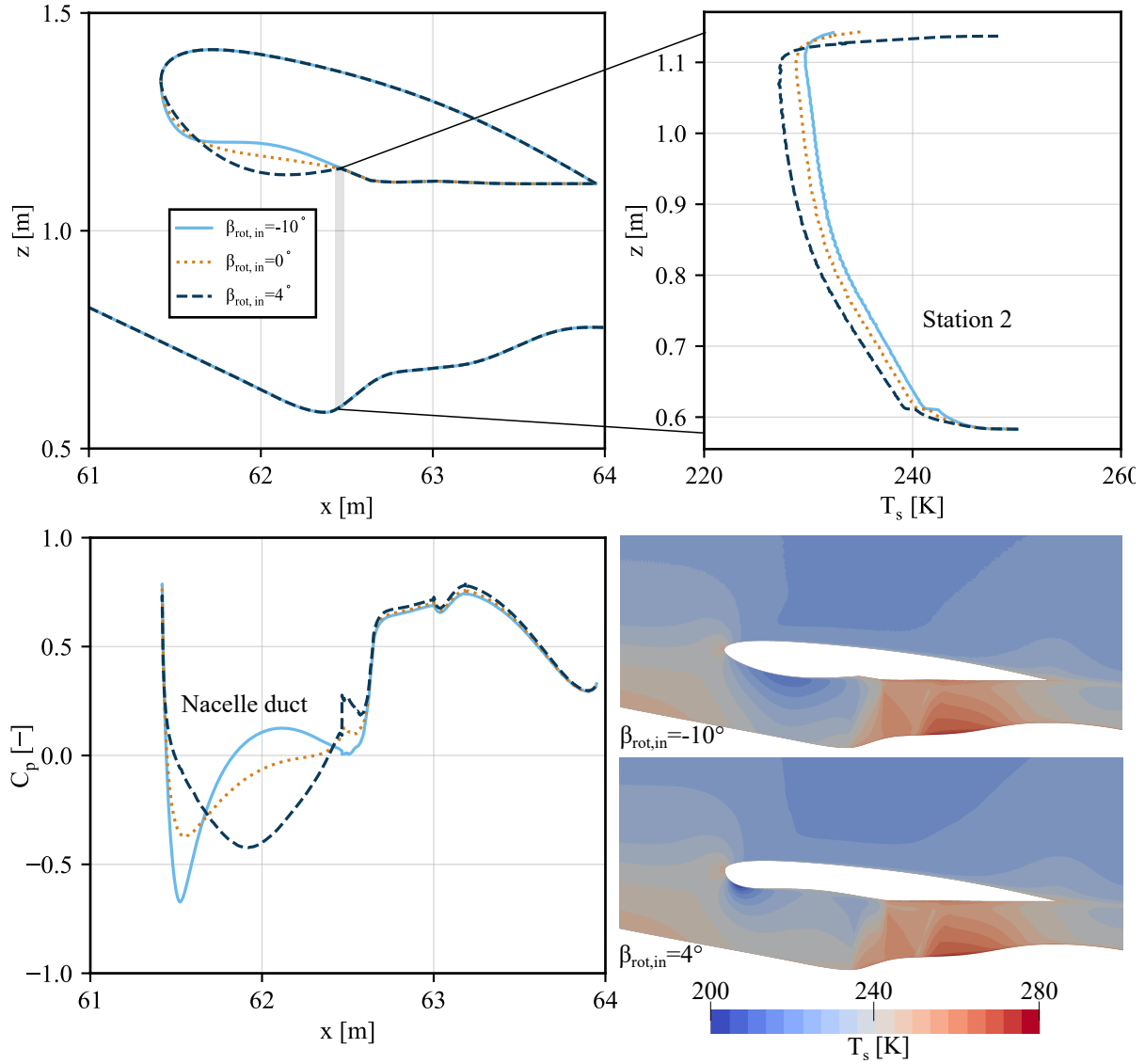


Figure 6.9: Nacelle and fuselage geometry (top left), static temperature at the rotor inlet (top right), pressure distribution along the nacelle duct contour (bottom left), and  $T_s$  distribution near the nacelle (bottom right) for  $\beta_{rot,in}$  variation.

between  $h_{duct}$  and the surface forces exhibits nonlinear characteristics. An observable trend indicates that  $F_{f,tot}$  rises with increasing  $h_{duct}$ , attributed to amplified pressure forces within the FF duct, while the impact on nacelle cowling forces remains marginal. In combination, the fuselage-propulsor force in drag direction improves for higher  $h_{duct}$ . Despite the significant increase in required shaft power, the enhancement of the  $NPP$  contributes to an improvement in  $f_{\eta,BLI,bare}$ . These findings are consistent with those of van Sluis et al. [106], who illustrated a 2nd-order polynomial relationship between  $h_{duct}$  and  $f_{\eta,BLI,bare}$  over a broader range of  $h_{duct}$  variations. Aero-propulsive results suggest favoring an increased  $h_{duct}$  to optimize the fuselage-propulsor performance. However, augmenting the duct height also entails increasing rotor and stator blade dimensions, posing challenges to FF structural integrity, increasing the rotor and stator disk weight and probably leading to issues related to high tip speeds. Consequently, a multi-disciplinary optimization of this parameter is imperative.

In addition to the geometric design parameters, two operational cruise parameters are studied:  $Ma$  and  $h_{alt}$  ( $FL$ ) serving as a proxy for the Reynolds number  $Re$ .

The findings regarding altitude variation corroborate those from a prior study [287] and a sensitivity analysis by van Sluis et al. [106]. With increasing altitude,  $p_{t,2}/p_{t,0}$ ,  $P_{FF,s,pol}$ , and  $NPF_{PFC,bare}$  decrease and a tendency for  $f_{\eta,BLI,bare}$  improvement can be observed. The alteration of the freestream conditions causes this. With a reduction in  $\rho_{\infty}$ ,  $u_{\infty}$ ,  $p_{\infty}$ , and  $T_{\infty}$  for higher altitudes,  $F_{PFC,bare}$  and  $F_{FF}$  decrease. As the variation in surface forces outweighs the alteration in  $F_{FF}$ ,  $NPF_{PFC,bare}$  demonstrates improvement. Transitioning from *FL250* to *FL400* results in a reduction of  $F_{PFC,bare}$  by  $\approx 50\%$ , alongside a decrease in  $F_{FF}$  and  $P_{FF,s,pol}$  by  $\approx 45\%$ . Additionally,  $p_{t,2}/p_{t,0}$  diminishes with increasing altitude, primarily due to the greater decline in mass flow-averaged total pressure at the fan face compared to the reduction in freestream total pressure. This shift is accompanied by increased radial distortion at the rotor inlet. Furthermore, despite significant alterations in absolute  $KED_A$  values at individual FF stations, variations in  $R_{KED_A}$ ,  $\beta_{KED_A}$ , and  $\beta_{MD}$  remain minor.

The variation in  $Ma$  induces substantial fluctuations in aero-propulsive performance, primarily driven by changes in  $NPF_{PFC,bare}$ . Increasing  $Ma$  from 0.73 to 0.86 results in a notable  $\approx 25\%$  increase in total surface force in drag direction, stemming from a combined rise in  $F_{f,tot}$  and  $F_{nac,tot}$ . Meanwhile,  $F_{FF}$  and  $P_{FF,s,pol}$  increase by a mere 100N and 1%, respectively. Consequently, the deterioration in aero-propulsive performance is predominantly governed by the degradation in  $NPF_{PFC,bare}$ . At  $Ma = 0.86$ , a shock manifests on the fuselage contour at the end of the constant center section, introducing nonlinearities in surface forces without instigating downstream flow separation. An increase in  $Ma$  prompts a reduction in  $p_{t,2}/p_{t,0}$ , in line with findings from the pre-study detailed in [287]. However, the trends for  $P_{FF,s,pol}$  and  $NPF_{PFC,bare}$  exhibited in this study demonstrate a higher degree of linearity compared to those reported in [287]. Further, for lower  $Ma$ ,  $\eta_{ad}$ ,  $R_{KED_A}$ ,  $\beta_{KED}$ , and  $\beta_{MD}$  improve. Consequently, the results suggest that a lower  $Ma$  is more favorable. Both operational parameters significantly influence the aero-propulsive performance of the fuselage-propulsor configuration. However, selecting optimal cruise conditions entails a complex process involving considerations of market requirements and the overall aircraft performance. Therefore, varying cruise conditions can offer valuable insights into aero-propulsive performance data for aircraft-level trade studies.

The exemplary sensitivity study demonstrates the efficacy and applicability of the HPFVM outlined in Section 5 for assessing the aero-propulsive performance of fuselage-propulsor configurations. The study not only corroborates findings from previous studies, such as the work by van Sluis [106], but also emphasizes the sensitivity of performance to even minor variations in design parameters. The results reveal a complex scenario where the impact of design parameters on aero-propulsive performance is nuanced and multifaceted. While some geometric parameters, particularly those defining the FF duct and nacelle cowling, demonstrate minimal impact, others, including  $r_{max}$ ,  $x_{FF}$ , and  $l_{f,cent}$ , exert significant influence on critical performance metrics such as  $NPF_{PFC,bare}$ . For most parameters, their impact on  $NPF_{PFC,bare}$  dominates over effects on the FF performance.

The analysis indicates that identifying specific trends for most parameters is challenging. However, the results highlight the importance of selecting an optimal fuselage contour incident to the FF to achieve optimal performance.

This investigation into the fuselage-propulsor design parameters brings to light the inherent complexities and interdependencies within the design parameters, often resulting in nonlinear responses in aerodynamic forces. Such complexity renders it challenging to determine which parameter values yield the optimal geometry given the holistic interplay of design parameters influenced by the chosen parameterization strategy and potential nonlinear flow phenomena. The findings further suggest that slight modifications to geometric design parameters around the baseline geometry offer substantial opportunities for improvement. The sensitivity analysis highlights the potential for further refinement, suggesting that a detailed, multi-dimensional parameter study is essential to identify the configuration that optimizes aero-propulsive performance.

Operational parameters also emerge as crucial factors, with performance varying significantly across operating conditions. This variation necessitates an extended evaluation of the fuselage-propulsor configuration's performance in off-design scenarios, encompassing the entire flight envelope.

Furthermore, the influence of fuselage-propulsor design parameters extends beyond aero-propulsive performance, affecting various aspects of aircraft performance and design directly and indirectly. This includes the structural weight of the fuselage (e.g., through  $r_{f,cent}$ ,  $l_{f,cent}$ , or  $x_{FF}$ ), the cowling (e.g.,  $r_{max}$ ,  $l_{nac}$ ), the rotor and stator weight (e.g., through  $h_{duct}$ ) and all other aircraft components, the FF propulsion system performance, which is directly impacted by  $P_{FF,s,pol}$ , and even the performance of the main engines, particularly in configurations involving a TEPT. Such wide-ranging effects call for an integrated, multi-disciplinary approach to aircraft optimization that combines aero-propulsive considerations with structural, propulsion, and operational demands. In conclusion, the findings from this study reinforce the potential of the developed hybrid numerical method in advancing the design and optimization of fuselage-propulsor configurations.

## 7 Aircraft Level Considerations

The aero-propulsive fuselage-propulsor performance has to be considered with respect to its impact on aircraft performance. Thus, an initial estimation of the effect of the fuselage-propulsor design parameters on aircraft-level characteristics is presented in Section 7.1. Section 7.2 outlines a practical approach to integrating the derived numerical methodology into an aircraft conceptual design framework (RQ 8).

### 7.1 Impact of Fuselage-Propulsor Design on Design Mission Block Fuel

For an initial estimation of the effect of the fuselage-propulsor geometry variation on aircraft performance, the results from the integrated aircraft design and sizing study conducted as part of the *CENTRELINE* project and documented in [110] are employed. The impact of the geometry variation on the aero-propulsive performance can be split up into two parts: the influence on the fuselage-propulsor aerodynamics, represented by  $NPF_{PFC,bare}$ , and the impact on the required FF shaft power  $P_{FF,s,pol}$ . Both factors, in turn, lead to cascade effects on aircraft level. As part of the aircraft-level sensitivity studies of the final *CENTRELINE* PFC, the impact of an isolated  $NPF_{PFC,bare}$  variation on the aircraft's performance was studied. Here, an artificial constant  $NPF_{PFC,bare}$  increment was introduced throughout the mission. It was found that an improvement in  $NPF_{PFC,bare}$  of 1 kN (an increase of the force in thrust direction) leads to a design mission *BF* reduction of  $-1.51\%$  [110]:

$$\frac{-1.51\% \text{ BF}}{1 \text{ kN } \Delta NPF} \quad (7.1)$$

The relationship between small changes in  $NPF_{PFC,bare}$  with respect to the reference aircraft configuration on *OEM* (Operating Empty Mass), *MTOM* (Maximum Take-Off Mass), and design mission *BF* is depicted in Figure 7.1 (left).

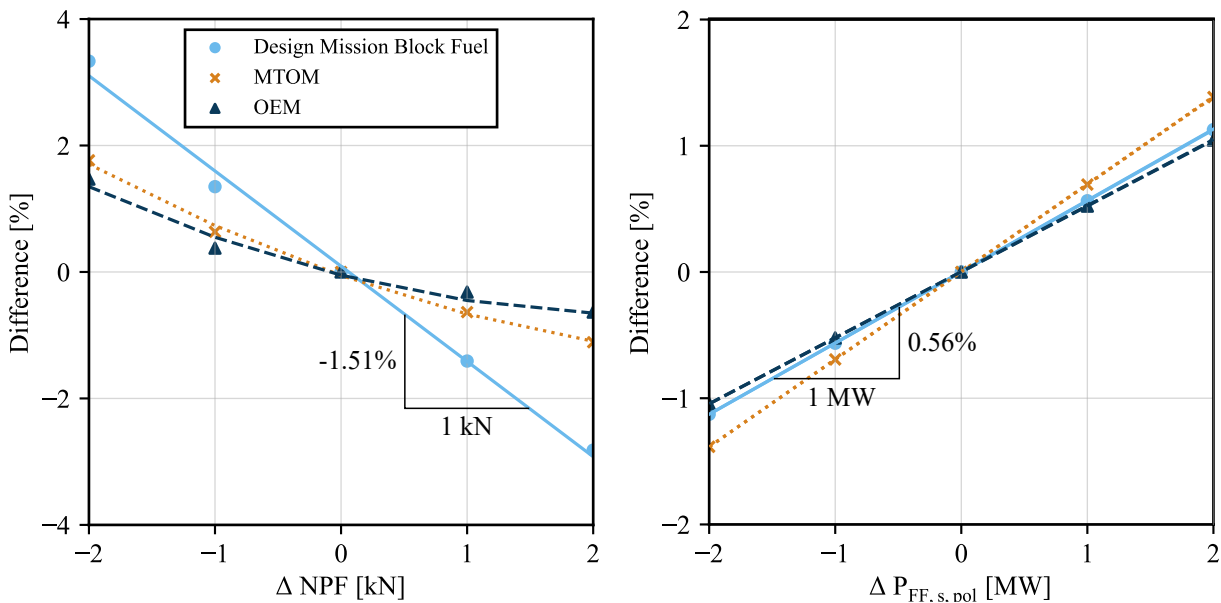


Figure 7.1: Aircraft sensitivity study results for  $NPF_{PFC,bare}$  adapted from [110] (left) and sensitivity for isolated FF isentropic design shaft power derived from [110] (right).

A study of the effect of an isolated  $P_{FF,s,pol}$  variation on aircraft-level parameters was not conducted in [110]. Thus, its impact is emulated by deriving an *OEM* alteration as a direct effect of an increase in FF shaft power. A positive  $P_{FF,s,pol}$  increment corresponds to a FF performance deterioration.

From [110], the gravimetric power density of the components of the TEPT is known. For the current approximation, it is assumed that the gravimetric power densities and the efficiencies of all components (propulsor, FF motor, generators, cables, and power electronics) are constant for the required power range. Further, the weight and fuel flow of the underwing podded gas turbines is unaffected, even though the required power off-takes vary. In addition, it is assumed that the fuselage structural mass does not change with the change in fuselage-propulsor geometry.

An *OEM* increment sensitivity study emulated the variation of component weight parameters in [110]. Based on integrated aircraft studies, the following relations, which are valid for small variations of the *OEM* with the PFC baseline aircraft as the pivot point, were derived [110]:

$$\frac{0.83\% \text{ BF}}{1 \text{ t } \Delta \text{OEM}} \text{ and } \frac{1.02\% \text{ MTOM}}{1 \text{ t } \Delta \text{OEM}} \quad (7.2)$$

For a range of  $P_{FF,s,pol}$ , the variation of *OEM* is calculated from the specified parameters of the final *CENTRELINE* PFC configuration. Using Equations 7.2, the effect of the *OEM* alteration on *MTOM* and design mission block fuel is estimated (see Figure 7.1 (right)). The following sensitivity of the design mission fuel burn to the  $P_{FF,s,pol}$  variation is derived:

$$\frac{0.56\% \text{ BF}}{1 \text{ MW } \Delta P_s} \quad (7.3)$$

Combining Equations 7.1 and 7.3 leads to the total design mission block fuel impact of the geometrical variation of the fuselage-propulsor geometry:

$$\Delta \text{BF}_{\text{tot}} = \frac{-1.51\% \text{ BF}}{1 \text{ kN } \Delta \text{NPF}} + \frac{0.56\% \text{ BF}}{1 \text{ MW } \Delta P_s} \quad (7.4)$$

Figure 7.2 provides an overview of  $NPF_{PFC,bare}$  and  $P_{FF,s,pol}$  impact on BF. The results are derived from the aero-propulsive results of the parameter study presented in Section 6. Figure 7.3 illustrates the impact of varying geometrical parameters on the design mission block fuel for selected parameters in detail. It can be observed that the geometry with the best aero-propulsive performance denoted by "+" in Figure 7.2 does not correspond to the geometry with the highest BF improvement. Instead, the configuration with the highest  $NPF_{PFC,bare}$  improvement ("⊕") shows the biggest BF improvement of  $\Delta \text{BF} = -0.8\%$ . Thus, for the current aircraft configuration,  $NPF_{PFC,bare}$  is deemed a more suitable optimization objective for the fuselage-propulsor geometry than  $f_{\eta,BLI,bare}$ .

In most cases where the flow remains free of shocks or separations, the *BF* alteration due to changes in  $NPF_{PFC,bare}$  is notably higher than alterations in  $P_{FF,s,pol}$ . However, for some parameters this trend reverses. For the geometric parameters  $f_{r,12}$  and  $A_8/A_3$ , the *BF* change due to alterations in the required FF shaft power  $P_{FF,s,pol}$  dominates over a *BF* alteration caused by  $NPF_{PFC,bare}$  variation. For these cases, the increase or decrease in  $F_{FF}$  is offset by a similar rise or reduction in  $F_{PFC,bare}$ , leading to a small  $NPF_{PFC,bare}$  alteration compared to the concurrent significant  $P_{FF,s,pol}$  increase (depicted for  $A_8/A_3$  in Figure 7.3, see also Section 6). The throat tip radius parameter  $f_{thr,tip}$ , which describes the ratio between the throat and highlight tip radius, is an example of the opposite behavior. When the factor is reduced by 1% compared to the reference,  $P_{FF,s,pol}$  decreases by 3.0%, while  $NPF_{PFC,bare}$  increases by 14.6% (in drag direction) due to a combination of a 2.8% reduction of  $F_{FF}$ , which is reinforced by a 2.2% increase of the surface forces (see Figure 7.3). For the studied fuselage-propulsor configuration,

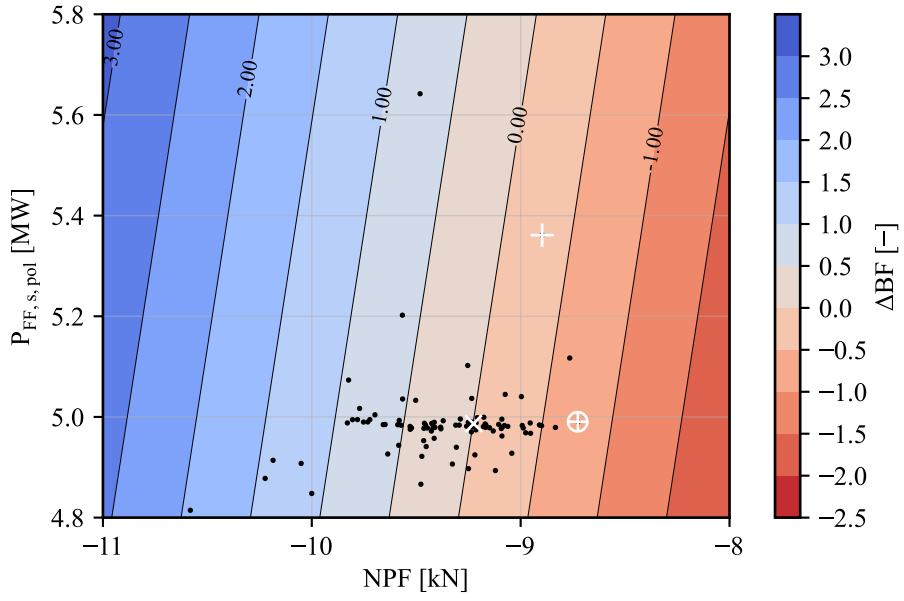


Figure 7.2: Relationship between  $NPF_{PFC,bare}$ , FF shaft power, and BF. Geometric parameters only.

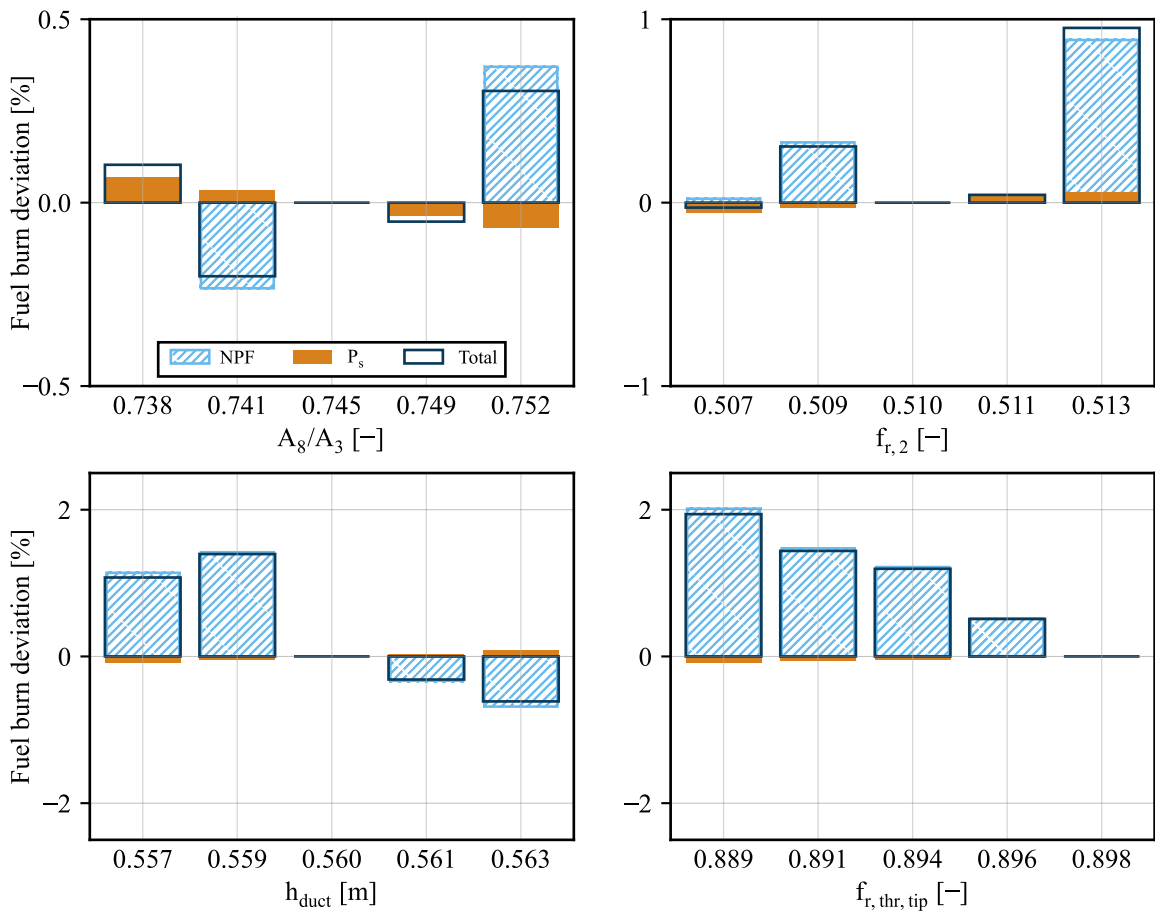


Figure 7.3: Design mission fuel burn impact of selected geometric parameters.

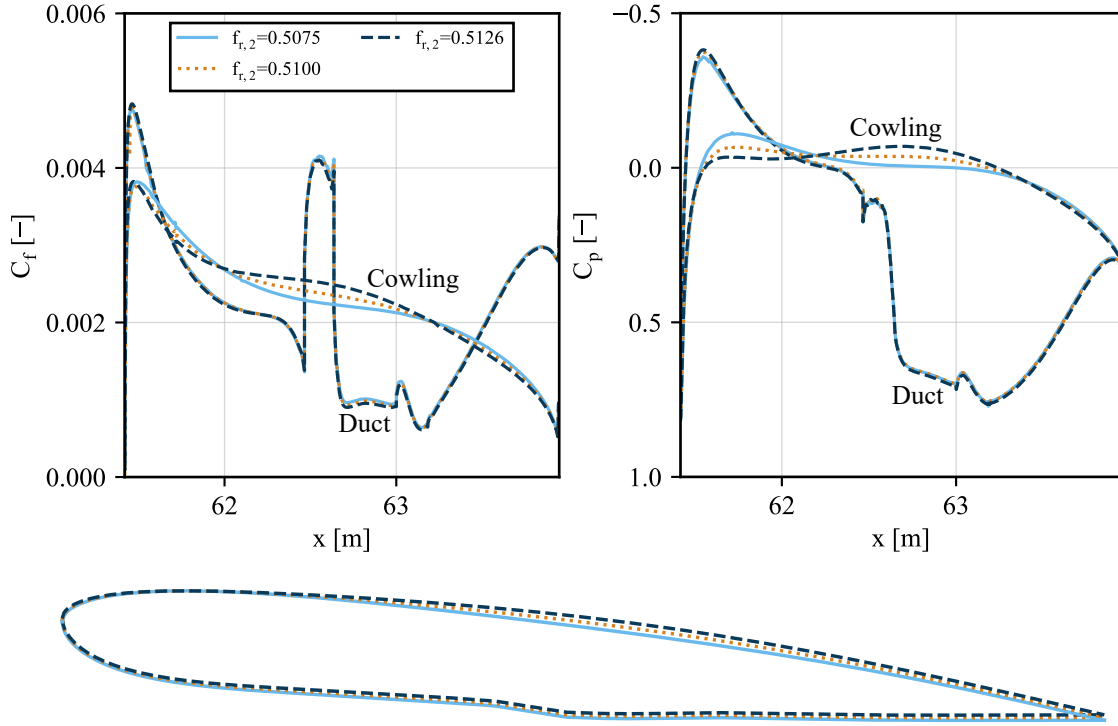


Figure 7.4:  $C_p$  and  $C_f$  distribution (top) along nacelle contour (bottom) for  $f_{r,2}$  variation.

where  $NPF < 0$  for all studied configurations, the following relations can be derived from Equations 7.1 and 7.3 for the reference geometry:

$$\frac{0.03\%BF}{1\%\Delta P_s} \text{ and } \frac{-0.14\%BF}{1\%\Delta NPF} \quad (7.5)$$

Thus, the deteriorating effect of the  $NPF_{PFC,bare}$  increase compared to the  $P_{FF,s,pol}$  reduction is further amplified on aircraft level. Consequently, reducing  $f_{thr,tip}$  leads to a small decrease in  $BF$  due to the reduction in  $P_{FF,s,pol}$ , which is dominated by the  $BF$  increase attributed to the deterioration of  $NPF_{PFC,bare}$ .

The results of some parameter studies indicate how geometric parameters can be altered to achieve a better aircraft-level performance of the PFC. Trends indicate that  $h_{duct}$  could be bigger and that the fuselage-propulsor configuration performs better for higher  $f_{thr,tip}$  ratios (Figure 7.3). Further, the performance is improved for a smaller duct angle at the rotor inlet  $\beta_{ff,in}$ . Within the studied parameter range, some parameters, such as  $\Theta_{f,cone}$ ,  $A_{thr}/A_2$ , and  $f_{thr,tip}$  show a local minimum for the reference geometry (Figures 7.3 and A.6 - A.14).

In general, however, the aircraft-level results mirror the geometric dependency and nonlinear aerodynamic effects of variations discussed in Section 6. Consequently, determining optimal values for most parameters is challenging, and no clear guidance can be derived for defining an optimum fuselage-propulsor geometry. One example is the hub-to-tip ratio at the FF rotor inlet  $f_{r,2}$ . When keeping all other parameters constant, changing  $f_{r,2}$  alters all other duct areas and, further, alters the nacelle cowling contour. Thus, the integrated surface forces in the FF duct and on the nacelle cowling change following a nonlinear trend. Figure 7.4 depicts the nacelle geometries of the studied  $f_{r,2}$  cases along with the skin friction and pressure coefficient distributions along cowling and duct. Consequently, even though the increase in  $f_{r,2}$  leads to an almost linear rise in  $FPR$ ,  $F_{FF}$ , and  $P_{FF,s,pol}$ , the total  $FB$  alteration, which depends mostly on the  $NPF_{PFC,bare}$  alteration does not follow a linear trend.

The analysis in Section 6 highlights that geometric variations within the fuselage-propulsor configuration can lead to notable changes in aero-propulsive figures of merit. Despite these variations, the design mission block fuel burn deviation remains within  $\pm 2\%$  for all studied configurations. However, considering that the actual geometric variations are small and that the  $NPF_{PFC,bare}$  variation is substantial, their impact on aircraft performance is deemed significant. Therefore, geometric optimization of the fuselage-propulsor configuration becomes imperative.

Moreover, the study reveals that variations in  $NPF_{PFC,bare}$  serve as a more pivotal indicator of improvements in BL than the aero-propulsive performance metric  $f_{\eta,BLI,bare}$ .

It is important to note that these results offer an initial insight into the parameter effects on aircraft-level performance, relying on trade studies of a single aircraft configuration. For a more comprehensive evaluation, integrated aircraft studies must be conducted.

## 7.2 Integration of Aero-Propulsive Performance Data in Aircraft Design Framework

In Section 2.2.2 it was established that models suitable for integrated aircraft design in the conceptual design phase must be fast-responding and capable of covering a broad design space. At the same time, they should accurately represent the physics of the component or discipline. Reviewing aero-propulsive models for PFC aircraft studies revealed that fuselage-propulsor performance is commonly modeled using uncoupled numerical models with simplifying assumptions (see also Section 2.2.3).

Directly integrating the developed hybrid numerical method into an aircraft design and sizing framework is impractical due to the time-consuming nature of simulating each geometry for all required design and off-design conditions. Therefore, a proposed solution is deriving and integrating a surrogate model based on numerical simulation data. Generating this surrogate model involves running and processing numerical simulations prior to the aircraft-level study, effectively decoupling the two. This approach, akin to the integration of engine performance data in an aircraft design framework demonstrated by [96, 288], has been previously employed for aero-propulsive surrogate models in the context of BLI in aircraft conceptual design by Ahuja [37].

Furthermore, the surrogate model facilitates an additional sensitivity analysis by allowing the investigation of the relative importance and impact of the input variables on the system's output. This helps understand the system's behavior and identify key factors influencing BLI performance.

Results from the parameter study confirm interdependencies among geometric and operational parameters, emphasizing the need for a multi-dimensional parameter variation to accurately assess their combined effects [117, 130, 133, 287]. In contrast to a 1D sensitivity study (see Section 6), the number of possible parameter combinations in a multi-dimensional parameter study is vast, even if the number of mutations per parameter is limited. Thus, surrogate modeling ensures an accurate representation of the design space while maintaining computational efficiency, enabling an efficient exploration, analysis, and optimization of the design space [289]. The steps involved in generating and applying a surrogate model include:

- Definition of the interface between surrogate model and aircraft framework, i.e., input and output parameter definition.
- Design of Experiment (DoE) selection.
- Sample plan generation, i.e., selection of input parameter combinations.
- Output data generation, i.e., HPFVM simulations, including simulation data processing.
- Surrogate model selection.

- Surrogate model training.
- Surrogate model validation.
- Surrogate model refinement.
- Surrogate model evaluation, including sensitivity analysis, uncertainty quantification, and optimization.

Once generated, the surrogate model can be integrated into the aircraft design framework. For each combination of aircraft level requirements (e.g., design flight conditions, fuselage center section width and length, FF propulsor geometry), the optimal fuselage-propulsor geometry and its aero-propulsive performance in design and off-design conditions can be extracted from the surrogate model and provided for the aircraft level design and sizing study. A wide range of methods exists for the DoE and surrogate model generation. A pre-study presented in [110] demonstrated the applicability of the following methods for the surrogate generation of the aero-propulsive performance of fuselage-propulsor configurations.

The systematic approach to creating a sampling plan, known as DoE [290], is essential for minimizing the computational effort in deriving an accurate surrogate model. Two main categories exist for generating a sampling plan: random sampling methods, which involve randomly generating sample points in the design space, providing diverse coverage and effective capturing of local variations, and deterministic sampling methods, aiming to systematically cover the design space with evenly distributed points to explore global system behavior. Examples of deterministic sampling methods include Latin Hypercube Sampling (LHS), orthogonal arrays, and uniform grids [289, 291]. LHS, a highly flexible method applicable to various scenarios, particularly suits high-dimensional problems. It ensures an even coverage of the design space and is space-filling. Compared to other techniques, LHS offers a high level of efficiency, i.e., a relatively small number of samples is required to obtain a reliable representation of the system's behavior. Thus, LHS is the most applied sampling technique for simulation-based experiments in aerodynamic design evaluation and optimization [292]. An extension of LHS by the maximin criterion, introduced by Johnson et al. [293], enhances efficiency and ensures space filling of the DoE. Given these advantages, Maximin LHS is considered suitable for creating the sampling plan for the multi-dimensional parameter study.

Due to the inherent nonlinearities of the aerodynamic functions, determining the sample size for a specified model accuracy is impossible for aerodynamic problems [292]. However, as a rule of thumb,  $n = 10 \cdot d$  is a reasonable size for an initial sample (e.g., [294]).  $n$  is the number of samples, and  $d$  is the dimension of the design space. Thus, for a total of 25 geometrical and operational design parameters, 250 samples have to be evaluated, where each sample point corresponds to a unique fuselage-propulsor geometry. The high flexibility of the geometry parameterization strategy (see Section 5.3) allows the generation of unphysical fuselage-propulsor geometries. These geometries must be identified in a pre-processing step and discarded from the sample. For each sampled design, operational design and off-design conditions have to be defined and calculated, significantly increasing the number of required simulations. Further, off-design terms for the BFM of the FF have to be defined and included in the existing model (see Section 5.6.3).

Various surrogate modeling approaches cater to different problems. The selection of an appropriate technique depends on the nature of the problem (number of design variables and linearity of response), available data, computational resources, and the desired balance between accuracy and computational efficiency. Data fit surrogate models can be categorized as interpolation or regression methods. Interpolation methods, such as radial basis functions and Kriging surrogates, accurately represent sampled data points and estimate the output response at the unobserved points within the range of the input variables. Regression methods, including linear, polynomial, support vector regression, or artificial neural networks, utilize statistical regression techniques to approximate the relationship between input variables and output responses. The prediction error is minimized by fitting a mathematical function or

model to the sampled data [289, 292, 295]. Reduced-order models for linear and nonlinear systems enable high-dimensional function modeling, which is beneficial for various applications in aerodynamics. Multi-fidelity models combine low- and high-fidelity data to solve high-fidelity optimization problems, and hybrid surrogate models combine several of the introduced surrogate models [292]. Selecting an appropriate surrogate modeling technique relies on the specific requirements and complexity of the design problem, the characteristics of the input and output data, and the desired trade-offs between accuracy, complexity, and generalizability. Choosing an appropriate modeling approach for aerodynamic design is especially challenging due to the lack of prior knowledge about the underlying function trends, which are often highly nonlinear and highly dimensional [292]. For the proposed application, an Ordinary Kriging or Gaussian process regression approach, initially presented by [296], is recommended for constructing the surrogate model. Kriging-based models are recognized for their high accuracy and flexibility in representing nonlinear system responses, which occur for aerodynamic design optimization problems. Additionally, they perform well for design problems with a high number of design variables (up to 50), such as the present problem [292, 297]. Successful applications of Kriging approaches include the aerodynamic design optimization of an airfoil [298], a wing [297], an engine nacelle [299], a separate-jet exhaust system design [300], and the optimization of a complete aircraft configuration [301].

Once the surrogate models are trained, the surrogate functions are validated by comparing their output with the CFD solution of a validation sample data set. The validation data can include the data points from the 1D sensitivity study (Section 6) and an additional set of geometries, which were not part of the original training data set. The prediction error is measured using the error metrics  $RMSE$ ,  $R^2$ , and the Mean Absolute Percentage Error ( $MAPE$ ) [302]. Additional simulations must be run to refine the surrogate functions if required.

The validated Kriging surrogate models can then be integrated into the aircraft design framework and utilized in optimization algorithms to efficiently identify optimal fuselage-propulsor solutions in the design space given a set of input parameters [292].

Conveniently, the *Python* toolboxes *pyDOE2* [303] and *pyKriging* [304] can be employed to generate the sampling plan and to train and evaluate the surrogate model.



## 8 Conclusion and Future Directions

Mitigating the environmental impact of aviation necessitates the exploration and development of innovative aircraft technologies and concepts. The PFC, characterized by a tight coupling of the airframe and propulsion system through efficient ingestion and re-energization of the fuselage's BL, stands out for its potential to substantially reduce the mission energy requirements of commercial aircraft. However, integrating a full annular propulsor at the aft section of the fuselage represents a radical departure from traditional aircraft design.

The research presented in this thesis assessed the coupled aero-propulsive performance of propulsive fuselages within the context of conceptual aircraft design. By developing a fast-responding, accurate numerical model, it sought to overcome the limitations of conventional design practices, addressing the distinctive challenges posed by fuselage BLI configurations. The dissertation systematically explored critical RQs, from establishing a consistent evaluation framework for concepts incorporating fuselage wake-filling to identifying, developing, validating, and applying a hybrid numerical method for the aero-propulsive assessment of such innovative designs in the aircraft conceptual design phase.

The systematic review of bookkeeping methods identified an integral momentum conservation approach as the most practical for ensuring consistency in the coupled aero-propulsive assessment of fuselage-propulsor configurations within multi-disciplinary aircraft design frameworks, addressing RQs 1 and 2. While providing fewer details for geometry optimization than energy and exergy-based evaluations, this approach facilitates the integration of PFC assessments with other disciplines. Several figures of merits were identified, which can be employed to quantify the performance of configurations with BLI. The propulsive efficiency factor  $f_{\eta,BLI,bare}$  was derived as a universal figure of merit to capture the coupled aerodynamic and propulsion system effect (RQ 3). These figures provide a nuanced understanding of the aero-propulsive interactions, offering valuable insights into optimizing the fuselage-propulsor design.

By identifying the requirements for estimating the potential of PFCs at the aircraft level and answering RQ 4, a critical gap was identified in existing numerical methodologies, notably in accurately modeling the complex, coupled aero-propulsive performance. Existing approaches neglect this coupling or rely on computationally intensive methods that are impractical for the rapid iterations required in conceptual design. Addressing RQs 5 and 6, the thesis proposed and implemented a novel hybrid numerical approach that balances computational speed and accuracy to address this deficiency. By combining viscous/inviscid PM calculations with FV solutions of the RANS equations and a BFM, this strongly coupled approach enables comparably fast and accurate assessments of aero-propulsive performance, supporting the design and optimization of PFCs in the early stages of aircraft development.

The application of the HPFVM to a sensitivity study emphasized the critical role of geometric optimization of the fuselage-propulsor configuration in aircraft design. This finding, linked to RQ 7, demonstrated that even minor geometry alterations could significantly impact aero-propulsive fuselage-propulsor and aircraft performance. Variation of most parameters caused a highly nonlinear behavior of the performance indicators, which highlighted the necessity of comprehensive, multi-dimensional parameter studies for geometry optimization. Further, the streamwise force  $NPF_{PFC,bare}$  was suggested as a more fitting optimization objective over the previously considered  $f_{\eta,BLI,bare}$ .

This research extends to integrated aircraft design, providing a systematic framework and a feasible approach to integrate parameterized BLI performance data in the form of a surrogate model to an aircraft design and sizing framework as an answer to RQ 8. These contributions can significantly enhance the representation of the aero-propulsive performance of FFs in aircraft design frameworks, facilitating the exploration of PFCs geared toward sustainable aviation. As the method is not limited to specific aircraft configurations or propulsion energy sources, it can be applied to various PFC designs, including

those powered by alternative energy sources such as batteries or hydrogen. Furthermore, the open-source availability of the HPFVM not only democratizes access to advanced research tools but also encourages collaborative efforts to refine and expand its applications, potentially accelerating the development of PFCs and similar configurations.

The numerical method developed and applied in this study has been successfully validated and verified. However, it is subject to several limitations that merit attention and suggest directions for future work. The method is confined to the assessment of isolated 2D-axisymmetric fuselage-propulsor configurations and cannot account for 3D effects, such as the impact of wing downwash or VTP, 3D fuselage shapes (elliptical cross-sections, fuselage upsweep), or the influence of the belly fairing. Additionally, it cannot handle unsteady flows, angles of attack, or sideslip angles. The parameterization strategy revealed inherent interdependencies among geometric design parameters that might pose challenges to optimizing the geometry.

The PM employed to determine the BL characteristics in the front part of the fuselage generally performs well, as shown by comprehensive validations. However, it cannot handle shocks or separation in front of the PM/FVM interface, and the transition modeling is simplified. The uncalibrated BFM, used to model the effect of the FF on the flow in the FVM, reduces the complexity of rotor and stator interactions to 2D-axisymmetric assumptions. Given these simplifications, and due to the scaling strategy applied to the original fan stage geometry from the *CENTRELINE* project, it is acknowledged that the fan might not perform optimally across all studied configurations. In future studies, a range of fan stage geometries optimized for different operating conditions might cover a broader design space. Further, the BFM will have to be calibrated with off-design fan stage performance data to adequately model the operational behavior of the fan in off-design conditions. Coupling the HPFVM with a more detailed FF model, such as the 1D TDC method outlined by Bijewitz [96], could potentially increase the fidelity of the FF performance modeling for aircraft design.

While being the fastest numerical approach for sufficiently accurate modeling of the aero-propulsive performance of a PFC, the HPFVM did not achieve impressive computational speed advantages over the simulation of the whole geometry with FVM. Even though the PM solution only requires several seconds, the FVM simulation time dominates (approx. 200 CPU hours per simulation). Due to the extensive influence of the FF far upstream of the fan stage, the number of cells in the FV domain and, thus, the total simulation time could only be reduced by 25%. Consequently, directly integrating the method into an aircraft design and sizing framework was deemed impractical, and employing FV RANS CFD to the full domain is considered a promising alternative. However, it has to be analyzed how the speed of the solution compares if the RANS CFD simulation included a transition model and calculation of the laminar BL region near the fuselage nose.

The present study focused on the configuration and associated design conditions of the *CENTRELINE* configuration. Its application to other configurations has to be demonstrated and validated. Additionally, future research could extend the current methodology to 2D planar configurations for BWB BLI applications. Further, 3D geometry effects should be studied systematically.

Although this study has explored viable options for adequately representing the aero-propulsive performance of fuselage-propulsor configurations in conceptual aircraft design and demonstrated the chosen approach's feasibility, the integration of aero-propulsive results into an aircraft design and sizing framework to simulate cascade effects is pending. For generating robust, multidisciplinary aircraft design results, a comprehensive, multi-dimensional parameter study and surrogate model derivation are essential. Furthermore, providing an off-design performance map for each geometry to cover the entire flight envelope is crucial. While this requires conducting more simulations, it is both feasible and necessary to advance the field, paving the way for more sustainable and efficient aircraft designs.

In conclusion, this research systematically identified the complexity of accurately assessing the aero-propulsive performance of PFCs adequate to the aircraft conceptual design phase and proposed a book-

keeping and a numerical simulation method to bridge critical gaps in existing PFC design and analysis practices. A novel hybrid numerical method was successfully developed, validated, and applied in a sensitivity study. Despite limitations, the groundwork laid here provides a robust platform for subsequent research.



# Bibliography

- [1] D. S. Lee, D. W. Fahey, A. Skowron, M. R. Allen, U. Burkhardt, Q. Chen, S. J. Doherty, S. Freeman, P. M. Forster, J. Fuglestedt, A. Gettelman, R. R. de León, L. L. Lim, M. T. Lund, R. J. Millar, B. Owen, J. E. Penner, G. Pitari, M. J. Prather, R. Sausen, and L. J. Wilcox, “The contribution of global aviation to anthropogenic climate forcing for 2000 to 2018,” *Atmospheric Environment*, vol. 244, p. 117834, 2020.
- [2] H. Ritchie, “Climate change and flying: what share of global co2 emissions come from aviation?” *Our World in Data*, 2020, <https://ourworldindata.org/co2-emissions-from-aviation>.
- [3] H. Ritchie, “Sector by sector: where do global greenhouse gas emissions come from?” *Our World in Data*, 2020, <https://ourworldindata.org/ghg-emissions-by-sector>.
- [4] “Aircraft Technology Roadmap to 2050,” International Air Transport Association, Tech. Rep., 2020.
- [5] E. van der Sman, B. Peerlings, J. Kos, R. Lieshout, and T. Boonekamp, “Destination 2050: A Route to Net Zero European Aviation,” Nederlands Lucht- en Ruimtevaartcentrum, Tech. Rep., 2020.
- [6] H. J. Steiner, A. Seitz, K. Wieczorek, K. Plötner, A. T. Isikveren, and M. Hornung, “Multi-Disciplinary Design and Feasibility Study of Distributed Propulsion Systems,” in *28th Congress of the International Council of the Aeronautical Sciences*, International Council of the Aeronautical Sciences, Ed., 2012.
- [7] A. Seitz, A. L. Habermann, F. Peter, F. Troeltsch, A. Castillo Pardo, B. Della Corte, M. van Sluis, Z. Goraj, M. Kowalski, X. Zhao, T. Grönstedt, J. Bijewitz, and G. Wortmann, “Proof of Concept Study for Fuselage Boundary Layer Ingesting Propulsion,” *Aerospace*, vol. 8, no. 1, p. 16, 2021.
- [8] A. A. Elmiligui, W. J. Fredericks, M. D. Guynn, and R. L. Campbell, “Numerical Investigation of a Fuselage Boundary Layer Ingestion Propulsion Concept,” in *AIAA Aviation Technology, Integration, and Operations Conference*, Los Angeles, CA, USA, 2013.
- [9] D. Raymer, *Aircraft Design: A Conceptual Approach*, 6th ed. Washington, DC, USA: American Institute of Aeronautics and Astronautics, Inc, 2018.
- [10] H. Schlichting and K. Gersten, *Boundary-Layer Theory*. Berlin and Heidelberg, Germany: Springer, 2017.
- [11] T. Cebeci, *Analysis of Turbulent Flows with Computer Programs*, 3rd ed. Amsterdam and Boston: Elsevier, 2013.
- [12] D. McLean, *Understanding Aerodynamics: Arguing from the Real Physics*. Chichester, West Sussex, UK: Wiley, 2013.
- [13] A. Nakayama, V. C. Patel, and L. Landweber, “Flow Interaction Near the Tail of a Body of Revolution: Part 2: Iterative Solution for Flow Within and Exterior to Boundary Layer and Wake,” *Journal of Fluids Engineering*, vol. 98, no. 3, pp. 538–546, 1976.
- [14] V. C. Patel, A. Nakayama, and R. Damian, “Measurements in the Thick Axisymmetric Turbulent Boundary Layer Near the Tail of a Body of Revolution,” *Journal of Fluid Mechanics*, vol. 63, no. 2, pp. 345–367, 1974.
- [15] H. Schlichting and E. Truckenbrodt, *Aerodynamik des Flugzeuges: Erster Band: Grundlagen aus der Strömungstechnik Aerodynamik des Tragflügels: Teil I*, 3rd ed. Berlin, Heidelberg, and New York: Springer, 2001.
- [16] P. Lv, *Power-Based Study of Boundary Layer Ingestion for Aircraft Application*. Singapore: Springer Nature, 2023.
- [17] A. Seitz, F. Peter, J. Bijewitz, A. Habermann, Z. Goraj, M. Kowalski, A. Castillo Pardo, C. Hall, F. Meller, R. Merkler, O. Petit, S. Samuelsson, B. Della Corte, M. van Sluis, G. Wortmann, and M. Dietz, “Concept Validation Study for Fuselage Wakefilling Propulsion Integration,” in *31st Congress of the International Council of the Aeronautical Sciences*, International Council of the Aeronautical Sciences, Ed., Belo Horizonte, Brazil, 2018.
- [18] J. S. Gray, C. A. Mader, G. K. W. Kenway, and J. R. R. A. Martins, “Coupled Aeropropulsive Optimization of a Three-Dimensional Boundary-Layer Ingestion Propulsor Considering Inlet Distortion,” *Journal of Aircraft*, vol. 57, no. 6, pp. 1014–1025, 2020.
- [19] M. van Sluis and B. Della Corte, “Final PFC Aircraft Aerodynamic Design and Performance,” CENTRELINE Consortium, CENTRELINE Public Project Deliverable D3.03, 2020.
- [20] A. Yildirim, J. S. Gray, C. A. Mader, and J. R. R. A. Martins, “Boundary-Layer Ingestion Benefit for the STARC-ABL Concept,” *Journal of Aircraft*, vol. 59, no. 4, pp. 896–911, 2022.
- [21] B. Della Corte, M. van Sluis, L. L. M. Veldhuis, and A. Gangoli Rao, “Power Balance Analysis Experiments on an Axisymmetric Fuselage with an Integrated Boundary-Layer-Ingesting Fan,” *AIAA Journal*, vol. 59, no. 12, pp. 5211–5224, 2021.
- [22] B. Della Corte, M. van Sluis, A. Gangoli Rao, and L. L. M. Veldhuis, “Aerodynamic Performance of an Aircraft with Aft-Fuselage Boundary-Layer-Ingestion Propulsion,” *Journal of Aircraft*, vol. 59, no. 4, pp. 1054–1070, 2022.
- [23] L. H. Smith, “Wake Ingestion Propulsion Benefit,” *Journal of Propulsion and Power*, vol. 9, no. 1, pp. 74–82, 1993.
- [24] W. J. G. Bräunling, *Flugzeugtriebwerke*. Berlin and Heidelberg, Germany: Springer, 2009.

- [25] A. Seitz and C. Gologan, "Parametric Design Studies for Propulsive Fuselage Aircraft Concepts," *CEAS Aeronautical Journal*, vol. 6, no. 1, pp. 69–82, 2014.
- [26] D. L. Rodriguez, "A Multidisciplinary Optimization Method for Designing Boundary Layer Ingesting Inlets," Ph.D. dissertation, Stanford University, Stanford, CA, USA, 2001.
- [27] D. L. Daggett, R. Kawai, and D. Friedman, "Blended Wing Body Systems Studies: Boundary Layer Ingestion Inlets with Active Flow Control," NASA Langley Research Center, Contractual Report 2003-212670, 2003.
- [28] R. Kawai, D. Friedman, and L. Serrano, "Blended Wing Body (BWB) Boundary Layer Ingestion (BLI) Inlet Configuration and System Studies," NASA, Tech. Rep. NASA/CR-2006-214534, 2006.
- [29] E. S. Hendricks, "Review of BLI Modeling Approaches in Conceptual Design," NASA, Technical Memorandum 2018-219926, 2018.
- [30] A. Plas, "Performance of a BLI Propulsion System," Master's thesis, Massachusetts Institute of Technology, Cambridge, MA, USA, 2006.
- [31] Plas, A.P., Sargeant, M.A., Crichton, D., Greitzer, E.M., Hynes, T.P., Hall, C.A., "Performance of a Boundary Layer Ingesting (BLI) Propulsion System," in *45th AIAA Aerospace Sciences Meeting and Exhibit*. Reston, VA, USA: American Institute of Aeronautics and Astronautics, 2007.
- [32] W. K. Lord, G. Tillman, S. S. Ochs, X. D. Cai, and B. Moffitt, "A Performance Methodology for Ducted Boundary Layer Ingesting Propulsion," in *AIAA SciTech Forum*. Reston, VA, USA: American Institute of Aeronautics and Astronautics, 2019.
- [33] M. Drela, "Power Balance in Aerodynamic Flows," *AIAA Journal*, vol. 47, no. 7, pp. 1761–1771, 2009.
- [34] A. Arntz, "Civil Aircraft Aero-thermo-propulsive Performance Assessment by an Exergy Analysis of High-fidelity CFD-RANS Flow Solutions," Ph.D. dissertation, Universite de Lille, Lille, France, 2014.
- [35] D. K. Hall, A. C. Huang, A. Uranga, E. M. Greitzer, M. Drela, and S. Sato, "Boundary Layer Ingestion Propulsion Benefit for Transport Aircraft," *Journal of Propulsion and Power*, vol. 33, no. 5, pp. 1118–1129, 2017.
- [36] S. Sato, "The Power Balance Method For Aerodynamic Performance Assessment," Ph.D. dissertation, Massachusetts Institute of Technology, 2012.
- [37] J. Ahuja and D. N. Mavris, "Sensitivity of Boundary Layer Ingestion Effects to Tube and Wing Airframe Design Features," in *AIAA SciTech Forum*. Reston, VA, USA: American Institute of Aeronautics and Astronautics, 2020, p. 19.
- [38] A. Arntz, O. Atinault, D. Destarac, and A. Merlen, "Exergy-based Aircraft Aeropropulsive Performance Assessment: CFD Application to Boundary Layer Ingestion," in *AIAA AVIATION Forum and Exposition*, Atlanta, GA, USA, 2014.
- [39] J. R. Welstead and J. L. Felder, "Conceptual Design of a Single-Aisle Turboelectric Commercial Transport with Fuselage Boundary Layer Ingestion," in *54th AIAA Aerospace Sciences Meeting*, San Diego, CA, USA, 2016.
- [40] H. D. Kim and J. L. Felder, "Control Volume Analysis of Boundary Layer Ingesting Propulsion Systems With or Without Shock Wave Ahead of the Inlet," in *49th AIAA Aerospace Sciences Meeting*. Reston, VA, USA: American Institute of Aeronautics and Astronautics, 2011.
- [41] S. Stückl, J. van Toor, and H. Libentanzer, "VoltAir - The All Electric Propulsion Concept Platform - A Vision for Atmospheric Friendly Flight," in *28th Congress of the International Council of the Aeronautical Sciences*, Brisbane, Australia, 2012.
- [42] A. T. Isikveren, A. Seitz, J. Bijewitz, A. Mirzoyan, A. Isyanov, R. Grenon, O. Atinault, J.-L. Godard, and S. Stückl, "Distributed Propulsion and Ultra-High By-Pass Rotor Study at Aircraft Level," *The Aeronautical Journal*, vol. 119, no. 1221, pp. 1327–1376, 2015.
- [43] K. R. Antcliff and F. M. Capristan, "Conceptual Design of the Parallel Electric-Gas Architecture with Synergistic Utilization Scheme (PEGASUS) Concept," in *18th AIAA/ISSMO Multidisciplinary Analysis and Optimization Conference 2017*. Red Hook, NY, USA: Curran Associates Inc, 2017.
- [44] G. Schrauf, "Status and Perspectives of Laminar Flow," *The Aeronautical Journal*, vol. 109, no. 1102, pp. 639–644, 2005.
- [45] A. L. Habermann, A. Gokhale, and M. Hornung, "Numerical Investigation of the Effects of Fuselage Upsweep in a Propulsive Fuselage Concept," *CEAS Aeronautical Journal*, vol. 12, no. 1, pp. 173–189, 2021.
- [46] B. T. Blumenthal, "Computational Investigation of a Boundary Layer Ingestion Propulsion System for the Common Research Model," Master's thesis, The Pennsylvania State University, PA, USA, 2016.
- [47] A. Seitz and C. Gologan, "Parametric Design Studies for Propulsive Fuselage Aircraft Concepts," *CEAS Aeronautical Journal*, vol. 6, no. 1, pp. 69–82, 2015.
- [48] H. D. Kim, J. L. Felder, M. T. Tong, J. J. Berton, and W. J. Haller, "Turboelectric Distributed Propulsion Benefits on the N3-X Vehicle," *Aircraft Engineering and Aerospace Technology*, vol. 86, no. 6, pp. 558–561, 2014.

- [49] J. S. Gray, G. K. Kenway, C. A. Mader, and J. R. R. A. Martins, "Aeropropulsive Design Optimization of a Turboelectric Boundary Layer Ingestion Propulsion System," in *AIAA AVIATION Forum and Exposition*. Atlanta, GA, USA: American Institute of Aeronautics and Astronautics, 2018.
- [50] J. S. Gray, C. A. Mader, G. K. W. Kenway, and J. R. R. A. Martins, "Modeling Boundary Layer Ingestion Using a Coupled Aeropropulsive Analysis," *Journal of Aircraft*, vol. 55, no. 3, pp. 1191–1199, 2017.
- [51] L. Lv, "Theoretical and Experimental Investigation of Boundary Layer Ingestion for Aircraft Application," Ph.D. dissertation, Delft University of Technology, Delft, The Netherlands, 2019.
- [52] J. Welstead, J. Felder, M. Guynn, B. Haller, M. Tong, S. Jones, J. S. Gray, I. Ordaz, J. Quinlan, B. Mason, S. Schnulo, and A. Sil, "Overview of the NASA STARC-ABL (Rev. B) Advanced Concept," Presentation, May 2018.
- [53] R. Schnell, X. Zhao, E. Rallis, M. Kavvalos, S. Sahoo, M. Schnoes, and K. Kyprianidis, "Assessment of a Turbo-Electric Aircraft Configuration with Aft-Propulsion Using Boundary Layer Ingestion," *Aerospace*, vol. 6, no. 12, p. 134, 2019.
- [54] A. Seitz, A. L. Habermann, F. Peter, F. Troeltsch, A. Castillo Pardo, B. Della Corte, M. van Sluis, Z. Goraj, M. Kowalski, X. Zhao, T. Grönstedt, J. Bijewitz, and G. Wortmann, "Proof of Concept Study for Fuselage Boundary Layer Ingesting Propulsion," *Aerospace*, vol. 8, no. 1, p. 16, 2021.
- [55] D. Silberhorn, M. J. Arzberger, M. Mennicken, F. Wolters, C. Hollmann, and M. Iwanizki, "Multidisciplinary Investigation of Partially Turboelectric, Boundary Layer Ingesting Aircraft Concepts: CleanSky2 LPA WP1.6.1 special session," in *AIAA SciTech Forum*. Reston, VA, USA: American Institute of Aeronautics and Astronautics, 2020.
- [56] P. Giannakakis, Y.-B. Maldonado, N. Tantot, C. Frantz, and M. Belleville, "Fuel Burn Evaluation of a Turbo-Electric Propulsive Fuselage Aircraft," in *AIAA Propulsion and Energy Forum*. Reston, VA, USA: American Institute of Aeronautics and Astronautics, 2019, p. 1992.
- [57] L. Menegozzo and E. Benini, "Boundary Layer Ingestion Propulsion: A Review on Numerical Modelling," *Journal of Engineering for Gas Turbines and Power*, vol. 142, no. 12, 2020.
- [58] D. E. Diamantidou, M. L. Hosain, and K. G. Kyprianidis, "Recent Advances in Boundary Layer Ingestion Technology of Evolving Powertrain Systems," *Sustainability*, vol. 14, no. 3, p. 1731, 2022.
- [59] N. G. Moirou, D. S. Sanders, and P. Laskaridis, "Advancements and Prospects of Boundary Layer Ingestion Propulsion Concepts," *Progress in Aerospace Sciences*, vol. 138, no. 12, p. 100897, 2023.
- [60] Armstrong Siddeley Motors Ltd. and F. A. M. Heppner, "Improvements Relating to Jet-Propelled Aircraft," German Patent GB577 950, 1946.
- [61] D. Eckardt, *Jet Web: Connections in the Development History of Turbojet Engines 1920 - 1950*. Wiesbaden, Germany: Springer Fachmedien, 2022.
- [62] F. Heppner, "The General Theory of Boundary Layer Propulsion," Armstrong Siddeley Motors, Tech. Rep. 18/1, 1944.
- [63] A. Smith and H. Roberts, "The Jet Airplane Utilizing Boundary Layer Air for Propulsion," *Journal of Aeronautical Sciences*, vol. 9, no. 1, pp. 74–82, 1947.
- [64] D. Küchemann and J. Weber, *Aerodynamics of Propulsion*. London, UK: McGraw-Hill, 1953.
- [65] W. Douglass, "Propulsive Efficiency with Boundary Layer Ingestion," Douglas Aircraft Company, Tech. Rep. J0860, 1970.
- [66] F. Goldschmied, "A Theoretical Aerodynamic Analysis of a Boundary Layer Controlled Airship Hull," Goodyear, Goodyear Aircraft Report GER-6251, 1954.
- [67] P. A. Cerreta, "Wind-Tunnel Investigation of the Drag of a Proposed Boundary-Layer-Controlled Airship," David W. Taylor Model Basin Aerodynamics Laboratory, Tech. Rep. 914, 1957.
- [68] G. F. Wislicenus, "Hydrodynamics and Propulsion of Submerged Bodies," *American Rocket Society Journal*, vol. 30, no. 12, pp. 1140–1148, 1960.
- [69] W. S. Gearhart and R. E. Henderson, "Selection of a Propulsor for a Submersible System," *Journal of Aircraft*, vol. 3, no. 1, pp. 84–90, 1966.
- [70] A. Betz, *Introduction to the Theory of Flow Machines*, 1st ed. Oxford, London, Edinburgh, New York, Toronto, Paris, Braunschweig: Pergamon Press, 1966.
- [71] Scopus. (Accessed September 1, 2023). [Online]. Available: <https://www.scopus.com>
- [72] A. Bolonkin, "A High Efficiency Fuselage Propeller ("Fusefan") for Subsonic Aircraft," in *SAE Technical Paper Series*. Warrendale, PA, USA: Society of American Engineers, 1999.
- [73] E. de La Rosa, C. Hall, and D. Crichto, "Special Session – Towards a Silent Aircraft Challenges in the Silent Aircraft Engine Design," in *45th AIAA Aerospace Sciences Meeting and Exhibit*, Reno, NV, USA, 2002.
- [74] M. Drela, "Development of the D8 Transport Configuration," in *29th AIAA Applied Aerodynamics Conference*. Reston, VA, USA: American Institute of Aeronautics and Astronautics, 2011, p. 83.

- [75] M. J. Armstrong, C. A. Ross, M. J. Blackwelder, and K. Rajashekara, "Trade Studies for NASA N3-X Turboelectric Distributed Propulsion System Electrical Power System Architecture," *SAE International Journal of Aerospace*, vol. 5, pp. 325–336, 2012.
- [76] M. K. Bradley, "Subsonic Ultra Green Aircraft Research: PhaseII: N+4 Advanced Concept Development," NASA, Tech. Rep. NASA/CR-2012-217556, 2012.
- [77] M. Mennicken, D. Schoenweitz, M. Schnoes, and R. Schnell, "Conceptual Fan Design for Boundary Layer Ingestion," in *Proceedings of the ASME Turbo Expo: Turbomachinery Technical Conference and Exposition*. New York, NY, USA: The American Society of Mechanical Engineers, 2019.
- [78] M. Mennicken, D. Schoenweitz, M. Schnoes, and R. Schnell, "Fan Design Assessment for BLI Propulsion Systems," *CEAS Aeronautical Journal*, vol. 13, no. 1, pp. 3–19, 2022.
- [79] X. Zhao, P. van Hoorn, H.-D. Yao, and J. Alderman, "Parameter Sensitivity Study on Inflow Distortion of Boundary Layer Ingested Turbofans," *Aerospace*, vol. 9, no. 8, p. 426, 2022.
- [80] J. Alderman, "Experimental Aspects of the SUBLIME Project Investigating Boundary Layer Ingestion Propulsion," Presentation at the 57th 3AF Applied Aerodynamics Conference, 2023.
- [81] A. Battiston, A. Magrini, R. Ponza, and E. Benini, "Fullscale Optimization and Fan Design of a Rear BLI Shrouded Propulsor," in *AIAA SciTech Forum*. National Harbor, MD, USA: American Institute of Aeronautics and Astronautics, 2023.
- [82] P. Giannakakis, C. Pernet, and A. Turnbull, "Turbo-Electric Propulsive Fuselage Aircraft BLI Benefits: A Design Space Exploration Using an Analytical Method," *The Aeronautical Journal*, vol. 124, no. 1280, pp. 1523–1544, 2020.
- [83] A. M. Fernández and H. Smith, "Effect of a Fuselage Boundary Layer Ingesting Propulsor on Airframe Forces and Moments," *Aerospace Science and Technology*, vol. 100, p. 105808, 2020.
- [84] M. Iwanizki, M. J. Arzberger, M. Plohr, D. Silberhorn, and T. Hecken, "Conceptual Design Studies of Short Range Aircraft Configurations with Hybrid Electric Propulsion," in *AIAA AVIATION Forum and Exposition*, Dallas, TX, USA, 2019.
- [85] J. Ahuja and D. N. Mavris, "Conceptual Design of Boundary-Layer-Ingesting Aircraft Capturing Aeropropulsive Coupling," *Journal of Aircraft*, vol. 59, no. 5, pp. 1267–1280, 2022.
- [86] K. A. Brown, J. L. Fleming, M. Langford, W. Ng, K. Schwartz, and C. Combs, "Development of a Ducted Propulsor for BLI Electric Regional Aircraft - Part I: Aerodynamic Design and Analysis," in *AIAA Propulsion and Energy Forum*. Reston, VA, USA: American Institute of Aeronautics and Astronautics, 2019, p. 2016.
- [87] K. Schwartz, R. Burdisso, B. Witcher, K. A. Brown, J. L. Fleming, and C. Combs, "Development of a Ducted Propulsor for BLI Electric Regional Aircraft - Part II: Aeroacoustic Analysis," in *AIAA Propulsion and Energy Forum*. Reston, VA, USA: American Institute of Aeronautics and Astronautics, 2019.
- [88] M. Secchi, P. T. Lacava, L. G. Trapp, and R. F. Gama Ribeiro, "Evaluation of a Regional Aircraft with Boundary Layer Ingestion and Electric-Fan Propulsor," *Journal of Aircraft*, vol. 58, no. 6, pp. 1204–1215, 2021.
- [89] A. M. Stoll and G. Veble Mikic, "Design Studies of Thin-Haul Commuter Aircraft with Distributed Electric Propulsion," in *AIAA AVIATION Forum and Exposition*, American Institute of Aeronautics and Astronautics, Ed. Washington, DC, USA: American Institute of Aeronautics and Astronautics, 2016.
- [90] C. P. Nasoulis, G. Protopapadakis, V. G. Gkoutzamanis, and A. I. Kalfas, "The Impact of Propulsive Architecture on the Design of a 19-Passenger Hybrid-Electric Aircraft," *IOP Conference Series: Materials Science and Engineering*, vol. 1226, no. 1, p. 012074, 2022.
- [91] R. H. Jansen and M. Celestina, "Electrical Propulsive Fuselage Concept for Transonic Transport Aircraft," in *ISABE Conference*. Canberra, Australia: International Society for Air Breathing Engines, 2019.
- [92] T. S. Tse and C. A. Hall, "Flow Field and Power Balance of a Distributed Aft-fuselage Boundary Layer Ingesting Aircraft," in *AIAA Propulsion and Energy Forum*. Reston, VA, USA: American Institute of Aeronautics and Astronautics, 2020.
- [93] P. D. Bravo Mosquera, H. D. Cerón-Muñoz, and F. Catalano, "Design and Computational Analysis of a Closed Non-Planar Wing Aircraft Coupled to a Boundary Layer Ingestion Propulsion System," in *AIAA Propulsion and Energy Forum*. Reston, VA, USA: American Institute of Aeronautics and Astronautics, 2019.
- [94] T. Y. Druot, N. Peteilh, P. Roches, and N. Monrolin, "Hydrogen Powered Airplanes, an Exploration of Possible Architectures Leveraging Boundary Layer Ingestion and Hybridization," in *AIAA SciTech Forum*. Reston, VA, USA: American Institute of Aeronautics and Astronautics, 2022.
- [95] J. Bijewitz, A. Seitz, A. T. Isikveren, and M. Hornung, "Multi-Disciplinary Design Investigation of Propulsive Fuselage Aircraft Concepts," *Aircraft Engineering and Aerospace Technology*, vol. 88, no. 2, pp. 257–267, 2016.
- [96] J. Bijewitz, "Conceptual Sizing Methods for Propulsive Fuselage Aircraft Concepts," Ph.D. dissertation, Technical University Munich, Munich, Germany, 2021.

- [97] S. Kaiser, R. Grenon, J. Bijewitz, A. Prendinger, O. Atinault, A. T. Isikveren, and M. Hornung, "Quasi-Analytical Aerodynamic Methods for Propulsive Fuselage Concepts," in *29th Congress of the International Council of the Aeronautical Sciences*, International Council of the Aeronautical Sciences, Ed. St. Petersburg, Russia: International Council of the Aeronautical Sciences, 2014.
- [98] A. T. Isikveren, A. Seitz, J. Bijewitz, M. Hornung, A. Mirzoyan, and A. Isyanov, "Recent Advances in Airframe-Propulsion Concepts With Distributed Propulsion," in *29th Congress of the International Council of the Aeronautical Sciences*, International Council of the Aeronautical Sciences, Ed., St. Petersburg, Russia, 2014.
- [99] A. Seitz, O. Schmitz, A. T. Isikveren, and M. Hornung, "Electrically Powered Propulsion: Comparison and Contrast to Gas Turbines," in *61. Deutscher Luft- und Raumfahrtkongress*, Deutsche Gesellschaft für Luft- und Raumfahrt, Ed., Berlin, Germany, 2012.
- [100] J. Bijewitz, A. Seitz, and M. Hornung, "Extended Design Studies for a Mechanically Driven Propulsive Fuselage Aircraft Concept," in *AIAA Aerospace Sciences Meeting*, Kissimmee, FL, USA, 2018, p. 10.
- [101] S. Samuelsson, O. Petit, R. Merkler, and G. Wortmann, "Adaption of a Turbofan Engine for High Power Offtakes for a Turbo-Electric Propulsive Fuselage Concept," in *ISABE Conference*, Canberra, Australia, 2019.
- [102] S. Biser, G. Wortmann, S. Ruppert, M. Filipenko, M. Noe, and M. Boll, "Predesign Considerations for the DC Link Voltage Level of the CENTRELINE Fuselage Fan Drive Unit," *Aerospace*, vol. 6, no. 12, p. 126, 2019.
- [103] R. Merkler, S. Samuelsson, and G. Wortmann, "Integration Aspects for large Generators into Turbofan Engines for a Turbo-Electric Propulsive Fuselage Concept," in *24th International Society of Air-breathing Engines Conference*, International Society for Air Breathing Engines, Ed., Canberra, Australia, 2019.
- [104] Z. J. Goraj, M. Kowalski, and B. Goliszek, "Stress, Strain and Displacement Analysis of Geodetic and Conventional Fuselage Structure for Future Passenger Aircraft," *Aircraft Engineering and Aerospace Technology*, vol. 91, no. 6, pp. 814–819, 2019.
- [105] M. Kowalski, Z. Goraj, and B. Goliszek, "The Use of FEA and Semi-Empirical Equations for Weight Estimation of a Passenger Aircraft," *Aircraft Engineering and Aerospace Technology*, vol. 93, no. 9, 2021.
- [106] M. van Sluis, B. Della Corte, and A. Gangoli Rao, "Aerodynamic Design Space Exploration of a Fuselage Boundary Layer Ingesting Aircraft," in *AIAA AVIATION Forum and Exposition*. San Diego, CA, USA: American Institute of Aeronautics and Astronautics, 2023.
- [107] A. Castillo Pardo and C. A. Hall, "Design of a Transonic Boundary Layer Ingesting Fuselage Fan," in *Proceedings of Global Power and Propulsion Society*, Zürich, Switzerland, 2020.
- [108] A. Castillo Pardo and C. A. Hall, "Aerodynamics of Boundary Layer Ingesting Fuselage Fans," *Journal of Turbomachinery*, vol. 143, no. 4, 2021.
- [109] F. Troeltsch, J. Bijewitz, and A. Seitz, "Design Trade Studies for Turbo-electric Propulsive Fuselage Integration," in *24th ISABE Conference*, Canberra, Australia, 2019.
- [110] A. L. Habermann, F. Troeltsch, F. Peter, P. Maas, M. van Sluis, M. Kowalski, G. Wortmann, J. Bijewitz, and A. Seitz, "Summary Report on Multi-Disciplinary Design Results," CENTRELINE Consortium, CENTRELINE Public Project Deliverable D2.11, 2020.
- [111] J. S. Gray, C. A. Mader, G. K. Kenway, and J. & Martins, "Approach to Modeling Boundary Layer Ingestion using a Fully Coupled Propulsion-RANS Model," in *58th AIAA/ASCE/AHS/ASC Structures, Structural Dynamics, and Materials Conference*. Grapevine, TX, USA: American Institute of Aeronautics and Astronautics, 2017.
- [112] J. S. Gray and J. R. R. A. Martins, "Coupled Aeropropulsive Design Optimisation of a Boundary-Layer Ingestion Propulsor," *The Aeronautical Journal*, vol. 123, no. 1259, pp. 1–17, 2018.
- [113] A. Yildirim, J. S. Gray, C. A. Mader, and J. Martins, "Aeropropulsive Design Optimization of a Boundary Layer Ingestion System," in *AIAA AVIATION Forum and Exposition*. Reston, VA, USA: American Institute of Aeronautics and Astronautics, 2019.
- [114] A. Yildirim, "Robust Methods for Aeropropulsive Design Optimization," Ph.D. dissertation, University of Michigan, Ann Arbor, MI, USA, 2021.
- [115] A. Yildirim, J. S. Gray, C. A. Mader, and J. R. Martins, "Coupled Aeropropulsive Design Optimization of a Podded Electric Propulsor," in *AIAA AVIATION Forum and Exposition*. Reston, VA, USA: American Institute of Aeronautics and Astronautics, 2021.
- [116] A. Yildirim, J. S. Gray, C. A. Mader, and J. R. R. A. Martins, "Performance Analysis of Optimized STARC-ABL Designs Across the Entire Mission Profile," in *AIAA SciTech Forum*. Reston, VA, USA: American Institute of Aeronautics and Astronautics, 2021.
- [117] G. K. Kenway and C. C. Kiris, "Aerodynamic Shape Optimization of the STARC-ABL Concept for Minimal Inlet Distortion," in *2018 AIAA/ASCE/AHS/ASC Structures, Structural Dynamics, and Materials Conference*. Kissimmee, FL, USA: American Institute of Aeronautics and Astronautics, 2018.

- [118] B. H. Mason, "Comparison of Structural Concepts for Transport Aircraft with an Aft Tail Cone Turbine," in *AIAA SciTech Forum*. Reston, VA, USA: American Institute of Aeronautics and Astronautics, 2019.
- [119] B. J. Lee and Liou, M.-F., Liou, M.-S., "Conceptual Aerodynamic Design of a Tail-Cone Thruster System under Axi-Symmetric Inlet Distortion," in *Proceedings of ASME Turbo Expo*. Oslo, Norway: The American Society of Mechanical Engineers, 2018.
- [120] B. J. Lee and M.-F. Liou, "Aerodynamic Design and Optimization of Fan Stage for Boundary Layer Ingestion Propulsion System," in *10th International Conference on Computational Fluid Dynamics*, Barcelona, Spain, 2018.
- [121] J. L. Kratz and G. L. Thomas, "Dynamic Analysis of the STARC-ABL Propulsion System," in *AIAA Propulsion and Energy Forum*. Reston, VA, USA: American Institute of Aeronautics and Astronautics, 2019.
- [122] A. K. Yoon, D. Lohan, F. Arastu, J. Xiao, and K. Haran, "Direct Drive Electric Motor for STARC-ABL Tail-Cone Propulsor," in *AIAA Propulsion and Energy Forum*. Reston, VA, USA: American Institute of Aeronautics and Astronautics, 2019.
- [123] D. K. Hall, A. Dowdle, J. Gonzalez, L. Trollinger, and W. Thalheimer, "Assessment of a Boundary Layer Ingesting Turboelectric Aircraft Configuration using Signomial Programming," in *AIAA AVIATION Forum and Exposition*. Atlanta, GA, USA: American Institute of Aeronautics and Astronautics, 2018.
- [124] *GasTurb 14. Design and Off-Design Performance of Gas Turbines.*, GasTurb GmbH, 2024.
- [125] J. Ahuja and D. N. Mavris, "A Method for Modeling the Aero-Propulsive Coupling Characteristics of BLI Aircraft in Conceptual Design," in *AIAA SciTech Forum*. Reston, VA, USA: American Institute of Aeronautics and Astronautics, 2021, p. 10.
- [126] J. Bijewitz, A. Seitz, M. Hornung, and A. T. Isikveren, "Progress in Optimizing the Propulsive Fuselage Aircraft Concept," *Journal of Aircraft*, vol. 54, no. 5, pp. 1979–1989, 2017.
- [127] J. Bijewitz, A. Seitz, and M. Hornung, "Power Plant Pre-Design Exploration for a Turbo-Electric Propulsive Fuselage Concept," in *Joint Propulsion Conference*, American Institute of Aeronautics and Astronautics, Ed. Reston, VA, USA: American Institute of Aeronautics and Astronautics, 2018.
- [128] O. Atinault, M. Méheut, and S. Defoort, "A mixed midelity conceptual design process for Boundary Layer Ingestion concepts," in *8th European Congress on Computational Methods in Applied Sciences and Engineering*, 2022.
- [129] A. Seitz, A. L. Habermann, and M. van Sluis, "Optimality Considerations for Propulsive Fuselage Power Savings," *Proceedings of the Institution of Mechanical Engineers, Part G: Journal of Aerospace Engineering*, vol. 235, no. 1, pp. 22–39, 2021.
- [130] A. Battiston, R. Ponza, and E. Benini, "Design Exploration for an Axisymmetric Rear BLI Propulsor," in *AIAA Propulsion and Energy Forum*. Reston, VA, USA: American Institute of Aeronautics and Astronautics, 2021.
- [131] A. Battiston, R. Ponza, and E. Benini, "Design of a Rear BLI Non-Axisymmetric Propulsor for a Transonic Flight Experiment," in *AIAA AVIATION Forum and Exposition*. Reston, VA, USA: American Institute of Aeronautics and Astronautics, 2022.
- [132] J. Matesanz García, "An Automated Approach for the Aerodynamic Design of Close-Coupled Propulsion/Airframe Configurations," in *1st Aerospace Europe Conference*, Bordeaux, France, 2020.
- [133] J. Matesanz-Garcia, T. Piovesan, and D. MacManus, "Aerodynamic Optimization of the Exhaust System of an Aft-Mounted Boundary Layer Ingestion Propulsor," in *56th 3AF International Conference on Applied Aerodynamics*, Toulouse, France, 2022.
- [134] J. Ahuja, "A Methodology for Capturing the Aero-Propulsive Coupling Characteristics of Boundary Layer Ingesting Aircraft in Conceptual Design," Ph.D. dissertation, Georgia Institute of Technology, Atlanta, GA, USA, 2020.
- [135] M. Drela, "Computational Modeling of Compressible Swirling Flows for Design and Analysis of Rotors and Turbomachinery: (MTFLOW 2.0)," Presentation, 2009.
- [136] P. Baskaran, B. Della Corte, M. van Sluis, and A. G. Rao, "Aeropropulsive Performance Analysis of Axisymmetric Fuselage Bodies for Boundary-Layer Ingestion Applications," *AIAA Journal*, vol. 60, no. 3, pp. 1592–1611, 2022.
- [137] D. S. Sanders and P. Laskaridis, "Full-Aircraft Energy-Based Force Decomposition Applied to Boundary-Layer Ingestion," *AIAA Journal*, vol. 130, no. 7, pp. 1–17, 2020.
- [138] J. S. Gray, "Design Optimization of a Boundary Layer Ingestion Propulsor Using a Coupled Aeropropulsive Model," Ph.D. dissertation, University of Michigan, Ann Arbor, MI, USA, 2018.
- [139] I. Ordaz, S. R. Rallabhandi, and E. J. Nielsen, "Mitigation of Engine Inlet Distortion Through Adjoint-Based Design," in *35th AIAA Applied Aerodynamics Conference*. Denver, CO, USA: American Institute of Aeronautics and Astronautics, 2017.
- [140] I. Ordaz, "Aero-Propulsion Analysis and Design Framework," Presentation at Propulsion-Airframe Integration Technical Interchange Meeting, May 2018.

- [141] B. T. Blumenthal, A. A. Elmiligui, K. A. Geiselhart, R. L. Campbell, M. D. Maughmer, and S. Schmitz, "Computational Investigation of a Boundary-Layer Ingesting Propulsion System for the Common Research Model," *Journal of Aircraft*, vol. 55, no. 3, pp. 1141–1153, 2018.
- [142] O. Petit, F. Costa, C. Bringham, and J. Tomita, "Aerodynamic Influence of Airframe Boundary Layer on Propeller Performance," in *24th International Society of Air Breathing Conference*, Canberra, Australia, 2019.
- [143] A. Martínez Fernández and H. Smith, "Effect of a Fuselage Boundary Layer Ingesting Propulsor on Airframe Forces and Moments," *Aerospace Science and Technology*, vol. 100, p. 105808, 2020.
- [144] A. Castillo Pardo, "Specification of Fan Design and Rig Test Campaign Plan," CENTRELINE Consortium, CENTRELINE Public Project Deliverable D3.04, 2018.
- [145] A. Castillo Pardo and C. A. Hall, "Aerodynamics of Boundary Layer Ingesting Fuselage Fans," in *24th ISABE Conference*, Canberra, Australia, 2019.
- [146] A. L. Habermann, J. Bijewitz, A. Seitz, and M. Hornung, "Performance Bookkeeping for Aircraft Configurations with Fuselage Wake-Filling Propulsion Integration," *CEAS Aeronautical Journal*, vol. 11, no. 2, pp. 529–551, 2020.
- [147] MIDAP Study Group, "Guide to in-flight thrust measurement of turbojets and fan engines," AGARD, AGARDograph 237, 1979.
- [148] M. B. Giles and R. M. Cummings, "Wake integration for three-dimensional flowfield computations - theoretical development," *Journal of Aircraft*, vol. 36, no. 2, 1999.
- [149] L. Hardin, G. Tillman, O. Sharma, J. Berton, and D. Arend, "Aircraft System Study of Boundary Layer Ingesting Propulsion," in *48th AIAA/ASME/SAE/ASEE Joint Propulsion Conference & Exhibit*. Reston, VA, USA: American Institute of Aeronautics and Astronautics, 2012.
- [150] A. Arntz, O. Atinault, and A. Merlen, "Exergy-Based Formulation for Aircraft Aeropropulsive Performance Assessment: Theoretical Development," *AIAA Journal*, vol. 53, no. 6, pp. 1–38, 2014.
- [151] L. Wiart, O. Atinault, B. Paluch, D. Hue, and R. Grenon, "Development of NOVA Aircraft Configurations for Large Engine Integration Studies," in *AIAA AVIATION Forum and Exposition*. Dallas, TX, USA: American Institute of Aeronautics and Astronautics, 2015.
- [152] L. Wiart, O. Atinault, J.-C. Bonifac, and R. Barrier, "Aeropropulsive Performance Analysis of the Nova Configurations," in *30th ICAS Congress*, Deajeon, Korea, 2016.
- [153] C. P. van Dam, "Recent experience with different methods of drag prediction," *Progress in Aerospace Sciences*, vol. 35, no. 8, pp. 751–798, 1999.
- [154] J. D. Anderson, *Fundamentals of Aerodynamics*, 5th ed. Singapore: McGraw-Hill, 2011.
- [155] M. Méheut and D. Bailly, "Drag-Breakdown Methods from Wake Measurements," *AIAA Journal*, vol. 46, no. 4, pp. 847–862, 2008.
- [156] E. A. Valencia, D. Nalianda, P. Laskaridis, and R. Singh, "Methodology to assess the performance of an aircraft concept with distributed propulsion and boundary layer ingestion using a parametric approach," *Proceedings of the Institution of Mechanical Engineers, Part G: Journal of Aerospace Engineering*, vol. 229, no. 4, pp. 682–693, 2014.
- [157] E. Valencia, P. Laskaridis, R. Singh, A. Aguinaga, E. Cando, C. Liu, and V. Hidalgo, "Review of the Investigation of Innovative Propulsion System Architectures for Aircraft," *Revista Politécnica*, vol. 35, no. 3, 2015.
- [158] C. Goldberg, D. Nalianda, D. MacManus, and P. Pilidis, "Installed Performance Assessment of a Boundary Layer Ingesting Distributed Propulsion System at Design Point," in *52nd AIAA/SAE/ASEE Joint Propulsion Conference, Propulsion and Energy Forum*. Salt Lake City, UT, USA: American Institute of Aeronautics and Astronautics, 2016.
- [159] C. Goldberg, D. Nalianda, and P. Pilidis, "Installed Performance Assessment of an Array of Distributed Propulsors Ingesting Boundary Layer Flow," *Journal of Engineering for Gas Turbines and Power*, vol. 140, no. 7, p. 071203, 2018.
- [160] J. S. Gray, C. A. Mader, G. K. Kenway, and J. R. R. A. Martins, "Approach to Modeling Boundary Layer Ingestion using a Fully Coupled Propulsion-RANS Model," in *58th AIAA/ASCE/AHS/ASC Structures, Structural Dynamics, and Materials Conference*. Grapevine, TX, USA: American Institute of Aeronautics and Astronautics, 2017, p. 140.
- [161] J. S. Gray and J. R. R. A. Martins, "Coupled aeropropulsive design optimisation of a boundary-layer ingestion propulsor," *The Aeronautical Journal*, vol. 30, pp. 1–17, 2018.
- [162] J. C. Gladin, "A Sizing and Vehicle Matching Methodology for Boundary Layer Ingesting Propulsion Systems," Ph.D. dissertation, Georgia Institute of Technology, Atlanta, GA, USA, 2015.
- [163] P. Lv and A. G. Rao, "Conceptual Analysis of Boundary Layer Ingestion towards aircraft propulsion integration," in *21st ISABE Conference*, Busan, Korea, 2013.
- [164] P. Lv, D. Ragni, T. Hartuc, L. Veldhuis, and A. G. Rao, "Experimental Investigation of the Flow Mechanisms Associated with a Wake-Ingesting Propulsor," *AIAA Journal*, vol. 55, no. 4, pp. 1332–1342, 2017.

- [165] S. A. Pandya, A. Huang, A. Espitia, and A. Uranga, "Computational Assessment of the Boundary Layer Ingesting Nacelle Design of the D8 Aircraft," in *AIAA SciTech Forum*. American Institute of Aeronautics and Astronautics, 2014.
- [166] S. Sato, "The Power Balance Method For Aerodynamic Performance Assessment," Ph.D. dissertation, Massachusetts Institute of Technology, Cambridge, MA, USA, 2012.
- [167] A. Uranga, M. Drela, E. Greitzer, N. Titchener, M. Lieu, N. Siu, A. Huang, G. M. Gatlin, and J. Hannon, "Preliminary Experimental Assessment of the Boundary Layer Ingestion Benefit for the D8 Aircraft," in *AIAA SciTech Forum*. National Harbor, MD, USA: American Institute of Aeronautics and Astronautics, 2014.
- [168] A. Uranga, M. Drela, E. M. Greitzer, D. K. Hall, N. A. Titchener, M. K. Lieu, N. M. Siu, C. Casses, A. C. Huang, G. M. Gatlin, and J. A. Hannon, "Boundary Layer Ingestion Benefit of the D8 Transport Aircraft," *AIAA Journal*, vol. 55, no. 11, pp. 3693–3708, 2017.
- [169] P. A. Weed, "Hybrid Wing-Body Aircraft Noise and Performance Assessment," Master's thesis, Massachusetts Institute of Technology, Cambridge, MA, USA, 2010.
- [170] B. M. Yutko, Chambers T. Jeffrey, Clinton S. Church, Christopher Courtin, Michael Lieu, Thomas W. Roberts, and Neil Titchener, "Conceptual Design of a D8 Commercial Aircraft," in *AIAA AVIATION Forum and Exposition*. Denver, CO, USA: American Institute of Aeronautics and Astronautics, 2017.
- [171] A. Arntz, O. Atinault, and D. Destarac, "Numerical Airframe Aerodynamic Performance Prediction: An Exergy Point of View," in *49th International Symposium of Applied Aerodynamics*. Lille, France: 3AF, 2014.
- [172] A. Couilleaux and A. Arntz, "Exergy Analysis for a CFD-Based Turbofan Exhaust Mixer Performance Improvement," in *53rd 3AF International Conference on Applied Aerodynamics*. Salon de Provence, France: 3AF, 2018.
- [173] A. Arntz and O. Atinault, "Exergy-Based Performance Assessment of a Blended Wing-Body with Boundary-Layer Ingestion," *AIAA Journal*, vol. 53, no. 12, pp. 3766–3776, 2015.
- [174] A. Arntz and D. Hue, "Exergy-Based Performance Assessment of the NASA Common Research Model," *AIAA Journal*, vol. 54, no. 1, pp. 88–100, 2016.
- [175] C. Tailliez and A. Arntz, "CFD Assessment of the Use of Exergy Analysis for Losses Identification in Turbomachines Flows," in *53rd 3AF International Conference on Applied Aerodynamics*. Salon de Provence, France: 3AF, 2018.
- [176] L. Wiart and C. Negulescu, "Exploration of the Airbus "Nautilus" Engine Integration Concept," in *31st Congress of the International Council of the Aeronautical Sciences*. Belo Horizonte, Brazil: ICAS, 2018.
- [177] M. A. Aguirre and S. Duplaa, "Epsilon v3: Exergy-Based Aerodynamic Analysis Tool for CFD and WTT Data," in *56th 3AF International Conference on Applied Aerodynamics*, Toulouse, France, 2022.
- [178] Plas, A.P., Sargeatn, M.A., Crichton, D., Greitzer, E.M., Hynes, T.P., Hall, C.A., "Performance of a Boundary Layer Ingesting (BLI) Propulsion System," *45th AIAA Aerospace Sciences Meeting and Exhibit*, 2007.
- [179] J. Sands, J. C. Gladin, B. Kestner, and D. Mavris, "Hybrid Wing Body Engine Cycle Design Exploration for Boundary Layer Ingesting (BLI) Propulsion Systems Under Design Uncertainty," in *48th AIAA/ASME/SAE/ASEE Joint Propulsion Conference Exhibit*. Atlanta, GA, USA: American Institute of Aeronautics and Astronautics, 2012.
- [180] A. Uranga, M. Drela, D. K. Hall, and E. M. Greitzer, "Analysis of the Aerodynamic Benefit from Boundary Layer Ingestion for Transport Aircraft," *AIAA Journal*, vol. 56, no. 11, pp. 4271–4281, 2018.
- [181] T. V. Marien, J. R. Welstead, and S. M. Jones, "Vehicle Level System Impact of Boundary Layer Ingestion for the NASA D8 Concept Aircraft," in *AIAA SciTech Forum*, Kissimmee, FL, USA, 2018.
- [182] J. F. Wendt and J. D. Anderson, *Computational Fluid Dynamics - An introduction: With contributions by John D. Anderson*. Berlin and Heidelberg, Germany: Springer, 2009.
- [183] T. L. Holst, "Transonic flow computations using nonlinear potential methods," *Progress in Aerospace Sciences*, vol. 36, no. 1, pp. 1–61, 2000.
- [184] F. A. Dvorak and F. A. Woodward, "A Viscous/Potential Flow Interaction Analysis Method for Multi-Element Infinite Swept Wings: Volume I," NASA Ames Research Center, NASA Contractor Report 2476, 1974.
- [185] F. A. Dvorak and F. A. Woodward, "A viscous/potential flow interaction analysis method for multi-element infinite swept wings: Volume II," NASA Ames Research Center, NASA Contractor Report 137550, 1974.
- [186] F. A. Dvorak, F. A. Woodward, and B. Maskew, "A Three-Dimensional Viscous/Potential Flow Interaction Analysis Method for Multi/Element Wings," NASA Ames Research Center, Analytical Methods Report 7603, 1977.
- [187] *Gas Turbine Engine Inlet Flow Distortion Guidelines*, Society of Automotive Engineers Aerospace Recommended Practice ARP 1420, Rev. C, 2002.
- [188] C. Geuzaine and J.-F. Remacle, "Gmsh: A 3-D finite element mesh generator with built-in pre- and post-processing facilities," *International Journal for Numerical Methods in Engineering*, vol. 79, no. 11, pp. 1309–1331, 2009.
- [189] J. A. Heyns, O. F. Oxtoby, and A. Steenkamp, "Modelling High-Speed Flow Using a Matrix-Free Coupled Solver," in *9th OpenFOAM Workshop*, Zagreb, Croatia, 2014.

- [190] A. Habermann, "ShapePFC repository," 2024. [Online]. Available: <https://github.com/BauhausLuftfahrt/ShapePFC>
- [191] G. Van Rossum and F. L. Drake, *Python 3 Reference Manual*, Scotts Valley, CA, 2009.
- [192] F. Meller and F. Kocvara, "Specification of Propulsive Fuselage Aircraft Layout and Design Features," CENTRELINE Consortium, CENTRELINE Public Project Deliverable D1.02, 2018.
- [193] R. D. Samuels, "Experimental Investigation of the Turbulent Boundary Layer on a Typical Subsonic Transport Fuselage," Langley Research Center, Hampton, VA, USA, NASA Technical Note D-5242, 1969.
- [194] D. C. Wilcox, *Turbulence Modeling for CFD*, 3rd ed. La Cañada, CA, USA: DCW Industries, 2006.
- [195] F. Zhu and N. Qin, "Intuitive Class/Shape Function Parameterization for Airfoils," *AIAA Journal*, vol. 52, no. 1, pp. 17–25, 2014.
- [196] E. W. Perkins, L. H. Jorgesen, and S. C. Sommer, "Investigation of the Drag of Various Axially Symmetric Nose Shapes of Fineness Ratio 3 for Mach Numbers from 1.24 to 7.4," NASA, Moffett Field, CA, USA, Tech. Rep. 1386, 1958.
- [197] D. Howe, *Aircraft conceptual design synthesis*. London, UK: Professional Engineering Publishing, 2010.
- [198] J. A. Samareh, "Survey of Shape Parameterization Techniques for High-Fidelity Multidisciplinary Shape Optimization," *AIAA Journal*, vol. 39, no. 5, pp. 877–884, 2001.
- [199] B. Kulfan, "'CST' Universal Parametric Geometry Representation Method With Applications to Supersonic Aircraft," in *4th International Conference on Flow Dynamics*, Sendai, Japan, 2007.
- [200] B. Kulfan and J. Bussoletti, "'Fundamental'" Parametric Geometry Representations for Aircraft Component Shapes," in *11th AIAA/ISSMO Multidisciplinary Analysis and Optimization Conference*. Reston, VA, USA: American Institute of Aeronautics and Astronautics, 2006.
- [201] H. Sobieczky, "Parametric Airfoils and Wings," in *Recent Development of Aerodynamic Design Methodologies*, ser. Notes on Numerical Fluid Mechanics, K. Fujii and G. Dulikravich, Eds. Braunschweig und Wiesbaden, Germany: Vieweg+Teubner Verlage, 1999, vol. 65, pp. 71–87.
- [202] R. W. Derksen and T. Rogalsky, "Bezier-PARSEC: An Optimized Aerofoil Parameterization for Design," *Advances in Engineering Software*, vol. 41, no. 7-8, pp. 923–930, 2010.
- [203] R. Christie, A. Heidebrecht, and D. MacManus, "An Automated Approach to Nacelle Parameterization Using Intuitive Class Shape Transformation Curves," *Journal of Engineering for Gas Turbines and Power*, vol. 139, no. 6, 2017.
- [204] R. Christie, M. Robinson, F. Tejero, and D. G. MacManus, "The Use of Hybrid Intuitive Class Shape Transformation Curves in Aerodynamic Design," *Aerospace Science and Technology*, vol. 95, p. 105473, 2019.
- [205] F. Tejero, D. MacManus, J. Matesanz-Garcia, A. Swarthout, and C. Sheaf, "Towards the Design and Optimisation of Future Compact Aero-Engines: Intakes/FanCowl Trade-Off Investigation," in *56th 3AF International Conference on Applied Aerodynamics*, Toulouse, France, 2022.
- [206] J. Matesanz-Garcia, T. Piovesan, and D. MacManus, "Aerodynamic Optimization of the Exhaust System of an Aft-Mounted Boundary Layer Ingestion Propulsor," in *56th 3AF International Conference on Applied Aerodynamics*, Toulouse, France, 2022.
- [207] Mendoza, Carlos Eduardo Ribeiro Santa Cruz, "Numerical Prediction of Turbulent Boundary Layer Characteristics to Feed the Design of Propulsive Fuselages," Master's thesis, University of Stuttgart, Stuttgart, Germany, 2020.
- [208] N. Romanow, "Extension of a Numerical Model for the Prediction of Turbulent Boundary Layer Characteristics on a Propulsive Fuselage Aircraft," Master's thesis, Technical University Munich, Munich, Germany, 2021.
- [209] A. Smith and J. Pierce, "Exact Solution of the Neumann Problem - Calculation of Non-Circulatory Plane and Axially Symmetric Flows about or within Arbitrary Boundaries," in *Proceedings of the Third U.S. National Congress of Applied Mechanics*, 1958, pp. 807–815.
- [210] J. L. Hess and A. Smith, "Calculation of Potential Flow About Arbitrary Bodies," *Progress in Aerospace Sciences*, vol. 8, pp. 1–138, 1967.
- [211] C. Haberland, E. Göde, and G. Sauer, "Calculation of the Flow Field around Engine-Wing-Configurations," in *International Council of Aerospace Sciences*, vol. 4, no. 1, 1980, pp. 144–157.
- [212] J. Katz and A. Plotkin, *Low-Speed Aerodynamics*, 13th ed. Cambridge, UK: Cambridge University Press, 2001.
- [213] E. Göde, "Ein Verfahren zur Berechnung des Strömungsfeldes um Strahltriebwerke," Ph.D. dissertation, Technische Universität Berlin, Berlin, Germany, 1978.
- [214] R. I. Lewis, *Vortex Element Methods for Fluid Dynamic Analysis of Engineering Systems*. Cambridge, NY, USA: Cambridge University Press, 1991.
- [215] K. G. Winter, J. C. Rotta, and K. G. Smith, "Studies of the Turbulent Boundary Layer on a Waisted Body of Revolution in Subsonic and Supersonic Flow," Aeronautical Research Council, London, UK, Reports and Memoranda 3633, 1968.

- [216] H. Glauert, "The Effect of Compressibility on the Lift of an Aerofoil," *Proceedings of the Royal Society of London. Series A, Containing Papers of a Mathematical and Physical Character*, vol. 118, no. 779, pp. 113–119, 1928.
- [217] T. von Karman, "Compressibility Effects in Aerodynamics," *Journal of Spacecraft and Rockets*, vol. 40, no. 6, pp. 992–1011, 1941.
- [218] D. F. Myring, "A Theoretical Study of Body Drag in Subcritical Axisymmetric Flow," *Aeronautical Quarterly*, vol. 27, no. 3, pp. 186–194, 1976.
- [219] E. V. Laitone, "New Compressibility Correction for Two-Dimensional Subsonic Flow," *Journal of the Aeronautical Sciences*, vol. 18, no. 5, 1951.
- [220] V. C. Patel, "On the Equations of a Thick Axisymmetric Turbulent Boundary Layer," Iowa Institute of Hydraulic Research, The University of Iowa, Iowa, USA, IHHR Report 143, 1973.
- [221] J. E. Green, "The Prediction of Turbulent Boundary Layer Development in Compressible Flow," *Journal of Fluid Mechanics*, vol. 31, no. 4, pp. 753–778, 1968.
- [222] T. Cebeci and P. Bradshaw, *Physical and Computational Aspects of Convective Heat Transfer*. New York, NY, USA: Springer, 1984.
- [223] N. Rott and L. F. Crabtree, "Simplified Laminar Boundary-Layer Calculations for Bodies of Revolution and Yawed Wings," *Journal of the Aeronautical Sciences*, vol. 19, no. 8, pp. 553–565, 1952.
- [224] W. M. Kays and M. E. Crawford, *Convective Heat and Mass Transfer*, 3rd ed. New York, NY, USA: McGraw Hill, 1993.
- [225] V. C. Patel, "A Simple Integral Method for the Calculation of Thick Axisymmetric Turbulent Boundary Layers," Iowa Institute of Hydraulic Research, The University of Iowa, Tech. Rep. 150, 1973.
- [226] A. Nakayama, V. C. Patel, and L. Landweber, "Flow Interaction Near the Tail of a Body of Revolution: Part 1: Flow Exterior to Boundary Layer and Wake," *Journal of Fluids Engineering*, vol. 98, no. 3, pp. 531–537, 1976.
- [227] J. E. Green, D. J. Weeks, and J. Brooman, "Prediction of Turbulent Boundary Layers and Wakes in Compressible Flow by a Lag-Entrainment Method," Aeronautical Research Council, Reports and Memoranda 3791, 1977.
- [228] J. D. Hoffman, *Numerical Methods for Engineers and Scientists*, 2nd ed. Boca Raton, FL, USA: CRC Press, 2001.
- [229] M. R. Head, "Entrainment in the Turbulent Boundary Layer," Aeronautical Research Council, Reports and Memoranda 3152, 1958.
- [230] F. A. Dvorak, "Calculation of Turbulent Boundary Layers on Rough Surfaces in Pressure Gradient," *AIAA Journal*, vol. 7, no. 9, pp. 1752–1759, 1969.
- [231] N. M. Standen, "A Concept of Mass Entrainment Applied to Compressible Turbulent Boundary Layers in Adverse Pressure Gradients," in *Proceedings of the 4th Congress of the International Council of the Aeronautical Sciences*, 1965, pp. 1101–1125.
- [232] B. Thompson, "A New Two-Parameter Family of Mean Velocity Profiles for Incompressible Turbulent Boundary Layers on Smooth Walls," Aeronautical Research Council, Tech. Rep. 3463, 1965.
- [233] M. R. Head and V. C. Patel, "Improved Entrainment Method for Calculating Turbulent Boundary Layer Development," Aeronautical Research Council, Reports and Memoranda 3643, 1968.
- [234] M. F. Zedan and C. Dalton, "Viscous Drag Computation for Axisymmetric Bodies at High Reynolds Numbers," *Journal of Hydronautics*, vol. 13, no. 2, pp. 52–60, 1979.
- [235] J. F. Nash and A. Macdonald, "A Turbulent Skin-friction Law for Use at Subsonic and Transonic Speeds," Aeronautical Research Council, Current Papers 948, 1966.
- [236] J. F. Nash and A. Macdonald, "The Calculation of Momentum Thickness in a Turbulent Boundary Layer at Mach Numbers up to Unity," Aeronautical Research Council, Current Papers 963, 1966.
- [237] H. Ludwig and W. Tillmann, "Untersuchungen über die Wandschubspannung in turbulenten Reibungsschichten," *Ingenieur-Archiv*, vol. 17, no. 4, pp. 288–299, 1949.
- [238] J. H. Preston, "The Minimum Reynolds Number for a Turbulent Boundary Layer and the Selection of a Transition Device," *Journal of Fluid Mechanics*, vol. 3, no. 4, pp. 373–384, 1958.
- [239] L. F. Crabtree, "Prediction of Transition in the Boundary Layer on an Aerofoil," *The Journal of the Royal Aeronautical Society*, vol. 62, pp. 525–528, 1958.
- [240] T. Cebeci, G. J. Mosinskis, and A. Smith, "Calculation of Viscous Drag and Turbulent Boundary-Layer Separation on Two-Dimensional and Axisymmetric Bodies in Incompressible Flows," McDonnell Douglas Corporation, Tech. Rep. MDC J0973-01, 1970.
- [241] A. Nakayama and V. C. Patel, "Calculation of the Viscous Resistance of Bodies of Revolution," *Journal of Hydro-nautics*, vol. 8, no. 4, pp. 154–162, 1974.

- [242] L. E. Olson and F. A. Dvorak, “Viscous/Potential Flow about Multi-Element Two-Dimensional and Infinite-Span Swept Wings - Theory and Experiment,” in *14th Aerospace Sciences Meeting*. Reston, VA, USA: American Institute of Aeronautics and Astronautics, 1976, p. 849.
- [243] G. E. Fujiwara, D. Chaparro, and N. T. Nguyen, “An Integral Boundary Layer Direct Method Applied to 2D Transonic Small-Disturbance Equations,” in *34th AIAA Applied Aerodynamics Conference*. Washington, DC, USA: American Institute of Aeronautics and Astronautics, 2016.
- [244] T. Cebeci, G. J. Mosinskis, and A. Smith, “Calculation of Separation Points in Incompressible Turbulent Flows,” *Journal of Aircraft*, vol. 9, no. 9, pp. 618–624, 1972.
- [245] T. Cebeci, K. C. Chang, R. W. Clark, and N. D. Halsey, “Calculation of Flow Over Multielement Airfoils at High Lift,” *Journal of Aircraft*, vol. 24, no. 8, pp. 546–551, 1987.
- [246] L. Landweber, “On Irrotational Flows Equivalent to the Boundary Layer and Wake,” David W. Tayler Naval Ship Research and Development Center, Bethesda, MD, USA, The Fifth David W. Tayler Lectures, 1978.
- [247] M. H. Buschmann and M. Gad-El-Hak, “Debate Concerning the Mean-Velocity Profile of a Turbulent Boundary Layer,” *AIAA Journal*, vol. 41, no. 4, pp. 565–572, 2003.
- [248] D. B. Spalding, “A Single Formula for the “Law of the Wall”,” *Journal of Applied Mechanics*, vol. 28, no. 3, pp. 455–458, 1961.
- [249] D. Coles, “The Law of the Wake in the Turbulent Boundary Layer,” *Journal of Fluid Mechanics*, vol. 1, no. 2, pp. 191–226, 1956.
- [250] J. O. Hinze, *Turbulence*, 2nd ed., ser. McGraw-Hill series in mechanical engineering. New York, NY, USA: McGraw-Hill, 1975.
- [251] F. M. White, *Viscous Fluid Flow*, 2nd ed., ser. McGraw-Hill series in mechanical engineering. New York, NY, USA: McGraw-Hill, 1991.
- [252] B. Thompson, “A New Two-Parameter Family of Mean Velocity Profiles for J Incompressible Turbulent Boundary Layers on Smooth Walls,” Aeronautical Research Council, Reports and Memoranda 3463, 1967.
- [253] P. S. Granville, “A Modified Law of the Wake for Turbulent Shear Layers,” *Journal of Fluids Engineering*, vol. 98, no. 3, pp. 578–580, 1976.
- [254] OpenFOAM: User Guide. (Accessed February 21, 2024). [Online]. Available: <https://www.openfoam.com/documentation/user-guide>
- [255] HiSA: CFD Verification and Validation Archive. CSIR. (Accessed February 21, 2024). [Online]. Available: <https://hisa.gitlab.io/archive.html>
- [256] Oxtoby, O. F. et al. (2017) HiSA Repository. (Accessed February 21, 2024). [Online]. Available: <https://gitlab.com/hisa/hisa>
- [257] P. R. Spalart and S. R. Allmaras, “A One-Equation Turbulence Model for Aerodynamic Flows,” in *30th Aerospace Sciences Meeting and Exhibit*. Reston, VA, USA: American Institute of Aeronautics and Astronautics, 1992.
- [258] F. R. Menter, “Two-Equation Eddy-Viscosity Turbulence Models for Engineering Applications,” *AIAA Journal*, vol. 32, no. 8, pp. 1598–1605, 1994.
- [259] W. Thollet, “Body Force Modeling of Fan-Airframe Interactions,” Ph.D. dissertation, Université Fédérale Toulouse Midi-Pyrénées, Toulouse, France, 2017.
- [260] D. K. Hall, “Analysis of Civil Aircraft Propulsors with Boundary Layer Ingestion,” Ph.D. dissertation, Massachusetts Institute of Technology, Cambridge, MA, USA, 2015.
- [261] E. C. Bunschoten, “Turbomachinery Analysis and Design Using Body-Force Modeling in SU2,” Master’s thesis, Delft University of Technology, Delft, The Netherlands, 2020.
- [262] J. J. Defoe, M. Etemadi, and D. K. Hall, “Fan Performance Scaling With Inlet Distortions,” *Journal of Turbomachinery*, vol. 140, no. 7, 2018.
- [263] E. Benichou, G. Dufour, Y. Bousquet, N. Binder, A. Ortolan, and X. Carbonneau, “Body Force Modeling of the Aerodynamics of a Low-Speed Fan under Distorted Inflow,” *International Journal of Turbomachinery, Propulsion and Power*, vol. 4, no. 3, p. 29, 2019.
- [264] B. Godard, E. de Jaeghere, and N. Gourdain, “Efficient Design Investigation of a Turbofan in Distorted Inlet Conditions,” in *Proceedings of the ASME Turbo Expo: Turbomachinery Technical Conference and Exposition*. New York, NY, USA: The American Society of Mechanical Engineers, 2019.
- [265] M. T. Latour, “Body Force Modeling of Axial Turbomachinery for Analysis and Design Optimization,” Ph.D. dissertation, Delft University of Technology, Delft, The Netherlands, 2020.
- [266] *OpenFOAM: User Guide: Boundary conditions*, (Accessed February 21, 2024). [Online]. Available: <https://www.openfoam.com/documentation/guides/latest/doc/openfoam-guide-boundary-conditions.html>

- [267] E. Svenning, "Implementation of an Actuator Disk in OpenFOAM," Bachelor's thesis, Chalmers University of Technology, Göteborg, Sweden, 2010.
- [268] P. Saini, "Numerical Prediction of Automotive Underhood Airflows using an Uncalibrated Fan Body Force Model," Master's thesis, University of Windsor, Windsor, ON, Canada, 2020.
- [269] B. Windén, "Adding a Simple Body Force Propeller Model to SIMPLEFoam," Texas A&M University, OCEN CFD Technical eport 220002, 2022.
- [270] OpenFOAM: User Guide: fvOptions. (Accessed February 21, 2024). [Online]. Available: <https://www.openfoam.com/documentation/guides/latest/doc/guide-case-system-fvoptions.html>
- [271] J. Riegel, W. Mayer, and Y. van Havre. FreeCAD. (Accessed February 21, 2024). [Online]. Available: <http://www.freecadweb.org>
- [272] P. Virtanen, R. Gommers, T. E. Oliphant, M. Haberland, T. Reddy, D. Cournapeau, E. Burovski, P. Peterson, W. Weckesser, J. Bright, S. J. van der Walt, M. Brett, J. Wilson, K. J. Millman, N. Mayorov, A. R. J. Nelson, E. Jones, R. Kern, E. Larson, C. J. Carey, Í. Polat, Y. Feng, E. W. Moore, J. VanderPlas, D. Laxalde, J. Perktold, R. Cimrman, I. Henriksen, E. A. Quintero, C. R. Harris, A. M. Archibald, A. H. Ribeiro, F. Pedregosa, and P. van Mulbregt, "SciPy 1.0: fundamental algorithms for scientific computing in Python," *Nature methods*, vol. 17, no. 3, pp. 261–272, 2020.
- [273] W. Jakob, J. Rhineland, and D. Moldovan. (2017) pybind11 – Seamless Operability Between C++11 and Python. (Accessed February 21, 2024). [Online]. Available: <https://github.com/pybind/pybind11>
- [274] E. C. Bunschoten, "Meangen2BFM repository," 2020, (Accessed February 21, 2024). [Online]. Available: <https://github.com/EvertBunschoten/Meangen2BFM>
- [275] C. Hughes, "Aerodynamic Performance of Scale-Model Turbofan Outlet Guide Vanes Designed for Low Noise," in *40th AIAA Aerospace Sciences Meeting & Exhibit*. Reston, VA, USA: American Institute of Aeronautics and Astronautics, 2002.
- [276] C. E. Hughes, G. G. Podboy, R. P. Woodward, and R. J. Jeracki, "The Effect of Bypass Nozzle Exit Area on Fan Aerodynamic Performance and Noise in a Model Turbofan Simulator," in *Volume 6: Turbo Expo 2005, Parts A and B*. The American Society of Mechanical Engineers, 2005, pp. 1241–1264.
- [277] *ANSYS Fluent User's Guide: Release 15.0*, ANSYS, Inc., Canonsburg, PA, USA.
- [278] E. A. Arrington and J. C. Gonzalez, "Flow Quality Improvements in the NASA Lewis Research Center 9- by 15-Foot Low Speed Wind Tunnel," NASA Lewis Research Center, NASA Contractor Report 195439, 1995.
- [279] *A Methodology for Assessing Inlet Swirl Distortion*, Society of Automotive Engineers Aerospace Information Report AIR 5686, 2017.
- [280] I. Celik, U. Ghia, P. Roache, C. Freitas, H. Coleman, and P. Raad, "Procedure for Estimation and Reporting of Uncertainty Due to Discretization in CFD Applications," *Journal of Fluids Engineering*, vol. 130, no. 7, 2008.
- [281] T. Cebeci and J. Cousteix, *Modeling and Computation of Boundary-Layer Flows: Laminar, Turbulent and Transitional Boundary Layers in Incompressible and Compressible Flows*, 2nd ed. Long Beach, CA, USA: Horizons Publ, 2005.
- [282] S. L. Dixon and C. A. Hall, *Fluid Mechanics and Thermodynamics of Turbomachinery*, 7th ed. Oxford, UK: Butterworth-Heinemann, 2013.
- [283] E. Dick, *Fundamentals of Turbomachines*, 2nd ed., ser. Fluid Mechanics and Its Applications. Cham, Switzerland: Springer Cham, 2022, vol. 130.
- [284] H. Grieb, *Projektierung von Turboflugtriebwerken*, ser. Technik der Turboflugtriebwerke. Basel, Switzerland: Birkhäuser, 2004.
- [285] *Aircraft Propulsion System Performance Station Designation and Nomenclature*, Society of Automotive Engineers Aerospace Recommended Practice ARP 755C, Rev. C, 2013.
- [286] OpenFOAM: User Guide: Coded fixed value. (Accessed February 21, 2024). [Online]. Available: <https://www.openfoam.com/documentation/guides/latest/doc/guide-bcs-general-coded-fixed-value.html>
- [287] A. L. Habermann, R. Zahn, A. Seitz, and M. Hornung, "Multidimensional Parametric Study of a Propulsive Fuselage Concept Using OpenFOAM," in *AIAA AVIATION Forum and Exposition*. Virtual: American Institute of Aeronautics and Astronautics, 2020.
- [288] A. Seitz, "Advanced Methods for Propulsion System Integration in Aircraft Conceptual Design," Ph.D. dissertation, Technische Universität München, Munich, Germany, 2012.
- [289] A. I. J. Forrester, A. Sóbester, and A. J. Keane, *Engineering Design via Surrogate Modelling: A Practical Guide*. Chichester, UK: John Wiley & Sons, 2008.
- [290] A. I. Forrester and A. J. Keane, "Recent Advances in Surrogate-Based Optimization," *Progress in Aerospace Sciences*, vol. 45, no. 1-3, pp. 50–79, 2009.

- [291] M. D. McKay, R. J. Beckman, and W. J. Conover, “A Comparison of Three Methods for Selecting Values of Input Variables in the Analysis of Output from a Computer Code,” *Technometrics*, vol. 21, no. 2, p. 239, 1979.
- [292] R. Yondo, E. Andrés, and E. Valero, “A Review on Design of Experiments and Surrogate Models in Aircraft Real-Time and Many-Query Aerodynamic Analyses,” *Progress in Aerospace Sciences*, vol. 96, pp. 23–61, 2018.
- [293] M. E. Johnson, L. M. Moore, and D. Ylvisaker, “Minimax and Maximin Distance Designs,” *Journal of Statistical Planning and Inference*, vol. 26, no. 2, pp. 131–148, 1990.
- [294] J. L. Loeppky, J. Sacks, and W. J. Welch, “Choosing the Sample Size of a Computer Experiment: A Practical Guide,” *Technometrics*, vol. 51, no. 4, pp. 366–376, 2009.
- [295] A. Bhosekar and M. Ierapetritou, “Advances in Surrogate Based Modeling, Feasibility Analysis, and Optimization: A Review,” *Computers & Chemical Engineering*, vol. 108, pp. 250–267, 2018.
- [296] D. G. Krige, “A Statistical Approach to some Basic Mine Valuation Problems on the Witwatersrand,” *Journal of the Southern African Institute of Mining and Metallurgy*, vol. 52, no. 6, pp. 119–139, 1951.
- [297] R. M. Paiva, A. R. D. Carvalho, C. Crawford, and A. Suleman, “Comparison of Surrogate Models in a Multidisciplinary Optimization Framework for Wing Design,” *AIAA Journal*, vol. 48, no. 5, pp. 995–1006, 2010.
- [298] A. Dumont, J.-L. Hantrais-Gervois, P.-Y. Passaggia, J. Peter, I. Salah el Din, and É. Savin, “Ordinary Kriging Surrogates in Aerodynamics,” in *Uncertainty Management for Robust Industrial Design in Aeronautics*, ser. Notes on Numerical Fluid Mechanics and Multidisciplinary Design, C. Hirsch, D. Wunsch, J. Szumbarski, Ł. Łaniewski-Wollk, and J. Pons-Prats, Eds. Cham, Switzerland: Springer International Publishing, 2019, vol. 140, pp. 229–245.
- [299] W. Song and A. J. Keane, “Surrogate-Based Aerodynamic Shape Optimization of a Civil Aircraft Engine Nacelle,” *AIAA Journal*, vol. 45, no. 10, pp. 2565–2574, 2007.
- [300] I. Goulos, J. Otter, T. Stankowski, D. MacManus, N. Grech, and C. Sheaf, “Aerodynamic Design of Separate-Jet Exhausts for Future Civil Aero-engines—Part II: Design Space Exploration, Surrogate Modeling, and Optimization,” *Journal of Engineering for Gas Turbines and Power*, vol. 138, no. 8, 2016.
- [301] Z.-H. Han, M. Abu-Zurayk, S. Görtz, and C. Ilic, “Surrogate-Based Aerodynamic Shape Optimization of a Wing-Body Transport Aircraft Configuration,” in *AeroStruct: Enable and Learn How to Integrate Flexibility in Design*, R. Heinrich, Ed. Braunschweig, Germany: Springer, 2018, vol. 138, pp. 257–282.
- [302] A. de Myttenaere, B. Golden, B. Le Grand, and F. Rossi, “Mean Absolute Percentage Error for regression models,” *Neurocomputing*, vol. 192, pp. 38–48, 2016.
- [303] R. Sjoergen. (2018) pyDOE2 1.3.0. (Accessed February 21, 2024). [Online]. Available: <https://pypi.org/project/pyDOE2/>
- [304] C. Paulson and G. Ragkousis, *pyKriging: A Python Kriging Toolkit (v0.1.0-alpha)*. Zenodo, 2015.

# Publications

The following publications related to the dissertation were published by the PhD candidate during the course of the dissertation:

- [Pub1] A. L. Habermann, J. Bijewitz, A. Seitz, and M. Hornung, “Performance Bookkeeping for Aircraft Configurations with Fuselage Wake-Filling Propulsion Integration,” *CEAS Aeronautical Journal*, vol. 11, no. 2, pp. 529–551, 2020.
- [Pub2] A. L. Habermann, R. Zahn, A. Seitz, and M. Hornung, “Multidimensional Parametric Study of a Propulsive Fuselage Concept Using OpenFOAM,” in *AIAA AVIATION 2020 FORUM*. Reston, Virginia: American Institute of Aeronautics and Astronautics, June 15, 2020, p. 2163.
- [Pub3] A. L. Habermann, F. Troeltsch, F. Peter, P. Maas, M. van Sluis, M. Kowalski, G. Wortmann, J. Bijewitz, and A. Seitz, “Summary Report on Multi-Disciplinary Design Results,” CENTRELINE Consortium, CENTRELINE Public Project Deliverable D2.11, 2020.
- [Pub4] A. L. Habermann, A. Gokhale, and M. Hornung, “Numerical Investigation of the Effects of Fuselage Upsweep in a Propulsive Fuselage Concept,” *CEAS Aeronautical Journal*, vol. 12, no. 1, pp. 173–189, 2021.
- [Pub5] F. Peter, A. L. Habermann, M. Lüdemann, K. Plötner, F. Troeltsch, and A. Seitz, “Definition of the CENTRELINE Reference Aircraft and Power Plant Systems,” in *Deutscher Luft- und Raumfahrtkongress*, Deutsche Gesellschaft für Luft- und Raumfahrt, Ed., 2020.
- [Pub6] A. Seitz, F. Peter, J. Bijewitz, A. L. Habermann, Z. Goraj, M. Kowalski, A. Castillo Pardo, C. Hall, F. Meller, R. Merkler, O. Petit, S. Samuelsson, B. Della Corte, M. van Sluis, G. Wortmann, and M. Dietz, “Concept Validation Study for Fuselage Wake-Filling Propulsion Integration,” in *31st Congress of the International Council of the Aeronautical Sciences*, International Council of the Aeronautical Sciences, Ed., 2018.
- [Pub7] A. Seitz, A. L. Habermann, and M. van Sluis, “Optimality Considerations for Propulsive Fuselage Power Savings,” *Proceedings of the Institution of Mechanical Engineers, Part G: Journal of Aerospace Engineering*, vol. 235, no. 1, pp. 22–39, 2021.
- [Pub8] A. Seitz, A. L. Habermann, F. Peter, F. Troeltsch, A. Castillo Pardo, B. Della Corte, M. van Sluis, Z. Goraj, M. Kowalski, X. Zhao, T. Grönstedt, J. Bijewitz, and G. Wortmann, “Proof of Concept Study for Fuselage Boundary Layer Ingesting Propulsion,” *Aerospace*, vol. 8, no. 1, p. 16, 2021.

# Supervised Student Theses

The following student theses related to the dissertation were supervised by the PhD candidate during the course of the dissertation:

- [StudTheses1] M. Freile Ramos, “Development of a Tool to Automate the Prediction of Fuselage Boundary Layer Characteristics,” Master’s thesis, University of Applied Sciences Wiener Neustadt, Wiener Neustadt, Austria, 2020.
- [StudTheses2] A. Gokhale, “Three Dimensional Numerical Investigation of the Effect of Variation in Configuration of Components in a Propulsive Fuselage Concept,” Master’s thesis, Technical University Munich, Munich, Germany, 2019.
- [StudTheses3] N. Romanow, “Extension of a Numerical Model for the Prediction of Turbulent Boundary Layer Characteristics on a Propulsive Fuselage Aircraft,” Master’s thesis, Technical University Munich, Munich, Germany, 2021.
- [StudTheses4] C. E. R. Santa Cruz Mendoza, “Numerical Prediction of Turbulent Boundary Layer Characteristics to Feed the Design of Propulsive Fuselages,” Master’s thesis, University of Stuttgart, Stuttgart, Germany, 2020.
- [StudTheses5] R. Zahn, “Aerodynamic Design Space Exploration of a Propulsive Fuselage Concept Using Computational Fluid Dynamics,” Master’s thesis, Technical University Munich, Munich, Germany, 2019.



# Appendix

## A.1 Appendix 1 - Code

All tools used within the workflow presented in Section 5, including the IBL method, *OpenFOAM* source code, and case setup can be downloaded from GitHub using the following link:

<https://github.com/BauhausLuftfahrt/ShapePFC>

## A.2 Appendix 2 - iCST Parameterization

	Parameter	Unit	Reference	Lower Limit	Upper Limit	
	$l_{f,cent}$	Fuselage nose and center section length	m	50.900	20.000	65.000
	$r_{f,cent}$	Fuselage center section radius	m	3.045	1.750	4.000
	$h_{duct} = r_{2,tip} - r_{2,hub}$	FF rotor inlet hub height	m	0.560	0.200	0.800
	$fl_{nose} = l_{f,nose}/d_{f,cent}$	Relative fuselage nose length	-	0.198	0.100	0.400
	$f_{x,FF} = x_{FF}/l_{f,tot}$ (S: $x_{FF}$ )	Relative FF rotor inlet position	-	0.928	0.850	0.950
	$fl_{nac} = l_{nac}/r_{12,hub}$ (S: $l_{nac}$ )	Relative nacelle length	-	4.341	2.000	10.000
	$fl_{int} = l_{f,int}/l_{nac}$	Relative FF intake length	-	0.380	0.100	0.500
	$fl_{thr} = l_{thr}/l_{f,int}$	Relative FF throat length	-	0.243	0.020	0.400
	$f_{r,max} = r_{max}/r_{f,cent}$ (S: $r_{max}$ )	Ratio max. nacelle radius to fuselage center section radius	-	1.053	1.000	1.300
	$f_{x,max} = l_{r,max}/l_{nac}$	Relative position of max. nacelle radius	-	0.118	0.100	0.500
	$f_{\rho LE}$	Upper inner nacelle LE radius factor	-	1.000	0.500	1.500
	$f_{r_{thr,tip}} = r_{thr,tip}/r_{hi,tip}$	Relative throat tip radius	-	0.898	0.800	0.975
	$f_{r,2} = r_{2,hub}/r_{2,tip}$	FF rotor inlet hub to tip ratio	-	0.510	0.300	0.700
	$f_{r_{8,hub}} = r_{8,hub}/r_{3,hub}$	Relative nozzle exit hub radius	-	1.134	1.000	1.500
	$f_{A_{hi},A_{thr}} = A_{hi}/A_{thr}$	Ratio FF highlight to FF throat area	-	1.304	1.000	1.500
	$f_{A_{thr},A_2} = A_{thr}/A_2$	Ratio FF throat to FF rotor inlet area	-	0.994	0.950	1.000
	$f_{A_8,A_3} = A_8/A_3$	Ratio FF nozzle exit to FF rotor inlet area	-	0.780	0.600	1.000
	$\theta_{f,cone}$	Fuselage angle of nozzle cone	°	14	5	20
	$\theta_{f,int}$	Fuselage angle at FF highlight	°	11	0	20
	$\theta_{rot,in}$	Fuselage angle at FF rotor inlet	°	-4	-10	4
	$\beta_{rot,in}$	Nacelle duct angle at FF rotor inlet	°	-4	-10	4
	$\beta_{TE,low}$	Nacelle lower boattail angle	°	0	-10	20
	$\Delta\beta_{TE} = \beta_{TE,up} - \beta_{TE,low}$	Difference of nacelle upper and lower boattail angle	°	13	0	20
	$Ma$	Mach number	-	0.820	0.760	0.860
	$h_{alt}$	Altitude	m	10680	7620	12192
	$\Omega_{rot}$	Rotor rotational speed	rad/s	293	-	-

Table A.1: Geometrical and operational design parameters. Lower and upper feasible limits for multi-dimensional parameter studies are provided. Parameters, which are fixed for the sensitivity study, are indicated with S.

Nacelle			Fuselage		
ID		Parameter	ID		Parameter
P.N.1	$r_{hi,tip}$	Highlight tip radius	P.F.1	$r_{f,cent}$	Fuselage center section radius
P.N.2	$r_{thr,tip}$	Throat tip radius	P.F.2	$l_{f,nose}$	Fuselage nose length
P.N.3	$x_{thr}$	X-location of throat	P.F.3	$l_{f,cent}$	Fuselage nose and center section length
P.N.4	$r_{2,tip}$	FF rotor inlet tip radius/y-position	P.F.4	$\theta_{f,int}$	Fuselage angle at highlight
P.N.5	$x_{nac,2}$	X-location of FF rotor inlet	P.F.5	$l_{f,pre-int}$	Fuselage pre-intake length
P.N.6	$\beta_{rot,in}$	FF stage tip angle at rotor inlet	P.F.6	$r_{hi,hub}$	Highlight hub radius
P.N.7	$l_{nac,int}$	Intake length	P.F.7	$r_{thr,hub}$	Throat hub radius
P.N.8	$r_{22,tip}$	FF rotor outlet tip radius/y-position	P.F.8	$r_{2,hub}$	FF rotor inlet hub radius/y-position
P.N.9	$x_{nac,22}$	X-location of FF rotor outlet	P.N.26	$x_{hi}$	X-location of nacelle highlight
P.N.10	$\beta_{rot,out}$	FF stage tip angle at rotor outlet	P.N.3	$x_{thr}$	X-location of throat
P.N.11	$r_{23,tip}$	FF stator inlet tip radius/y-position	P.F.9	$l_{f,int}$	FF intake length
P.N.12	$\beta_{stat,in}$	FF stage tip angle at stator inlet	P.F.10	$x_{f,2}$	X-location of FF rotor inlet
P.N.13	$l_{nac,gap}$	FF stage gap length	P.F.11	$\theta_{rot,in}$	FF stage hub angle at rotor inlet
P.N.14	$x_{nac,23}$	X-location of FF stator inlet	P.F.12	$r_{22,hub}$	FF rotor outlet hub radius/y-position
P.N.15	$r_{3,tip}$	FF stator outlet tip radius/y-position	P.F.13	$x_{f,22}$	X-location of FF rotor outlet
P.N.16	$x_{nac,3}$	X-location of FF stator outlet	P.F.14	$r_{23,hub}$	FF stator inlet hub radius/y-position
P.N.17	$\beta_{stat,out}$	FF stage tip angle at stator outlet	P.F.15	$x_{f,23}$	X-location of FF stator inlet
P.N.18	$\beta_{TE,low}$	Nacelle inner boattail angle	P.F.16	$l_{f,rot}$	FF rotor chord length
P.N.19	$l_{nac,noz}$	Nozzle length	P.F.17	$l_{f,gap}$	FF gap length
P.N.20	$r_{8,tip}$	Nacelle trailing edge tip radius	P.F.18	$r_{3,hub}$	FF stator outlet hub radius/y-position
P.N.21	$l_{nac}$	Nacelle length	P.F.19	$x_{f,3}$	X-location of FF stator outlet
P.N.22	$\rho_{LE,up}$	Inner leading edge radius of nacelle cowling	P.F.20	$\theta_{stat,out}$	FF stage hub angle at stator outlet
P.N.23	$x_{max}$	X-location of max. nacelle radius	P.F.21	$r_{8,hub}$	FF nozzle exit hub radius/y-position
P.N.24	$r_{max}$	Max. thickness radius	P.F.22	$l_{f,noz}$	Nozzle total length
P.N.25	$\beta_{TE,up}$	Nacelle outer boattail angle	P.F.23	$\theta_{f,cone}$	Fuselage angle of nozzle cone
P.N.26	$x_{hi}$	X-location of nacelle highlight	P.F.24	$l_{f,cone}$	Fuselage cone length
			P.F.25	$\theta_{stat,in}$	FF stage hub angle at stator inlet

Table A.2: Design parameters used for iCST parameterization.

Curve ID	Constraint ID	Constraint	k	Type	$\Psi$	$\xi^{(k)}(\Psi)$	Influence on weighting coefficients
F1	C.F.1	Fuselage LE position	0	Position	Haack minimum drag nose function		
	C.F.2	Nose TE position	0	Position			
F2	C.F.2	Nose TE position	0	Position	1st order Bezier curve		
	C.F.3	Center section TE position	0	Position			
F3	C.F.3	Center section TE position	0	Position	0.0	$r_{f,cent}/l_{f,pre-int}$	-
	C.F.4	Center section TE gradient	1	Gradient	0.0	0.0	bp0
	C.F.5	Center section TE curvature	2	2nd Derivative	0.0	0.0	bp1, bp2
	C.F.6	Highlight hub curvature	2	2nd Derivative	1.0	0.0	bp1, bp2
	C.F.7	Highlight hub gradient	1	Gradient	1.0	$\tan(\theta_{f,int})$	bp3 (=bpn)
	C.F.8	Highlight hub position	0	Position	1.0	$r_{hi,hub}/l_{f,pre-int}$	-
	C.F.8	Highlight hub position	0	Position	0.0	$r_{hi,hub}/l_{f,int}$	-
	C.F.7	Highlight hub gradient	1	Gradient	0.0	$\tan(\theta_{f,int})$	bp0
F4	C.F.6	Highlight hub curvature	2	2nd Derivative	0.0	0.0	bp1, bp2
	C.F.9	Throat hub position	0	Position	$(x_{thr} - x_{hi})/l_{f,int}$	$r_{thr,hub}/l_{f,int}$	bp1, bp2
	C.F.10	FF rotor inlet hub gradient	1	Gradient	0.0	$\tan(\theta_{rot,in})$	bp3 (=bpn)
	C.F.11	FF rotor inlet hub position	0	Position	1.0	$r_{2,hub}/l_{f,int}$	-
F5	C.F.11	FF rotor inlet hub position	0	Position	0.0	$r_{2,hub}/(l_{f,rot} + l_{f,gap})$	-
	C.F.10	FF rotor inlet hub gradient	1	Gradient	0.0	$\tan(\theta_{rot,in})$	bp0
	C.F.12	FF rotor outlet position	0	Position	$(x_{f,22} - x_{f,2})/(l_{f,rot} + l_{f,gap})$	$r_{22,hub}/(l_{f,rot} + l_{f,gap})$	bp1
	C.F.13	FF stator inlet hub gradient	1	Gradient	1.0	$\tan(\theta_{stat,in})$	bp2 (=bpn)
	C.F.14	FF stator inlet hub position	0	Position	1.0	$r_{23,hub}/(l_{f,rot} + l_{f,gap})$	-
	C.F.14	FF stator inlet hub position	0	Position			
F6	C.F.14	FF stator inlet hub position	0	Position	1st order Bezier curve		
	C.F.15	FF stator outlet hub position	0	Position			
F7	C.F.15	FF stator outlet hub position	0	Position	0.0	$r_{3,hub}/l_{f,noz}$	-
	C.F.16	FF stator outlet hub gradient	1	Gradient	0.0	$\tan(\theta_{stat,out})$	bp0
	C.F.17	FF stator outlet hub curvature	2	2nd Derivative	0.0	0.0	bp1, bp2
	C.F.18	Nozzle max. hub radius curvature	2	2nd Derivative	1.0	0.0	bp1, bp2
	C.F.19	Nozzle max. hub radius gradient	1	Gradient	1.0	0.0	bp3 (=bpn)
	C.F.20	Nozzle max. hub radius position	0	Position	1.0	$r_{8,hub}/l_{f,noz}$	-
	C.F.19	Nozzle max. hub radius gradient	1	Gradient	0.0	0.0	-
	C.F.20	Nozzle max. hub radius position	0	Position	0.0	$r_{8,hub}/l_{f,cone}$	bp0
F8	C.F.21	Fuselage TE curvature	2	2nd Derivative	1.0	0.0	bp1
	C.F.22	Fuselage TE cone angle	1	Gradient	1.0	$\tan(\theta_{f,cone})$	bp2 (=bpn)
	C.F.23	Fuselage TE position	0	Position	1.0	0.0	-

Table A.3: Constraints used for fuselage iCST parameterization.

Curve ID	Constraint ID	Constraint	k	Type	$\Psi$	$\xi^{(k)}(\psi)$	Influence on weighting coefficients
N1	C.N.1	Highlight position	0	Position	0.0	$r_{hi,tip}/l_{nac,int}$	-
	C.N.2	Throat position	0	Position	$(x_{thr} - x_{hi})/l_{n,int}$	$r_{thr,tip}/l_{nac,int}$	bp0, bp1
	C.N.3	FF rotor inlet curvature	2	2nd Derivative	1.0	0.0	bp0, bp1
	C.N.4	FF rotor inlet gradient	1	Gradient	1.0	$\tan(\beta_{rot,in})$	bp2 (=bpn)
	C.N.5	FF rotor inlet position	0	Position	1.0	$r_{2,tip}/l_{nac,int}$	-
N2	C.N.5	FF rotor inlet position	0	Position	1st order Bezier curve		
	C.N.6	FF rotor outlet position	0	Position			
N3	C.N.6	FF rotor outlet position	0	Position	0.0	$r_{22,tip}/l_{nac,gap}$	-
	C.N.7	FF rotor outlet gradient	1	Gradient	0.0	$\tan(\beta_{rot,out})$	bp0
	C.N.8	FF rotor outlet curvature	2	2nd Derivative	0.0	0.0	bp1, bp2
	C.N.9	FF stator inlet curvature	2	2nd Derivative	1.0	0.0	bp1, bp2
	C.N.10	FF stator inlet gradient	1	Gradient	1.0	$\tan(\beta_{stat,in})$	bp3 (=bpn)
	C.N.11	FF stator inlet position	0	Position	1.0	$r_{23,tip}/l_{nac,gap}$	-
N4	C.N.11	FF stator inlet position	0	Position	1st order Bezier curve		
	C.N.12	FF stator outlet position	0	Position			
N5	C.N.12	FF stator outlet position	0	Position	0.0	$r_{23,tip}/l_{nac,noz}$	-
	C.N.13	FF stator outlet gradient	1	Gradient	0.0	$\tan(\beta_{stat,out})$	bp0
	C.N.14	FF stator outlet curvature	2	2nd Derivative	0.0	0.0	bp1, bp2
	C.N.15	Nacelle TTE curvature	2	2nd Derivative	1.0	0.0	bp1, bp2
	C.N.16	Nacelle lower TTE gradient	1	Gradient	1.0	$\tan(\beta_{TE,low})$	bp3 (=bpn)
N6	C.N.17	Nacelle TTE position	0	Position	1.0	$r_{8,tip}/l_{nac,noz}$	-
	C.N.1	Highlight position	0	Position	0.0	$r_{hi,tip}/l_n$	-
	C.N.18	Highlight upper radius	1	Radius of Curvature	0.0	$PL_{E,up}$	bp0
	C.N.19	Max. radius position	0	Position	$(x_{max} - x_{hi})/l_{nac}$	$r_{max}/l_{nac}$	bp1, bp2, bp3
	C.N.20	Max. radius gradient	1	Gradient	0.0	0.0	bp1, bp2, bp3
	C.N.21	Nacelle upper TTE curvature	2	2nd Derivative	1.0	0.0	bp1, bp2, bp3
C.N.22	Nacelle upper TTE gradient	1	Gradient	1.0	$\tan(\beta_{TE,up})$	bp4 (=bpn)	
C.N.17	Nacelle TTE position	0	Position	1.0	$r_{8,tip}/l_{nac}$	-	

Table A.4: Constraints used for nacelle iCST parameterization.



### A.3 Appendix 3 - Overview of Validation Cases

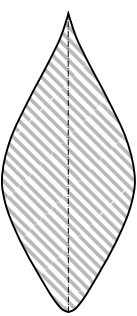
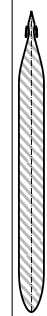
Case	Conditions	Geometry	Data Type	Sources	Usage
<b>Waisted Body</b>	$Ma=0.597$ , $Re=9.85 \times 10^6$ $Ma=0.801$ , $Re=9.98 \times 10^6$		Experimental	[215]	PM compressibility correction (Section 5.4.1.2) IBL (Section 5.4.3) Velocity profile prediction (Section 5.5.3) FV setup (Section 5.6.2)
<b>Equivalent Fuselage</b>	$Ma=0.75$ , $Re=9.7 \times 10^6$		Experimental	[193]	PM compressibility correction (Section 5.4.1.2)
<b>Fuselage</b>	-		Experimental	[214]	Incompressible PM (Section 5.4.1.1)
<b>Akron Airship</b>	$Ma=0.15$ , $Re=1.7 \times 10^7$		Experimental	[241]	IBL transition prediction (Section 5.4.2.3)
<b>Low-Drag F-57 Body</b>	$Ma=0.045$ , $Re=1.2 \times 10^6$		Experimental	[241]	IBL transition prediction (Section 5.4.2.3)
<b>6:1 Spheroid</b>	$Ma=0.0365$ , $Re=1.2 \times 10^6$		Experimental	[14]	IBL viscous/inviscid coupling (Section 5.4.2.5)
<b>Single Blade Passage</b>	$p_t = 1053\text{hPa}$		Numerical	[261, 274]	BFM verification (Section 5.6.3.3)
<b>NASA SDT Fan Stage</b>	$p_t = 900\text{hPa}$		Experimental Numerical	[275, 276] [133]	BFM validation (Section 5.6.3.4)
<b>CENTRELINE Rev 07</b>	$Ma=0.82$ , $FL=330$ , $ISA+10K$		Numerical	[19]	HPFVM (pseudo-)validation (Section 5.7)

Table A.5: Overview of employed validation cases.

## A.4 Appendix 4 - Interface Location Definition

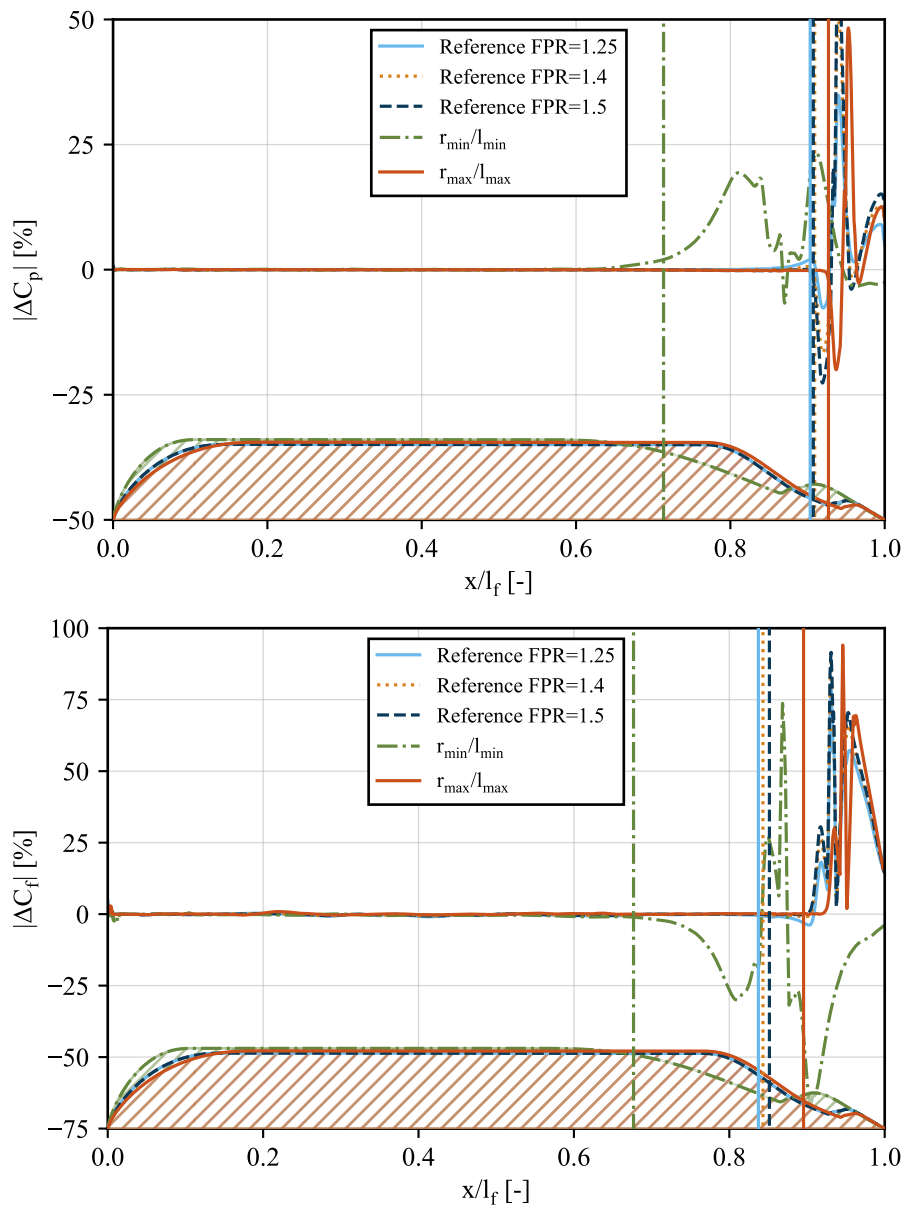


Figure A.1: Pressure (top) and skin friction (bottom) coefficient difference between full fuselage-propulsor and isolated fuselage configuration for different geometries.  $r_{min} = 1.75$  m,  $r_{max} = 4.0$  m,  $l_{min} = 36$  m,  $l_{max} = 86$  m.

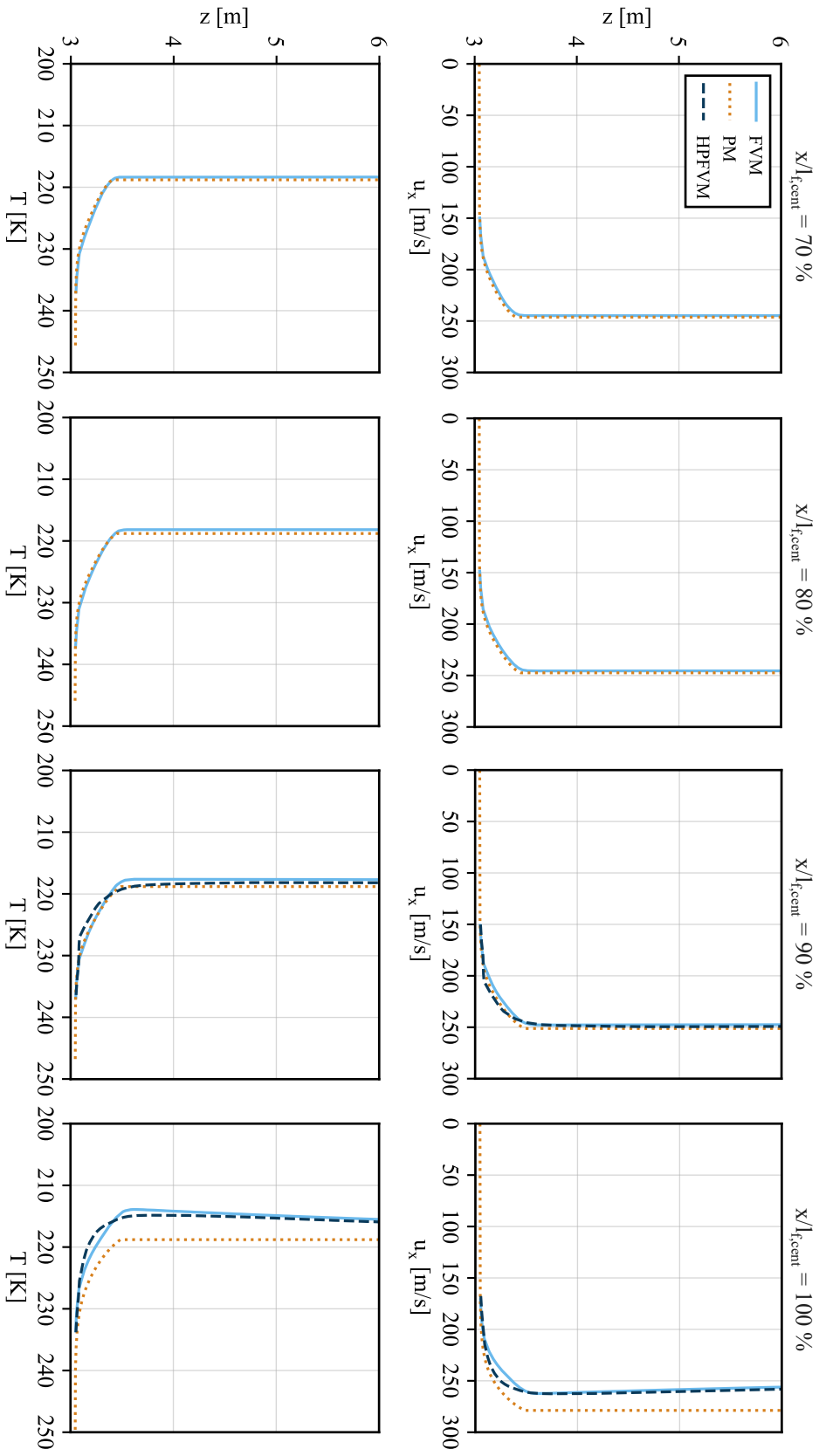


Figure A.2: Velocity and temperature profiles at different fuselage locations for the reference geometry. Comparison of PM, FVM, and HPPFVM results.



### A.5 Appendix 5 - Velocity Profile Validation

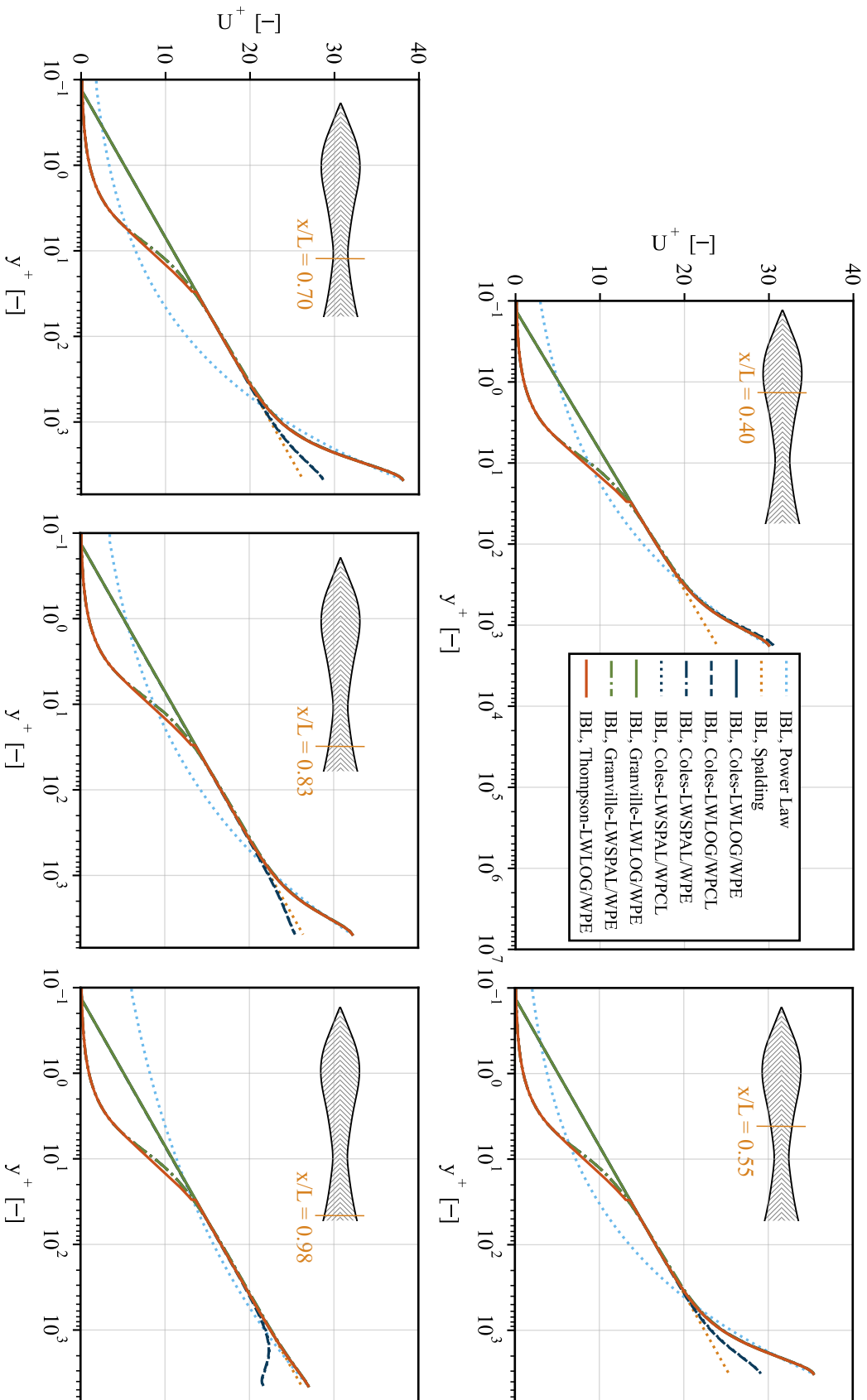


Figure A.3: Distribution of dimensionless velocity in the boundary layer for different velocity profile models based on the results of the IBL method. Results for a number of  $x/L$  locations on the *Waisted Body* by [215]. Law of the Wall - LOGarithmic (LWLOG) or SPALding (LWSPAL). Wake Parameter calculation - Clauser pressure gradient parameter (WPCL) or evaluated at Edge (WPE).

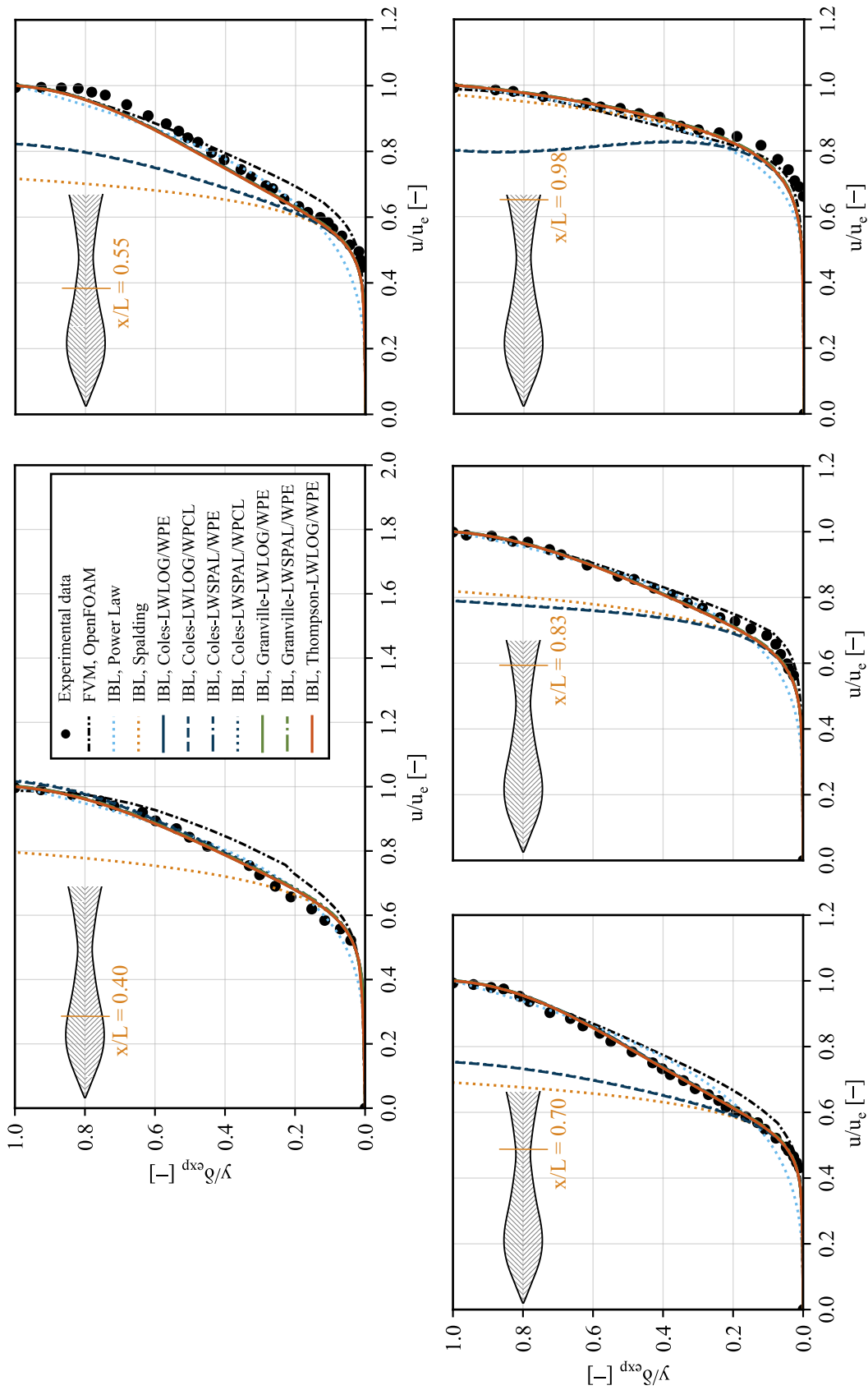


Figure A.4: Validation of velocity profile prediction for IBL method. Compared against experimental data for *Waisted Body* by [215] at a number of  $x/L$  locations indicated in the subfigures. Law of the Wall - LOGarithmic (LWLOG) or SPALding (LWSPAL). Wake Parameter calculation - CLauser pressure gradient parameter (WPCL) or evaluated at Edge (WPE).



### A.6 Appendix 6 - Full Finite Volume Grid Convergence Study

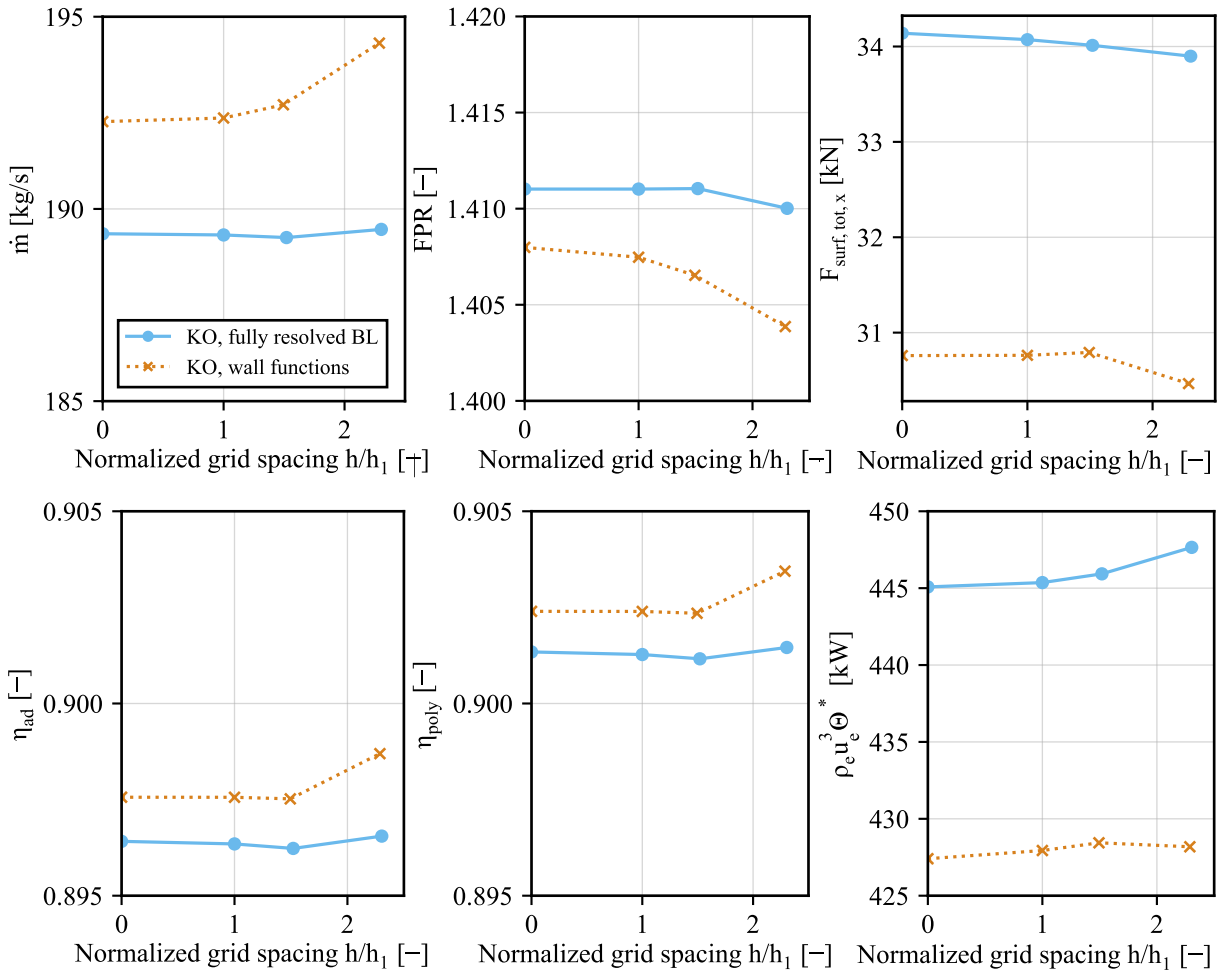


Figure A.5: Grid convergence for full BLI FV domain. BL resolution study. Reference fuselage-propulsor configuration. KO:  $k-\omega$ -SST.

BL resolution	$\Phi: \dot{m}$ [ $\frac{kg}{s}$ ]		$\Phi: FPR_{st}$ [-]		$\Phi: F_x$ [kN]	
	FR	WF	FR	WF	FR	WF
$N_1, N_2, N_3$	1819709, 787721, 342767	727877, 326082, 139077	1819709, 787721, 342767	727877, 326082, 139077	1819709, 787721, 342767	727877, 326082, 139077
$\Phi_1$	189.32314	192.36540	1.41102	1.40747	34.07216	30.76221
$\Phi_2$	189.25554	192.70983	1.41104	1.40653	34.01215	30.79231
$\Phi_3$	189.46761	194.31359	1.41002	1.40387	33.89861	30.46523
$\Phi_{ext21}$	189.35476	192.27119	1.41102	1.40799	34.13941	30.75916
$p$	2.7312	3.8312	8.8747	2.5932	1.5235	5.9423
$e_a^{21}$ [%]	0.04	0.18	0.00	0.07	0.18	0.10
$e_{ext}^{21}$ [%]	0.05	0.23	0.00	0.10	0.37	0.11
$GCI_{32}^{medium}$ [%]	0.07	0.25	0.00	0.12	0.47	0.11
$GCI_{21}^{fine}$ [%]	0.02	0.06	0.00	0.05	0.25	0.01
			$\Phi: \eta_{rad, st}$ [-]		$\Phi: KED_A$ [kN]	
BL resolution	FR	WF	FR	WF	FR	WF
$N_1, N_2, N_3$	1819709, 787721, 342767	727877, 326082, 139077	1819709, 787721, 342767	727877, 326082, 139077	1819709, 787721, 342767	727877, 326082, 139077
$\Phi_1$	0.89635	0.89756	0.90127	0.90239	445.36159	427.93784
$\Phi_2$	0.89623	0.89752	0.90116	0.90235	445.93031	428.44047
$\Phi_3$	0.89655	0.89870	0.90146	0.90344	447.65178	428.18202
$\Phi_{ext21}$	0.89641	0.89756	0.90134	0.90240	445.08101	427.40581
$p$	2.4048	8.3679	2.3301	7.7852	2.6456	1.6566
$e_a^{21}$ [%]	0.01	0.00	0.01	0.01	0.13	0.12
$e_{ext}^{21}$ [%]	0.02	0.00	0.02	0.01	0.19	0.24
$GCI_{32}^{medium}$ [%]	0.03	0.00	0.03	0.01	0.24	0.07
$GCI_{21}^{fine}$ [%]	0.01	0.00	0.01	0.00	0.08	0.16

Table A.6: Results for grid discretization study for full FV BLI domain with k- $\omega$ -SST turbulence model. Reference fuselage-propulsor configuration. FR: Fully Resolved, WF: Wall Functions.

## **A.7 Appendix 7 - Parameter Study Results**

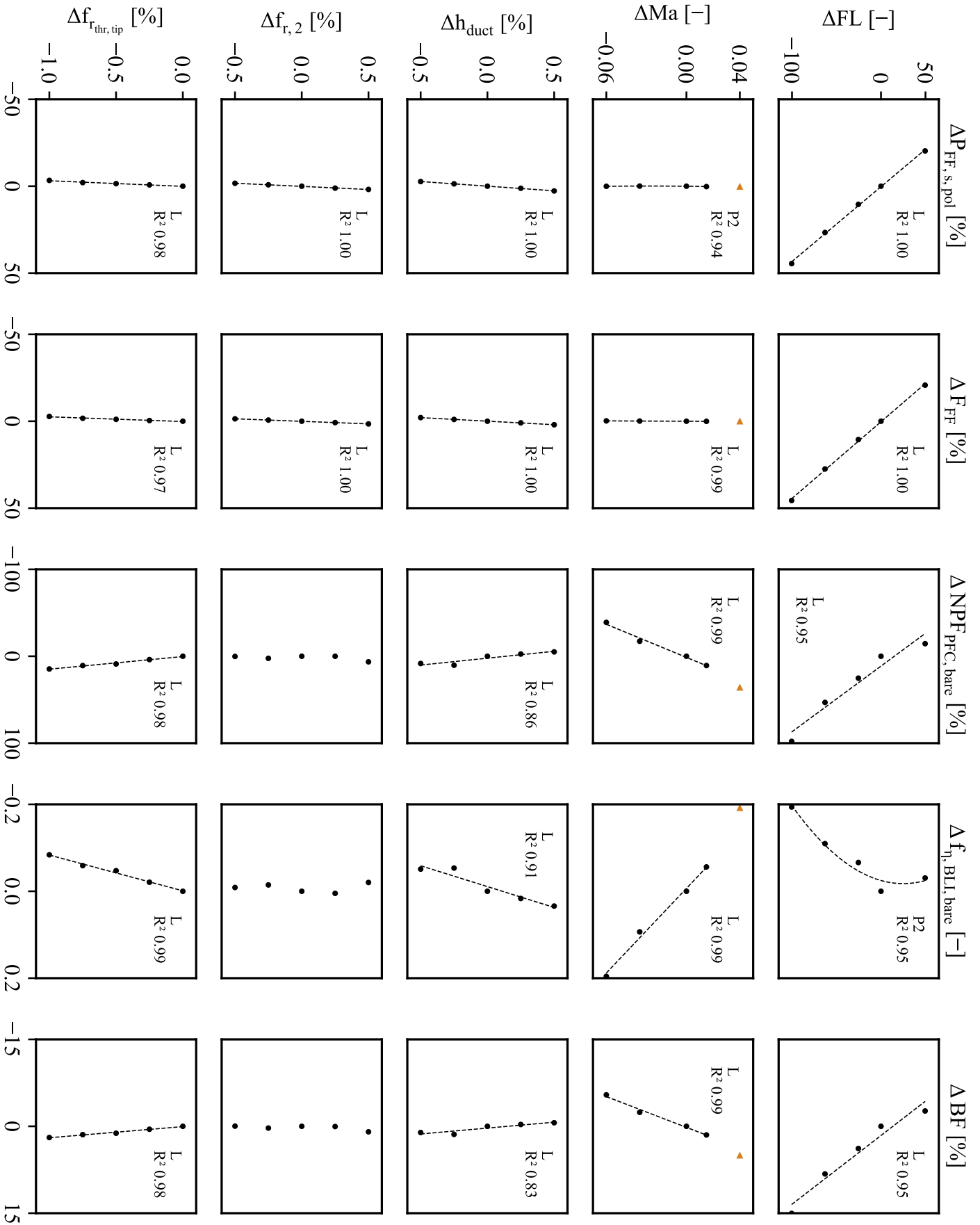


Figure A.6: Sensitivity study results 1/9. Linear (L) and Second Order Polynomial (P2) regressions are indicated for cases with  $R^2 > 0.8$ .

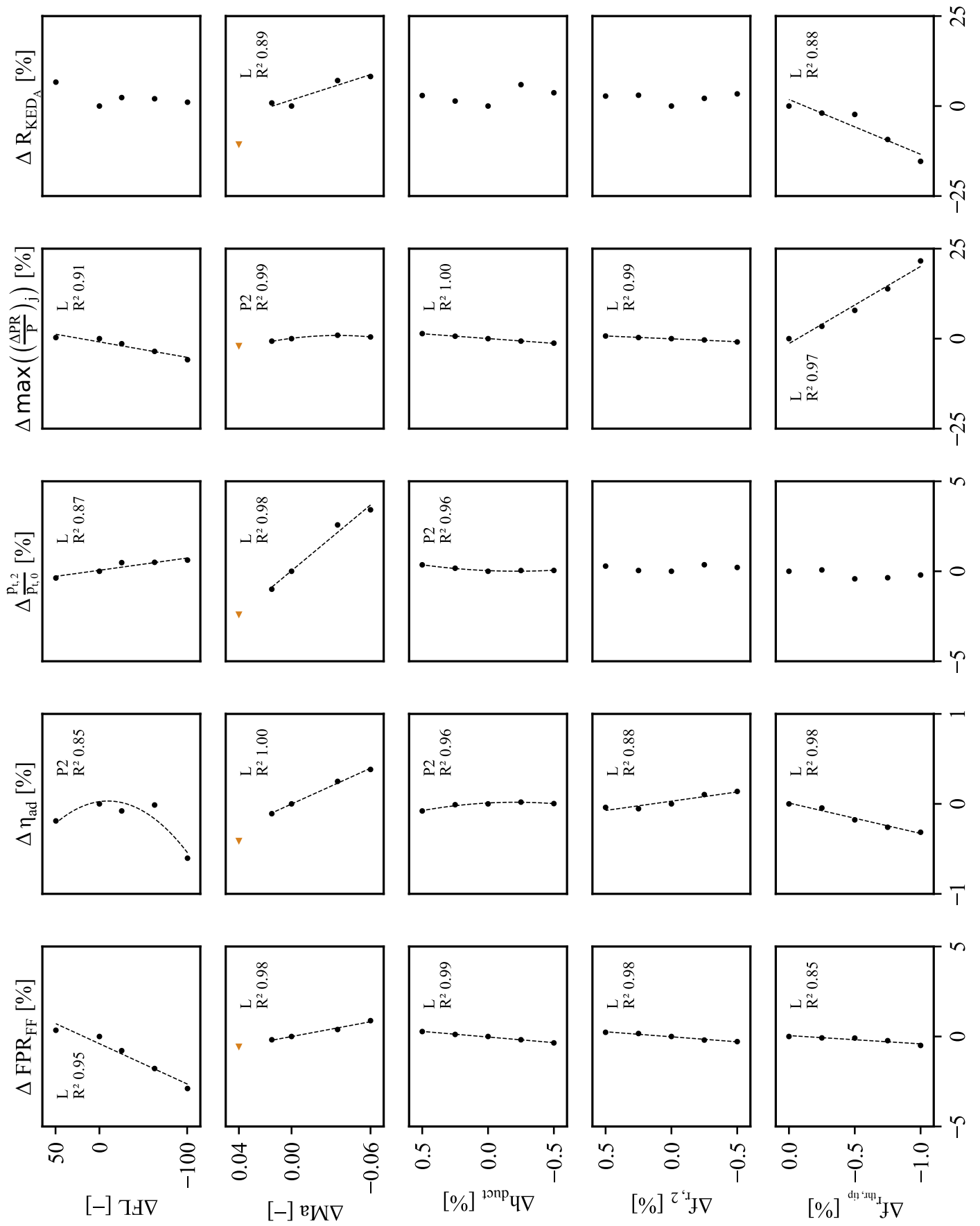


Figure A.7: Sensitivity study results 2/9. L and P2 regressions are indicated for cases with  $R^2 > 0.8$ .

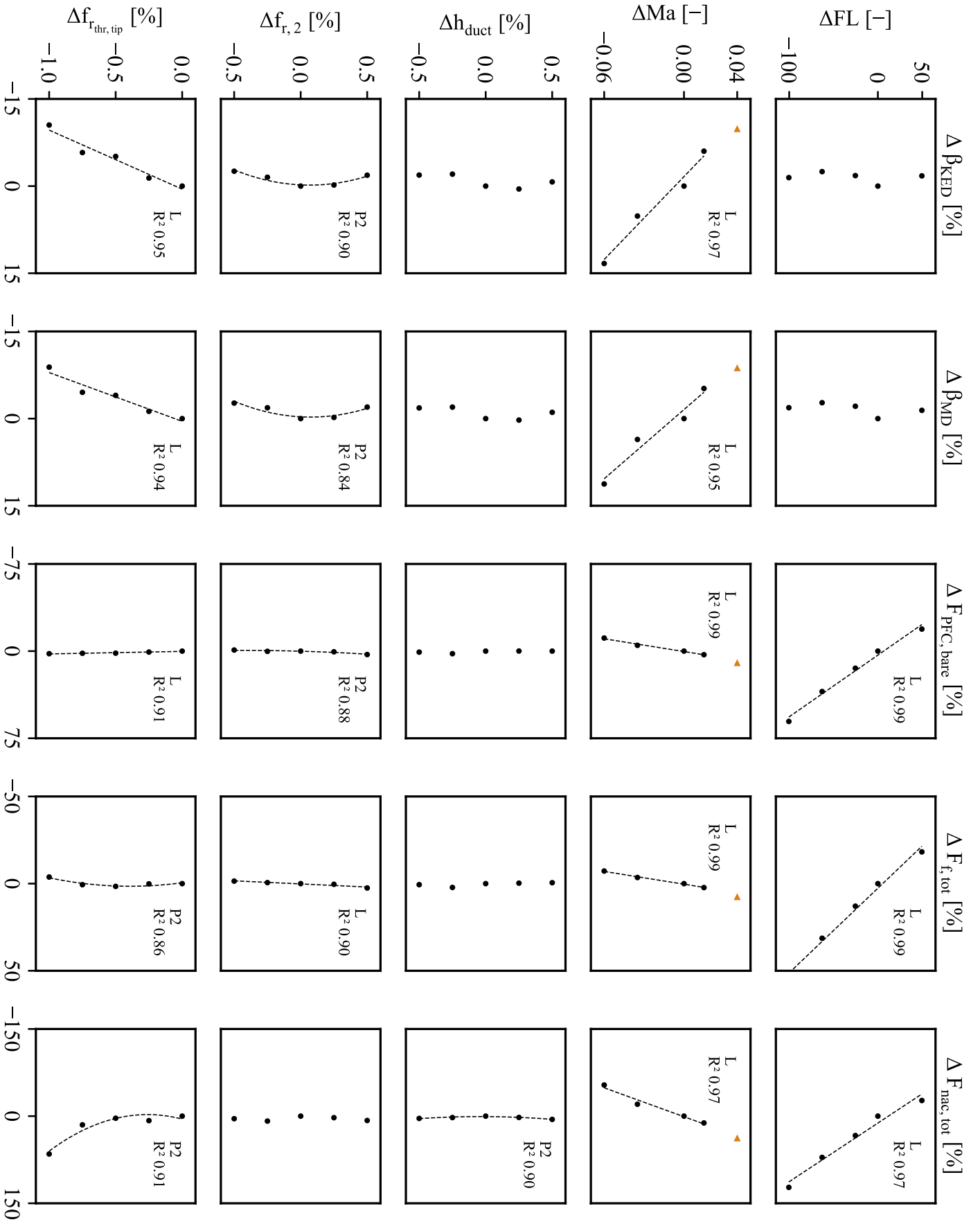


Figure A.8: Sensitivity study results 3/9. L and P2 regressions are indicated for cases with  $R^2 > 0.8$ .

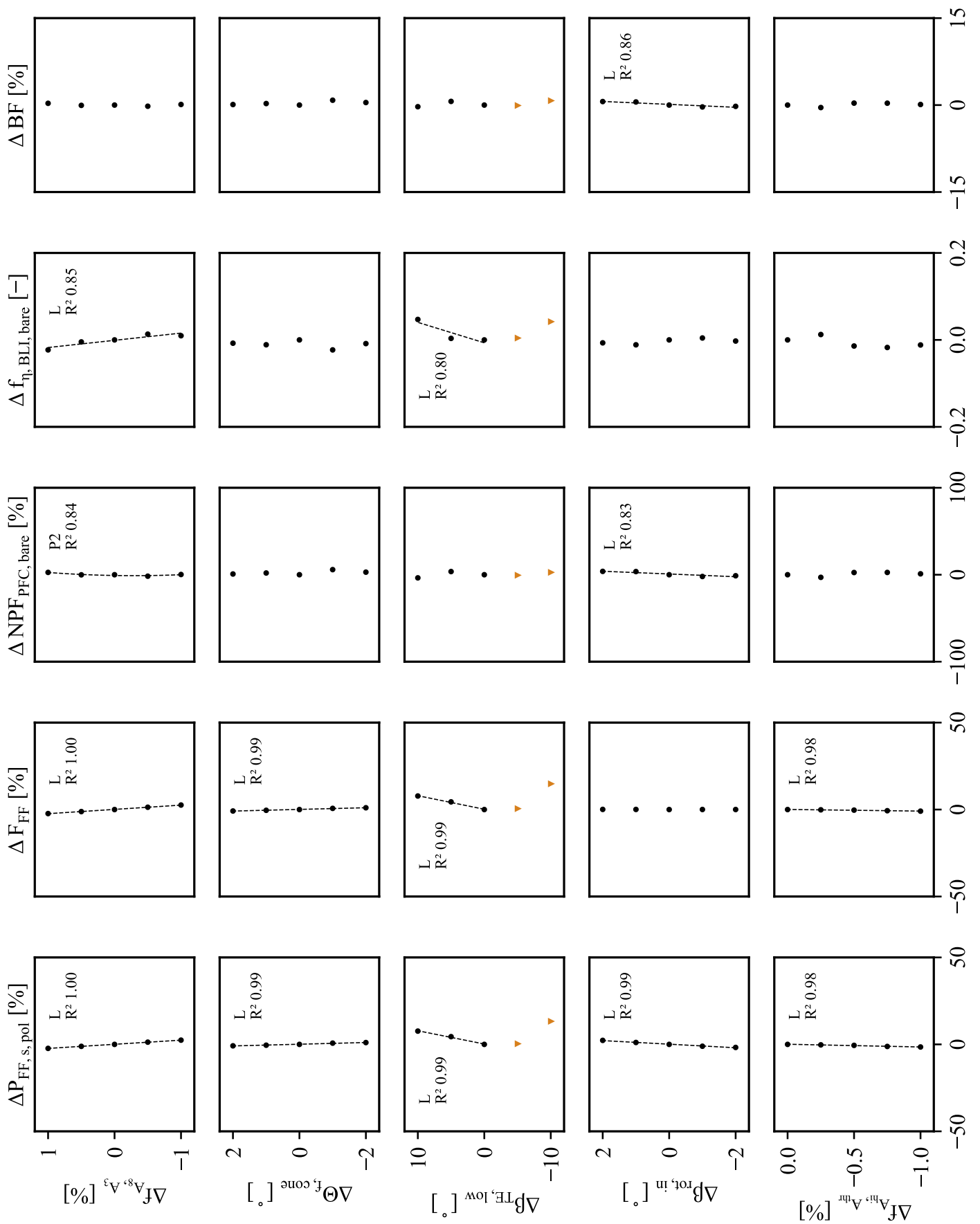


Figure A.9: Sensitivity study results 4/9. L and P2 regressions are indicated for cases with  $R^2 > 0.8$ .

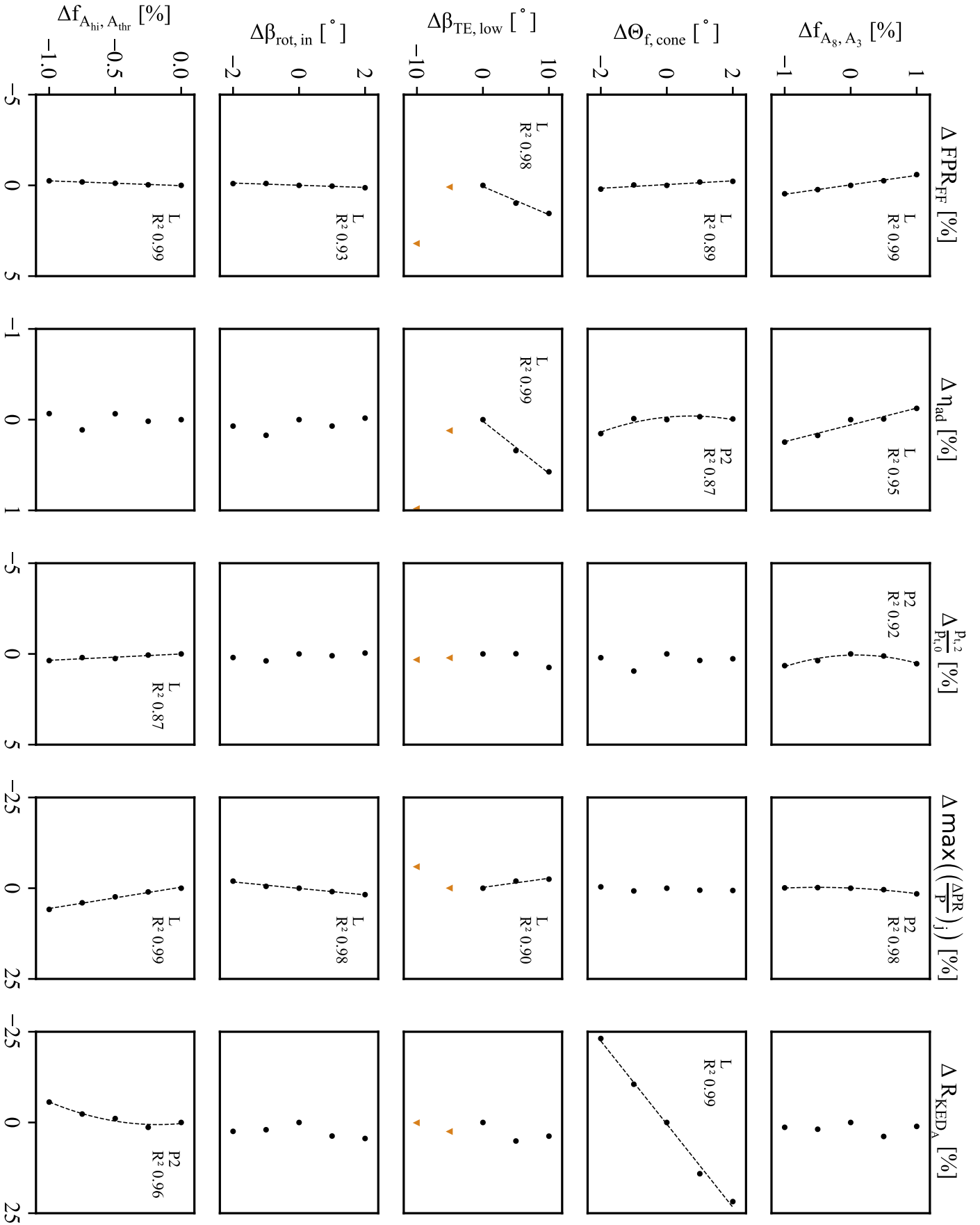


Figure A.10: Sensitivity study results 5/9. L and P2 regressions are indicated for cases with  $R^2 > 0.8$ .

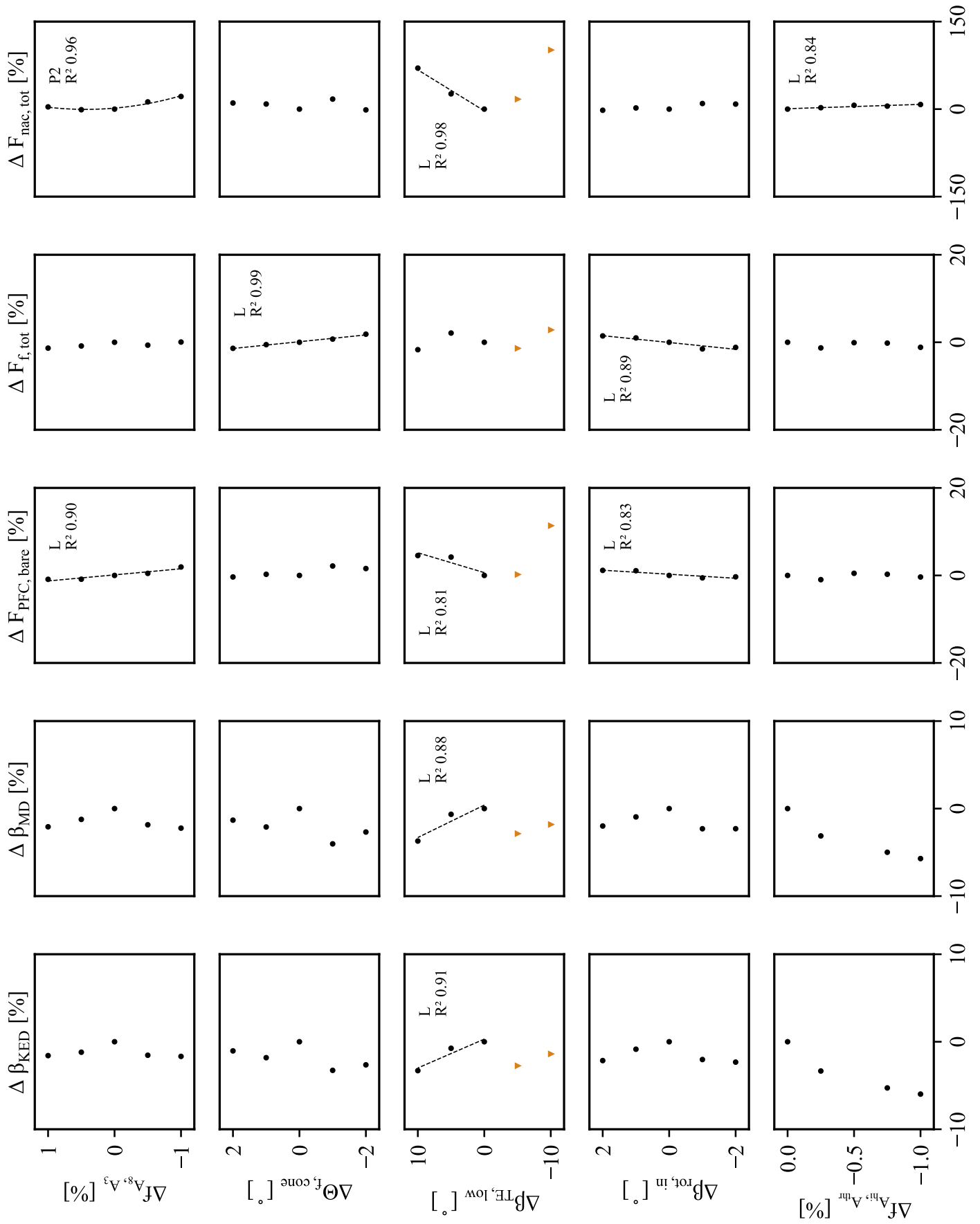


Figure A.11: Sensitivity study results 6/9. L and P2 regressions are indicated for cases with  $R^2 > 0.8$ .

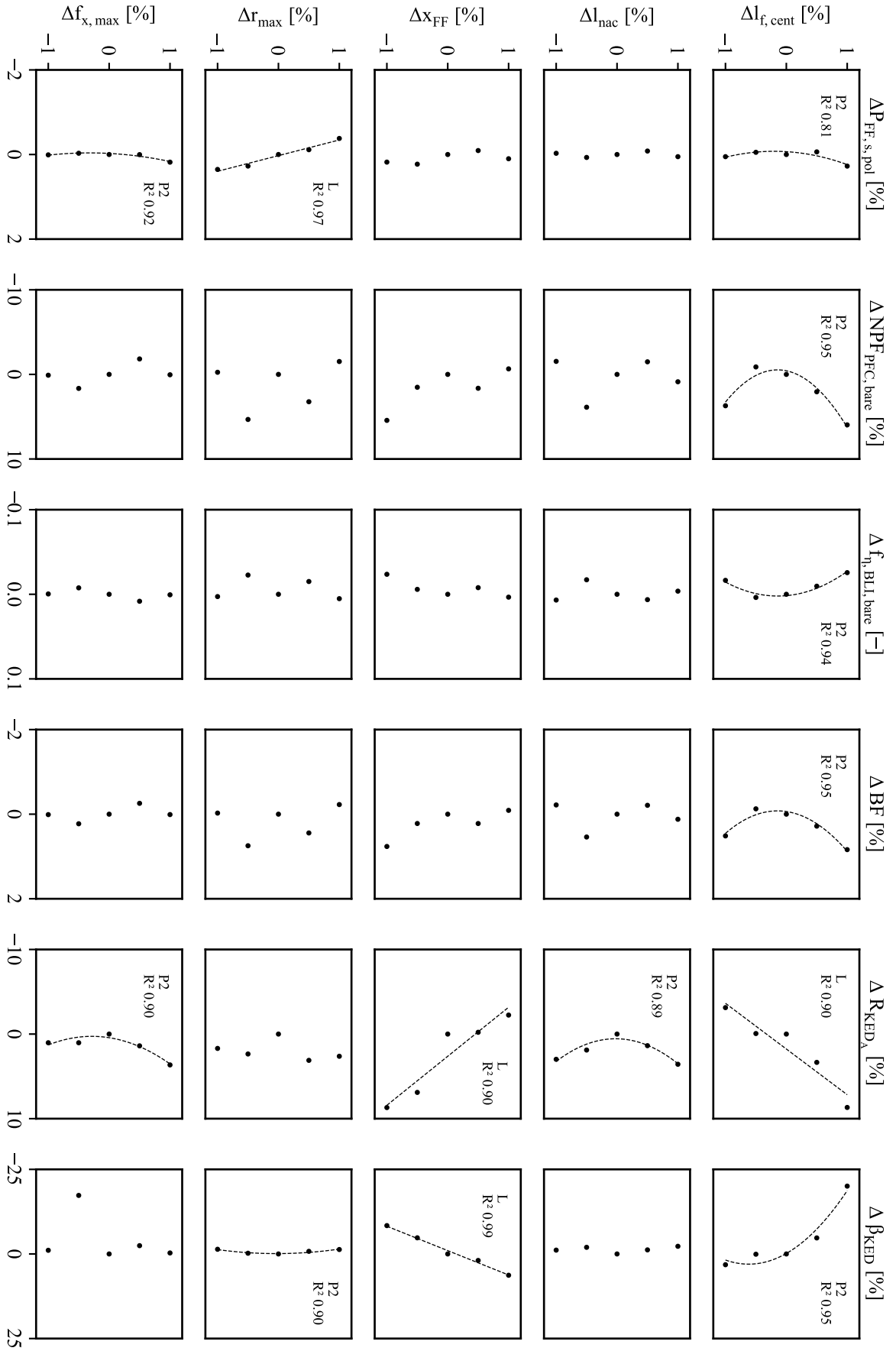


Figure A.12: Sensitivity study results 7/9. L and P2 regressions are indicated for cases with  $R^2 > 0.8$ .

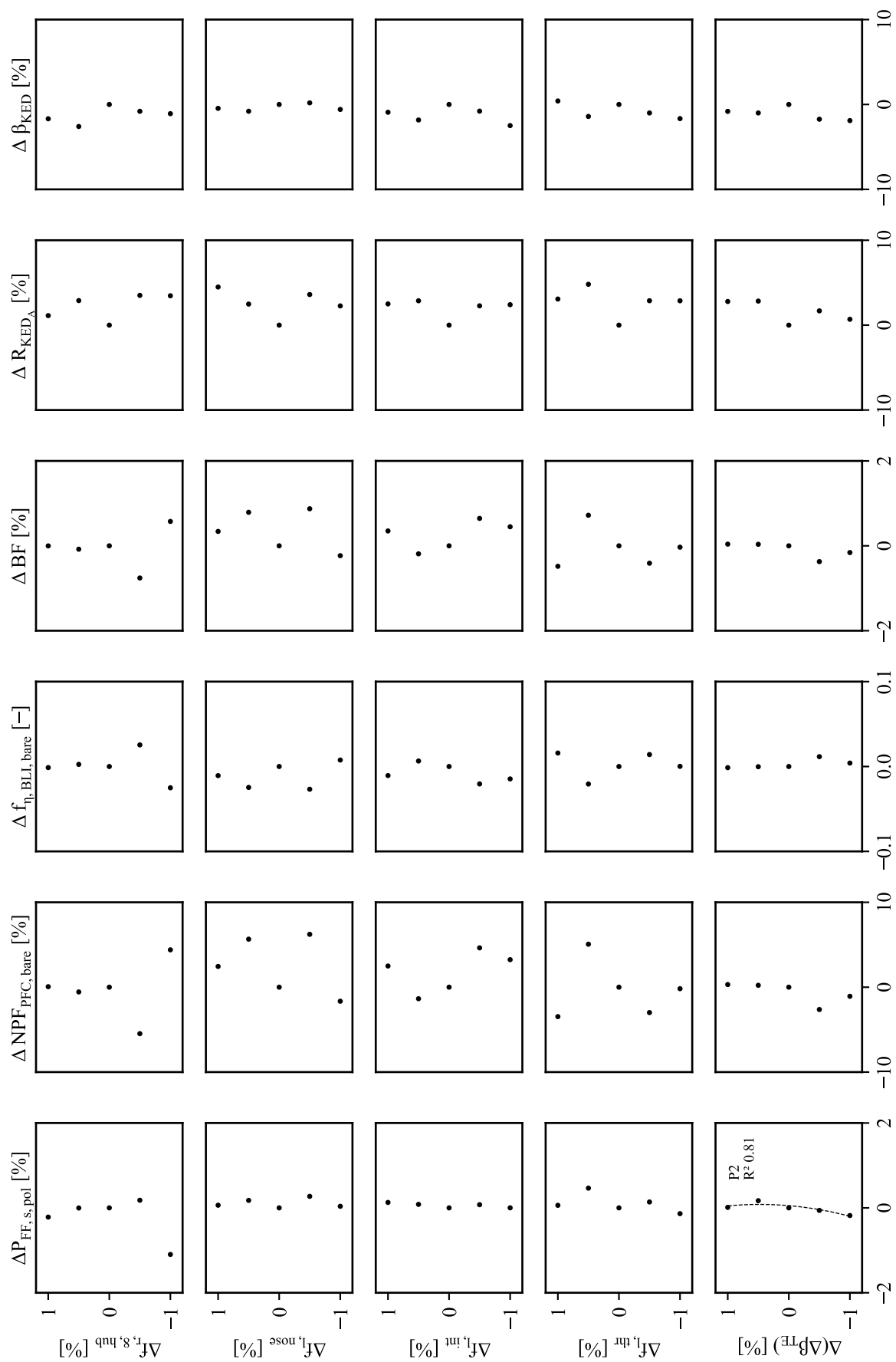


Figure A.13: Sensitivity study results 8/9. L and P2 regressions are indicated for cases with  $R^2 > 0.8$ .

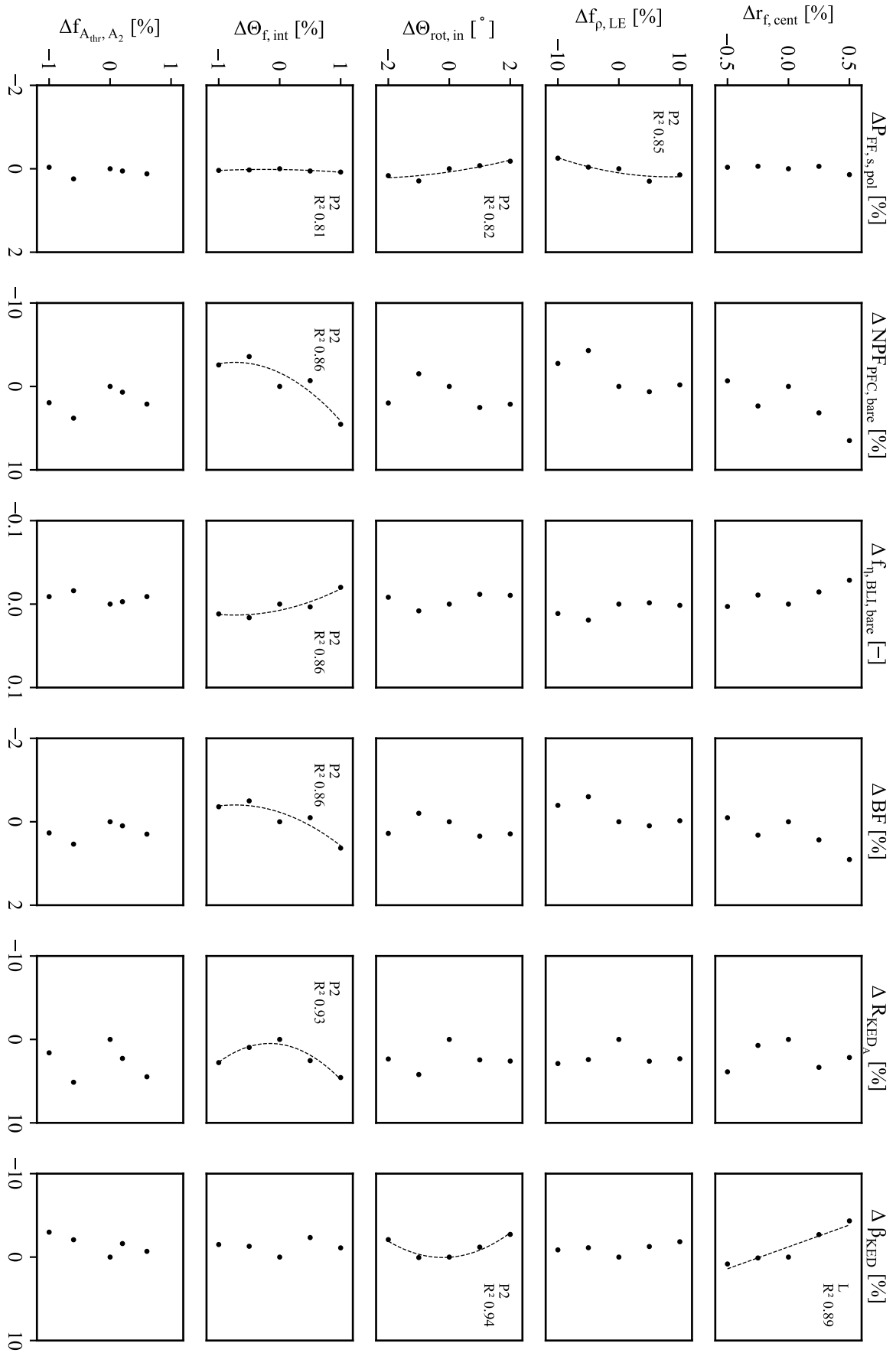


Figure A.14: Sensitivity study results 9/9. L and P2 regressions are indicated for cases with  $R^2 > 0.8$ .

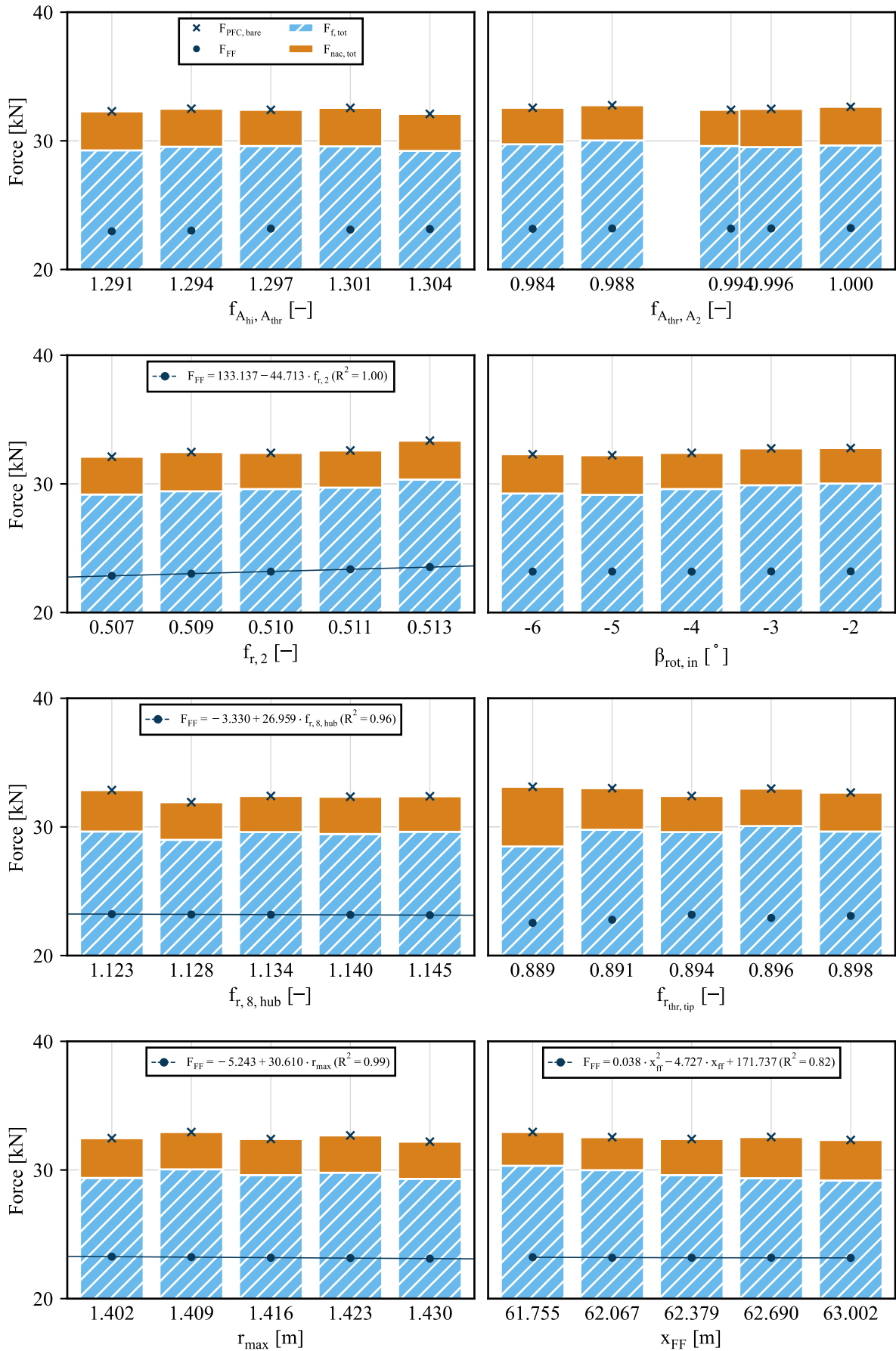


Figure A.15: Selected sensitivity study results - surface and FF forces. Regressions are indicated for  $F_{FF}$  with  $R^2 > 0.8$ .